DOE/ER-0313/75
ORNL/TM-2024/3325

FUSION MATERIALS
SEMIANNUAL PROGRESS REPORT
FOR THE PERIOD ENDING

December 31, 2023

Prepared for
DOE Office of Fusion Energy Sciences
(AT 60 20 10 0)

DATE PUBLISHED: March 2024

Prepared by
OAK RIDGE NATIONAL LABORATORY
Oak Ridge, Tennessee 37831
Managed by
UT-Battelle, LLC
For the
U.S. DEPARTMENT OF ENERGY

FOREWORD

This is the seventy-fifth in a series of semiannual technical progress reports on fusion materials science activity supported by the Fusion Energy Sciences Program of the U.S. Department of Energy. It covers the period ending December 31, 2023. This report focuses on research addressing the effects on materials properties and performance of exposure to the neutronic, thermal and chemical environments anticipated in the chambers of fusion experiments and energy systems. This research is a major element of the national effort to establish the materials knowledge base for an economically and environmentally attractive fusion energy source. Research activities on issues related to the interaction of materials with plasmas are reported separately.

The results reported are the products of a national effort involving a number of national laboratories and universities. A large fraction of this work, particularly in relation to fission reactor irradiations, is carried out collaboratively with partners in Japan, Russia, and the European Union. The purpose of this series of reports is to provide a working technical record for the use of program participants, and to provide a means of communicating the efforts of fusion materials scientists to the broader fusion community, both nationally and worldwide.

This report has been compiled by Stephanie Melton, Oak Ridge National Laboratory. Her efforts, and the efforts of the many persons who made technical contributions, are gratefully acknowledged.

Guinevere Shaw
Research Division
Office of Fusion Energy Sciences

TABLE OF CONTENTS

1 FERRITIC/MARTENSITIC STEEL DEVELOPMENT

2 ODS AND NANOCOMPOSITED ALLOY DEVELOPMENT

3 CERAMIC COMPOSITE STRUCTURAL MATERIAL DEVELOPMENT

TABLE OF CONTENTS

4 **PLASMA-FACING AND HIGH HEAT FLUX MATERIALS AND COMPONENT TESTING**

5.0 **HYDROGEN AND HELIUM EFFECTS**

TABLE OF CONTENTS

6.0 FUSION CORROSION AND COMPATIBILITY SCIENCE

7.0 ADVANCED MANUFACTURING

No contributions this reporting period.

8.0 MECHANISMS AND ANALYSIS

9.0 MODELING AND COMPUTATIONAL STUDIES

10 FUSION SYSTEM DESIGN

No contributions this reporting period.

11 IRRADIATION & TESTING METHODS, EXPERIMENTS AND SCHEDULES

TABLE OF CONTENTS

1. FERRITIC/MARTENSITIC STEEL DEVELOPMENT

1.1 MICROHARDNESS MEASUREMENT UPDATE FOR SELECTED SPECIMENS IN FH51, FH61, FH62, AND RB19J CAPSULES

—X. Chen, A. Guajardo, C. On, Y. Katoh (Oak Ridge National Laboratory), T. Nozawa (National Institutes for Quantum Science and Technology)

The extended abstract presents updates of hot cell microhardness measurements on selected SSJ3 and M4CVN specimens in FH51, FH61, FH62 and RB19J capsules

Vickers microhardness measurements were performed on selected SSJ3 and M4CVN specimens in FH51, FH61, FH62 and RB19J capsules. Measurements were made according to the schematic shown in Figure 1. The hardness tester used was a Mitutoyo model HV-120B tester located in Cell #4 of the Irradiated Materials Examination and Testing Facility at Oak Ridge National Laboratory. All tests were performed with 1 kg force and 15 sec dwell time. For each measurement result, the indentation image was checked to make sure the indentation is of sufficient quality for the hardness measurements. The measurement results are summarized in Tables 1 and 2. Except for M4CVN specimens TRCz, 0RFc, and TRDa, all other specimens showed reasonably small standard deviation in hardness measurements (≤5% of the average hardness values). To further investigate the fidelity of microhardness results, it is necessary to evaluate the irradiation condition, especially the irradiation temperature, of these specimens. Table 3 compares the target irradiation conditions with the achieved conditions. The irradiation temperature was measured by dilatometry measurements on SiC thermometry specimens which were in direct contact with irradiated specimens except for M4CVN specimens in FH61 and FH62 capsules which included a stainless steel filler bar between the M4CVN specimen and SiC thermometry specimen. Based on results in Table 3, the average irradiation temperatures were within a reasonable range, i.e., +/-30°C, from the design target. However, some individual irradiation temperature measurements were lower in FH51, FH61, and FH62 capsules while individual measurements were higher in the RB19J 300C position 3 holder.

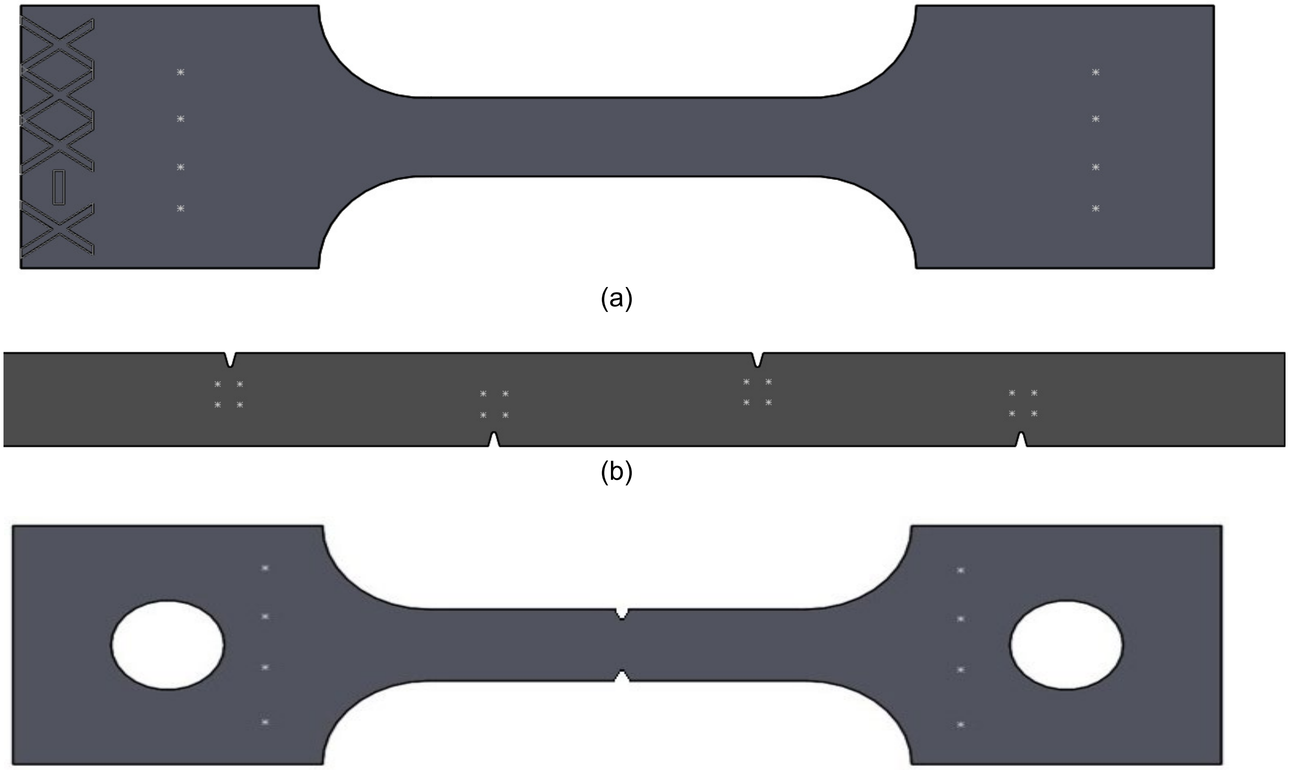

(a)

(b)

(c)

Figure 1. Schematic for indentations made for specimens in (a) FH51 (some specimens may contain notches), (b) FH61/FH62, and (c) RB19J capsules.

Table 1. Summary of microhardness measurement results for selected SSJ3 specimens in FH51 and RB19J capsules

Capsule ID	Specimen ID	Materials	Hardness measurements (HV)								Avg. HV	Std. Dev. HV
			Left tab				Right tab					
			1	2	3	4	1	2	3	4		
FH51	0RCk	F82H-IEA	331.2	314.9	328.4	331.2	329.8	318.9	327.7	327.1	326.2	6.00
	0RDy	F82H-IEA	335.5	322.9	320.2	334.1	321.6	317.6	310.4	316.9	322.4	8.55
	0RCh	F82H-IEA	326.4	326.4	327.7	327.7	334.8	329.1	341.4	339.1	331.6	6.02
	0RZ	F82H-IEA	296.2	299.2	311.1	309.8	312.3	309.8	307.2	308.5	306.8	5.85
	0RDu	F82H-IEA	312.3	309.1	312.3	311.7	316.9	320.9	329.8	325.0	317.3	7.34
	TRBu	F82H-BA12	339.9	340.8	353.8	349.8	325.3	323.2	329.8	337.5	337.5	11.00
	TRAp	F82H-BA12	352.9	369.3	358.2	378.8	371.0	369.0	363.7	363.4	365.8	8.04
	TR2	F82H-BA12	356.9	347.9	345.2	332.6	359.8	349.5	358.8	353.8	350.6	8.97
	TRBs	F82H-BA12	360.5	360.1	361.4	362.4	350.1	360.8	357.6	359.2	359.0	3.88
	TR4	F82H-BA12	355.4	356.3	363.0	363.0	365.3	347.0	340.7	365.3	357.0	9.09
	TRBt	F82H-BA12	354.3	355.8	358.2	355.8	364.6	368.7	352.7	355.0	358.1	5.59
	TR1	F82H-BA12	346.6	370.4	354.3	347.3	346.6	342.8	348.9	366.3	352.9	10.12
	TRAm	F82H-BA12	354.3	372.1	354.3	359.0	379.7	376.3	380.6	364.6	367.6	11.01
	0RU	F82H-IEA	290.9	306.0	306.6	301.0	298.6	300.4	301.0	314.9	302.4	6.98
	TRAo	F82H-BA12	369.6	369.6	363.0	378.9	365.4	357.4	352.7	359.8	364.6	8.23
	0RDx	F82H-IEA	315.6	314.3	305.4	319.6	299.2	307.9	299.8	306.0	308.5	7.42
	TR3	F82H-BA12	372.9	378.9	355.0	354.3	375.4	374.6	373.7	368.7	369.2	9.41
	TRAn	F82H-BA12	325.7	341.4	347.3	348.1	351.9	344.3	345.8	352.7	344.7	8.51
	0RCf	F82H-IEA	304.7	296.2	292.1	299.8	288.6	300.4	289.2	282.9	294.2	7.29
	0RAa	F82H-IEA	334.8	332.7	332.0	314.9	319.6	320.2	316.9	321.6	324.1	7.83
	0RAb	F82H-IEA	310.4	321.6	307.2	318.9	316.3	310.4	290.3	318.2	311.7	9.96
	0RCg	F82H-IEA	306.0	301.0	312.3	320.2	309.1	311.7	302.9	309.8	309.1	6.03
	TRBr	F82H-BA12	359.8	353.5	351.9	347.3	363.8	362.2	367.1	380.6	360.8	10.41
	0RDw	F82H-IEA	329.8	339.9	320.9	327.1	332.0	315.6	329.1	323.6	327.3	7.39
RB19J	TV53	F82H-BA12	293.2	276.9	295.6	279.1	264.4	285.2	286.3	289.7	283.8	10.12
	0V54	F82H-IEA	259.4	263.9	265.9	268.0	266.9	269.0	262.9	263.4	264.9	3.14
	TV77	F82H-BA12	298.6	302.3	306.0	302.9	290.3	293.2	298.6	307.9	300.0	6.05
	0V52	F82H-IEA	265.9	259.0	274.2	259.9	261.4	250.4	258.0	265.4	261.8	6.96
	SV54	F82H-BA07	262.4	280.7	273.7	265.4	-	269.5	267.5	277.5	271.0	6.63
	0V55	F82H-IEA	237.9	244.5	246.7	244.5	264.4	260.4	257.0	245.8	250.2	9.26
	SV77	F82H-BA07	274.8	263.4	255.6	247.6	244.5	250.4	263.4	266.4	258.3	10.45
	0V53	F82H-IEA	239.6	249.9	250.4	243.1	250.9	248.6	256.1	262.9	250.2	7.19

	0V76	F82H-IEA	250.4	252.7	253.2	265.9	256.5	262.4	255.6	252.3	256.1	5.39
	0V78	F82H-IEA	254.6	266.9	265.9	259.0	263.4	257.5	265.4	265.4	262.3	4.59
	0V77	F82H-IEA	252.7	257.0	259.0	253.7	263.4	249.9	256.1	259.9	256.5	4.34
	SV53	F82H-BA07	268.0	275.8	269.5	256.5	254.2	254.6	253.2	253.7	260.7	8.95
	TV78	F82H-BA12	292.7	295.0	298.6	295.6	299.8	299.8	286.9	284.1	294.1	5.88
	TV54	F82H-BA12	299.2	296.2	295.0	300.4	309.1	302.3	305.4	281.8	298.7	8.23
	TV76	F82H-BA12	282.9	290.3	282.4	277.5	257.0	280.7	285.7	287.4	280.5	10.29
	SV52	F82H-BA07	273.7	282.9	284.6	274.8	283.5	286.3	285.2	276.9	281.0	5.03
	TV52	F82H-BA12	296.2	302.9	297.4	307.9	305.4	304.1	305.4	303.5	302.9	4.04
	SV76	F82H-BA07	285.7	280.7	292.7	282.4	284.1	286.9	284.1	278.0	284.3	4.40
	SV78	F82H-BA07	290.9	286.9	287.4	285.2	279.6	285.7	289.2	285.7	286.3	3.34

Table 2. Summary of microhardness measurement results for M4CVN specimens in FH61 and FH62 capsules

Capsule ID	Specimen ID	Materials	Notch ID	Hardness measurements (HV)				Avg. notch HV	Avg. specimen HV	Std. Dev. HV
				1	2	3	4			
FH61	TRCz	F82H-BA12	D	505.4	473.4	491.3	494.9	491.3	418.9	54.87
			M1	364.3	354.1	394.9	359.5	368.2		
			M2	367.6	366.0	381.2	419.9	383.7		
			U	464.8	404.2	469.1	392.3	432.6		
	TRCy	F82H-BA12	D	376.3	388.5	378.0	392.2	383.8	372.2	15.16
			M1	358.2	359.0	376.3	377.2	367.7		
			M2	387.7	351.9	359.0	369.6	367.1		
			U	385.9	337.7	382.3	374.6	370.1		
	0RFe	F82H-IEA	D	328.4	327.1	325.7	319.6	325.2	322.6	7.56
			M1	316.9	316.3	325.0	310.4	317.2		
			M2	325.0	312.3	319.6	316.9	318.5		
			U	322.3	334.1	323.6	339.1	329.8		
	0RFc	F82H-IEA	D	399.5	372.1	378.9	449.6	400.0	385.1	24.50
			M1	378.9	392.2	-	350.4	373.8		
			M2	385.9	385.0	-	352.7	374.5		
			U	407.1	373.7	371.2	394.0	386.5		
FH62	TRDa	F82H-BA12	D	360.6	407.1	351.2	413.9	383.2	351.7	33.16
			M1	333.4	305.4	306.0	378.0	330.7		
			M2	313.0	376.3	318.9	379.7	347.0		
			U	342.1	351.2	351.2	339.1	345.9		

	0RFg	F82H-BA12	D	325.0	319.6	325.7	334.1	326.1	334.2	13.40
			M1	321.6	352.7	327.1	333.4	333.7		
			M2	334.1	353.5	339.9	303.5	332.8		
			U	345.1	345.8	345.1	341.4	344.4		
	0RFf	F82H-IEA	D	310.4	316.9	310.4	325.7	315.9	307.8	8.55
			M1	308.5	316.3	309.8	295.0	307.4		
			M2	312.3	301.0	299.2	292.1	301.2		
			U	303.5	304.1	312.3	307.9	307.0		
	TRDb	F82H-IEA	D	348.9	343.6	357.4	337.7	346.9	341.9	10.47
			M1	334.8	336.2	335.5	345.1	337.9		
			M2	332.0	333.4	337.7	319.6	330.7		
			U	350.4	345.1	356.6	356.6	352.2		

Table 3. Target vs. achieved irradiation conditions for FH51, FH61, FH62, and RB19J

Capsule	Target dose (dpa)	Target irradiation temperature (°C)	Thermometry ID	Measured irradiation temperature (°C)	Avg. irradiation temperature (°C)	Irradiation temperature std. dev. (°C)
FH51	5	300	001 (tier 1)	296	275	28.4
			006 (tier 2)	287		
			011 (tier 3)	243		
FH61	5	300	07-top	276	278	17.8
			07-middle	303		
			07-bottom	262		
			05-middle	270		
FH62	5	300	11-top	264	283	16.1
			11-middle	303		
			11-bottom	280		
			09-middle	286		
RB19J (300C position 3 holder)	~2.5-3	300	11-6-2	333	328	6.6
			11-6-4	318		
			11-6-6	332		
			11-6-8	331		
			11-6-9	324		
			11-6-10	316		
			11-6-11	330		
			11-6-12	325		
			11-6-13	330		
			11-6-14	336		

Correlation of Vickers hardness from Tables 1 and 2 and the irradiation temperature from Table 3 is shown in Figure 2 for F82H-BA12, F82H-IEA, and F82H-BA07 irradiated in designated capsules. A few key observations can be made here:

- Lower irradiation temperature (275-283°C vs. 328°C) and higher irradiation dose (~2.5-3 vs. 5 dpa) resulted in higher Vickers hardness in F82H-BA12 and F82H-IEA
- For the same irradiation condition, F82H-BA12 exhibited higher Vickers hardness than F82H-IEA
- Specimens irradiated in FH61 showed much higher Vickers hardness than the same material irradiated in similar conditions (i.e., FH51 and FH62). A recheck of hardness indentation for specimens in FH61 will be performed

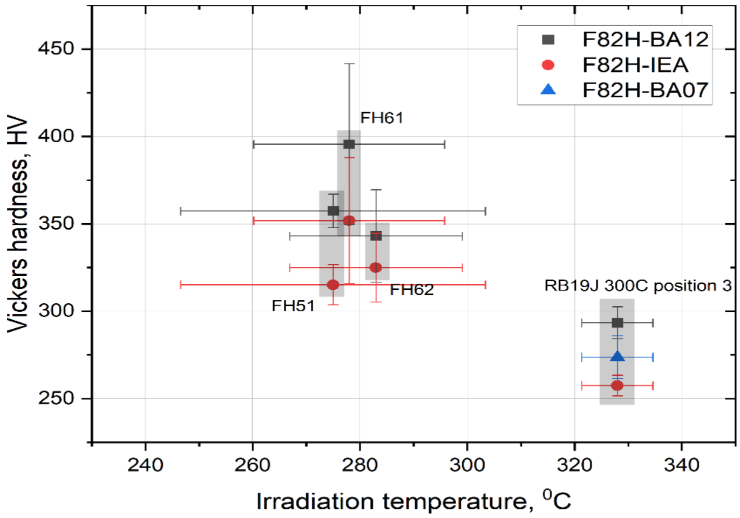

Figure 2. Correlation of Vickers hardness and irradiation temperature for F82H-BA12, F82H-IEA, and F82H-BA07 irradiated in designated capsules.

1.2 SINGLE ION REIRRADIATION OF DUAL ION IRRADIATED TEMPERED MARTENSITIC ALLOYS EXPERIMENT TO MEASURE POST INCUBATION VOID SWELLING RATES

—T. Yamamoto, G. R. Odette (University of California Santa Barbara), P. Hosemann, S. R. Lam, K. Yoon (University of California Berkeley)

OBJECTIVE

The objective of this research is to characterize how cavity and other microstructural evolutions under single ion irradiations following dual-ion irradiation to start void-swelling in 9Cr tempered martensitic steels (TMS). This report describes irradiation plan details and experimental preparation.

SUMMARY

Re-irradiation experiments of dual-ion irradiated (DII) F82H TMS alloys to measure post-incubation swelling rate have been designed. Sink-evolution and defect-partitioning based swelling models are applied to estimate anticipated post-incubation swelling for DII-induced microstructures.

BACKGROUND

Void swelling (S_v) is defined in terms of the observed void volume fraction (f_v) in an irradiated alloy as $S_v = f_v/(1-f_v)$. Swelling generally involves three stages of microstructural evolution [1,2]: a) an incubation stage of the stable growth of gas bubbles by the addition of transmutant helium atoms, but with negligible swelling; b) a transient stage, associated with an increasing fraction of the stably growing bubbles converting to unstably growing voids (due to an excess vacancy flux to void sinks) beyond a critical size, which defines an incubation dose (dpa_i); and, c) a quasi-steady-state swelling rate stage, associated with growing voids. The incubation dpa_i is sensitive to many material and irradiation variables, such as alloy type, composition, and starting microstructure, the dpa and dpa rate (dpa'), irradiation temperature, and the He/dpa ratio (appm He/dpa). The transient stage is somewhat less sensitive, while the steady state is least sensitive, eventually reaching a swelling rate, of $f_v' \approx 1\%/dpa$ in austenitic stainless steels [3]. For a number of reasons, bcc TMS are much more swelling resistant than fcc austenitic stainless steels, but they generally behave in a qualitatively similar manner [1,2]. Specifically, TMS have much larger dpa_i in low He/dpa fast reactor irradiations, as well as inherently lower post-incubation swelling rates of up to $f_v' \approx 0.2\%/dpa$ [2, 3]. However, as illustrated in Figure 1 [2], TMS do swell, reaching high levels at large dpa-dpa_i. The swelling can be described by a master curve shape, which collapses data over a wide range of ion irradiation conditions [2]. The goal of the research is to use post-incubation irradiated steels, which contain a population of voids and bubbles, to measure the post-incubation swelling rate and to provide a foundation for multiscale multi-physics models. Note: post-incubation swelling rate data also provides critical input to models that predict the incubation dpa_i [1].

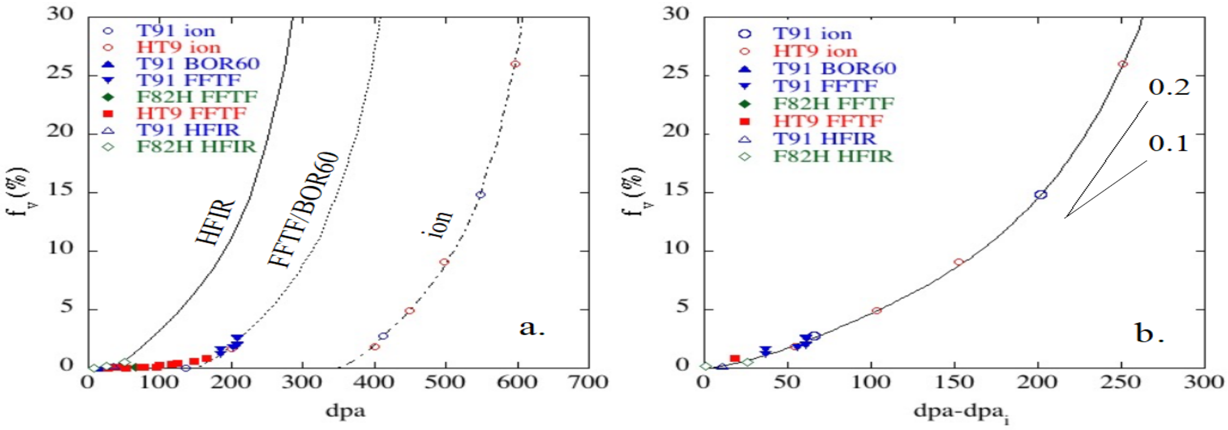

Figure 1. a) Literature f_v data as a function of dpa for low He single ion and fission neutron irradiations and b) the corresponding $f_v(\text{dpa} - \text{dpa}_i)$, with the same master same curve shape [2].

PROGRESS AND STATUS

Introduction

Figure 1 shows that the nominal TMS dpa$_i$ ranges from ≈ 150 to 350 for fission and ion irradiations, respectively [2]. Our hypothesis is that by re-irradiating TMS, with a pre-existing population of voids and bubbles, it will be possible to establish the post-incubation swelling behavior up to high dpa and, especially, how it is affected by the starting pre-irradiated microstructure. The specimens to be single ion irradiated, at the University of Michigan Ion Beam Laboratory (MIBL), were previously DII in the DuET facility at the Institute of Advanced Energy, Kyoto University in Japan. There, Fe^{3+} and He^+ ions were accelerated to 6.4 MeV and 1 MeV, respectively, to generate the dpa damage and implant He at controlled He/dpa [1]. The He^+ ion beam passes through a rotating energy degrader foil with varying thicknesses to create four ion energies, and corresponding He ranges, resulting in a broad and relatively uniform He/dpa deposition profile from ~ 200 to 1100 nm. The He (appm)/dpa ranged from ~ 5 to 60. This is, of course, much higher than in fission neutron irradiations, which are typically produce much less than 1 appm He/dpa. However, the dual ion irradiations resulted in much lower dpa$_i$ as shown in Figure 2a. Indeed, dpa$_i$ systematically decreases with increasing He/dpa as shown in Figure 2b. The swelling rate ($\Delta f_v/\Delta \text{dpa}$) also decreases with He/dpa as shown in Figure 2c. Thus, the dual ion irradiation conditions result in a population of growing void containing regions with f_v up to more than 4%, as shown in Figure 2d. The dual ion irradiation conditions also results in a varying population of helium bubbles and an evolved dislocation structures resulting a sufficient net interstitial bias needed to generate an excess flux of vacancies at growing voids.

Post-incubation swelling can be understood in terms of simple partitioning of vacancy and self-interstitial defects between the various sinks, with the corresponding excess flux of vacancies accumulating at voids, while the excess flux of self-interstitial atoms goes to biased dislocations. Neglecting vacancy emission from voids and recombination, a simple model for the post-incubation swelling rate (f_v’), for such partitioning, is given by

$$f_v' \approx \eta k_v k_d B_d /[(k_d + k_b + k_v)(k_d(1 + B_d) + k_b + k_v] \quad (1)$$

Here, η is the vacancy generation per dpa; the subscripts b, v and d label bubbles, voids and dislocations, respectively; the k are sink strengths; and B is the net dislocation interstitial bias factor. As shown in Figure 2f, the post-incubation swelling rate is maximum, $f_v' \approx 0.25\eta B_d$, when $k_v = k_d$ and $k_b = 0$. Bubble sinks (larger k_b) and imbalances between ($k_d \neq k_v$) decrease f_v’.

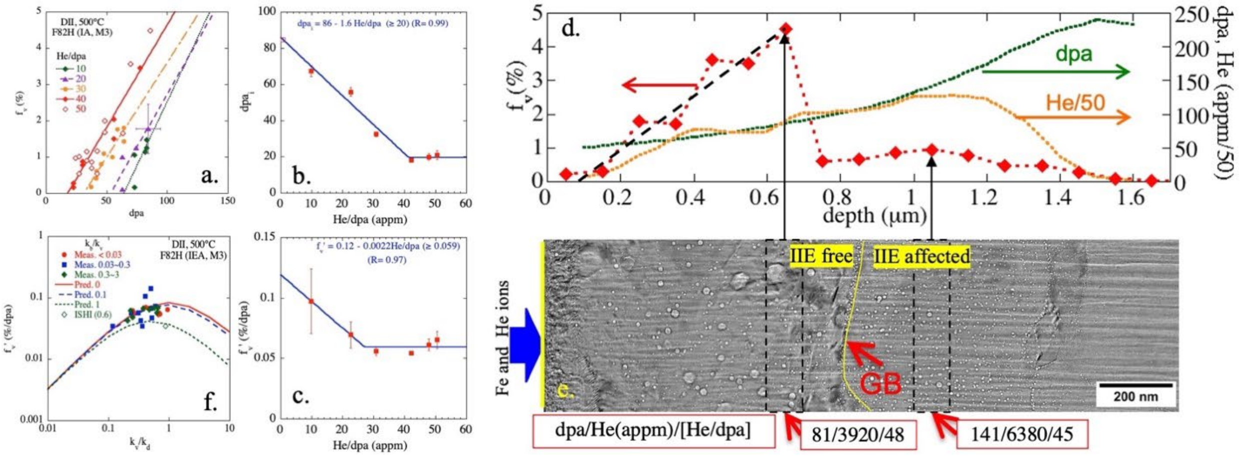

Figure 2. a) f_v vs. dpa at various He/dpa; b) cross plots of dpa_i (f_v extrapolated to 0) vs. He/dpa; c) cross plots of f_v' vs. He/dpa; d) f_v vs. depth along with He and dpa profiles; e) corresponding TEM images of the bubbles and voids as a function of depth (note the interface highlighted in yellow protects the shallower regions from the injected interstitial effect which would otherwise suppress swelling); f) post-incubation f_v' as a function of the microstructure (k_v/k_d, k_b/k_v).

Experimental Procedure

Table 1 summarizes DII conditions for the specimens selected for the re-irradiation. The cavity microstructures of the specimens were fully characterized as reported in [1]. They show populations of bubbles and voids, which vary with depth and location (hence, dpa and He conditions) in each specimen. Each specimen is being cut to 5mm length, which consists of 2mm long DII area and an unirradiated support area, as shown in Figure 3a. Parts of the DII and the adjacent areas are being trenched to refer surfaces for swelling height measurements, which are masked during the single ion irradiation (SII).

The micro-machined specimens are loaded in the irradiation target in a holder assembly as illustrated in Figure 3b. The assembly will be irradiated with 9 MeV Fe^{3+} ion to a nominal dose of 150 dpa at ~ 500°C. Then the macroscopic swelling will be first measured with a profile as an increase in the step height between the irradiated and the reference surface. Liftouts of the irradiated region will be extracted for detailed microstructural studies us a variety of characterization techniques. The irradiation will be repeated in two more to a total nominal dose of 450 dpa. The mask size will be changed between each dpa increment to retain the part of previously irradiated area, which will then be available for further characterization.

Table 1. Dual-ion Irradiation conditions of the Selected Re-irradiation Specimens

Exp ID	T (°C)	Nominal Condition (@550-650nm)				Peak He (@1000-1100 nm)			Alloys
		dpa	He (appm)	He/dpa	dpa/s	dpa	He (appm)	He/dpa	
DI13B1	500	30	848	29	1.5×10^{-3}	51	1467	29	IEA
DI14A1	500	30	1200	47	1.3×10^{-3}	45	2100	47	M3
DI15A1	500	51	1360	27	8.6×10^{-4}	88	2350	27	IEA M3
DI16A+19A	500	82	3700	45	6.5×10^{-4}	142	6400	45	M3

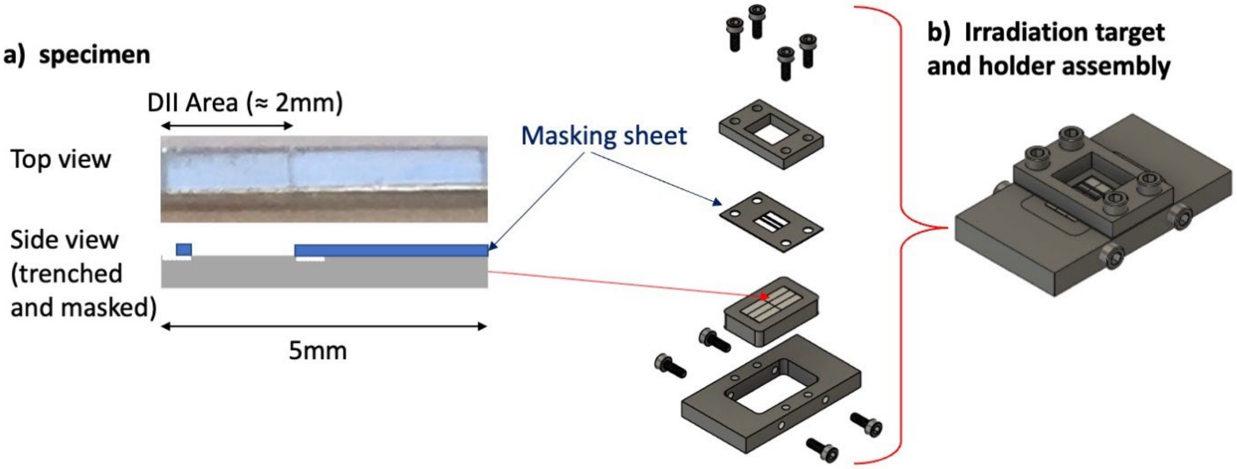

Figure 3. a) DII specimens for re-irradiation; b) design of the re-irradiation target and holder assembly.

Defect partitioning models for post-incubation swelling

While Equation (1) gives a good approximation of swelling rate estimation, actual biases (B_j) depend on the dislocations and cavity microstructures that evolve under irradiation. Simple models treating the bias and cavity evolutions have been developed [1]. Here, these models are used to estimate an anticipated swelling during the re-irradiations, for different starting microstructures. Figure 4a shows examples of the models for the microstructures observed in F82H Mod.3 at various depths for the DII14A1 irradiation (see Table 1). The blue diamonds are the observed swelling at the depths from 1100 to 1600 nm from the irradiation surface, while the red lines show predicted trends of swelling for the corresponding microstructures. The predictions show anticipated post-incubation swelling rate varies from ~0.04%/dpa to ~ 0.07%/dpa to result in the swelling levels of ~ 8 to ~13% after the first 150 dpa re-irradiation leading a total (DII + SII) dpa ranging from 206 to 239. Figures 4b to d show similar predictions in other locations in the same Mod.3 DII14A1 specimen as well as in various locations in other four specimens. A few cases indicating no further swelling are due to the bubble sizes not large enough to turn overall dislocation bias positive for void growth. In all other cases, void swelling rates of ~ 0.01 to ~ 0.06 %/dpa or ~ 0.03%/dpa on average are predicted.

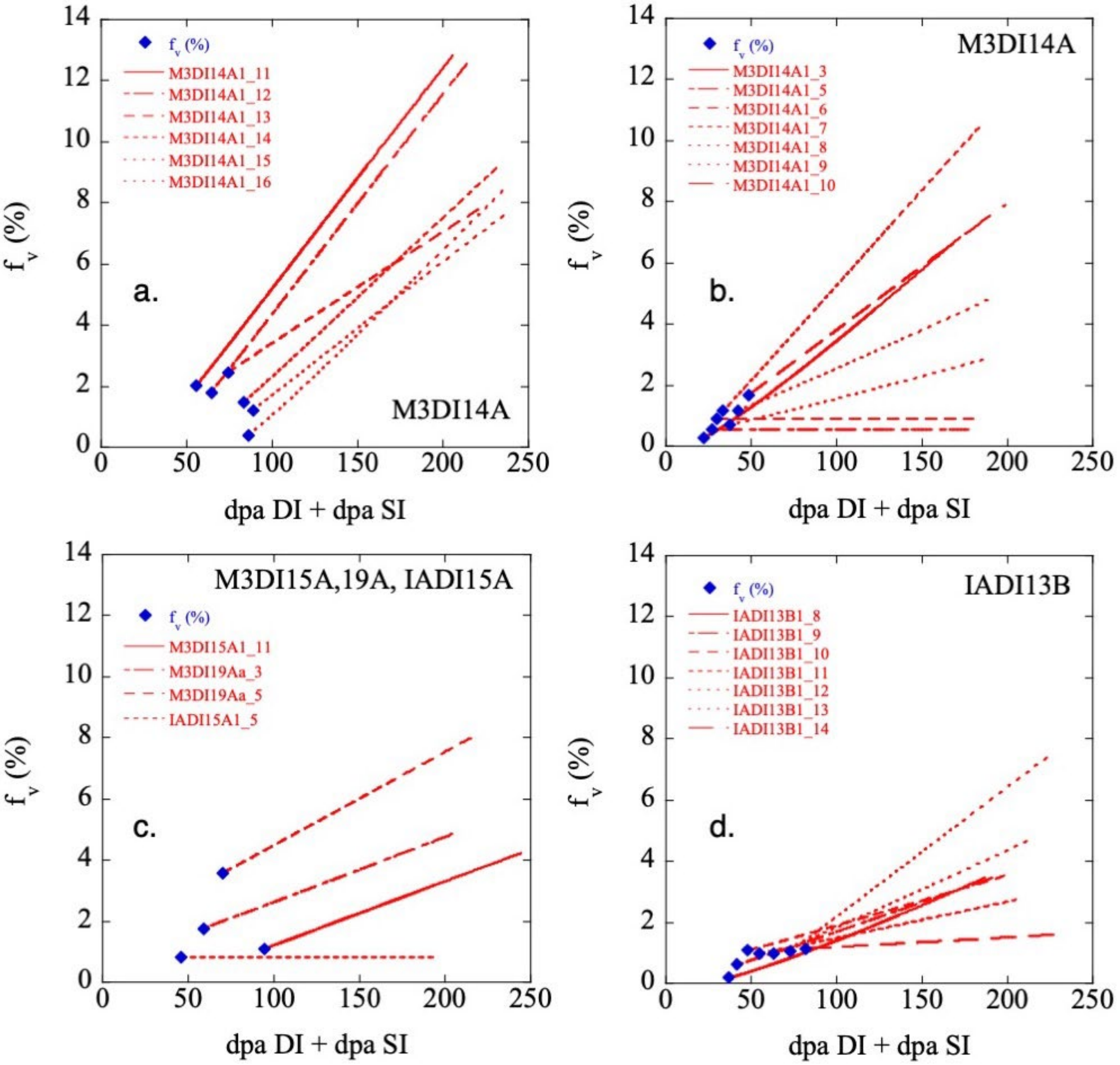

Figure 4. Examples of post-incubation swelling prediction models based on the defect-partitioning to evolving sink. The models were applied to previously observed microstructures in the microstructures observed after the original DII in the selected alloys.

Results

Re-irradiation experiments of DII F82H TMS alloys to measure post-incubation swelling rate have been designed. Sink-evolution and defect-partitioning based swelling models have been applied here to estimate, in advance, the anticipated post-incubation swelling for a range of DI microstructures.

Acknowledgments

The work being performed at the University of California Santa Barbara (UCSB) is supported by the U. S. Department of Energy (DOE), Office of Fusion Energy Sciences, under contract DE-FG03-94ER54275. The work being performed at the University of California Berkeley (UCB) is supported by Office of Fusion Energy Sciences, under contract DE-SC0023092. The MIBL irradiation is being supported by DOE Office of Nuclear Energy Rapid Turnaround Experiment Project #4662.

References

[1] T. Yamamoto, Y. Wu, K. Yabuuchi, J. Haley, K. Yoshida, A. Kimura, G.R. Odette, J. Nucl. Mater. 576 (2023) 154201.
[2] T. Yamamoto, G.R. Odette, J. Nucl. Mater. 576 (2023) 154085.
[3] F.A. Garner, M.B. Toloczko, B.H. Sencer, J. Nucl. Mater. 376 (2000) 123.

1.3 IRRADIATION STABILITY OF MX PRECIPITATES AT ELEVATED TEMPERATURES

—T. M. Green (Los Alamos National Laboratory), K. Field (University of Michigan), W. Zhong, T. Graening, Y. Yang (Oak Ridge National Laboratory)

OBJECTIVE

The goal of this project is to test the stability of strengthening MX precipitates in an advanced reduced activation ferritic martensitic (RAFM) steel subjected to intensive ion fluences and elevated temperatures. This initial set of experiments used single ion beam (Fe) irradiations to isolate the effects of damage level (dpa) and temperature on precipitate stability as preliminary testing to ultimately assess the effects of helium on MX precipitate response under dual beam (Fe + He) irradiations.

SUMMARY

The CNA9 is one model alloy from the Castable Nanostructured Alloy (CNA) family with the composition designed and manufactured to contain a high density of MX-TiC precipitates but no $M_{23}C_6$ precipitates [1]. As such, this simplified microstructure was chosen for fundamental studies of MX precipitate stability under fusion-relevant ion irradiation conditions. The current testing established the baseline behavior of the MX precipitates under single ion (9 MeV Fe^{3+}) irradiations to 1, 5, 15, 50, and 100 dpa at various temperatures (300, 400, 500, and 600°C) using a damage rate of 7×10^{-4} dpa/s. At 15 dpa, the MX precipitates underwent partial dissolution at low temperatures (300, 400°C) but radiation-enhanced growth at elevated temperatures (500, 600°C). At 500°C, the precipitates had a dose-dependent evolution: stable at low doses (1, 5 dpa), growth at intermediated dose (15 dpa), and complete dissolution at high doses (50, 100 dpa). Thus, MX precipitates in CNA9 displayed dependencies on both damage level and temperature.

PROGRESS AND STATUS

As outlined in previous reports [1-6], CNAs have undergone extensive composition and fabrication optimization to achieve improved mechanical properties over traditional RAFM steels. It was hypothesized that the reason for these improvements was partially due to the increased phase fraction of nanoscale MX precipitates in the CNAs, in addition to smaller grain sizes and higher dislocation line densities [5-14]. These precipitates were also hypothesized to increase the onset of steady-state swelling under fusion operation due to acting as sinks for transmuted helium [15]. However, no previous studies have systematically evaluated the irradiation stability of the MX precipitates in CNAs or related materials (traditional FM and RAFM steels) in detail.

As such, CNA9 underwent extensive irradiation testing in this work. The first set of irradiations are shown in Table 1. The irradiation experiments were split between two series: the temperature series and the dose series. Precipitate behavior was characterized with Energy Dispersive X-ray Spectroscopy (EDS) capability on a scanning transmission electron microscope (STEM). The CNA9 had a pre-existing MX precipitate number density of $(2.7\pm0.3)\times10^{21}$ m^{-3}. Figure 1 shows the most notable trends in the MX precipitate responses to irradiation, summarized below.

- Temperature series to 15 dpa: MX precipitates had significant ballistic dissolution at low temperature irradiations and significant radiation-enhanced growth at high temperature irradiations.
- Dose series at 500°C: MX precipitates remained stable at low doses, grew at intermediate dose, and entirely dissolved at high doses.

Therefore, the diffusion of Ti, which is the rate-limiting species present in the MX precipitates, is theorized to be the driving factor for precipitate behavior during the temperature series experiments, where low diffusivity caused ballistic dissolution at low temperatures and radiation-enhanced diffusivity caused growth at elevated temperatures. However, the results of the evolution of precipitate behavior during the dose series at 500°C suggest precipitate stability is also a function of dose when temperature is held constant.

There are many factors why this may be the case, including Ti solute redistribution away from the MX precipitates [16], a low volume fraction of the MX phase causing a lack of Ti solute exchange between precipitates [17-19], and the loss of stabilizing interfacial dislocation structures [20-24].

Table 1. Details of the irradiation experiments as well as the resulting characterization of MX precipitates for each condition: the number density of precipitates (ρ), the equivalent diameters of precipitates (d_{eq}), and the volume fraction of precipitates (f). Bolded and italicized values mean a significant change was detected in that parameter. N.O. = not observed.

T_{irr} (°C)	Total dpa	Dose rate (dpa/s)	ρ (m^{-3})	d_{eq}(nm)	f
Control			$(2.7\pm0.3)\times10^{21}$	7.9±0.3	$(9.0\pm1.4)\times10^{-4}$
300/298.2	15/15.1	$7\times10^{-4}/7\times10^{-4}$	***$(0.9\pm0.2)\times10^{21}$***	8.7±0.6	***$(3.9\pm1.0)\times10^{-4}$***
400/399	15/15	$7\times10^{-4}/7.2\times10^{-4}$	***$(1.5\pm0.2)\times10^{21}$***	7.6±0.4	$(4.4\pm0.9)\times10^{-4}$
500/503	1/1.1	$7\times10^{-4}/7.4\times10^{-4}$	$(3.3\pm0.9)\times10^{21}$	6.6±0.4	$(6.9\pm0.2)\times10^{-4}$
500/502	5/5.3	$7\times10^{-4}/6.8\times10^{-4}$	$(2.9\pm0.9)\times10^{21}$	7.4±0.4	$(9.3\pm3.4)\times10^{-4}$
500/500.6	15/15	$7\times10^{-4}/7.1\times10^{-4}$	***$(1.7\pm0.3)\times10^{21}$***	***10.4±0.9***	$(11.1\pm2.3)\times10^{-4}$
500/499.8	50/50	$7\times10^{-4}/7.3\times10^{-4}$	N.O.	N.O.	N.O.
500/499.6	100/100	$7\times10^{-4}/7.4\times10^{-4}$	N.O.	N.O.	N.O.
600/601	15/15.4	$7\times10^{-4}/6.9\times10^{-4}$	***$(1.3\pm0.2)\times10^{21}$***	***14.9±2.2***	***$(42.0\pm11.0)\times10^{-4}$***

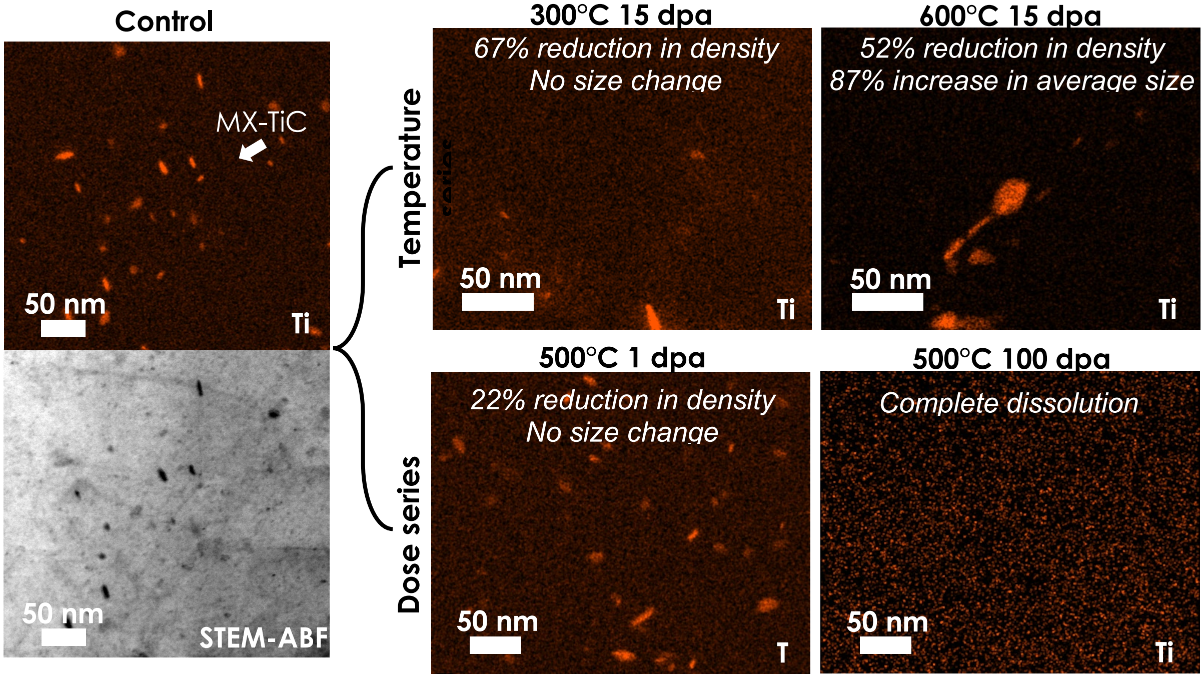
Control

300°C 15 dpa

67% reduction in density
No size change

600°C 15 dpa

52% reduction in density
87% increase in average size

500°C 1 dpa

22% reduction in density
No size change

500°C 100 dpa

Complete dissolution

Figure 1. The effects of irradiation on MX precipitate behavior during the temperature and dose series summarized with selected irradiation conditions. The STEM-EDS maps of Ti are shown for each condition, displaying the MX-TiC precipitates. ABF = annular bright field.

Results

The behavior of MX precipitation under single ion beam irradiation was analyzed in an advanced Fe9Cr steel called CNA9. Crucially, this work shows the instability of precipitates as a function of temperature and doses. Additional work is needed to understand how this instability impacts the mechanical strength and sink strength as a function of temperature and dose. The next report will present results of MX phase stability during corresponding dual beam (Fe + He) irradiations.

Acknowledgements

The experimental work presented here was funded by the Fusion Energy Sciences program (DOE-FOA-0002173). The authors also acknowledge the University of Michigan-Ann Arbor College of Engineering for financial support and the Michigan Center for Materials Characterization for use of the instruments and staff assistance. Partial support for T.M. Kelsy Green for drafting and analysis of the work contained within was supported under the Laboratory Directed Research and Development program of Los Alamos National Laboratory under project number XXPV.

References

[1.] *Fusion Materials Semiannual Progress Report for the Period Ending June 2021*. ORNL.
[2.] *Fusion Materials Semiannual Progress Report ending December 31 2021*. ORNL.
[3.] *Fusion Materials Semiannual Progress Report for the Period ending December 31 2022*. ORNL.
[4.] *Fusion Materials Semiannual Progress Report for the Period ending December 31, 2020*. ORNL.
[5.] Tan, L., *Report on the Down-Selected Nanoprecipitates-Strengthened Advanced Ferritic Alloys for Nuclear Reactor Applications*. 2019.
[6.] Tan, L., et al., *Recent status and improvement of reduced-activation ferritic-martensitic steels for high-temperature service.* Journal of Nuclear Materials, 2016. **479**: p. 515-523.
[7.] Tan, L., Y. Katoh, and L.L. Snead, *Development of castable nanostructured alloys as a new generation RAFM steels.* Journal of Nuclear Materials, 2018. **511**: p. 598-604.
[8.] Tan, L., *Development of Nanoprecipitates- Strengthened Advanced Ferritic Alloys for Nuclear Reactor Applications*. 2019.
[9.] Tan, L., L.L. Snead, and Y. Katoh, *Development of new generation reduced activation ferritic-martensitic steels for advanced fusion reactors.* Journal of Nuclear Materials, 2016. **478**: p. 42-49.
[10.] Zinkle, S.J., et al., *Development of next generation tempered and ODS reduced activation ferritic/martensitic steels for fusion energy applications.* Nuclear Fusion, 2017. **57**(9).
[11.] Tan, L., *Mechanical Properties and Radiation Resistance of Nanoprecipitates-Strengthened Advanced Ferritic Alloys*. 2017.
[12.] Tan, L., C.M. Parish, and X. Hu, *Microstructure and property tailoring of castable nanostructured alloys through thermomechanical treatments.* Journal of Nuclear Materials, 2018. **509**: p. 267-275.
[13.] Tan, L., T.S. Byun, Y. Katoh, and L.L. Snead, *Stability of MX-type strengthening nanoprecipitates in ferritic steels under thermal aging, stress and ion irradiation.* Acta Materialia, 2014. **71**: p. 11-19.
[14.] Tan, L., Y. Katoh, and L.L. Snead, *Stability of the strengthening nanoprecipitates in reduced activation ferritic steels under Fe2+ ion irradiation.* Journal of Nuclear Materials, 2014. **445**(1-3): p. 104-110.
[15.] Zinkle, S.J., A. Möslang, T. Muroga, and H. Tanigawa, *Multimodal options for materials research to advance the basis for fusion energy in the ITER era.* Nuclear Fusion, 2013. **53**(10).
[16.] T. Kimoto, H.S., *Void swelling and precipitation in a titanium-modified austenitic stainless steel under proton irradiation.* Journal of Nuclear Materials, 1985. **132**: p. 266-276.
[17.] Lescoat, M.L., et al., *In situ TEM study of the stability of nano-oxides in ODS steels under ion-irradiation.* Journal of Nuclear Materials, 2012. **428**(1-3): p. 176-182.
[18.] H.J. Frost, K.C.R., *Particle stability with recoil resolution.* Acta Metallurgica, 1982. **30**: p. 953-960.
[19.] Russell, K.C., *Phase instability under cascade damage irradiation.* Journal of Nuclear Materials, 1993. **206**: p. 129-138.

[20.] Markus Mock, P.S., Celine Hin, Karsten Albea, *Modeling the influence of strain fields around precipitates on defect equilibria and kinetics under irradiation in ODS steels: A multi scale approach.* Journal of Nuclear Materials, 2019. **527**(151807).

[21.] Vattre, A., et al., *Non-random walk diffusion enhances the sink strength of semicoherent interfaces.* Nat Commun, 2016. **7**: p. 10424.

[22.] Chen, T., et al., *Temperature dependent dispersoid stability in ion-irradiated ferritic-martensitic dual-phase oxide-dispersion-strengthened alloy: Coherent interfaces vs. incoherent interfaces.* Acta Materialia, 2016. **116**: p. 29-42.

[23.] Wang, L., et al., *Effect of sink strength on coherency loss of precipitates in dilute Cu-base alloys during in situ ion irradiation.* Acta Materialia, 2021. **210**.

[24.] Vaidya, W.V., *Modification of the precipitate interface under irradiation and its effect on the stability of precipitates.* Journal of Nuclear Materials, 1979. **83**: p. 223-230.

1.4 ALLOY MODIFICATION OF PWHT-FREE REDUCED-ACTIVATION BAINITIC STEELS—Y. Yamamoto, T. Graening (Oak Ridge National Laboratory)

OBJECTIVE

This work aims to evaluate the advantages in the mechanical performance of newly proposed, modified 3Cr-3WVTa bainitic steels developed at Oak Ridge National Laboratory (ORNL). The proposed steel was designed to eliminate the need for post-weld heat treatment (PWHT), as well as providing improved mechanical properties of both base metal and weldments compared to those of existing commercial bainitic steels or ferritic-martensitic (F-M) steels. The target applications are high-temperature structural components in fusion reactors, such as helium-cooled vacuum vessels operating up to 450°C and blanket support structures operating up to 550°C. The first-generation steel containing an increased Mn and reduced C content showed significant improvement in high-temperature mechanical properties but suffered from embrittlement after a thermal exposure, which could be exacerbated by irradiation embrittlement. The present target is to seek new composition ranges of the steels with the same PWHT-free design concept, targeting no potential embrittlement after a thermal treatment at operating temperature or irradiation.

SUMMARY

A new alloy modification of the reduced-activation 3Cr-3WVTa bainitic ferritic steel with PWHT-free design was proposed. The target is to avoid the significant drop of the impact toughness observed in MLC02T (modified 3Cr-3WVTa steel) after a short-term thermal exposure at 500°C. A new series of alloy compositions with 5 wt.% of Cr, instead of the increased Mn addition in the MLC02T, were selected with expectation of improved hardenability by stabilizing the austenite phase at elevated temperature. The lowered C content was also applied to maintain low hardness in the as-welded or as-normalized conditions. Small additions of Ni were also evaluated. Thermodynamic calculation predicted that the increased Cr addition to 5 wt.% lowered the bainite and martensite start temperature compared to the original 3Cr-3WVTa steel, suggesting an improved hardenability. However, it was shown that a reduction of the carbon content from 0.1 to 0.03 wt.% cancelled out the effect of the Cr addition on the hardenability. Further addition of 1 wt.% Ni resulted in improving the hardenability similar to that of previously evaluated MLC02T. The experimental validation study of newly proposed alloys revealed that the calculation overestimated the hardenability improvement. Most of the proposed alloys formed ferrite and only the alloy with 5Cr-0.03C-1Ni formed fully bainitic structure after normalization. It is concluded that the alloys with 5Cr would not achieve the same characteristics observed in MLC02T.

PROGRESS AND STATUS

A compositionally modified 3Cr-3WVTa bainitic ferritic steel (Mod. 3Cr-3WVTa steel, ID: MLC02T) was proposed with an advanced alloy design to achieve a reduced property inhomogeneity across the weldment in as-welded condition, targeting a PWHT-free bainitic ferritic steel for fusion structural applications. The design strategy included to maintain or improve the hardenability of the steel and lower the hardness in the as-normalized or as-welded condition. The target characteristics was achieved by the increased addition of manganese together with the lowered carbon content. The modified steel also revealed the improved high-temperature creep properties in both, the base metal and the cross-weld specimens, and lower the ductile-brittle transition temperature in the as-normalized and as-welded condition than those of the original 3Cr-3WVTa steel. The experimental results suggested that the modified steel met with the expected characteristics for PWHT-free design. However, it was recently found that a short-term exposure at the potential service temperature (500°C) of the modified steel resulted in a significant drop of the impact toughness, which could be attributed to high Mn content of the steel similar to the irradiation embrittlement promoted by manganese.

Based on the background described above, a new alloy modification of the 3Cr-3WVTa bainitic steel with the same PWHT-free design concept was proposed, without using the Mn addition. Since the Cr addition up to 7 wt.% is also known to increase the stability of austenite phase at elevated temperature and retard the phase transformation, the addition of 5 wt.% of Cr, instead of the increased Mn addition in the MLC02T, was selected with expectation of improved hardenability. The lowered C content was also applied to maintain low hardness in the as-normalized or as-welded conditions. Because of potentially less effect of the Cr addition on the austenite stabilization, small additions of Ni (0.5 and 1.0 wt.%) were also included in the evaluation. Table 1 summarizes the nominal composition of newly proposed bainitic steels in the present study.

Table 1. Nominal composition of newly proposed bainitic steels (balanced Fe)

Name	Alloy composition, wt.%	Remarks
5Cr	5Cr-3W-0.2V-0.16Si-0.2Mn-0.1C	Based on original with additional Cr
5Cr-LC	5Cr-3W-0.2V-0.16Si-0.2Mn-0.03C	Low carbon content
5Cr-LCN1	5Cr-3W-0.2V-0.16Si-0.2Mn-0.03C-0.5Ni	Low carbon with 0.5 wt.% Ni addition
5Cr-LCN2	5Cr-3W-0.2V-0.16Si-0.2Mn-0.03C-1Ni	Low carbon with 1 wt.% Ni addition
Original	3Cr-3W-0.2V-0.16Si-0.4Mn-0.1Ta-0.1C	Require PWHT, proposed in 1990's [ref.]
MLC02T	3Cr-3W-0.2V-0.16Si-2Mn-0.1Ta-0.03C	Modified 3Cr-3WVTa, PWHT-free design

[ref.] R.L. Klueh et al., Int. J. Pressure Vessels and Piping, 84 (2007) 29-36.

The continuous cooling transformation (CCT) curves of the alloys proposed in this study were calculated by a thermodynamic calculation software, JMatPro v.11, as shown in Figure 1. The prediction revealed that the increased Cr addition to 5 wt.% lowered the bainite and martensite start temperature compared to the original 3Cr-3WVTa steel, suggesting that the improved hardenability is expected by the Cr addition. The ferrite formation was significantly retarded and disappeared in the calculated CCT. The reduction of the carbon content from 0.1 to 0.03 wt.% negatively impacted to the effect on the hardenability. Further addition of Ni, however, recovered the hardenability improvement, and the addition of 1 wt.% Ni ended up with the CCT curves similar to that of previously evaluated MLC02T.

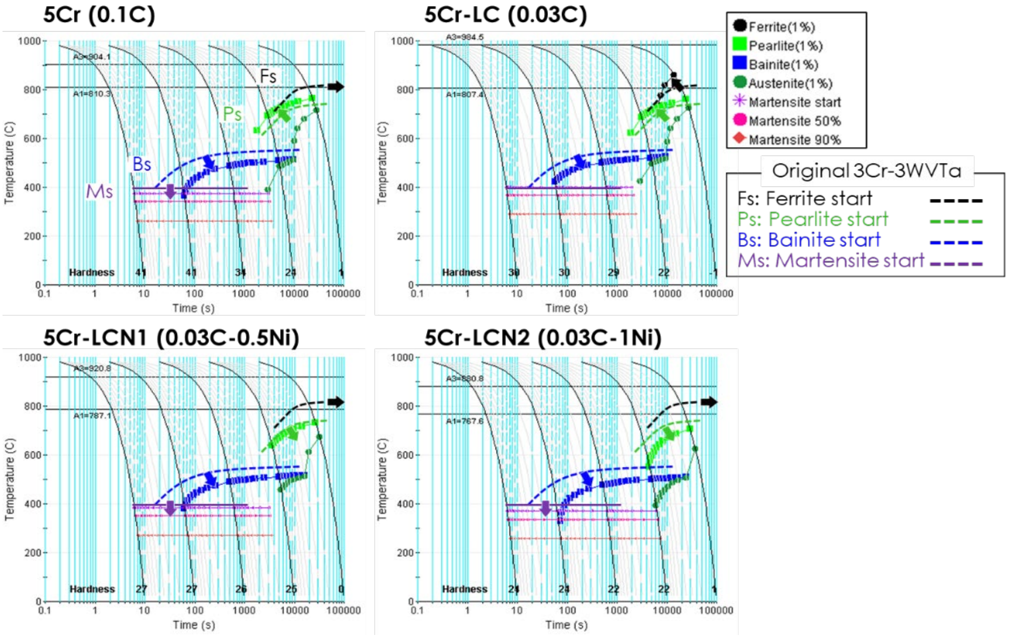

Figure 1. The CCT diagrams of 5Cr bainitic steels calculated by JMatPro v.11, showing the changes in various C-curves with the alloying additions compared to the original 3Cr-3WVTa.

The experimental validation study of newly proposed alloys was conducted by preparing laboratory heats with the target compositions in Table 1. The columnar ingots with the size of 36 mm in diameter and 90 mm in length were produced by arc-melting and drop-casting. They were homogenized at 1,200°C, and then forged at 1,000°C from the side of the ingot to make ~12 mm thickness plate. The ingots were subsequently annealed at 1,000°C for 1h, and then air-cooled to room temperature (= "as-normalized”). It should be emphasized that all four alloys are in the austenite single-phase region at 1,000°C, based on the thermodynamic calculations.

The optical micrographs of the as-normalized specimens are shown in Figure 2. Despite the calculation predicted all alloys would form fully bainitic structure with no ferrite formation after air cooling to room-temperature, three alloys out of four revealed that the calculation overestimated the hardenability improvement. The alloy 5Cr showed formation of ferrite grains inside the bainite ferrite matrix, suggesting that the increased Cr addition did not improve stabilizing austenite and suppress the ferrite formation as expected. The alloy 5Cr-LC formed a ferrite phase in the majority of the volume with a limited amount of bainite or martensite structure. Further addition of 0.5 wt.% Ni in 5Cr-LC resulted eliminating majority of the ferrite grains and mostly transforming into bainite, similar to those in the alloy 5C. Only the alloy 5Cr-LCN2 with 1 wt.% Ni demonstrated the formation of fully bainitic structure with no ferrite formation.

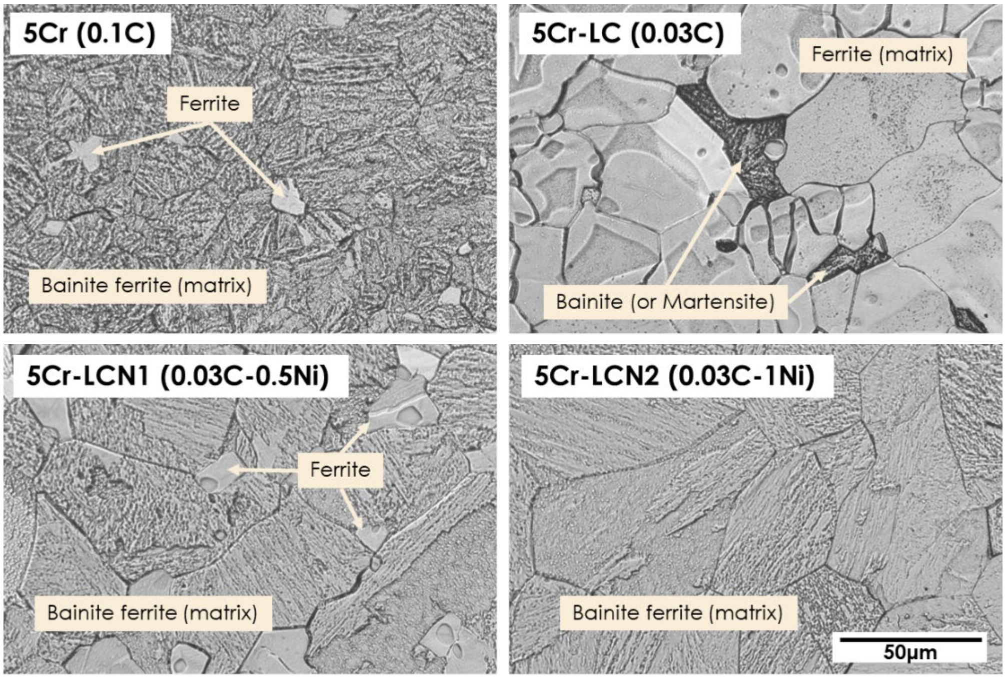

Figure 2. Optical micrographs showing as-normalized microstructure of newly proposed 5Cr steels.

Micro-Vickers hardness of newly proposed alloys in the as-normalized condition were compared with the original 3Cr-3WVTa steel and MLC02T, as shown in Table 2. The results were averaged from 25 indents with 500gf loading and 10 sec dwell time. The alloy 5Cr showed the highest hardness among all samples in this study, and the original 3Cr-3WVTa steel followed, which were attributed to higher C contents (0.1 wt.%) than the others. The alloy 5Cr-LC fell into the lowest hardness due to mostly ferritic microstructure with very little bainite formation. The alloys 5Cr-LCN1 and -LCN2 exhibited lower hardness than MLC02T, which might be due to not only the ferrite formation but also less hardenability improvement than that expected in the 5Cr-containing alloys.

Table 2. Micro-Vickers hardness (load: 500gf) of newly proposed alloys in as-normalized condition

	5Cr	5Cr-LC	5Cr-LCN1	5Cr-LCN2	Original 3Cr-3WVTa	MLC02T
HV0.5	367 ± 6	119 ± 4	238 ± 14	272 ± 7	339 ± 7	309 ± 7

Based on all these results together, it is concluded that the alloy modification of “Mn-free” 3Cr-3WVTa steel with the increased Cr addition would not reproduce the microstructural characteristics or the hardness observed in MLC02T. The addition of Ni compensates the loss of the hardenability for the “Mn-free + low C” alloy design. More Ni addition may be required for further hardenability improvement, although it would be prohibitive due to the tradeoff of irradiation penalty from high Ni contents. Therefore, no further property evaluation is to be conducted in the present alloys. Another approach to modify the alloy composition is needed, with its development currently in progress.

Results

The alloys with 3 wt.% Cr, low Mn, and low C are selected to be the basis for next-generation PWHT-free reduced-activation bainitic ferritic steels. The combined additions of austenite stabilizing elements, such as Ni, N, etc., will be evaluated with the controlled amounts to minimize the irradiation penalty from the additions. The role of Mn in the embrittlement of MLC02T also needs to be identified, and the detailed characterization of the long-term aged specimens is currently in progress.

1.5 CARBON CONTENT EFFECT ON CREEP BEHAVIORS OF CASTABLE NANOSTRUCTURED ALLOYS

—W. Zhong, Y. Yang (Oak Ridge National Laboratory), E. Proehl (University of Tennessee)

OBJECTIVE

The $Cr_{23}C_6$ and MC (M = V/Ta/Ti primarily) are two common types of precipitates in Reduced Activation Ferritic Martensitic (RAFM) steels. The equilibrium volume fraction of these precipitates is primarily controlled by carbon content. The objective of this work is to investigate the carbon content effect on the creep behaviors of castable nanostructured alloys (CNAs). In this work, creep behaviors of CNAs with two different carbon contents are reported, and the microstructure of the CNAs after creep fracture are also presented.

SUMMARY

Two heats of CNAs, CNA8 and CNA9, were designed to have different carbon content (0.1 and 0.05 wt% respectively). The different carbon contents lead to different precipitate formation in the alloys. Our previous report showed that CNA8 and CNA9 have similar tensile behaviors with respect to their strength and elongation. However, these two CNAs show different creep behaviors. Low-C CNA9 shows lower minimum creep rate but shorter creep life whereas high-C CNA8 has higher minimum creep rate but longer creep life. The results demonstrate the effects of $Cr_{23}C_6$ precipitate on the creep behaviors of CNAs.

PROGRESS AND STATUS

The CNAs were tested at 650˚C with various stress (150MPa, 110MPa, 90MPa, and 65MPa). Figure 1a shows the creep strain as a function of time and Figure 1b shows creep rate as a function of creep strain. In both figures, high-C CNA8 and low-C CNA9 were plotted using dashed lines and solid lines respectively. The creep test for high-C CNA8 at 650˚C, 65MPa is still on-going. Both CNAs exhibit common creep behaviors that consists of primary, secondary and tertiary stages. For all investigated creep conditions in this work, CNA9 exhibits lower or comparable minimum creep rate than CNA8. On the other hand, CNA8 has delayed the onset of tertiary creep, and it has higher creep life than CNA9.

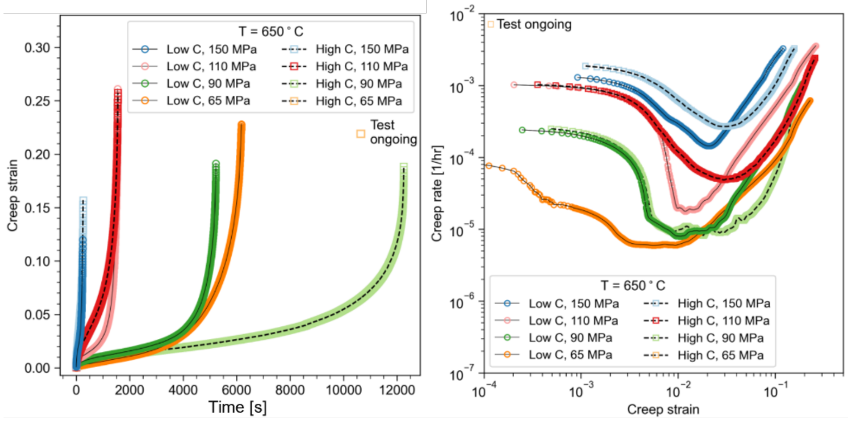

Figure 1. (left) Creep strain as a function of time for low-C CNA9 (solid lines) and high-C CNA8 (dashed line) CNAs, (right) creep rate as a function of creep strain for low-C CNA9 (solid lines) and high-C CNA8.

Microstrucuture characterization was performed on the tab and gauge region of the creep-fracture samples to investigate the grain structure and the preciptiate evolution. No significant change of the grain structure was observed on the tab section for both CNAs, which shows tempered martensite grain structure in Figure 2, similar to the as-received CNAs. On the other hand, the grain structure changes for the gauge section of creep-tested CNAs.

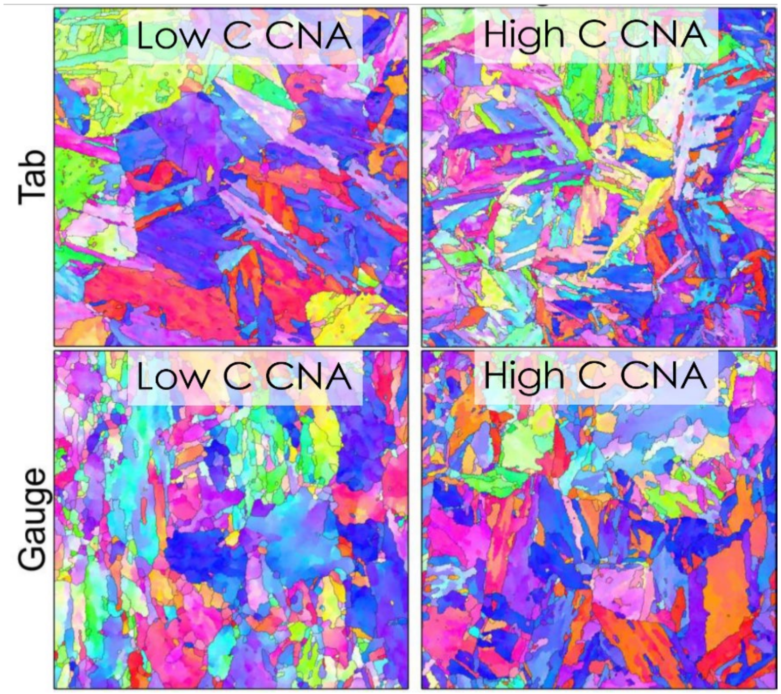

Figure 2. Inverse pole figure for tab and gauge region of low-C CNA9 and high-C CNA8 after creep fracture.

Fine (5-10nm) TiC precipitates were observed inside the grains of the as-received CNA9, as shown in the Figure 3a. However, the number density of such TiC precipitates reduces after the creep tests. Figure 3b shows the Ti map in the gauge region of the creep tested CNA9, and only a few TiC precipitates were observed. Such observation may suggest the instability of these TiC precipitates under the creep condition.

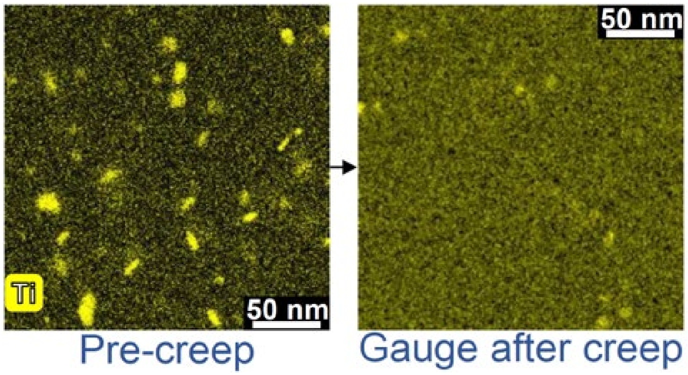

Figure 3. Ti-rich precipitates in low-C CNA9 before and after creep test.

Results

Creep mechanism of CNAs will be examined to understand the effect of carbon content on creep behaviors.

1.6 ADVANCED CASTABLE NANOSTRUCTURED ALLOYS (CNAS) FOR FIRST-WALL/BLANKET APPLICATIONS—Y. Yang, W. Zhong, X. Chen, T. Graening, W. Tang, Y. Wang, B. Pint, M. Romedenne, Y. Katoh (Oak Ridge National Laboratory)

OBJECTIVE

The objective of this project is to establish a United States reduced-activation ferritic-martensitic (RAFM) steel based on the carbide-strengthened Castable Nanostructured Alloys (CNAs) and to demonstrate the viability and advantages of CNAs through the production and performance of industry-scale heats for use in integrated first-wall and blanket systems. This project is intended to establish or demonstrate a path toward technical feasibility for the fusion energy subsystem of integrated first-wall and blanket technologies, and improve the ease of maintainability, reduce regulatory risk, and increase environmental friendliness.

SUMMARY

During the period from 07/01/2023 to 12/31/2023, the project efforts were primarily focused on property evaluation on the 0.25 ton-scale CNA rods (CNAR) and procurement of the 5-ton plates (CNAP). Mechanical properties including (tensile, creep, low-cycle fatigue, fracture toughness), welding performance, PbLi compatibility and ion-irradiation of the CNAR have been evaluated. For the 5-ton scale heat, VIM, VAR, hot forging, and hot rolling have been completed and the resulted chemistry met the design specification. The optimization of the final heat treatment (normalization and tempering) is ongoing to meet the design hardness and grain size requirements.

PROGRESS AND STATUS

Experimental Procedure

<u>Chemical analysis on the CNAR and CNAP</u>

The chemical analysis results for the rods and plates are listed in Table 1 below, which meets the design specification.

Table 1. The chemical analysis results of CNA rods and the design specification

CNA	C	Cr	Mn	Si	Ta	Ti	W	V	Fe
CNAR	0.1	8.38~8.43	0.41~0.54	0.15	0.04~0.05	0.12	1.18	0.05	Bal.
CNAP	0.08~0.09	8.45~8.52	0.52~0.55	0.1	0.07	0.12~0.13	1.25	0.06	Bal.
Nominal	0.1	8.5	0.5	0.12	0.045	0.12	1.3	0.05	Bal.
Design spec.	0.08~0.12	8.40~8.60	0.45~0.6	0.08~0.15	0.05~0.1	0.1~0.15	1.2~1.4	0.04~0.08	Bal.

The delivered CNAR have met the desired composition specification; however, the as delivered CNAR was normalized at 1080°C for 30 min and tempered at 750°C for 30 min, which led to lower hardness 190HV than the design specification of 255±10HV. To increase the hardness or strength of CNAs, we optimized the final heat treatment scheme as 1180°C for 10m followed by 710°C for 60 min so that the resulted hardness is within design specification.

Evaluation of the 0.25-ton CNA rods

Mechanical behavior

Because the in-house furnace has limited capability to heat treat the rods in one batch, they were heat treated in different batches, which caused some variations in mechanical behavior from batch to batch. In general, the CNA rods show lower strength and larger elongation than laboratory heats. The lower strength in CNA rod may also be contributed from different sizes of tensile specimen and different tensile frames. In laboratory heats, all tensile specimens are SSJ3 but in CNA rods, the specimen size follows the ASTM standards, which is much larger than the SSJ3 size. We tested the tensile property from the same heat-treated material and confirmed the ASTM specimen would result in lower yield and tensile strength. For creep test, the creep rupture life of the rods at 600 and 650°C tested in air is consistent with the trend observed for the laboratory heats. One specimen that was tested in inert gas atmosphere at 650°C and 90MPa showed longer creep rupture life than that of the laboratory CNA heats. Additional tests are currently ongoing to reproduce the test results. In summary, both tensile strength and creep rupture life of the 0.25-ton CNA rods are consistent or slightly worse than the laboratory heats but better than E97. For the Charpy impact test results, the CNA rods show a higher DBTT (~2°C) than laboratory heats and other RAFM steels (E97 and F82H). A possible reason for the elevated DBTT is due to the lower tempering temperature used in CNA rods, i.e., 710°C, which is lower than 750°C used for laboratory scale heat. To understand how tempering temperature affects the DBTT, selected rods were tempered at 750°C for 1 h, similar to the laboratory heats and other RAFMs. The higher tempering temperature reduced the DBTT by 14 degrees and increased the upper shelf energy by almost 100 J. Careful microstructural characterization is currently ongoing to understand the underlying mechanism. Additional and creep-rupture tests were also ongoing to see how the tempering temperature would affect these properties.

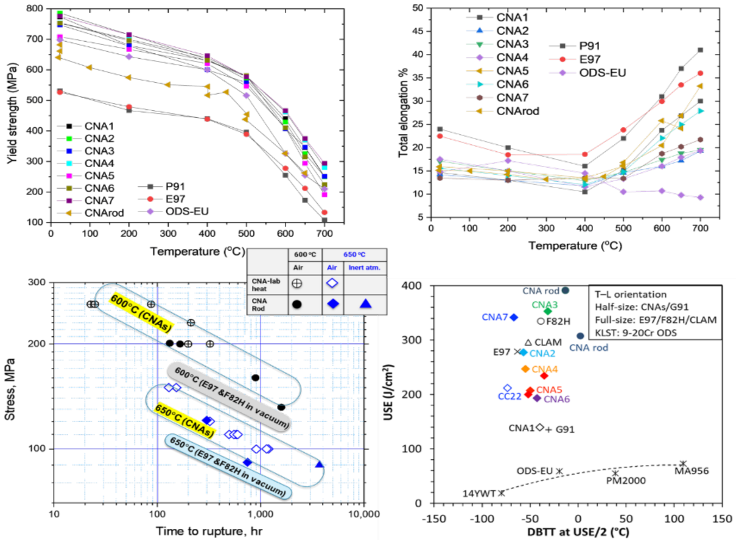

Figure 1. Tensile property, creep rupture life, DBTT and upper shelf energy of CNA rods compared to laboratory heats.

Welding performance

In the reporting period, a gas tungsten arc welding (GTAW) process for CNA plates using the CNA welding wire (produced from CNA rods) was developed and the microstructure and mechanical properties of the welded joint were evaluated in both the as-welded and post weld heat-treated conditions. The welded joint successfully passed the radiographic and dye penetration tests. Post weld heat treatments (PWHT) that is the same as the final heat treatment of the CNA rods (normalization at 1170°C for 30 min and tempering at 750°C for 1h) were applied to coupons removed from the welded joint. Optical and scanning electron microscopy (SEM) microstructural characterization were performed on the weld zone and heat affect zone. It was found that non-tempered martensite at the welded zone and over-tempered martensite at the heat affected zone lead to non-uniform hardness distribution across the weldment. The uniform hardness distribution can be restored through PWHT. Transverse tensile tests were performed on welded joint specimens in the as welded and PWHT conditions. The specimen in the PWHT condition exhibited ~5% higher yield strength than the as-welded condition, and they all exhibited similar tensile strength as the CNA rods. The elongation and reduction of area (RoA) of the PWHT specimens resulted in an ~40% increase compared with the as welded condition. This improvement is believed to be caused by eliminating the strain localization in HAZ soft zones through PWHT and the presence of non-tempered martensite.

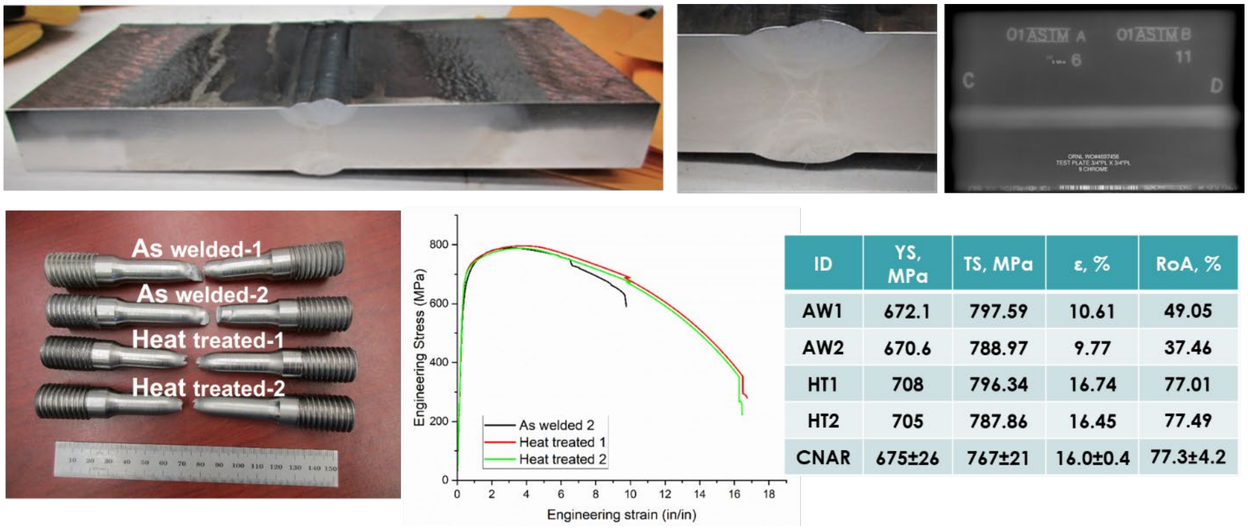

ID	YS, MPa	TS, MPa	ε, %	RoA, %
AW1	672.1	797.59	10.61	49.05
AW2	670.6	788.97	9.77	37.46
HT1	708	796.34	16.74	77.01
HT2	705	787.86	16.45	77.49
CNAR	675±26	767±21	16.0±0.4	77.3±4.2

Figure 2. A CNA welded joint made from the GTAW process and tensile test results of the as welded and PWHT conditions.

Pb-Li compatibility

Coupons of CNA rods were contained in a specially designed capsules, and coolant compatibility test of these capsules was performed at 500, 600 and 700°C, respectively for 1000 h in Pb-17at%Li coolant. The E97 and F82H were tested at 600°C as well to serve as references. The results in Figure 3 show the weight changes for all three materials are comparable at 600°C with experimental uncertainty, suggesting similar performance of CNA to other RAFMs in Pb-17at%Li coolant. The results also show the weight loss increases with temperature. Similar coupons were cut from the weldment in as welded and PWHT conditions. These coupons were made into the similar capsules and are currently undergoing the coolant compatibility test.

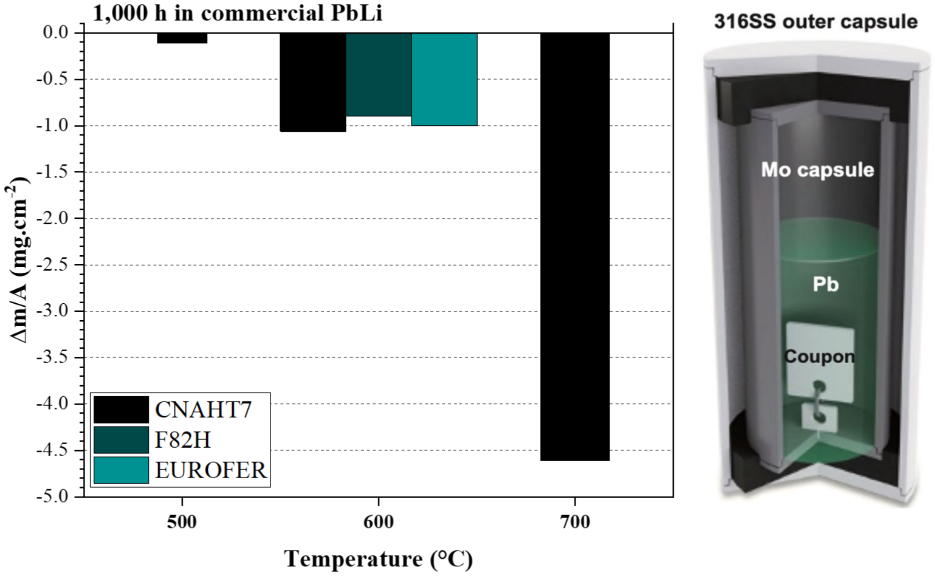

Figure 3. Testing capsules in Pb-Li coolant and the resulted weight loss at 500, 600 and 700°C, for 1000h.

<u>Procurement of 5-ton scale CNA heat</u>

A 5-ton CNA ingot has been casted through vacuum induction melting and refined through vacuum arc remelting at SaarSchimiede Inc. The ingot was then subjected to hot forging and hot rolling, which leads to the plate form. The resulted chemistry and plate dimension satisfactorily met the design specification. Before applying the final normalization and tempering, a few trial heat treatments were requested to make sure that the hardness and Charpy results meet the design specification. The preliminary results from trial heat treatment suggested a nonhomogeneous grain size in the plate and high ductile-brittle transition. It is not clear if the non-homogeneity in grain size was due to the overshooting of tempering temperature, leading to the partial austenization of microstructure. A piece of as-rolled material was requested and an inhouse normalization and tempering will be performed at Oak Ridge National Laboratory (ORNL), followed by microstructural characterization. The final heat treatments will be instructed to SaarSchimiede based on inhouse heat treatment results. Because of this, the final delivery of the 5-ton scale CNA plates is anticipated to be delayed until the Q2 of FY24.

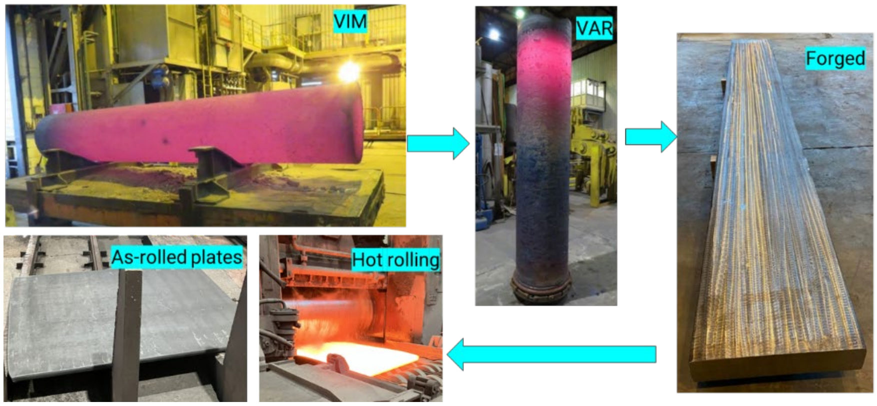

Figure 4. Production steps that have been completed for the 5-ton scale CNA plates.

2. ODS AND NANOCOMPOSITED ALLOY DEVELOPMENT

2.1 COLD SPRAY AND FRICTION STIR PROCESSING OF ODS ALLOYS ON A FERRITIC MARTENSITIC STEEL SUBSTRATE—D. Zhang, X. Wang, J. T. Darsell, K. A. Ross, L. Li, W. Setyawan (Pacific Northwest National Laboratory)

OBJECTIVE

The objective of this work is to explore alternative route of fabricating oxide dispersion strengthened (ODS) alloys, including the potential of plating such ODS plate onto a substrate of reduced activation ferritic martensitic (RAFM) steel. We have demonstrated successful cold spray of ODS steel powder onto ferritic martensitic steel (P92) plates. Two large plates, i.e., #1 and #2, were prepared for subsequent development of friction stir processing (FSP) to (a) eliminate pores and defects in cold sprayed deposit and fully densify ODS steel; (b) further disperse Y-(Ti)-O particles with severe plastic deformation in FSP; (c) maintain and possibly improve bonding between ODS steel deposit and the substrate. In addition, the cold spray + FSP workflow is also being used to incorporate a thin “interlayer” material between ODS plate and the substrate, with the goal of using an interlayer to enhance the bonding between ODS steel and tungsten or tungsten alloys.

SUMMARY

Cold spray was used to successfully deposit ODS steel powder onto ferritic martensitic steel (P92) plate. The feedstock ODS steel powder was provided by collaborators at Ames Laboratory, made with their unique gas atomization reaction synthesis (GARS). The GARS ODS steel powder had the nominal composition of 14YWT (14Cr-0.4Ti-3W-0.35Y-0.1O, wt.%). Meanwhile the largely spherical powder was not ball milled, hence it can be cold sprayed. P92 steel plate was used as a surrogate for RAFM steel, having nominal composition of 9Cr-2W-Si0.5-Mn0.5-Mo0.4-Ni0.3-V0.2-C0.1, wt.%. The state-of-the-art cold spray system was used with helium carrier gas and robust processing parameters to ensure good deposition quality. Subsequently FSP was successfully used to further process the cold sprayed plates. Multiple “single pass” FSP runs were performed on plate #1 to optimize FSP parameters, including FSP tool plunge depth, compression force, and automated temperature control program. #2 plate was processed with a multi-pass FSP raster to impact an extended area (i.e., ~4’’ long, ~3’’ wide), followed by another iteration of cold spray and FSP, resulting in a solid ODS steel plate of ~5 mm thickness on P92 steel substrate. Preliminary microstructure characterization and mechanical testing were performed for plate #2. In addition, cold spray of ~1 mm thick layer of pure Ni powder followed by ~2 mm thick of GARS ODS steel powder on P92 steel substrate were done. Such a composite deposit underwent FSP, and the cross-section was examined with optical microscopy and hardness.

PROGRESS AND STATUS

Introduction

The conventional fabrication route [1] of ODS steel plate involves production of powder by gas atomization, ball milling, powder vacuum canning, hot isostatic pressing, hot cross rolling, cold rolling, with annealing steps often required in-between rolling steps. This route is time consuming, expensive, hard to scale up, and extremely delicate as cracks can develop and the plate can “bend out of shape” during the laborious rolling process. Based on the realistic consideration that conventional route is not capable of producing tons of ODS steel for fusion energy application, some researchers [1] proposed to “plate” a mm-level thickness of ODS steel onto RAFM steel, with the idea that the ODS steel plating would be a critical top layer to handle expected extreme temperature and radiation dose in a fusion environment. This means that on top of the laborious plate fabrication process, additional bonding step (e.g., diffusion bonding) is required to make ODS steel plating. Therefore, it would be highly desirable to directly deposit an ODS steel layer onto a RAFM steel without the abovementioned laborious steps. Unfortunately, melt-based additive methods won’t be suitable as dispersed particles tend to agglomerate in molten metal. Cold spray is a solid-state based method that could offer a potential solution. Yet effective cold spray would require the feedstock powder to be largely spherical for aerodynamic purposes. Namely, the flaky ball milled ODS steel powder won't work well with cold spray.

The GARS method produces spherical precursor ODS steel powder with an outer shell of Cr-rich oxide, whereas the nano-oxide forming species, i.e., Y and Ti, are at the powder interior in the form of Fe-intermetallics. Upon heating and consolidation (e.g., hot isostatic pressing, HIP), oxygen atoms diffuse into the powder interior to react with Y/Ti, forming the Y-Ti-O nano-oxides [2]. Therefore, GARS ODS steel powder offers the geometrical (i.e., spherical) and compositional (i.e., Y/Ti/O species all contained in the powder) requirements for cold spray deposition. Moreover, FSP can be used to further process the GARS ODS steel powder cold spray deposit, leading to full consolidation of the bulk material and further disperse the formation of Y-Ti-O particles.

Experimental Procedure

Figure 1(a) shows a cross-section overview in a scanning electron microscope (SEM) of the GARS ODS steel powder provided by Ames Laboratory. The powder size ranges between 45 μm and 108 μm. Figure 1(b) is a medium magnification SEM image of several powder particles, showing the grain substructure inside. Figure 1(c) is a high magnification image inside one powder particle, showing bright spots mainly decorating grain boundaries. Energy dispersive X-ray spectroscopy (EDS) mapping in Figure 1(d) reveals that these bright spots correspond to Y signals, namely these are Fe-Y intermetallic particles.

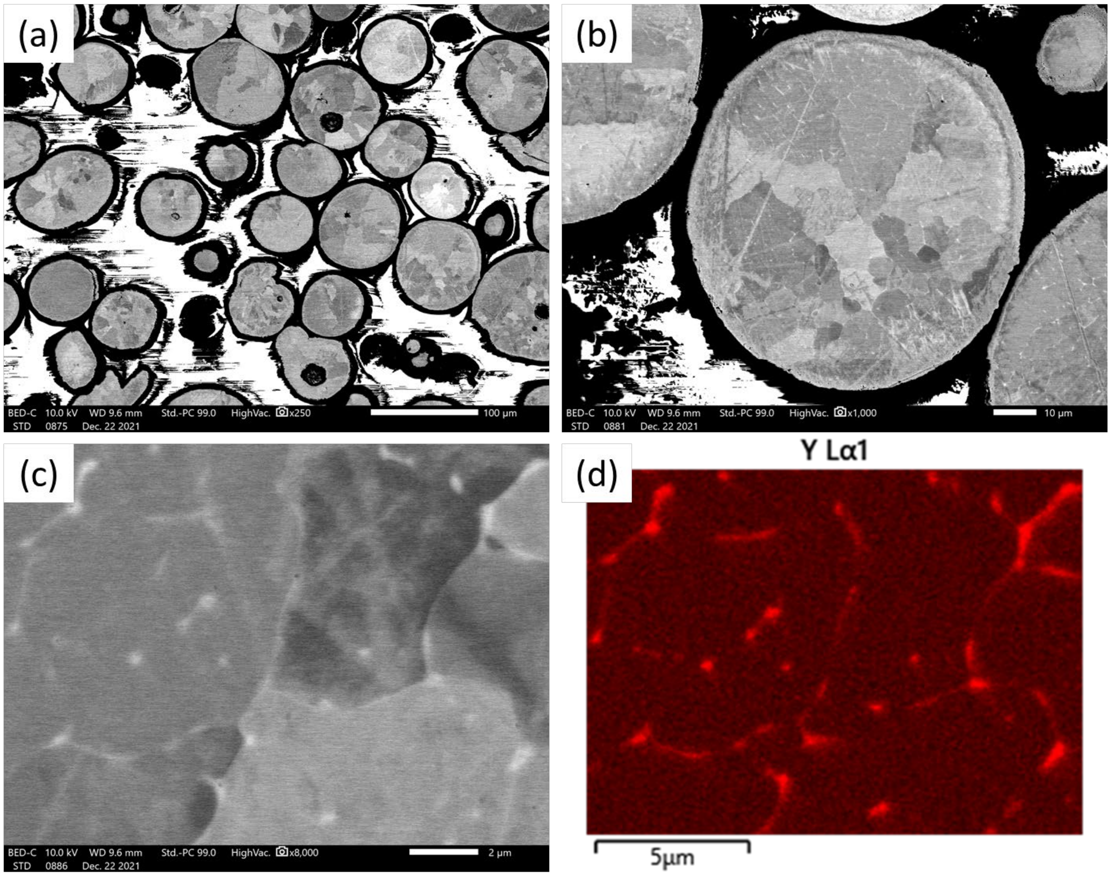

Figure 1. (a) Cross-section SEM overview of the GARS ODS steel powder. (b) Grain substructure inside powder particles. (c) Bright spots decorating grain boundaries. (d) EDS map showing that the bright spots are Fe-Y intermetallic particles.

The P92 steel substrates had an as-machined surface which could be beneficial for bonding at the cold spray interface. Based on prior experience with steels and Ni alloys, a set of robust cold spray parameters was chosen to ensure effective deposition and preserve limited GARS powder. For example, helium carrier gas was used at 600 psi, with the gas temperature at 650°C. It is noted that 650°C would still be considered "cold" for ODS steel powder since such a temperature would not alter the powder microstructure. As shown in Figure 2, two large-area ODS steel deposits (#1 and #2) were cold sprayed onto P92 substrates, respectively. The #1 was used for optimization of the FSP step, where 4 trail FSP passes were performed. First to determine the optimal FSP tool plunge depth where abundant material was getting processed while also ensuring that the tool was not "buried" in the material to the point of damaging the tool itself. Then the compression force on the FSP tool was fine tuned to enable temperature controlled FSP run (at 750°C) through a combination of steady force and tool rotation speed (rotation per minute [RPM]). After these optimizations, a "1.5" pass was performed where after one complete pass along the "X" direction for 4'', the tool traversed in the "Y" direction for 8 mm then travelled back in the "X" direction again for 2''. In this way, cross-section samples can be extracted from the tracks of both the single pass and the "overlapping" 2 passes. Upon examination of the two samples with optical microscopy (OM) and hardness mapping, #2 plate was FSP processed with an 8-pass raster.

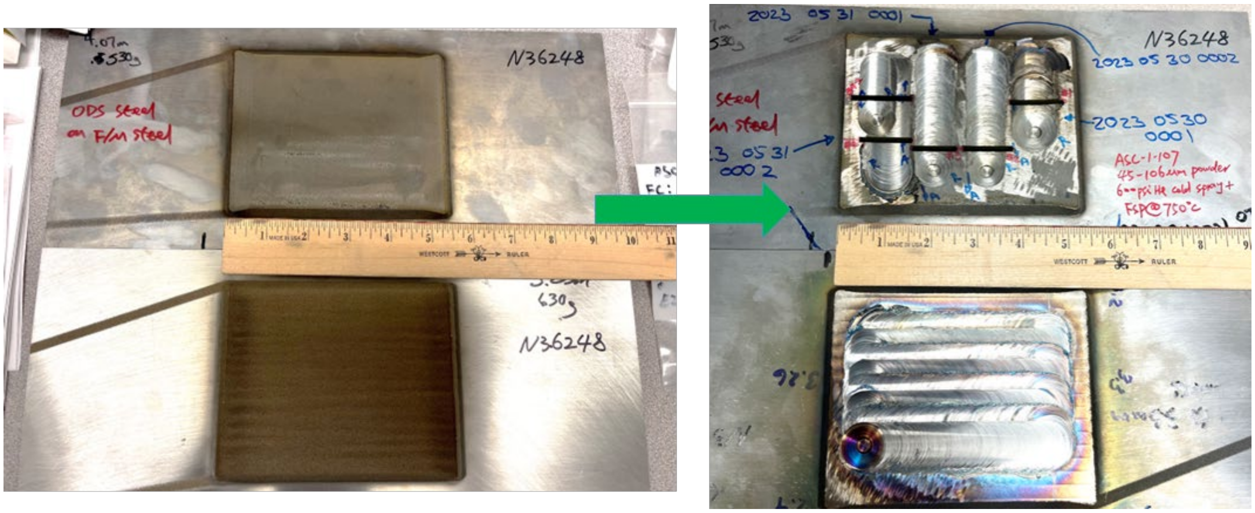

Figure 2. Two large-area ODS steel deposits (#1 and #2) were cold sprayed onto P92 substrates, respectively. The #1 plate was used for optimization of the FSP step. The #2 plate was FSP processed with an 8-pass raster.

Results

Figure 3(a) shows the #2 plate after the second iteration of cold spray and FSP (also 8-pass raster), yielding a total ODS layer thickness of ~5 mm. The yellow dashed box outlines the cross section extracted from the plate, crossing the 8-pass processed area as well as a small portion of as-cold spray areas at the two ends. The red dashed boxes outline the portions of the processed area extracted for making creep test specimens. Note that specimens along the FSP direction and normal to it would be made, respectively. Figure 3(b) shows the OM montage image of the extracted cross section, containing both the ~5 mm ODS layer (top) and the P92 steel substrate (bottom). No cracks or defects can be seen between the processed ODS layer and the substrate. The hardness map also indicates a very uniform structure in the processed area, with the average hardness ~200 HV.

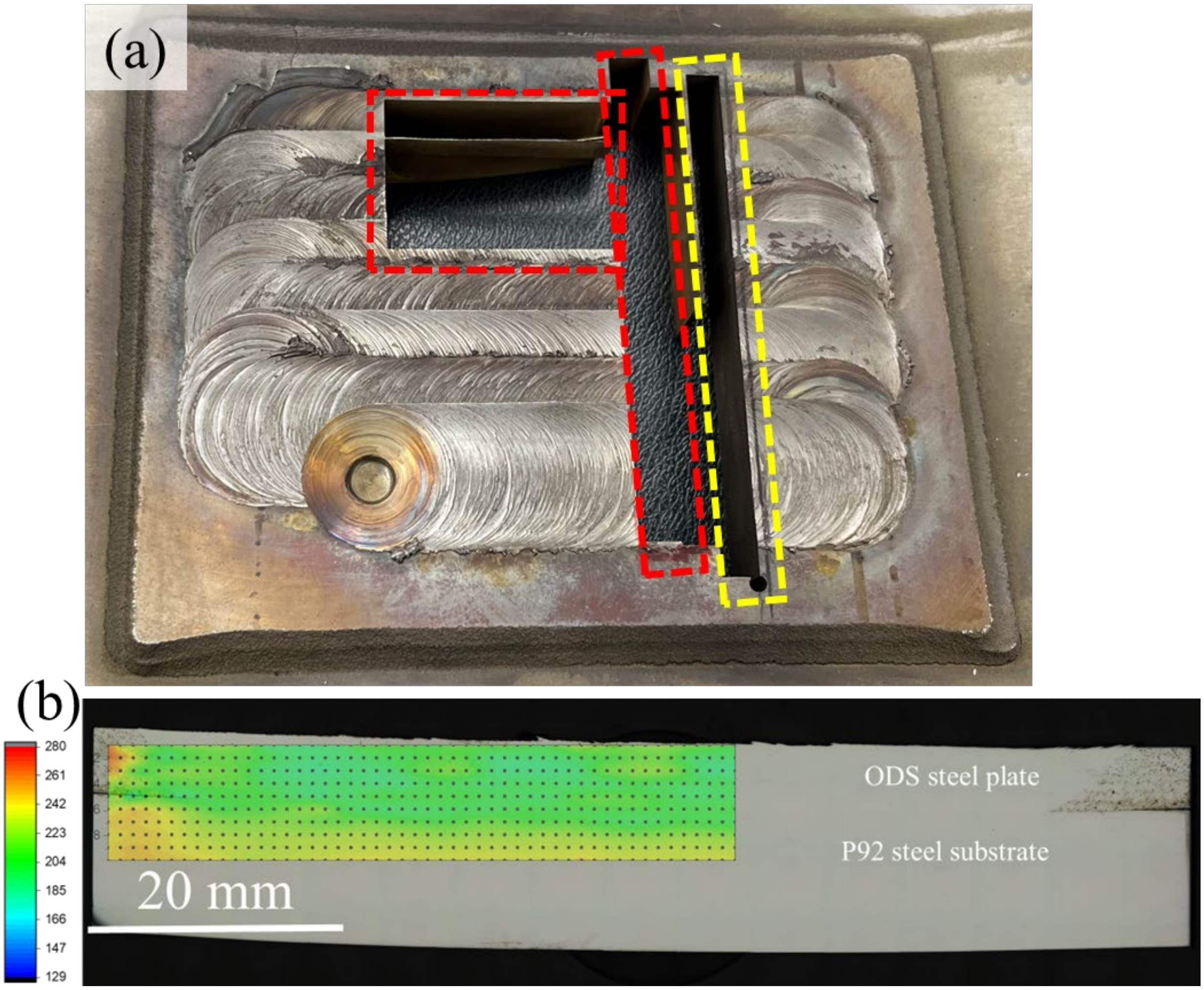

Figure 3. (a) The #2 plate after second iteration of cold spray and FSP. Cross section (yellow box) has been extracted from the plate for OM and hardness. Creep specimens were also extracted in two directions (red boxes). (b) OM montage image of the plate cross section, with the ODS layer (~5 mm thick) on top, and P92 steel substrate below. At the left and right corners of the ODS layer, un-processed, slightly porous remnant cold spray structure can be seen. Hardness map of the ODS layer shows that the hardness is ~200 HV and very uniform across all the processed area.

Using the same cold spray + FSP workflow, ~1 mm layer of pure Ni powder was deposited on P92 steel substrate, followed by ~2 mm layer of GARS ODS steel powder. The composite layers were processed with 1 pass of FSP as an initial trial. Figure 4(a) shows the OM montage image of the cross section of the processed layers along with the P92 steel substrate. Note that the sample was etched to reveal fine details, especially at interfaces. The black dashed line approximately outlines the FSP processed zone. Outside the processed zone, both the ODS steel layer and the pure Ni layer show as-cold spray porous structure, as also evidenced by the occasional low-hardness spots in the hardness map in Figure 4(b). Inside the processed zone, the two layers are mostly consolidated and uniform. However, at the interface between the two layers, especially on the left side (i.e., the “advancing side” of friction stir), there appears to be “inter-flow” of two materials. Such inter-flow is much less prominent at the interface between pure Ni and the substrate.

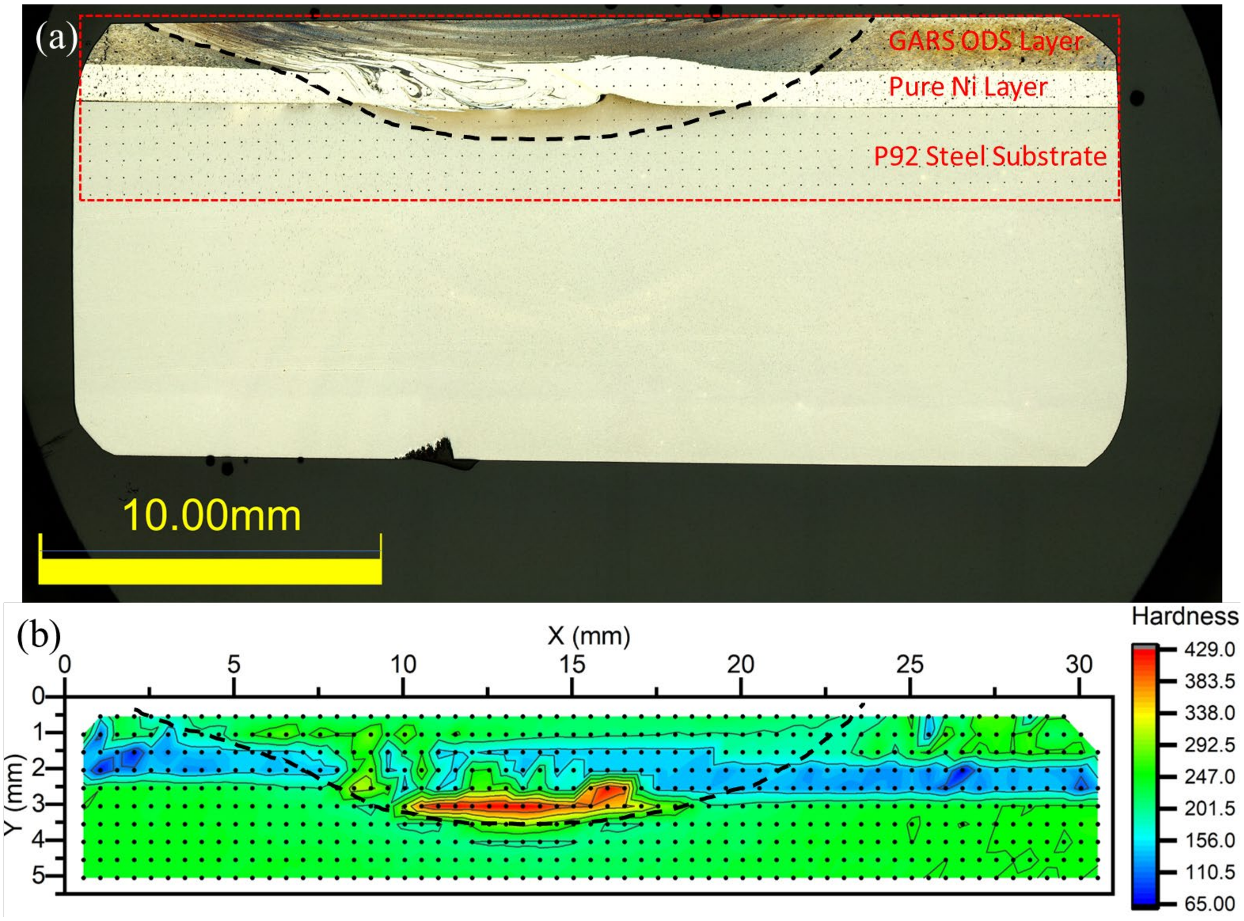

Figure 4. (a) The OM montage image of the cross section of the FSP processed layers of pure Ni and GARS ODS steel along with the P92 steel substrate. (b) Hardness map of the highlighted portion of the sample.

Future work will focus on subsequent characterization and mechanical testing of the #2 large plate after FSP raster to quantify dispersed oxide particles and grain structure, hence their effects on tensile strength, ductility, fracture toughness, and creep behavior at 650°C and above. In addition, ODS-Ni powder is being produced at Ames Laboratory and will be used in the cold spray + FSP workflow.

Acknowledgements

This research is funded by the U.S. Department of Energy Office of Fusion Energy Sciences under contract DE-AC05-76RL01830. We are grateful to cold spray technical support provided by Chris Smith, Justin Olson, and Mark Rhodes.

References

[1] M. Rieth, M. Dürrschnabel, S. Bonk, G. Pintsuk, G. Aiello, J. Henry, Y. de Carlan, B.E. Ghidersa, H. Neuberger, J. Rey, C. Zeile, N. De Wispelaere, E. Simondon, J. Hoffmann, Impact of materials technology on the breeding blanket design – Recent progress and case studies in materials technology, Fusion Engineering and Design 166 (2021) 112275.

[2] J. Rieken, Gas atomized precursor alloy powder for oxide dispersion strengthened ferritic stainless steel, Ames Laboratory (AMES), Ames, IA (United States), 2011, p. 362.

2.2 RESPONSE OF F82H-IEA TO DOSE RATE AND H INJECTION RATE IN DUAL AND TRIPLE ION IRRADIATION TO UNDERSTAND THE SYNERGIES BETWEEN H, HE AND RADIATION DAMAGE—L. Clowers, Z. Jiao, G. Was (University of Michigan)

OBJECTIVE

The objective of this project is to understand the synergy between transmutation gasses H and He on cavity evolution in ferritic/martensitic fusion blanket materials.

SUMMARY

The ferritic/martensitic steel F82H-IEA was studied to understand the synergistic effects of H, He and radiation damage on cavity evolution and swelling via dual ion beam (Fe^{2+}+He^{2+}) and triple ion beam (Fe^{2+}+He^{2+}+H^{+}) irradiation. Irradiations were conducted at a damage level of 50 dpa and temperature of 500°C at damage rates of $2.5x10^{-4}$ to $2.5x10^{-3}$ dpa/s with H injection rates of 0, 40 and 80 appm/dpa and a nominal He injection rate of 10 appm/dpa. The cavity microstructure of each irradiation condition was characterized using electron microscopy on cross sectional lamella created via focused ion beam techniques. Across nearly all conditions, hydrogen co-injection with helium resulted in an increased cavity number density and cavity size, producing an increase in swelling over that from helium injection alone. Preceding work is published in Clowers, et al [1].

PROGRESS AND STATUS

Introduction

The reduced activation ferritic/martensitic (RAFM) steel F82H-IEA, a highly characterized heat provided by the National Institutes of Quantum and Radiological Science and Technology in Japan was irradiated in a series of dual and triple ion beam irradiations. Ion irradiations were conducted at the Michigan Ion Beam Laboratory (MIBL) using the 3 MV Pelletron accelerator to provide a defocused beam of 5 MeV Fe^{2+} for irradiation damage, the 1.7 MV Tandetron to provide a raster-scanned beam of 2.85 MeV He^{2+} to be passed through a ~6.2 μm thick Al degrader foil for helium implantation, and an ion implanter to provide a raster-scanned beam of 390 keV H^{+} through a second ~2.3 μm Al degrader foil for hydrogen implantation. Both types of ion irradiation, dual ion beam (Fe^{2+}+He^{2+}) and triple ion beam (Fe^{2+}+He^{2+}+H^{+}), were nominally conducted at 500°C to a damage level of 50 dpa with single value variations across each of these parameters. The damage profiles from self-ions and the concentration profiles of injected H/He calculated using a custom MATLAB script along with SRIM-2013 [2]. At a nominal damage rate of $\sim 1x10^{-3}$ dpa/s, the nominal injection ratios for hydrogen and helium were 40 appm/dpa and 10 appm/dpa, respectively, at the depth of analysis (400-800nm from the surface). A narrower band of 500-700nm was used to minimize dpa variation in cavity data.

Following irradiation, transmission electron microscopy (TEM) samples were prepared using standard FIB lift-out methods in a TFS Nova 200 or a Helios 650 Nanolab SEM/FIBs at the Michigan Center for Materials Characterization (MC^2). Cavities greater than 5 nm were characterized using high-angle annular dark-field scanning transmission electron microscopy (HAADF-STEM) while cavities less than 5 nm were characterized using the bright field (BF) TEM focus-defocus technique with a defocus of +/- 1 μm in the TFS Talos TEM/STEM microscope. Typically, greater than 500 cavities were characterized in the region of interest (500-700nm) per irradiation condition. The TEM lamella thicknesses were measured to be in the range 50-120 nm via electron energy loss spectroscopy (EELS). Errors in cavity size, density and swelling were estimated to be 7%, 10% and 30%, respectively.

Experimental Procedure

To determine the effect of damage rate on the resulting cavity microstructure, a series of dual and triple ion irradiations were conducted at 2.5×10^{-4}, 1.0×10^{-3} and 2.5×10^{-3} dpa/s with otherwise equivalent conditions of 50 dpa and 40/10 appm/dpa of H/He all at 500°C. A visual comparison of the microstructural evolution across each damage level is shown in the STEM-HAADF images in Figure 1. For all damage rates swelling increased with triple ion irradiation, as shown in Figure 2, where co-injection of H along with He and radiation damage resulted in a substantial increase in swelling, showing that these synergistic effects promote cavity swelling across wide damage rates. The cavity size distributions shown in Figure 3 indicate that this increase in swelling between dual and triple ion irradiation is the result of both increases in maximum cavity size as well as increases in cavity density in the triple ion irradiated condition in comparison to that of dual ions. While the slight decrease in swelling when going from 1.0×10^{-3} to 2.5×10^{-3} dpa/s was expected, as in Taller, et al. [3], the distinct drop in swelling at 2.5×10^{-4} dpa/s for both dual and triple ion irradiation was not. This drop in swelling may be due to a variety of factors including the heightened influence of the sample surface and/or the injected interstitials at this lower damage rate where thermal diffusion may play a more substantial role. The exact source of this difference is currently being investigated.

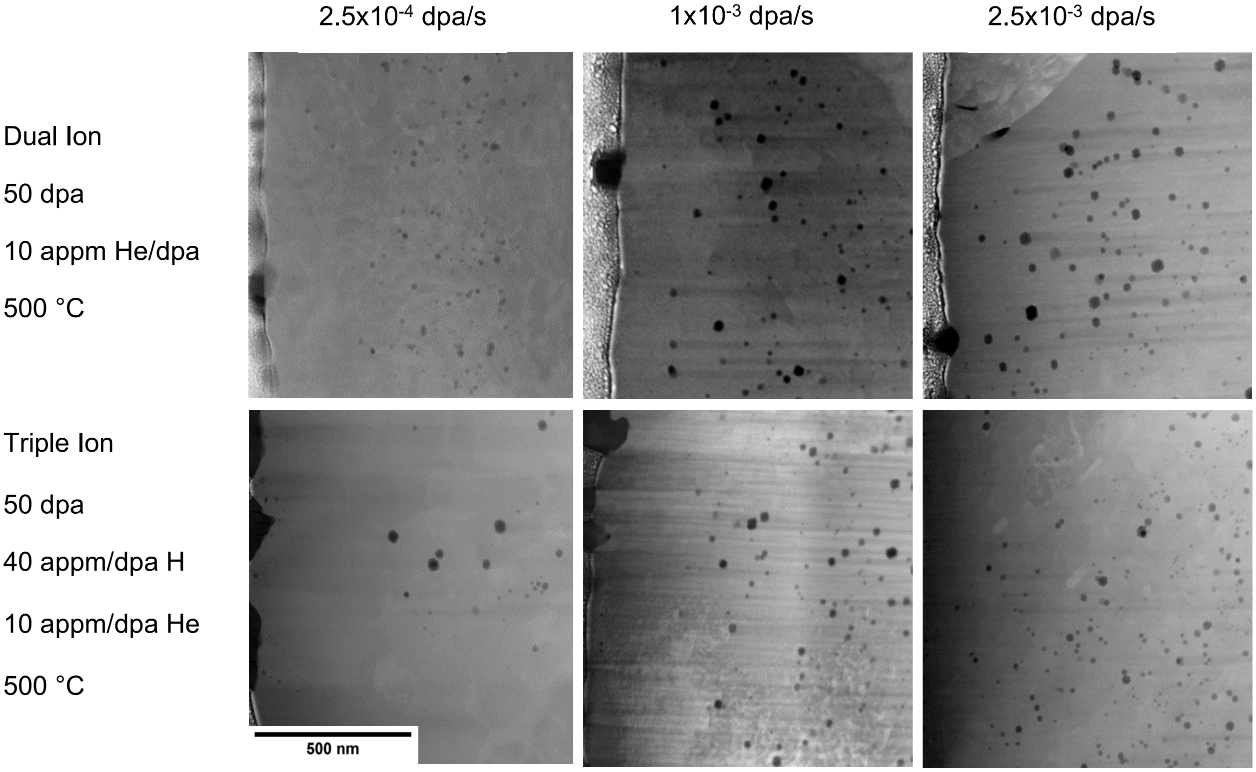
2.5×10^{-4} dpa/s

1×10^{-3} dpa/s

2.5×10^{-3} dpa/s

Dual Ion

50 dpa

10 appm He/dpa

500 °C

Triple Ion

50 dpa

40 appm/dpa H

10 appm/dpa He

500 °C

Figure 1. The HAADF images of cavities in dual beam (Fe^{2+}+He^{2+}) and triple beam (Fe^{2+}+He^{2+}+H^{+}) irradiated F82H at 2.5×10^{-4}, 1.0×10^{-3} and 2.5×10^{-3} dpa/s.

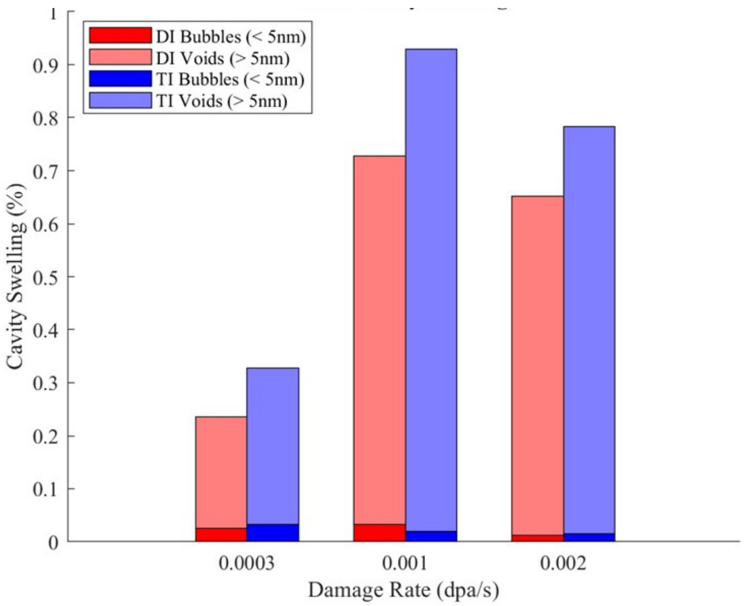

Figure 2. Evolution of cavity swelling across damage rates in dual and triple ion irradiated F82H.

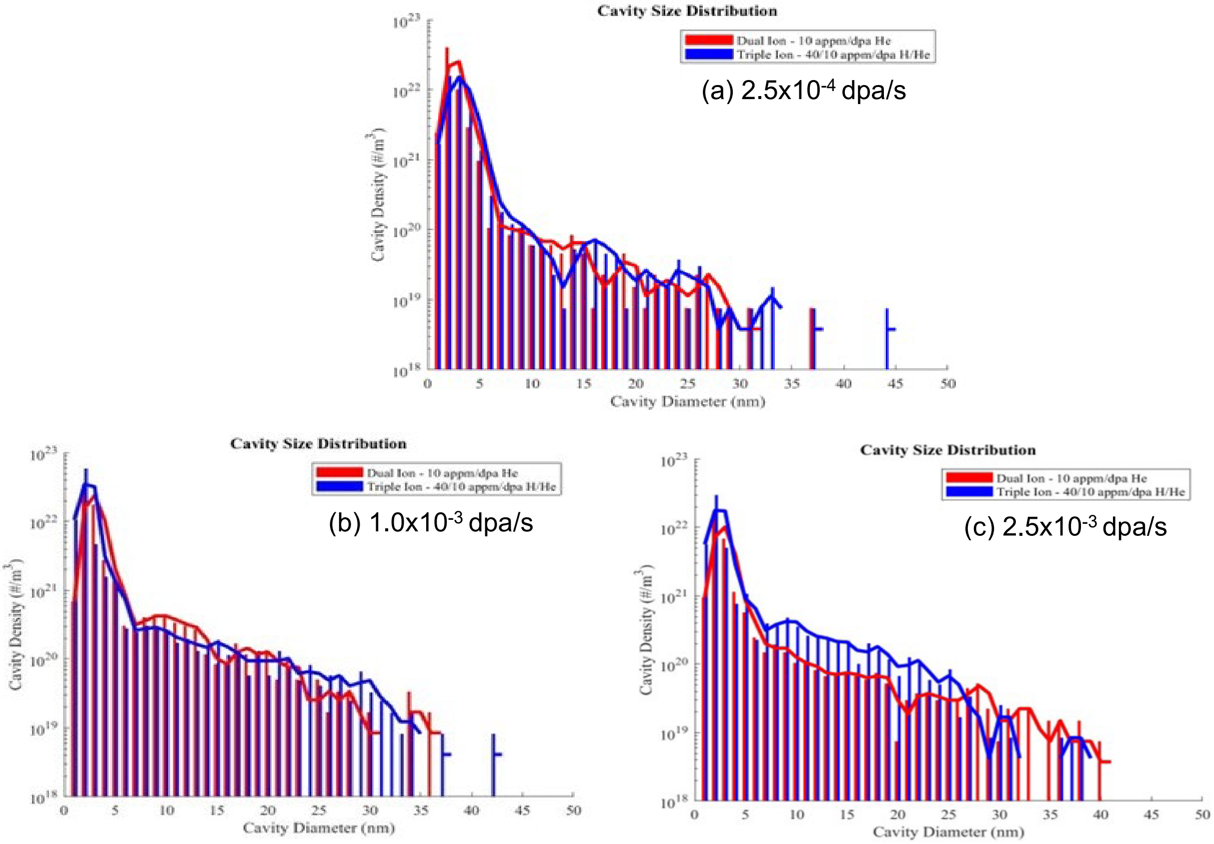

Figure 3. Comparison of the cavity size distributions resulting from dual and triple ion irradiated F82H at (a) 2.5x10^{-4}, (b) 1.0x10^{-3} and (c) 2.5x10^{-3} dpa/s.

Another series of dual and triple ion irradiation experiments was done to determine the dependence of the synergies between H, He and radiation damage on the rate of H co-injection during irradiation. Performed at both 450°C and 500°C, these experiments were conducted at otherwise equivalent conditions of 50 dpa, $1x10^{-3}$ dpa/s, and 10 appm/dpa of He, with variations in hydrogen injection from 0 to 40 and 80 appm/dpa. A visual comparison of the irradiated microstructures across these changes in hydrogen injection is shown in the TEM-BF images in Figure 4. When going from 0 to 40 appm/dpa of hydrogen, swelling was significantly increased while going from 40 to 80 appm/dpa of hydrogen swelling was instead suppressed to that below what was observed at 0 appm/dpa of hydrogen, trends that were consistent at both 450°C and 500°C as observable in Figure 5.

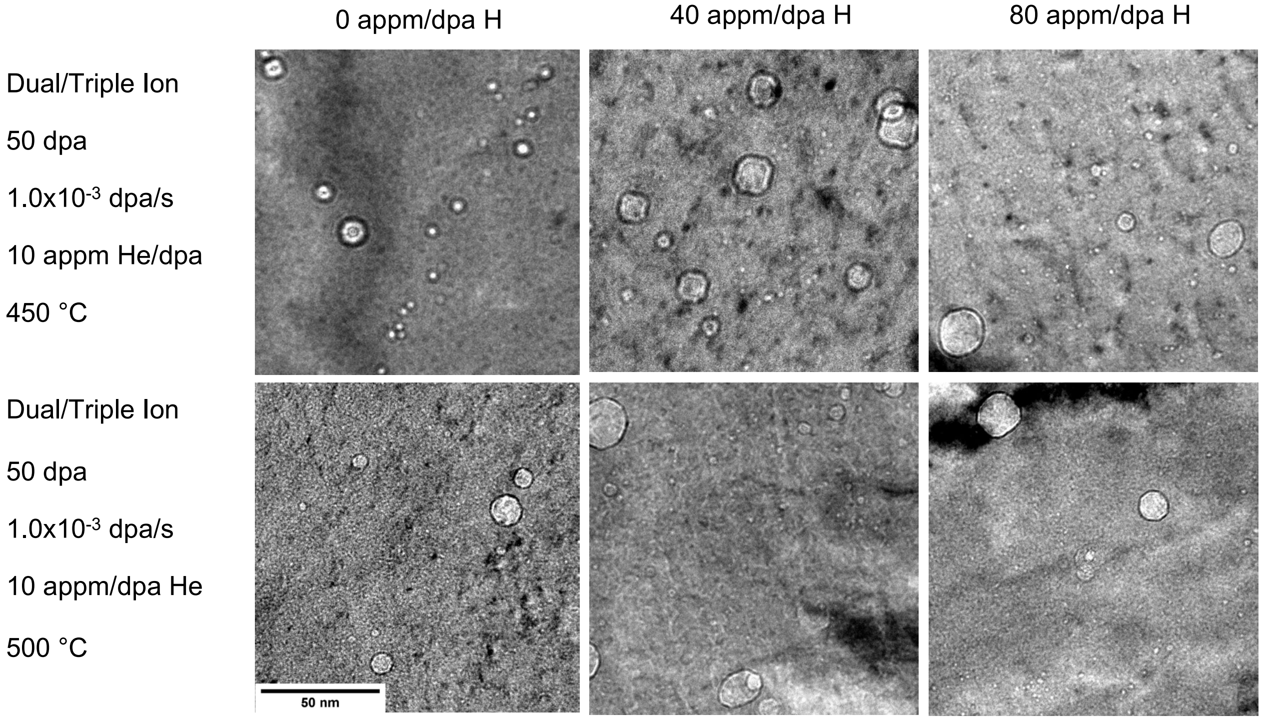

Figure 4. The TEM-BF images of cavities in F82H dual and triple ion irradiated to 50 dpa, $1x10^{-3}$ dpa/s, and 10 appm/dpa of He from 0 to 80 appm/dpa of H.

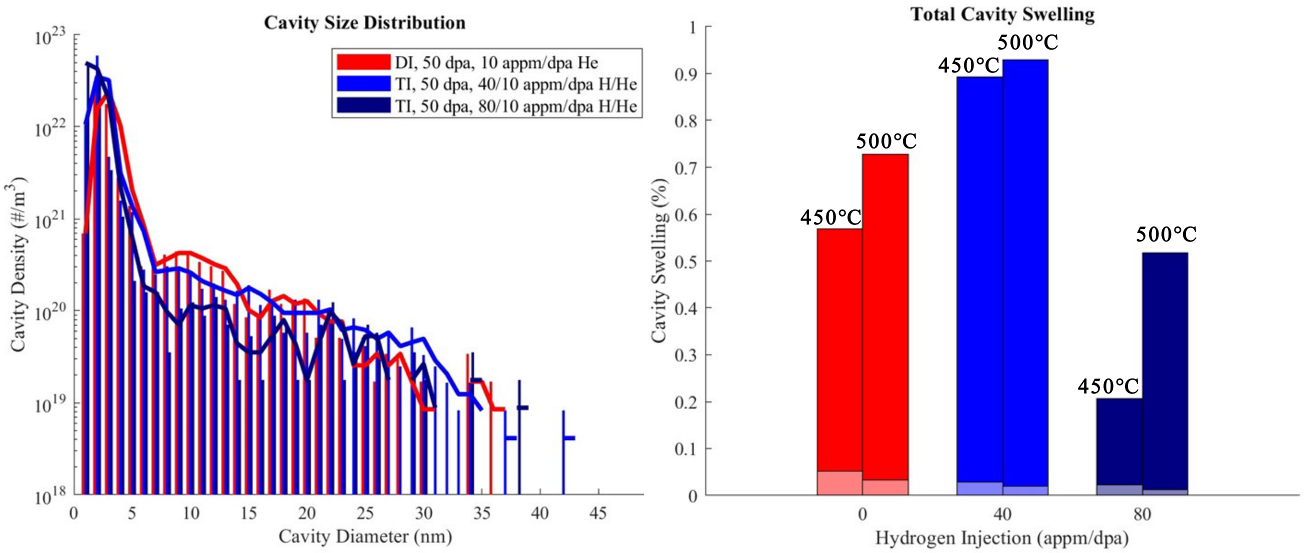

Figure 5. (a) Cavity size distributions and (b) swelling comparison for dual and triple ion irradiated F82H from 0 to 80 appm/dpa of H.

Results

Further experiments and characterization are planned to investigate the dependence of the microstructure as a whole on the synergistic effects of hydrogen including dislocation loops and dislocation networks, precipitate morphology and radiation induced segregation. Additional experiments are also planned to isolate the role of hydrogen in these phenomena through targeted ion irradiation conditions. Additional characterization will also assist the understanding of the role of hydrogen in cavity swelling and its location in the microstructure through advanced microscopy techniques including elemental mapping and real-time observation through in-situ ion irradiation.

References

[1] L. N. Clowers, Z. Jiao, and G. S. Was, "Synergies between H, He and radiation damage in dual and triple ion irradiation of candidate fusion blanket materials," *J. Nucl. Mater.*, vol. 565, p. 153722, 2022, doi: 10.1016/j.jnucmat.2022.153722.

[2] S. Taller *et al.*, "Multiple ion beam irradiation for the study of radiation damage in materials," *Nucl. Instruments Methods Phys. Res. Sect. B Beam Interact. with Mater. Atoms*, vol. 412, pp. 1–10, 2017, doi: 10.1016/j.nimb.2017.08.035.

[3] S. Taller, G. VanCoevering, B. D. Wirth, and G. S. Was, "Predicting structural material degradation in advanced nuclear reactors with ion irradiation," *Sci. Rep.*, vol. 11, no. 1, pp. 1–15, 2021, doi: 10.1038/s41598-021-82512-w.

2.3 MECHANICAL AND MICROSTRUCTURAL CHARACTERISTICS OF LOW-COST ODS ALLOYS

—T.S. Byun, T. Lach, Y. Lin (Oak Ridge National Laboratory)

OBJECTIVE

This research is to develop an economically attractive, technically feasible processing route for oxide dispersion strengthened (ODS) ferritic alloys for fusion reactor applications. The ODS alloys produced using a continuous thermomechanical processing (CTMP) method were down-selected based on mechanical properties to analyze detailed microstructure and to pursue further development.

SUMMARY

To overcome the practical hurdles in the ODS steel production method based on high-power mechanical alloying [1], we pursued a solid-state ODS alloy processing approach consisting of only CTMP. A combination of powder consolidation process at 900°C and continuous thermomechanical processing at 600°C yielded both the nanograin structure and the nanoparticle distribution and thus a good combination of strength and ductility. This report discusses the mechanical properties of the 14YWT-based ODS alloy processed by low-cost processing routes, in comparison with the conventional ODS Fe-(9-14)Cr alloys, and the result of microstructure analysis focusing on grain structure and particle distribution is discussed.

PROGRESS AND STATUS

Introduction

The ODS ferritic alloys that have been processed through the solid-state thermomechanical processing–high temperature severe plastic deformation (SPD)–and delivered desirable mechanical properties were down-selected for further microstructural analysis. Table 1 describes the details of powder mixtures, consolidation conditions, CTMP conditions, and the total plasticity amounts applied by the hot-rolling steps for powder consolidation and CTMP.

Table 1. Summary of base materials and select processes for production of ODS ferritic alloys

Materials ID	Powder Mixture (in wt.%)	Consolidation Process	HT-SPD Process (CTMP)
HR1(T1/T2)	**14YWT alloy doped with Y & O**: Fe-13.7Cr-2.9W-0.38Ti-0.23Y-0.07O (no oxide powder addition)	Six hot-rolling cycles at 900 ºC for 80% plastic strain	Eight hot-rolling cycles at 600–900 ºC for 220–310% plastic strain
HR2(T1/T2)	**14YWT base+Fe_2O_3:** Fe-13.7Cr-2.9W-0.38Ti -0.23Y+0.22Fe_2O_3	Four to six hot-rolling cycles at 900 ºC or 1200 ºC for 60–80% plastic strain	Six to eight hot-rolling cycles at 600–900 ºC for 220–310% plastic strain
HR3(T1/T2)	**14YWT base+Y_2O_3:** Fe-13.7Cr-2.9W-0.38Ti-0.12Y+0.3Y_2O_3	Six hot-rolling cycles at 900 ºC for 80% plastic strain	Eight hot-rolling cycles at 600–700 ºC for 240% plastic strain
HR4(T1/T2)	**Fe-10Cr base+Y_2O_3:** Fe-9.7Cr-0.97W-0.15Ti-0.18V-0.23Y+0.3Y_2O_3	Four to six hot-rolling cycles at 900 ºC or 1200 ºC for 60–80% plastic strain	Six to eight hot-rolling cycles at 600 ºC for 220–270% plastic strain

Uniaxial tensile testing was performed for the newly produced ODS alloys, and the tensile property data such as the strength and ductility parameters were used as criteria for down-selecting the processing routes and further characterization. Microstructural analysis was performed using an FEI Talos 200 keV scanning transmission electron microscope (STEM) equipped with a high brightness-field emission gun source, bright field (BF) and multiple annular dark field detectors, and a quadrupole FEI ChemiSTEM energy dispersion x-ray spectroscopy collection system.

Experimental Procedure

The mechanical properties of an Fe-Cr alloy, with or without oxide-dispersion strengthening, are strongly dependent on the processing route taken for production of the alloy [2,3]. A common behavior observed in the ODS ferritic steels and conventional FM steels is that the strength of an alloy is inversely proportional to the ductility (and toughness) of the alloy [2]. That is, an ODS alloy with a very high strength (YS or UTS >> 1 GPa) usually show a low ductility. Such an inverse-proportionality relationship can work in the elastic-plastic regime only and might become invalid once the material gets embrittled (to retain nil-ductility). In Figures 1 and 2, the tensile strength and ductility data of the newly processed alloys are compared with those of the ODS alloys produced via mechanical milling to test if the ODS alloys produced with and without mechanical milling still follow the inverse strength-ductility relationship. The ODS alloy group in comparison was selected such that their YS data spread over a large range of 500–2100 MPa. It is noted that the detailed descriptions on the mechanically milled and consolidated ODS alloys–14YWT-SM10 (Fe-14Cr-3W-0.4Ti alloy), 14YWT-SM11 (Fe-14Cr-3W-0.4Ti alloy), 9YWTV-PM1 ((Fe-9Cr-2W-0.4Ti-0.2V high-carbon alloy), 9YWTV-PM2 (Fe-9Cr-2W-0.4Ti-0.2V low carbon alloy), MA957 (Fe-14Cr-1Ti-0.3Mo alloy), and ODS Eurofer-97 (Fe-9Cr-1W-0.2V alloy)–have been published in open literature [4-12] and that the nominal amount of oxide powder blended to these ODS alloys before processing was 0.3 wt.%.

The comparison of tensile strength data in Figure 1 shows that the strength of some mechanically milled ODS alloys–14YWT-SM10, 14YWT-SM11, 9YWTV-PM1, and 9YWTV-PM2–are significantly higher than those of the HR1–HR4 alloys produced without mechanical milling. Meanwhile, the other two alloys produced by mechanical milling, MA957 and ODS Eurofer-97 [11,12], have similar strengths as those of the HR-series alloys. The strength of these ODS alloys might be determined by microstructural parameters including the size and density of oxide (and carbide) particles and grain structures. The four higher-strength ODS alloys contain high densities of oxygen-enriched nanoparticles on the order of $10^{23}/m^3$ or similar in nanograin (typically < 1 μm) structures [7,13], which are thus called the nanostructured ferritic alloys (NFAs). The other alloys compared together in the two figures contain nanoparticles at relatively lower densities either in nanograin structures (the HR-series alloys) or in relatively coarser grain structures (MA957 and ODS Eurofer-97). Although little data is available, dislocation density might be also an influential factor in the strength of ODS alloys.

The uniform and total ductility data for the ten ODS alloys are compared in Figure 2. As expected in the inverse proportionality relationship, the highest strength materials, 14YWT-SM10 and -SM11, show the lowest ductility's; in particular, the UE values of these alloys are very small (< 1%). The ODS Eurofer-97 demonstrates consistently high UE and TE values at both test temperatures, whose strength and ductility are similar to those of HR2(900ºC/600ºC). Some alloys including 9YWT-PM1, 9YWT-PM2 and HR3 show very low uniform elongations at 500°C, while the other ductility data for these alloys are relatively high. These strength and ductility comparisons confirm that the strength of an alloy is inversely proportional to its ductility, at least, in the ten ODS alloy group. If an alloy group follows the inverse proportionality between strength and ductility, any processing route designed for a specific properties should not excessively sacrifice the other properties. It can be positively interpreted that the new ODS alloys, the HR2(900ºC/600ºC) in particular, show a good combination of strength and ductility, without sacrificing either of these properties.

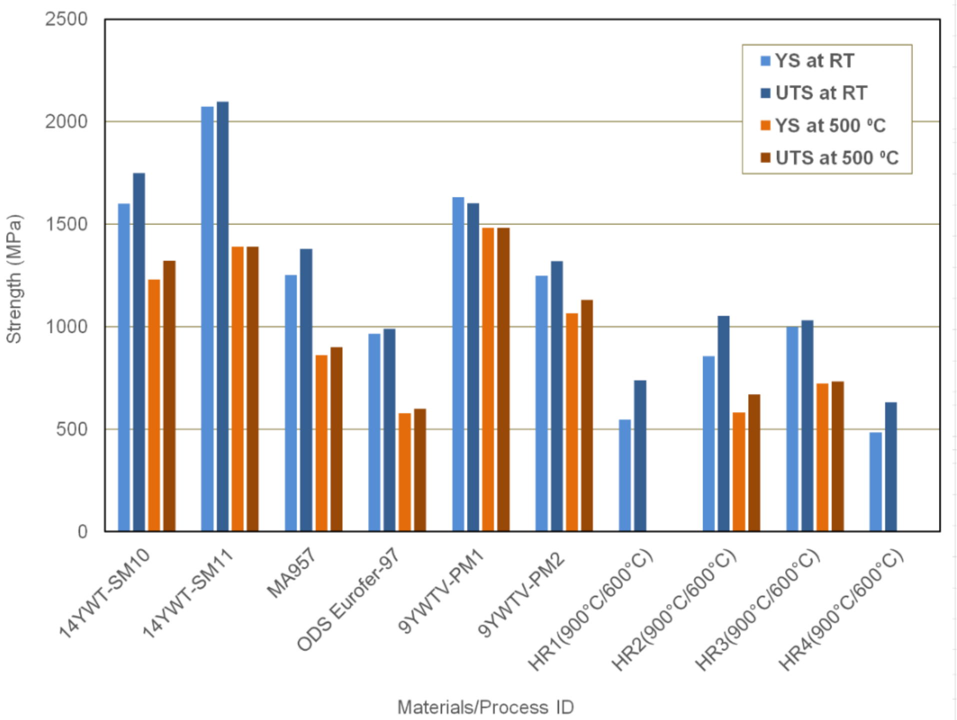

Figure 1. Comparison of yield and ultimate tensile strengths among the ODS alloys processed with or without mechanical milling.

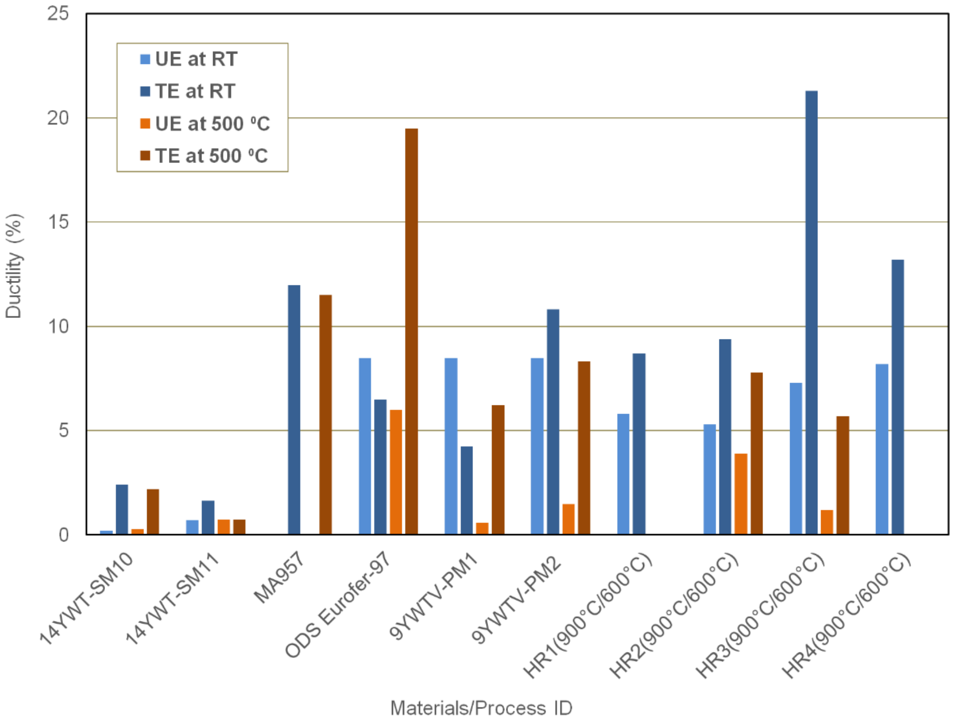

Figure 2. Comparison of uniform and total elongations among the ODS alloys processed with or without mechanical milling.

Particle distribution

The main microstructural factors in the ODS alloys required for desirable mechanical properties and radiation resistance would be a very fine grain structure and a proper distribution of nanoparticles [7]. Among the new ODS alloys, the ODS material HR2(900ºC/600ºC) is considered as the best alloy showing distributions of nanograins and nanoparticles. The alloy shows an inhomogeneous distribution of nanoparticles, where the Ti-rich particles can be either oxide or carbide particles. This section intends to display two 250 nm × 250 nm elemental maps representing, respectively, the high oxide density and relatively high carbide density regions and to compare their elemental (particle) distribution characteristics.

The elemental maps in the high oxide region of HR2(900ºC/600ºC) obtained using STEM are displayed in Figure 3. In the multigrain area (seen as the BF image) the TiY-rich oxide particles and TiWV-rich carbide particles coexist in a mixed distribution. Note that the carbon content, which was not intentionally alloyed in the powder but contained as an impurity element in 14YWT, is usually kept below 0.1 wt.% in 14YWT alloys while the oxygen content is added by the mixed-in oxide powder. A few of the W-rich particles coincide with the Ti-rich carbides, which indicates TiW carbides: the V and Mo distributions are relatively weak in these particles and sometimes W (or possibly W-C) tends to distribute on the surface of Ti-rich carbide or separately from the other carbides or oxides. Comparing the carbon and oxygen maps in detail, indeed, many of their distribution areas (i.e., particles) are not overlapping, which should indicate that the carbide and oxide particles are formed separately. It is also observed that some elements such as W and Ti are enriched in both large carbide and large oxide particles, which might because both elements have strong affinity with the carbon and oxygen atoms.

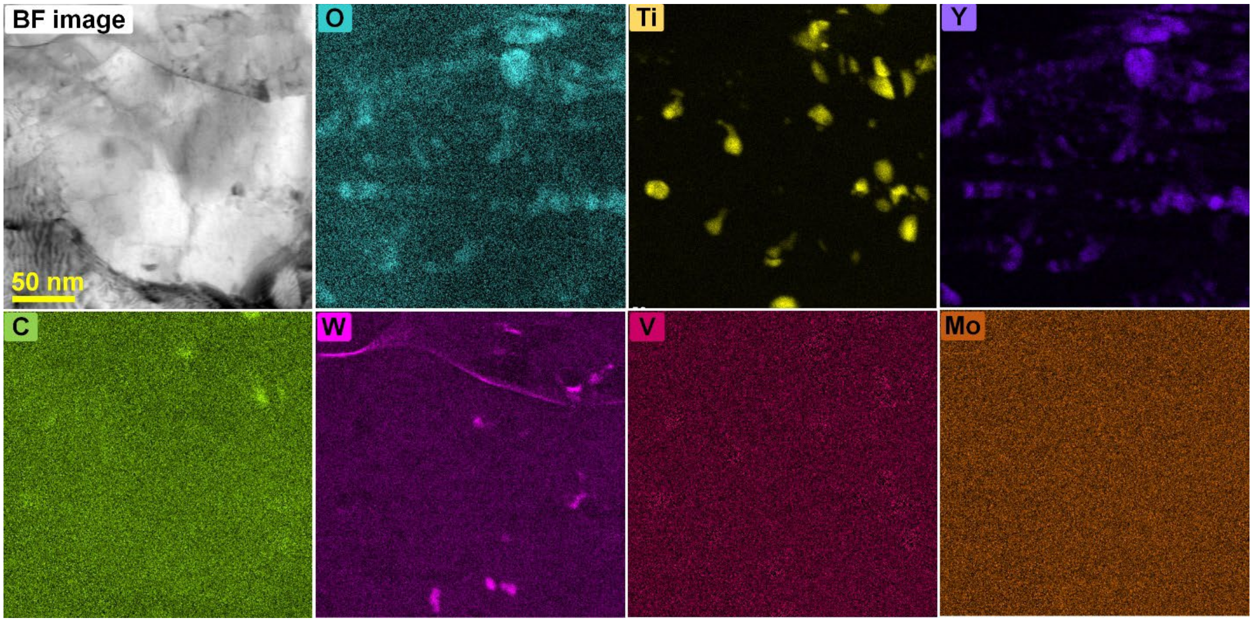

Figure 3. Elemental maps of oxide-rich grain area showing TiY-rich oxide (top) and TiWV-rich carbide (bottom) particles.

A region with little oxide but a few carbide particles was mapped with the same elements as in Figure 3 and the TiWV-rich carbide containing region is displayed in Figure 4. Elongated carbides with a strong concentration of C, Ti, and W are shown in Figure 4. The V-concentration at these carbide particles is relatively low, and Mo-concentration at the elongated carbides is almost non-detectable. As commonly shown in the bright field images, the nanograin structure produced via the low-cost processing using CTMP only has a grain size (effective grain boundary intercept distance) range of ~100–500 nm and it is a semi-annealed structure with a high density of dislocations. These elemental maps show residual element segregation at some preferred features like grain boundaries and precipitates along grain boundaries. Carbides are formed both in matrix and at grain boundaries and often have relatively high aspect ratio (or elongated shape), showing clearly preferred formation at grain boundaries. Analysis of carbide particles also indicates the majority of carbides are within the size range of ~10–50 nm while the oxide particles are smaller (> ~5 nm). Note that larger (up to ~80 nm) oxide and carbide particles are also occasionally observed, which are considered to be fragmented from the pre-existing particles but not completely dissolved during the thermomechanical processing applied in the limited temperature range. Finally, the total density of oxide and carbide particles is estimated to be at least an order of magnitude lower than that of the well-developed 14YWT (i.e., < 1×10^{23} m^{-3}) [7,13]. More number of samples need to be examined for more accurate particle density data.

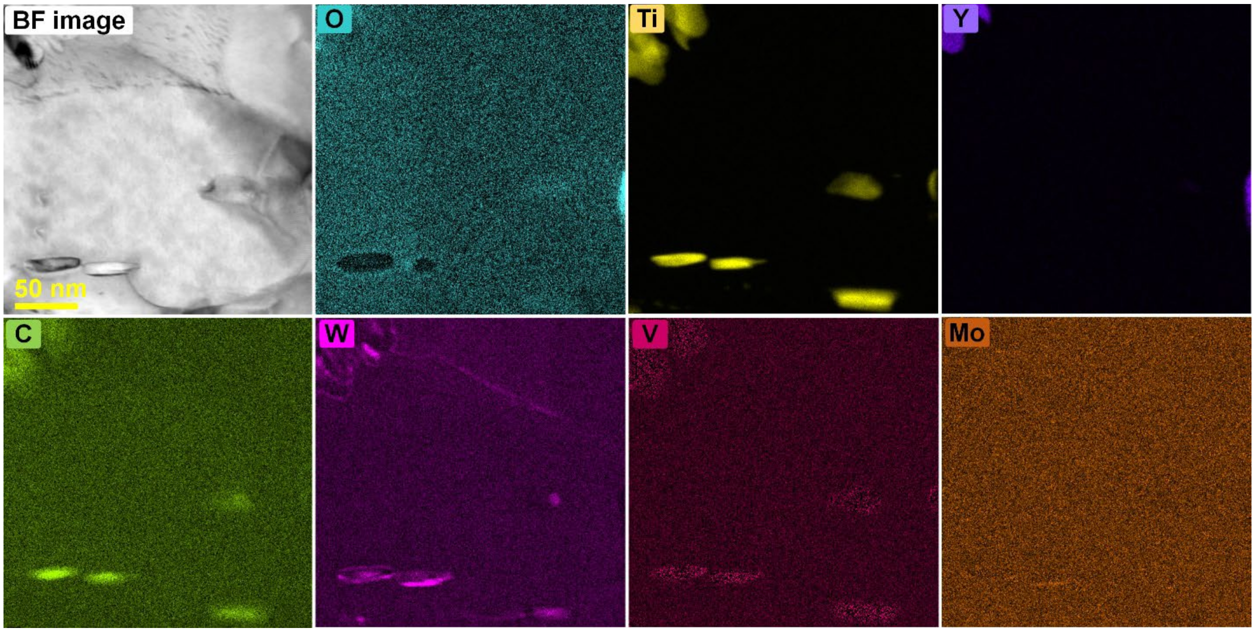

Figure 4. Elemental maps of carbide-rich grain area showing few oxide (top) and several TiWV-rich carbide (bottom) particles.

Results

It should be an encouraging outcome that the traditional thermomechanical activation cycles only can create the ODS alloys with desirable nanostructures and mechanical properties. The select TMP only approach to develop a low-cost production route for ODS demonstrated a good combination of high strength (YS > 800 MPa, UTS > 1 GPa) and significant ductility (UE and TE > 5%). The result of microstructural analysis also confirmed that nanocrystalline structure and distribution of nanoparticles (includes both oxides and carbides) were created in those ODS alloys by the continuous TMP method.

This low-cost ODS processing method might offer substantial flexibilities in manufacturing of ODS alloy components, without significant limitations in economical scale-up production. It is still recommended that the solid-state thermomechanical processing is further optimized for more desirable particle distribution characteristics with finer and higher-density oxide particles. Further optimization of processing route with a designated alloy powder and extended qualification testing and evaluation are necessary.

References

[1] D.T. Hoelzer, History and outlook of ODS/NFA ferritic alloys for nuclear applications, *Trans. American Nuclear Society,* 118 (2018) 1587-1590.

[2] T.S. Byun, D.T. Hoelzer, J.H. Kim, S.A. Maloy, "A Comparative Assessment on the Fracture Toughness Behavior of Ferritic-Martensitic Steels and Nanostructured Ferritic Alloys," *J. Nucl. Mater.,* 484 (2017) 157-167.

[3] D.T. Hoelzer, K.A. Unocic, M.A. Sokolov, T.S. Byun, "Influence of processing on the microstructure and mechanical properties of 14YWT," *J. Nucl. Mater.,* 471 (2016) 251-265.

[4] M.K. Miller, C.M. Parish, Q. Li, "Advanced oxide dispersion strengthened and nanostructured ferritic alloys," *Mater. Sci. Tech.,* 29 (2013) 174-1178.

[5] N. Baluc, J.L. Boutard, S.L. Dudarev, M. Rieth, J. Brito Correia, B. Fournier, J. Henry, F. Legendre, T. Leguey, M. Lewandowska, R. Lindau, E. Marquis, A. Muñoz, B. Radiguet, Z. Oksiuta, "Review on the EFDA work programme on nano-structured ODS RAF steels," *J. Nucl. Mater.,* 417 (2011) 149-153.

[6] D.T. Hoelzer, J. Bentley, M.A. Sokolov, M.K. Miller, G.R. Odette, M.J. Alinger, "Influence of particle dispersions on the high-temperature strength of ferritic alloys," *J. Nucl. Mater.,* 367–370 (2007) 166-172.

[7] P Song, Z Zhang, K Yabuuchi, A Kimura, "Helium bubble formation behavior in ODS ferritic steels with and without simultaneous addition of Al and Zr," *Fusion Engi. Des.,* 125 (2017) 396-401.

[8] Z.F. Wu, L.D. Xu, H.Q. Chen, Y.X. Liang, J.L. Du, Y.F. Wang, S.L. Zhang, X.C. Cai, B.R. Sun, J. Zhang, T.D. Shen, J. Wang, E.G. Fu, "Significant suppression of void swelling and irradiation hardening in a nanograined/nanoprecipitated 14YWT-ODS steel irradiated by helium ions," *J. Nucl. Mater. ,* 559 (2022) 153418.

[9] K. Edalati et al. , "Nanomaterials by severe plastic deformation: review of historical developments and recent advances,," *Mater. Res. Lett. ,* 10 (2022) 163-256.

[10] K. Edalati, Q. Wang, N.A. Enikeev, L.J. Peters, M.J. Zehetbauer, E. Schafler, "Significance of strain rate in severe plastic deformation on steady-state microstructure and strength," *Mater. Sci. Engi. A,* 859 (2022) 144231.

[11] Y. Estrin, A. Vinogradov, "Extreme grain refinement by severe plastic deformation: A wealth of challenging science," *Acta Mater.,* 61 (2013) 782-817.

[12] T.C. Lowe, R.Z. Valiev, "The use of severe plastic deformation techniques in grain refinement," *JOM,* 56 (2004) 64–68.

[13] H.J. McQueen, N.D. Ryan, "Constitutive analysis in hot working," *Mater. Sci. Engi. A,* 322 (2002) 43-63.

3. CERAMIC COMPOSITE STRUCTURAL MATERIAL DEVELOPMENT

3.1 RESPONSE OF ^{11}B ENRICHED ZrB$_2$ ULTRA-HIGH TEMPERATURE CERAMIC TO NEUTRON IRRADIATION AT ELEVATED TEMPERATURES

—Y. Lin, T. Koyanagi, C. Petrie, Y. Katoh (Oak Ridge National Laboratory), D. Sprouster (Stony Brook University), W. Fahrenholtz, G. Hilmas (Missouri University of Science and Technology)

Extended Abstract: Full manuscript submitted to Acta Materialia

OBJECTIVE

Investigate the effects of neutron irradiation on ultrahigh temperature ceramics (UHTCs) for potential applications in fusion reactors, with a specific focus on ^{11}B-enriched ZrB$_2$.

SUMMARY

The ZrB$_2$, a UHTC, is being considered for use in fusion reactor first-wall structures, yet its response to irradiation remains poorly understood. This study employed scanning/transmission electron microscopy (S/TEM), synchrotron X-ray diffraction (XRD), and thermal property measurements to thoroughly investigate the neutron-irradiation effects on ^{11}B-enriched ZrB$_2$. Neutron irradiations were conducted at 220°C and 620°C, with a neutron fluence of 2.2×10^{25} neutron/m^2 (energy > 0.1 MeV), resulting in 3.9 dpa and 4200 appm He. The study revealed the unusual prevalence of prism loops and a>c anisotropic lattice swelling, likely linked to the low c/a ratio of ZrB$_2$, leading to grain boundary microcracking. Reducing the grain sizes was effective in reducing intergranular cracking and macroscopic swelling. The observation of cavities in ZrB$_2$ irradiated at 620°C, as opposed to 220°C, prompts questions about the temperature at which vacancies in ZrB$_2$ become mobile, and the role of neutron absorption by ^{10}B in elevating irradiation temperatures. Isotopic enrichment in ^{11}B proves to be a viable strategy for mitigating helium production in transition-metal diborides, which is a critical consideration for nuclear applications. Irradiation-induced defects reduce the thermal diffusivity and conductivity of ZrB$_2$ by a factor of 4-9, which has important implications for its role as a plasma-facing material in fusion reactors that drive high heat fluxes through first-wall materials. This comprehensive study lays the foundation for understanding ZrB$_2$ behavior under neutron irradiation and highlights important phenomena to consider for various nuclear applications.

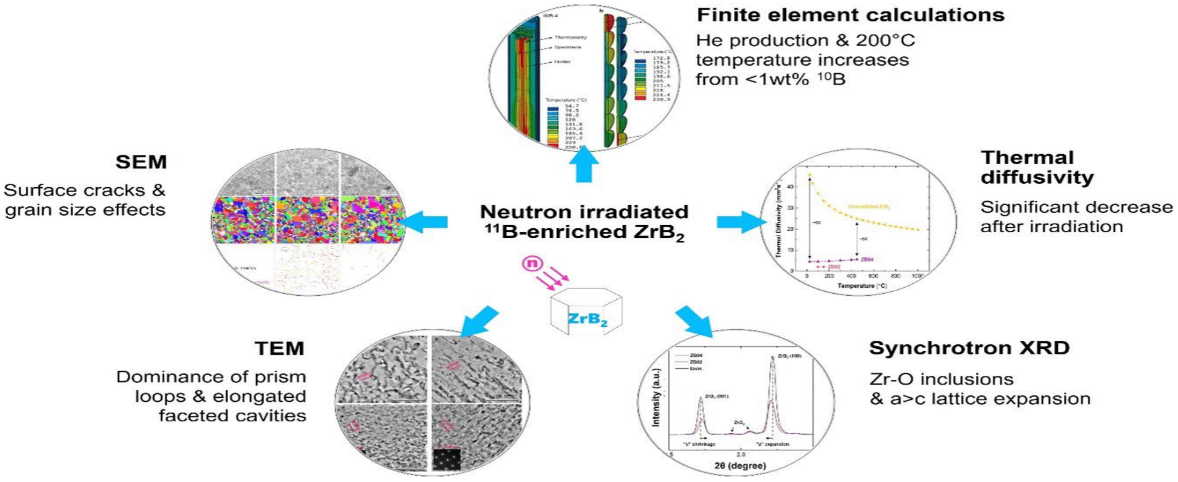

Figure 1. Graphic abstract highlighting the important findings of the study on neutron-irradiated ZrB$_2$ at 220°C and 620°C, up to 3.9 dpa, and 4200 appm He.

Results

Future work will focus on post-irradiation examination of neutron irradiated ZrB$_2$ and TiB$_2$ at 1000°C.

4. PLASMA-FACING AND HIGH HEAT FLUX MATERIALS AND COMPONENT TESTING

4.1 FABRICATION OF Cu-Cr-Nb-Zr (CCNZ) ALLOYS FOR FUSION APPLICATIONS—M. S. Haque, A. Sharma, M. Ouyang, D.J. Sprouster, L.L Snead (Stony Brook University)

SUMMARY

Copper alloys with high strength and high creep resistance have been extensively used as heat sink materials for nuclear fusion applications. In this work, CCNZ alloys were fabricated by Direct Current Sintering (DCS) (also known as Spark Plasma Sintering) method. The presence of Cr_2Nb and Cr-rich precipitates have been identified by conducting X-ray Diffraction (XRD) of the samples. These precipitates are located in the grain and at sub-grain boundaries and play an important role in strengthening the alloys at high temperatures [1]. In this report, we report our recent efforts to increase the number of Cr-rich precipitates through post-sintering heat treatments. Specimens were fabricated through Direct Current Sintering, and X-ray Diffraction was used to quantify the microstructure.

PROGRESS AND STATUS

Gas-atomized feedstock powder with composition of Cu- Cr 2-Nb 1.35-Zr 0.15 was used to sinter the alloys. The average particle size of the feedstock powder is ~19.1μm. For each DCS experiment, 18 grams of feedstock powder was loaded to a 25 mm diameter graphite die and placed in a DCS System. Powders have been sintered at temperatures 900°C and 970°C with a heating rate of 10°C/min. After finishing sintering, the die was kept at the peak temperature for two different time periods (e.g., 5 mins and 10 mins). Throughout the sintering process, a fixed uniaxial compressive pressure of 50MPa and a vacuum of <10Pa were maintained to hinder oxidation of the alloys. The as-sintered CCNZ samples were cleaned by sandblasting. The density of the samples was measured using Archimedes' Principle.

The as-sintered samples were then annealed at 970°C for 20 mins followed by water quenching. Annealing was performed to enable the complete solutionizing of Cr atoms in the Cu matrix and to facilitate precipitation [2]. After that, water quenched samples were aged at 500°C for 16 hrs. and cooled in air. Muffle furnace was used for annealing and aging purposes. Samples were polished using different grades of polishing papers. In order to identify the phases, XRD patterns were collected for mirror polished as sintered, annealed, and aged samples. The XRD patterns were collected in Bragg-Brentano mode utilizing Cu K radiation source in a Bruker D8 diffractometer from 20° to 120° two-theta angular range with 0.5 °/s time per step and 0.01° step size. Background of the obtained patterns was corrected by Igor pro software. Phase identification was performed using Match3! Software (Crystal Impact, Bonn, Germany).

Experimental Procedure

The density was found to be ~99% for all the samples. The XRD patterns for the samples in as sintered, annealed, and aged conditions are shown in Figure 1. The XRD peaks obtained for the samples were indexed to three different crystal phases; Cu (space group: Fm-3m), Cr_2Nb (space group: Fd-3m), Cr (space group: Im-3m). Subtle peaks from the Cr_3Cu (space group: Pm-3m) are potentially buried underneath the major Cu peaks in the 16-hour aged specimen. The lattice parameter for the major FCC Cu phase was found to expand upon aging, as shown in Table 1, potentially indicative of an increase in precipitation.

Results

- Phase quantification will be completed by using TOPAS software.
- Mechanical testing (Creep, Vickers, Tensile) will be carried out to determine the hardness of the prepared samples.
- The SEM/EDS characterizations will be performed for microstructural observations.
- Thermal properties (Creep, Thermal conductivity) and electrical property (Electrical resistance) will also be measured for CCNZ samples.

- Comparing XRD and electron microscopy results to computational thermodynamics in collaboration with Oak Ridge National Laboratory (ORNL).

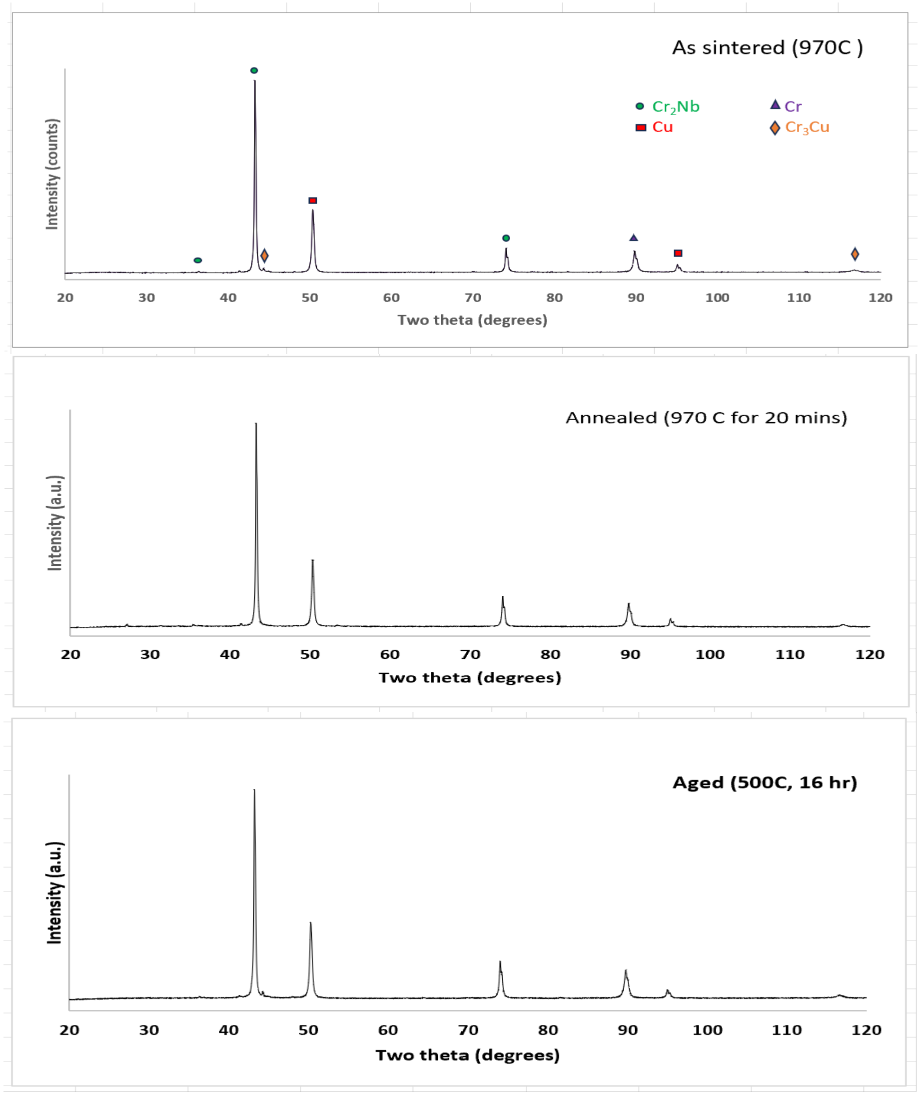

Figure 1. The XRD patterns collected for CCNZ alloys in three different conditions.

Table 1. Quantitative lattice parameters for the FCC matrix determined from the XRD data in Figure 1

Specimen (id)	**lattice parameter (Å)**
As sintered	3.61755 ± 0.00002
970°C 20 mins	3.61970 ± 0.00002
500°C 16 hrs.	3.62163 ± 0.00002

Acknowledgements

The work was funded under Grant DE-SC0018332 to the Research Foundation at State University of New York, Stony Brook by the US Department of Energy Office of Fusion Energy Sciences.

References

[1.] X. Guo, Z. Xiao, W. Qiu, Z. Li, Z. Zhao, X. Wang, Y. Jiang, Microstructural and properties of Cu-Cr-Nb alloy with high strength, high electrical conductivity and good softening resistance performance at elevated temperature, Materials Science and Engineering: A, 749, (2019), 281.

[2.] B. Cheng, L. Wang, D.J. Sprouster, J.R Trelewicz, W. Zhong, Y. Yang, S. J Zinkle, L. L. Snead, Tailoring microstructure in sintered Cu-Cr-Nb-Zr alloys for fusion components, Journal of Nuclear materials, 551, (2021).

4.2 IN-SITU MICROMECHANICAL TESTING ON W/NiFe DUCTILE-PHASE TOUGHENED TUNGSTEN

—A. V. Garcia Caraveo, T. Chen (Oregon State University), W. Jiang, J. V. Haag IV, W. Setyawan (Pacific Northwest National Laboratory)

OBJECTIVE

The objective of this project is to evaluate the radiation-induced mechanical property changes in ductile phase toughened (DPT) W-NiFe alloys, combining small-scale mechanical testing, ion irradiation, and mechanistic modeling techniques.

SUMMARY

In the report period (July – December 2023), we received the ion-irradiated sample from Pacific Northwest National Laboratory (PNNL), performed electron backscatter diffraction (EBSD) characterization, preliminarily characterized the mechanical response to irradiation damage via nanoindentation techniques, and designed micro-tensile testing experiments to study the mechanical properties of the W/NiFeW interface, with and without radiation damage. Through this project, a graduate student from an under-represented group was recruited. The student has demonstrated satisfactory academic performance and finished several essential training courses to be successful in graduate school and in conducting research for this project. The training includes scanning and transmission electron microscopy, focused ion beam, and micromechanical testing techniques. This effort promotes the Department of Energy's (DOE's) education mission and the future workforce pipeline for United States (US) energy sectors.

PROGRESS AND STATUS

Introduction

The DPT W-NiFe alloys have significantly improved fracture toughness compared to tungsten, mitigating the brittleness of W-based plasma-facing materials. With the strong interface between the hard and the ductile phases, microcracks initiate in the hard W phase are arrested and blunted by the ductile NiFeW phase, which also bridges co-planar microcracks [1, 2]. However, after ion irradiation (which emulates helium accumulation and radiation damage effects of 14 MeV neutrons), helium cavities were observed at the W/NiFeW interface [3], raising concerns about possible interfacial debonding, which impairs the above toughening mechanisms. Further development, evaluation, and qualification of DPT alloys for fusion applications require answering the following questions. (1) To what extent does the radiation evolution of the W/NiFeW interface affect the mechanical properties and microcrack initiation and propagation behavior? (2) Should we expect new toughening mechanisms to emerge due to the local mechanical property changes? And (3) Can we tailor the microstructure of the DPT alloys for better performance in radiation environments? One critical step to answering these questions and understanding the mechanisms is quantifying the microstructure-specific properties, which will also provide input to computational models for performance prediction and microstructure optimization. Yet, given the shallow irradiated zones of ion irradiation samples, small-scale mechanical testing is the only feasible technique.

Small-scale mechanical testing has demonstrated success in characterizing mechanical responses to ion irradiation. Prior studies mainly applied nanoindentation based techniques to understand irradiation hardening effects [4–6]. On the other hand, instrumented nanomechanical stages for in-situ scanning electron microscopy (SEM) enable mechanical testing on focused-ion beam (FIB) milled specimens with different geometries, introducing different stress fields to derive different micromechanical properties. Our previous project report summarized the demonstrations of notched and unnotched microcantilever bending and micropillar compression techniques in obtaining microscopic fracture toughness, elastic modulus, and critical resolved shear stress of the W phase [7].

In this report, we present the irradiation hardening of W and NiFeW phases under different irradiation conditions. The results indicate potential reduction of the fracture toughness of the W particles and degradation of the fracture arresting capability at the W/NiFeW interface. After literature view, we proposed micro-tensile single edge notched tension (SENT) testing to characterize such changes [8, 9] and fabricated several SENT specimens within the irradiated area.

Experimental Procedure

The DPT alloy used for this research is W-NiFe alloy sample W90, which contains 90W-7Ni3Fe (by wt%) supplied and mechanically polished by PNNL. The irradiation was performed at Texas A&M University, at 500°C. Ni^+ and He^+ ions of multiple energies were irradiated at different glancing angles to create flat damage and helium profiles up to the depth of 1.5 µm. As shown in Figure 1, the irradiated sample contains four different regions, namely, Ni^+ irradiated, $Ni^+ + He^+$ irradiated, He^+ irradiated, and unirradiated.

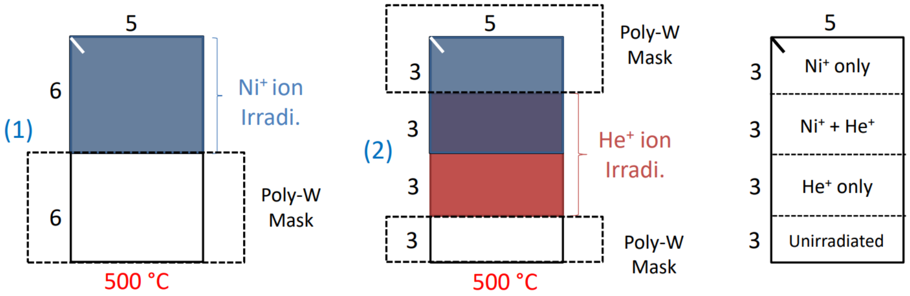

Figure 1. Irradiation layout and location for each ion irradiation condition.

To study the irradiation hardening effect, nanoindentation with a Berkovic tip was performed using the FemtoTools FT-NMT04 nanoindenter. Within each region of a certain irradiation condition, forty-five tests were performed. Displacement-controlled mode was used to reach a maximum depth of 250 nm. In order to obtain continuous hardness data at different indentation depth, continuous stiffness measurement (CSM) technique was applied.

The SENT dogbones were fabricated using a Helios Hydra Plasma FIB system. The micro-milling was done using Xe ions of 30 keV. Initial milling employs a high beam current of 1 µA to remove materials and perform cross-section cuts. The beam current was gradually reduced to 1 nA to perform finer cuts and eventually to 0.5 nA for sample surface polishing. To cut the sharp notch, a current of 18 pA was used.

Results

Irradiation hardening

Figure 2 shows the hardness vs indentation depth obtained from the W and NiFeW phases from the regions of different irradiation conditions. The lower tails of these curve reflect the surface effect, showing high hardness due to the geometrically necessary dislocations. As a rule of thumb, the radius of the plastic zone underneath indentation is approximately 5 to 10 times of the indentation depth. Thus, the flat ranges of these curves, between 0.1 and 0.175 µm, reflect the mechanical properties of the irradiated zone. The average hardness of this range was calculated and provided in Table 1 to compare the phase-specific mechanical responses to different ion irradiation conditions. There is a clear hardening effect from each irradiation condition compared to the unirradiated sample on W single crystals. In both phases, hardness increases in the order of unirradiated, He^+ irradiated, Ni^+ irradiated, and He^++Ni^+ irradiated. Irradiation hardening is more significant in the W than the NiFeW phase.

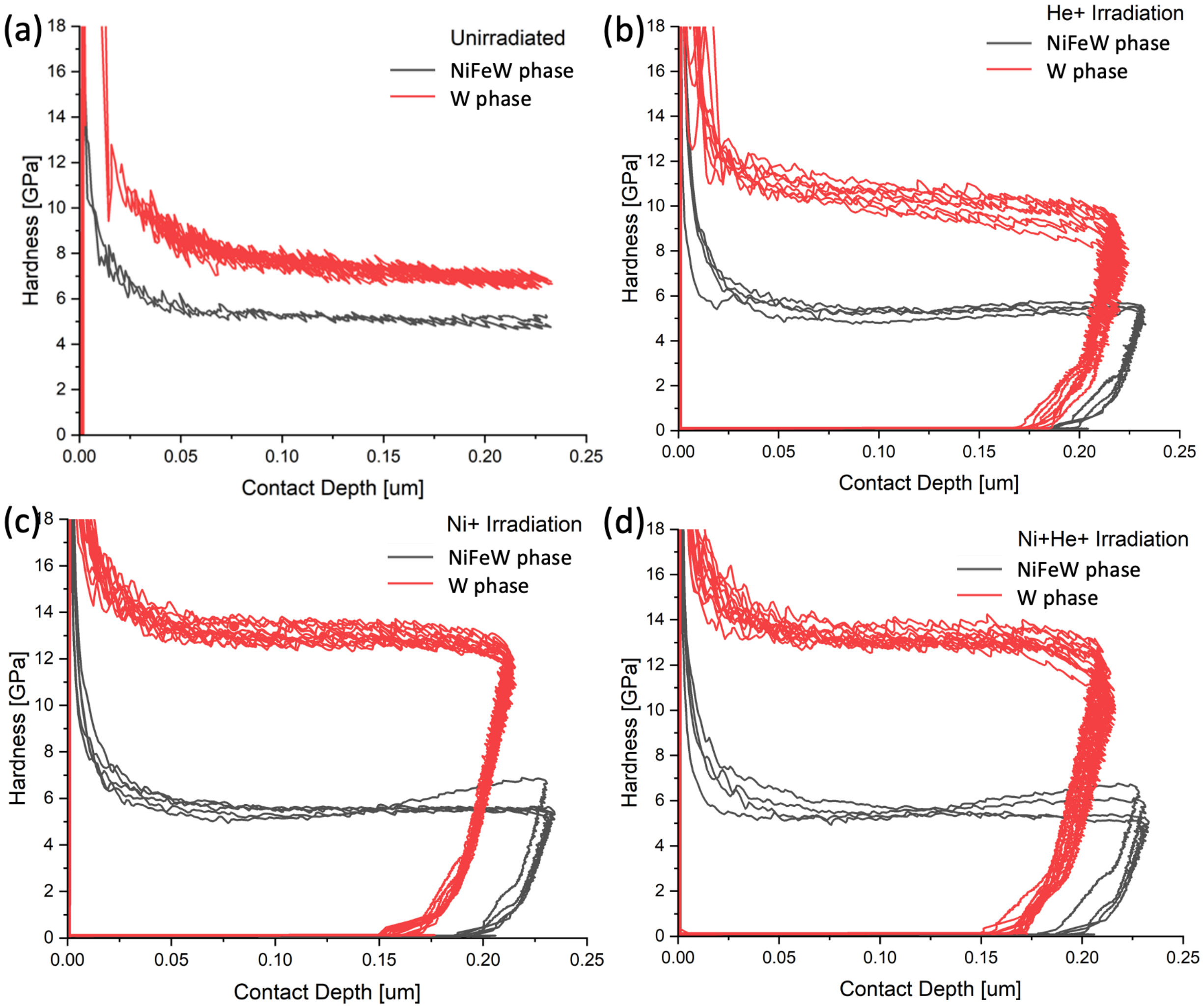

Figure 2. Phase-specific hardness profiles in the unirradiated (a), He⁺ irradiated (b), Ni⁺ irradiated (c), and Ni⁺ and He⁺ irradiated (d) samples.

Table 1. Average hardness and the standard deviations (STD) for W and NiFeW phases exposed to different ion irradiation conditions

	Av. Hardness (GPa)		**STD**	
	W	**NiFeW**	**W**	**NiFeW**
Unirradiated	8.167	4.918	0.0945	0.0671
He$^+$	10.22	5.256	0.3458	0.1605
Ni$^+$	12.95	5.496	0.3236	0.0804
Ni$^+$ + He$^+$	13.17	5.503	0.2911	0.1317

The He^+ irradiated zone presents observable hardness increase compared to the unirradiated zone. Besides defects, He^+ irradiation at high temperatures produce helium bubbles. According to Cui et al., He^+ bubble accumulation is the main cause of hardening at an irradiation temperature of around 800°C (the homologous temperature $T_h = 0.29$) in Tungsten [10, 11]. In this study, at a lower irradiation temperature of 500°C, where $T_h = 0.21$ for W and $T_h = 0.45$ for NiFeW, He^+ irradiation may also introduce dislocations that contribute additional hardening.

Ni^+ irradiation primarily introduced hardening via the formation of voids and dislocation loops. Following Ni^+ irradiation, the relative hardness increase is more significant in the W phase than in the NiFeW phase. This can be rationalized by the lower homologous irradiation temperature of W than NiFeW. The irradiation temperature of 500°C is below the Stage-III defect recovery temperature of W but beyond that of NiFeW. That is to say, during irradiation, vacancies are immobile in W but mobile in NiFeW. In the latter case, vacancy-interstitial and vacancy-loop interactions are expected to suppress the accumulation of defect structures [12].

Between Ni^+ and $Ni^+ + He^+$ irradiation zones, the hardness differences are insignificant for both W and NiFeW phases. It is possible that the similar hardness values for both irradiated zones were a result of the sequence of the irradiation. The $Ni^+ + He^+$ irradiated zone was firstly exposed to Ni^+ irradiation, causing high concentration of voids and dislocation loops. When He^+ ions were implanted later, the existing defect structures may serve as sinks to both He atoms and point defects, mitigating the hardening effect from He^+ irradiation. It is possible that simultaneous irradiation of Ni^+ and He^+ ions may introduce more pronounced He^+ bubble formation [10] and thus more significant hardening effects than observed herein. To fully understand the hardening effect caused by He^+, Ni^+ and $He^+ + Ni^+$ irradiation at 500°C, a transmission electron microscopy (TEM) study of both W and NiFeW phases is necessary. The TEM results will help correlate the irradiation-induced microstructure evolution to the mechanical property changes.

Future work

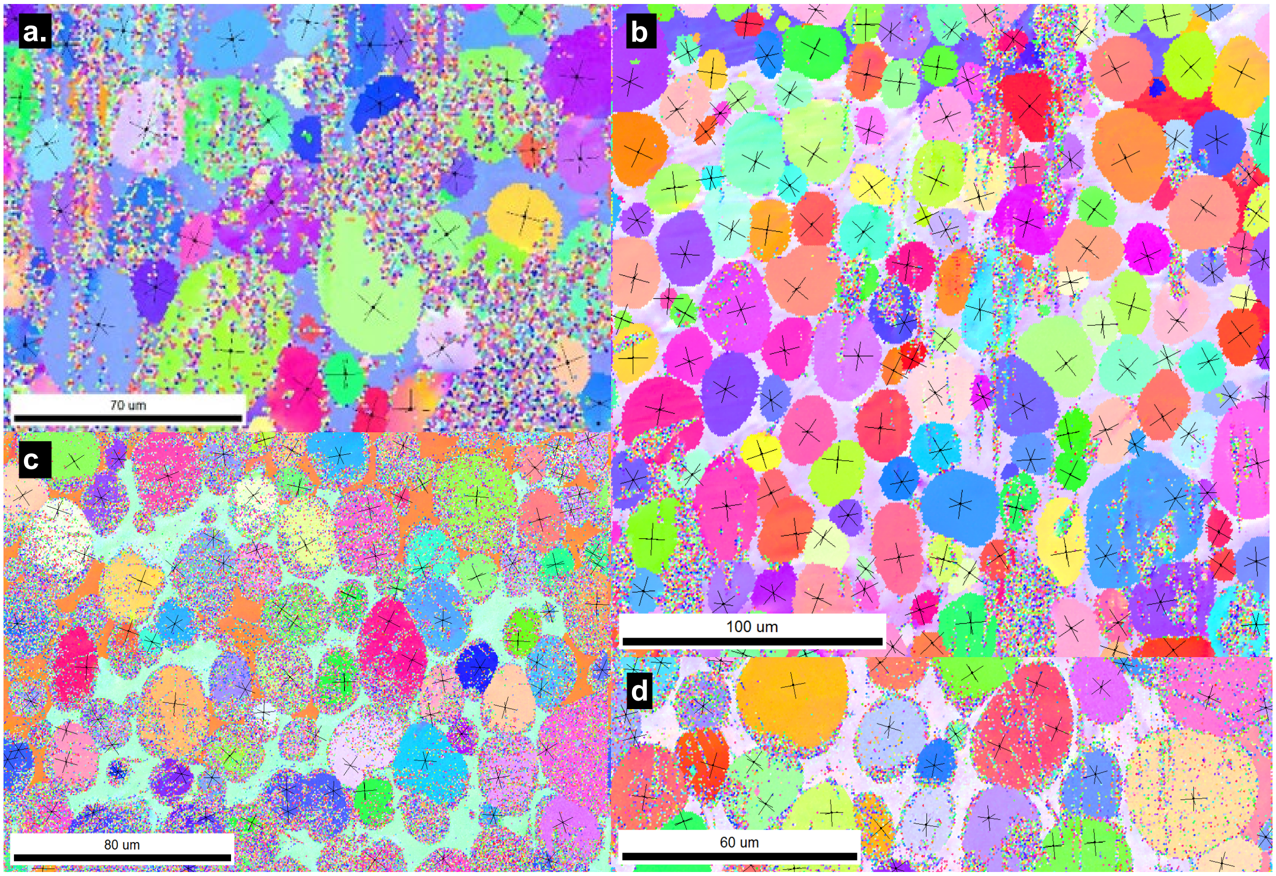

Figure 3. The EBSD analysis with the single-phase W <100> orientations highlighted with a black trace for a) Unirradiated b) He^+ irradiated c) Ni^+ irradiated and d) Ni^+ & He^+ irradiated conditions.

Based on the above results, we expect suppression of plasticity in both phases by irradiation. This can potentially result in a reduction of the fracture toughness of the W phase, and changes in crack resistance properties at the W/NiFe interface. For the rest of FY24, we plan to study the changes of the fracture behavior in response to ion irradiation. Some preparation has been put into effort. Shown in Figure 3, EBSD has been performed on the irradiated sample to obtain the crystallographic information and orientation relationships between different phases. An electron voltage of 30 kV and a current of 1.5 nA were used to generate EBSD maps at a step size of 0.5 um. Although the quality of the EBSD maps is not optimum, such maps are sufficient to aid the following fabrication of micromechanical specimens. Guided by the EBSD survey shown in Figure 3, SENT dogbone specimens were fabricated with controlled crystal orientations. Specimens containing a single crystal W only and a W/ductile-phase interphase boundary were prepared in each irradiated condition, except He^+ irradiated, with the W {100} crack plane oriented to the fabricated edge notch. The micro dogbones have a gauge length of 11 μm and width of 3 μm. The notch to gauge width ratio was determined to be 0.4-0.5 following the ASTM standards [9, 13]. The specimen thickness is set to be equal to 1 μm so that the whole thickness is within the irradiated zone. Figure 4 shows examples of the fabricated SENT specimens in different regions of the irradiated sample.

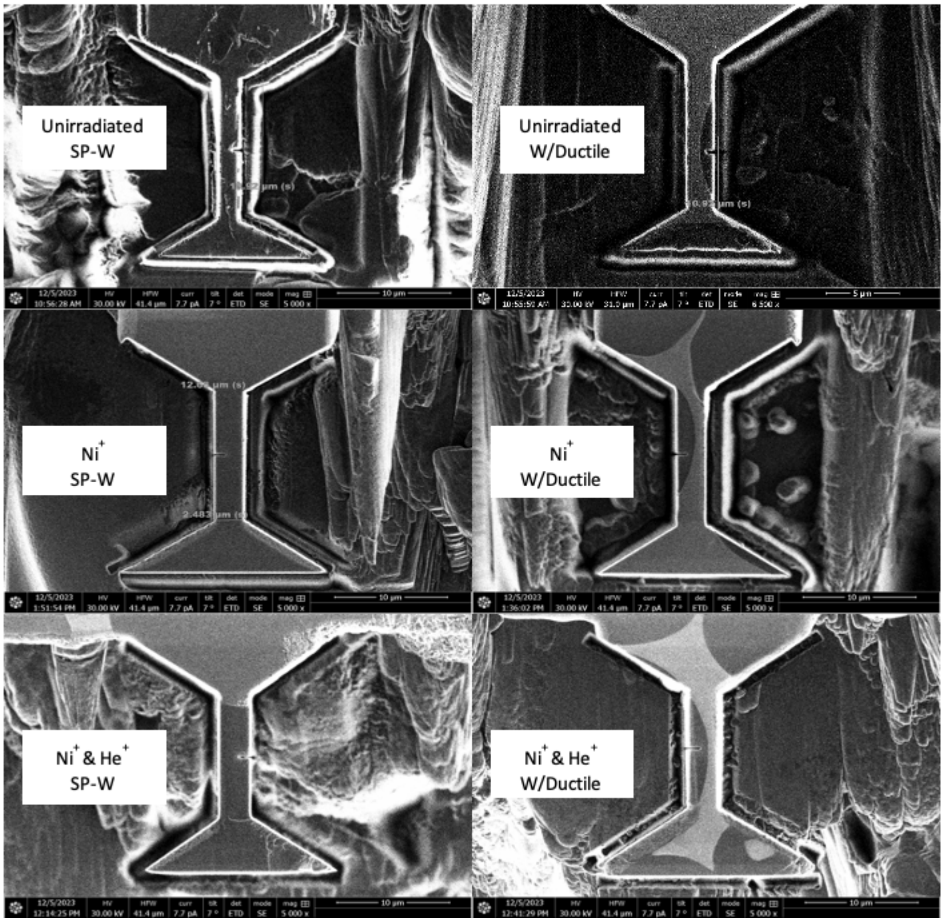

Figure 4. The SENT dogbone specimens containing single-phase W only (SP-W) shown on the left panels and W/NiFeW interphase boundary (W/Ductile) shown on the right panels. Unirradiated, Ni^+ irradiated, and Ni^+& He^+ irradiated specimens are shown on the top, middle, and bottom panels, respectively.

Acknowledgements

The research was supported by the Office of Fusion Energy Science, US DOE and performed under the Contract DE-AC05-76RL01830. The authors acknowledge Ramprashad Prabhakaran for providing the samples.

References

[1.] Alam ME, Odette GR (2020) On the remarkable fracture toughness of 90 to 97W-NiFe alloys revealing powerful new ductile phase toughening mechanisms. *Acta Materialia*, 186:324–340. https://doi.org/10.1016/j.actamat.2020.01.012.

[2.] Haag JV, Edwards DJ, Henager CH, Setyawan W, Wang J, Murayama M (2021) Characterization of ductile phase toughening mechanisms in a hot-rolled tungsten heavy alloy. *Acta Materialia*, 204:116523. https://doi.org/10.1016/j.actamat.2020.116523.

[3.] Jiang W, Zhang D, Li D, Heo J, Wang Z, Zhang L, Overman N, Varga T, Hu Z, Wang X, Shao L, Setyawan W (2022) Behavior of helium cavities in ion-irradiated W-Ni-Fe ductile-phase toughened tungsten. *Journal of Nuclear Materials*, 561:153565. https://doi.org/10.1016/j.jnucmat.2022.153565.

[4.] Hosemann P (2018) Small-scale mechanical testing on nuclear materials: bridging the experimental length-scale gap. *Scripta Materialia*, 143:161–168. https://doi.org/10.1016/j.scriptamat.2017.04.026.

[5.] Chen T, He L, Cullison MH, Hay C, Burns J, Wu Y, Tan L (2020) The correlation between microstructure and nanoindentation property of neutron-irradiated austenitic alloy D9. *Acta Materialia*, 195:433–445. https://doi.org/10.1016/j.actamat.2020.05.020.

[6.] Hosemann P, Vieh C, Greco RR, Kabra S, Valdez JA, Cappiello MJ, Maloy SA (2009) Nanoindentation on ion irradiated steels. *Journal of Nuclear Materials*, 389(2):239–247. https://doi.org/10.1016/j.jnucmat.2009.02.026.

[7.] Garcia Caraveo AV, Chen T (2022) Application of microcantilever bending tests to local fracture toughness determination in W-Ni-Fe ductile-phase toughened tungsten. *Fusion Reactor Materials Program Semiannual Progress Report*, DOE/ER313/73(73):36-43.

[8.] Jaya BN, Kirchlechner C, Dehm G (2015) Can microscale fracture tests provide reliable fracture toughness values? A case study in silicon. *Journal of Materials Research*, 30(5):686–698. https://doi.org/10.1557/jmr.2015.2.

[9.] Gong B, Xia C, Lacidogna G, Xu Q, Liu Y, Li Y (2020) Constraint analysis of thickness effects on fracture resistance behavior of clamped single-edge notch tension specimen. *Theoretical and Applied Fracture Mechanics*, 110:102802. https://doi.org/10.1016/j.tafmec.2020.102802.

[10.] Cui MH, Shen TL, Zhu HP, Wang J, Cao XZ, Zhang P, Pang LL, Yao CF, Wei KF, Zhu YB, Li BS, Sun JR, Gao N, Gao X, Zhang HP, Sheng YB, Chang HL, He WH, Wang ZG (2017) Vacancy like defects and hardening of tungsten under irradiation with He ions at 800 °C. *Fusion Engineering and Design*, 121:313–318. https://doi.org/10.1016/j.fusengdes.2017.05.043.

[11.] Cui M, Shen T, Pang L, Zhu Y, Jin P, Liu C, Fang X, Wang Z (2018) He ion implantation induced He bubbles and hardness in tungsten. *Nuclear Materials and Energy*, 15:232–236. https://doi.org/10.1016/j.nme.2018.05.004.

[12.] Gao N, Yao ZW, Lu GH, Deng HQ, Gao F (2021) Mechanisms for interstitial dislocation loops to diffuse in BCC iron. *Nature Communications*, 12(1):225. https://doi.org/10.1038/s41467-020-20574-6.

[13.] Zheng X, Ghassemi-Armaki H, Hartwig KT, Srivastava A (2021) Correlating Prior Austenite Grain Microstructure, Microscale Deformation and Fracture of Ultra-High Strength Martensitic Steels. *Metals*, 11(7):1013. https://doi.org/10.3390/met11071013.

4.3 RECENT PROGRESS IN THE MICROSTRUCTURAL CHARACTERIZATION OF HEAVY ION IRRADIATED TUNGSTEN HEAVY ALLOYS—James V. Haag IV, Matthew J. Olszta, Weilin Jiang, Danny J. Edwards, Wahyu Setyawan (Pacific Northwest National Laboratory)

OBJECTIVE

This report summarizes the recent progress in the characterization of unrolled and hot-rolled heavy ion irradiated tungsten heavy alloy specimens.

SUMMARY

Transmission electron microscopy (TEM) and electron backscattered diffraction (EBSD) have been conducted on as-sintered and hot-rolled tungsten heavy alloy (WHA) specimens. This was done to provide a comparative analysis of the irradiation behavior between the as-sintered and hot-rolled conditions. While the constituent phases and composition of these specimens remains constant with the applied thermomechanical processing, their microstructures vary substantially. The original hypothesis of hot-rolling introducing additional boundaries that contribute to increased radiation resistance is under investigation, revealing that new interfaces introduced during hot-rolling act as defect trapping sites. This is theorized to lead to comparatively lower damage segregation per boundary through an increase of sink sites and reduced boundary embrittlement. This effect is expected to be conflated with surface damage found in the hot-rolled specimen, likely from mechanical polishing prior to irradiation.

PROGRESS AND STATUS

In this reporting period, this analysis of heavy ion irradiated WHAs has been further expanded to observe the effects of thermomechanical processing on the manifestation of irradiation damage in different WHA microstructures. Pacific Northwest National Laboratory (PNNL) has been actively pursuing the introduction of a hot-rolling process to tailor WHA microstructures for improved mechanical response [1], and the next thrust of this work is the characterization of both an as-received industrial material and an in-house produced hot-rolled WHA after high temperature heavy ion irradiation. The details for these irradiations can be found in the work by Jiang et al. in prior reporting periods [2] but have been constructed to simulate five years of service in a theoretical fusion power plant [3].

The specimens of interest to this work are a liquid phase sintered 90W-7Ni-3Fe WHA from MiTech Metals which will be referred to as the 'unrolled' specimen, and an identical composition alloy sintered at PNNL and sequentially hot-rolled and annealed to an approximately 87% thickness reduction, here called the 'hot-rolled' specimen [4]. These two samples were sectioned, polished, and sent for identical high temperature (700°C) sequential Ni^+ and He^+ ion irradiations to mimic the fusion environment. Both samples were masked during irradiation to present four distinct exposed regions, a unirradiated control region, Ni^+ only exposed, He^+ only exposed, and a $Ni^+ + He^+$ exposed. It is noted that for the hot-rolled sample, the bulk specimen sent for irradiation has been found to exhibit surface damage consistent with improper metallurgical preparation pre-irradiation. This has been confirmed via EBSD of the control region from the hot-rolled specimen, and it will be discussed in more detail below.

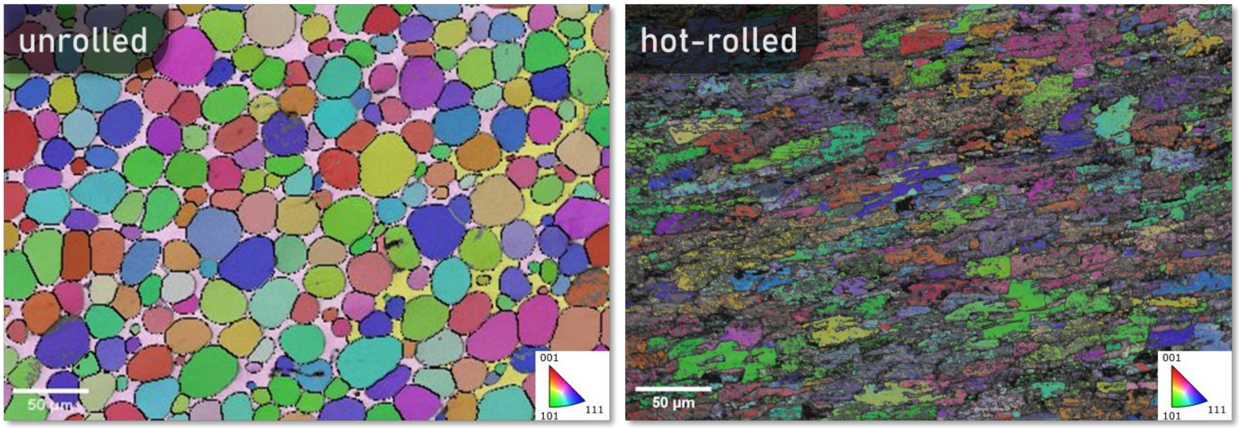

Figure 1. The EBSD maps of the unirradiated control regions from an unrolled (left) and hot-rolled (right) WHA.

In an effort to determine the comparative effects of irradiation on the different WHA microstructures, EBSD analyses were conducted on the unirradiated control regions of the unrolled and hot-rolled specimens post ion-irradiation. The control region allows for direct comparison between the two sample sets, as well as the separation of purely thermal effects from that of the irradiation. An inverse pole figure (IPF) map of the sample surfaces, Figure 1, highlights the differences in internal grain structure between the two samples. The control region of the unrolled specimen presents single-crystal spherical domains of W and a continuous network of the γ phase with very little intragranular misorientation, while the control region of the hot-rolled specimen possesses a high degree of internal misorientation present within the W phase with the γ phase almost un-indexable due to strain. These same features are not found in EBSD maps of the same hot-rolled specimen in prior investigations [5], which indicates potential surface damage artifacts from preparation of the specimen prior to irradiation. This finding is of particular note as the damage depth for ion irradiation is comparatively shallow (a few hundred nm) and coincides with the near-surface damage region from conventional grinding/polishing. This difference in specimen surface quality therefore introduces an additional degree of freedom in the comparative analysis of the unrolled and hot-rolled microstructures. It is assumed that the surface damage region from polishing in the hot-rolled sample will extend far beyond the maximum ion implantation depth as calculated from SRIM (~750nm) [2] and is likely on the order of several microns in depth.

Characteristic examples of γ phase domains in the Ni+He exposed regions of the hot-rolled specimen have been shown in Figure 2, with an abundance of dislocations found within the grains and an approximately Gaussian distribution of cavities found in the implantation depth dimension. Scanning transmission electron microscopy (STEM) investigation of these regions show that the cavities introduced from He^+ ion implantation appear to decorate γ phase dislocation lines and that grain boundaries in the γ phase possess a high density of cavities on the boundary planes. With the introduction of strain to the material in the form of damage from surface polishing prior to irradiation as well as from approximately 31dpa of Ni^+ implantation damage into the γ phase, further complicated by an irradiation temperature of $0.56T_m$ for the γ phase ($T_m \approx 1450^oC$), the kinetics of damage evolution in these materials is undeniably difficult to discern. Yet with this complexity comes the ability to observe the characteristic damage in an irradiated WHA material with an abundance of damage features in the irradiated near-surface region. With the sensitivity of STEM to these defect populations, it is then possible to gain additional insight into the irradiation damage accommodation in these materials.

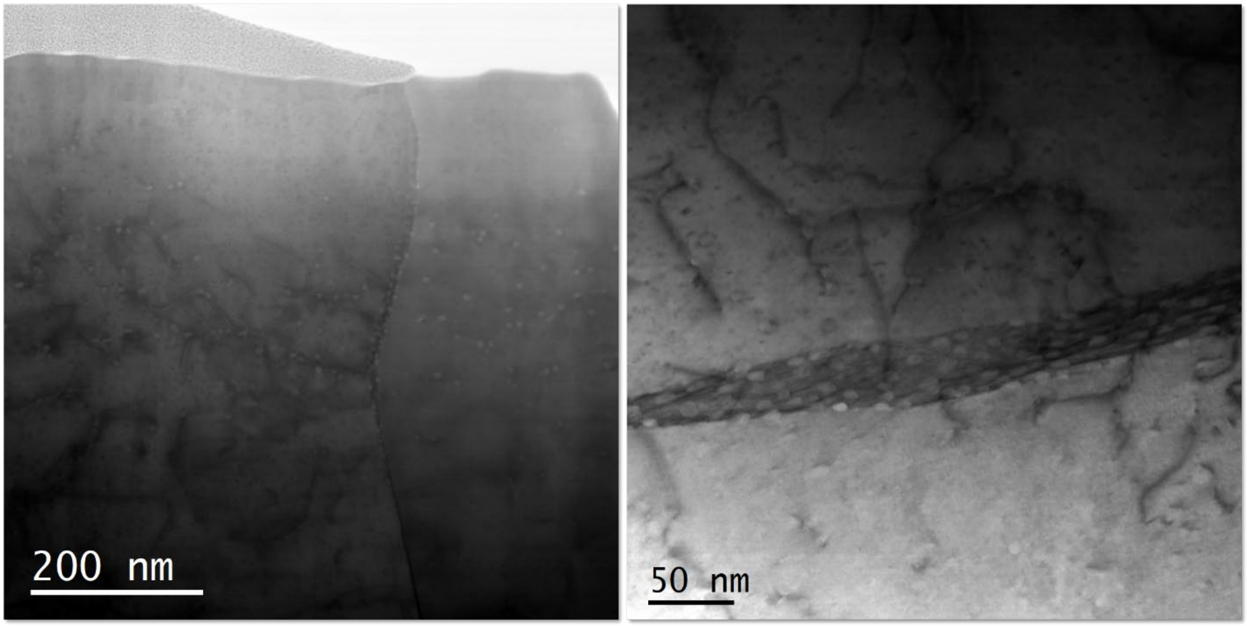

Figure 2. Bright field STEM micrographs of γ phase domains in the Ni+He exposed region of the hot-rolled specimen. A higher density of cavities is noted at γ-γ grain boundaries and cavities are noted to be associated with dislocations in the grain interiors.

The effect of cavity segregation at γ phase grain boundaries, Figure 2, is expected to be a significant finding as prior analyses of boundary character have revealed a substantial increase in the amount of γ-γ boundaries in the hot-rolled versus the unrolled specimens [6]. Ductile phase grain boundaries are notably rare in the unrolled material, which possesses extremely coarse grains of the γ phase, and therefore γ-γ boundaries constitute only about 2% of the total grain boundary area in the unrolled alloy. On the other hand, the ductile phase grain boundaries in the hot-rolled alloy constitute approximately 19% of the total grain boundary area [6]. This is in addition to prior research on the behavior of interphase (W-γ) boundaries under irradiation, revealing a predominance of cavity-type defects lying along interphase boundaries in both the unrolled and hot-rolled specimens. Boundary character analyses have revealed that the total density of boundaries appears to double with hot-rolling [6], providing a higher density of trapping sites for defects, and therefore a lower density of these defects per boundary in the hot-rolled material. As the hot-rolled material does not suffer a substantial reduction in ductility as compared to its unrolled counterpart prior to irradiation [7], this could be a net-positive result for the application of hot-rolled WHA materials for fusion applications. This suggests the hot-rolled material may perform better in the retention of its ductility over prolonged irradiation exposure due to a lessened net accumulation of defects per boundary, lessening the effects of selective embrittlement through grain/phase boundary embrittlement.

Rigorous mechanical testing and quantitative defect characterization are clearly required to substantiate this hypothesis as the nature of the irradiation is complex. Further complicating this issue are the inherent drawbacks to the simulation of the fusion reactor environment: the inability of ion irradiation to provide a sufficient volume of irradiated material for bulk scale mechanical testing, although this issue is currently under investigation via micro- and meso-scale mechanical testing of these irradiated materials in collaboration with Oregon State University [8]. While a perfect analogue for the fusion environment does not yet exist, high magnification investigation of the characteristic damage in a heavy ion irradiated tungsten heavy alloy nonetheless allows us to tease out the phenomena which will be responsible for the degradation of these materials and ultimately informs and guides the selection process for the furtherance of fusion material implementation.

References

[1.] C. H. Henager, Jr., R. J. Kurtz, T. J. Roosendaal, B. A. Borlaug, E. A. Nyberg, C. A. Lavender, G. R. Odette, K. H. Cunningham, and F. W. Zok, “RECENT PROGRESS IN THE DEVELOPMENT OF DUCTILE-PHASE TOUGHENED TUNGSTEN FOR PLASMA-FACING MATERIALS: W-Ni-Fe COMPOSITES”, DOE0313/57, pp. 93-96.

[2.] W. Jiang, D. Zhang, D. Li, J. Heo, Z. Wang, L. Zhang, N. Overman, T. Varga, W. Setyawan, Z. Hu, X. Wang, L. Shao, “BEHAVIOR OF HELIUM CAVITIES IN ION-IRRADIATED W-Ni-Fe DUCTILEPHASE TOUGHENED TUNGSTEN” DOE0313/72, pp. 64-65.

[3.] W. Jiang et al., “Behavior of helium cavities in ion-irradiated W-Ni-Fe ductile-phase toughened tungsten,” Journal of Nuclear Materials 561 (2022) 153565.

[4.] C.H. Henager, W. Setyawan, N.R. Overman, B.A. Borlaug, E.L. Stevens, K.B. Wagner, R.J. Kurtz, G.R. Odette, N. Nguyen, K.H. Cunningham, “Ductile-phase toughened tungsten for plasma-facing materials in fusion reactors,” Int. J. Powder Metall. 53 (2017) 18.

[5.] J. V. Haag, D. J. Edwards, C. H. Henager, W. Setyawan, J. Wang, and M. Murayama, “Characterization of ductile phase toughening mechanisms in a hot-rolled tungsten heavy alloy,” Acta Materialia 204 (2021) 116523.

[6.] J. V. Haag, J. Wang, D. J. Edwards, W. Setyawan, and M. Murayama, “A boundary-based approach to the multiscale microstructural characterization of a W-Ni-Fe tungsten heavy alloy,” Scripta Materialia 213 (2022) 114587.

[7.] M. E. Alam and G. R. Odette, “On the remarkable fracture toughness of 90 to 97W-NiFe alloys revealing powerful new ductile phase toughening mechanisms,” Acta Materialia 186 (2020) 324.

[8.] A.V. Garcia Caraveo, T. Chen, W. Setyawan, “IN-SITU MICROMECHANICAL TESTING ON W/NiFe DUCTILE-PHASE TOUGHENED TUNGSTEN,” DOE0313/74, pp. 72-83.

4.4 DOSE RATE EFFECTS ON HELIUM CAVITIES IN DUCTILE-PHASE-TOUGHENED TUNGSTEN

—W. Jiang, J. V. Haag IV, W. Setyawan (Pacific Northwest National Laboratory), Z. Hu, L. Shao (Texas A&M University)

OBJECTIVE

The aim of this work is to study the dose-rate effects on the helium cavity size and number density in ion-irradiated ductile-phase-toughened tungsten alloys.

SUMMARY

Compared to pure tungsten (W), ductile-phase-toughened tungsten (DPT W) alloys exhibit significantly higher fracture toughness while retaining the major thermomechanical properties of W. The material in this study is composed of W particles embedded in a ductile-phase NiFeW matrix. Fusion neutron irradiation of DPT W produces defects and gas species from elemental transmutation. Property degradation of the material is expected to occur as dose increases and gas concentration accumulates. We have applied sequential irradiation of Ni^+ and He^+ ions at 700°C to emulate the microstructure in the fusion neutron irradiated DPT W. In addition to irradiation temperature effects, it is also important to study the dose-rate effects on the He cavity behavior in DPT W. In this report, we describe an ion irradiation experiment for DPT W irradiated at two dose rates of 2.17 and 0.217 dpa/h at 700°C. The results will be compared to our previous data for 21.7 dpa/h at 700°C.

PROGRESS AND STATUS

SRIM Simulation

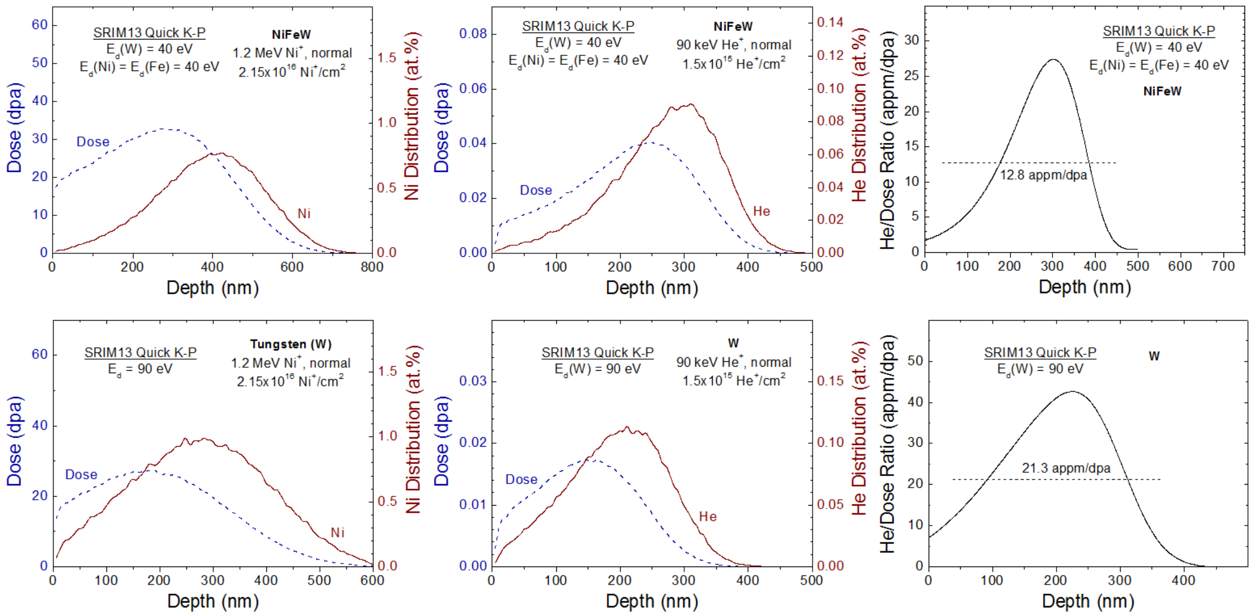

Figure 1. Depth profiles of the dpa dose, He concentration and the ratio of the He concentration to the total dose from Kinchin-Pease SRIM13 simulations of Ni and He ion irradiations in NiFeW and W.

The composition of the DPT W (90W-7Ni-3Fe) alloy used in this study is 88 wt.% W and 12 wt.% NiFeW that consist of 54.68 wt.% Ni, 22.57 wt.% Fe and 22.75 wt.% W, corresponding to 63.83 at.% Ni, 27.69 at.% Fe and 8.48 at.% W [1]. El-Guebaly *et al.* [2] calculated the dpa dose and gas concentration in DPT

W alloys in the front of the divertor in a conceptual ARIES-ACT2 fusion reactor. The total dose after 10 years of operation (8.65 full power years) was reported to be 91.7 dpa in NiFeW of WHA-2 (94.1 wt.% W, 4.1 wt.% Ni and 1.8 wt.% Fe) with the DP composition of 62 at.% Ni, 26 at.% Fe and 12 at.% W. For the same exposure, the He concentration in the DP was calculated to be 1,174 appm based on the reported data of 1620 appm He from Ni, 645 appm He from Fe and 16.2 appm He from W [2]. Therefore, the ratio of the He concentration to the dose is 12.8 appm/dpa in the ductile phase of NiFeW. Although this ratio is obtained from the total dose and accumulated gas concentration over 10 years of operation, it also provides a good estimate at any point of time during operation as the ratio is expected to remain largely unchanged over time.

Table 1. SRIM13 simulation results for Ni and He ion irradiations in NiFeW and W

Ion	Material	Damage Peak Depth (nm)	Peak Dose (dpa)	Ni or He Peak Depth (nm)	Ni or He Peak Concentration (at.%)	Ave. He to Dose Ratio (appm/dpa)
1.2 MeV Ni^+ **2.15×10^{16} Ni^+/cm^2**	W	168	27.05	294	0.98	---
90 keV He^+ **1.5×10^{15} He^+/cm^2**	W	160	0.017	215	0.11	21.3
1.2 MeV Ni^+ **2.15×10^{16} Ni^+/cm^2**	NiFeW	296	32.6	416	0.76	---
90 keV He^+ **1.5×10^{15} He^+/cm^2**	NiFeW	250	0.04	295	0.09	12.8

In order to estimate the displacement dose and He atomic distributions in the body-centered cubic W and face-centered cubic NiFeW phases, quick Kinchin-Pease (K-P) SRIM13 (Stopping and Range of Ions in Matter, version 2013 [3]) simulations were carried out for 1.2 MeV Ni^+ and 90 keV He^+ ions in NiFeW and W, where the threshold displacement energies of $E_d(W)=90$ eV in W and $E_d(Ni)=E_d(Fe)=40$ eV in NiFeW were adopted [4]. As W served as a minor element in NiFeW, its threshold displacement energy was chosen to be the same as that for Ni or Fe, i.e., $E_d(W)=40$ eV in NiFeW. In each case, the lattice binding energy was set to 0 eV [5]. The theoretical densities of 19.25 g/cm^3 (or 6.3×10^{22} $at./cm^3$) and 9.50 g/cm^3 (or 8.3×10^{22} $at./cm^3$) were adopted for W and NiFeW, respectively. The self-ion (Ni) irradiation was used to emulate high-energy neutron irradiation without introducing impurities. The results based on the vacancy.txt file are shown in Figure 1 and summarized in Table 1. It should be noted that SRIM simulations do not involve any thermal diffusion of point defects and implanted species. For 1.2 MeV Ni^+ ion irradiation at normal incidence to 2.15×10^{16} Ni/cm^2 in W, the peak dose is 27 dpa at 168 nm; for the same ion fluence, the peak dose in NiFeW is 32.6 dpa at 296 nm. For 90 keV He^+ ion irradiation at normal incidence to 1.5×10^{15} He/cm^2 in NiFeW, the maximum He concentration is 0.09 at.% at 295 nm. The He concentration peak is spatially overlapped with the Ni ion damage peak, as intended. The ratio of the He concentration to the dpa dose is plotted as a function of depth, as shown in Figure 1. The average ratio is 12.8 appm/dpa in NiFeW, corresponding to 10-year neutron irradiation of the front divertor in a conceptual ARIES-ACT2 fusion reactor [2]. It should be noted that the average ratio in W is 21.3 appm/dap under the ion irradiation conditions, which is much higher than that (0.62 appm/dpa based on the reported data [2]) in the neutron irradiated W phase. While irradiation effects in pure W have been extensively investigated, this study focuses on the emulation of neutron irradiation effects in the NiFeW ductile phase. Note that SRIM simulations are performed at the temperature of 0 K. The actual He depth profiles are expected to be broader in W and NiFeW due to diffusion during He^+ ion irradiation at an elevated temperature. In addition to the interaction of He atoms and vacancies to form He cavities, a fraction of the implanted He atoms is expected to diffuse to the surface and escape from the sample.

Ion Irradiation

Similar to what has been described in [1], sequential irradiation with Ni^+ and He^+ ions was performed in different areas of two DPT W alloy samples with different dose rates at 700°C, as shown in Figure 2. The DPT W samples in this study have a dimension of 12 mm long × 5 mm wide × 2 mm thick. An area of 6 mm × 5 mm on Sample 1 was irradiated uniformly with 1.2 MeV Ni^+ ions to an ion fluence of 2.15×10^{16} Ni^+/cm^2. Subsequently, an area of 6 mm × 5 mm shifted downward by 3 mm was irradiated with 90 keV He^+ ions to an ion fluence of 1.5×10^{15} He^+/cm^2, as given in Table 2. There is an overlapping area of 4 mm × 3 mm between the Ni^{2+} and He^+ ion irradiations, as illustrated in Figure 2, thus creating three 6 mm × 5 mm irradiation regions of Ni^+ ions only, Ni^+ and He^+ ions, and He^+ ions only, in addition to an unirradiated area of 3 mm × 5 mm. For Sample 2, The irradiations were performed with a defocused 1.2 MeV Ni^+ beam and a rastered 90 keV He^+ beam to achieve uniform irradiation over the intended area of 6 mm × 5 mm. The average ion flux was 4.0×10^{11} $(Ni^+/cm^2)/s$ and 1.8×10^{12} $(He^+/cm^2)/s$, corresponding to dose rates of 2.17 and 0.17 dpa/h. The total irradiation duration was 15 h for the Ni^+ ion irradiation and 13m 53s for the He^+ ion irradiation. These values are given in Table 2. For Sample 2, the dose rate reduces an order of magnitude, and the corresponding irradiation conditions are also listed in the table.

Table 2. 1.2 MeV Ni^+ and 90 keV He^+ ion irradiations in NiFeW within 0R DPT W at 700°C

ID	Flux (ions/cm²/s)	Fluence (ions/cm²)	Dose Rate (dpa/h)	Dose (dpa)	Time
Sample 1	4.00E11 (Ni^+)	2.15E16	2.17	32.6	15 h
Sample 1	1.80E12 (He^+)	1.5E15	0.17	0.040	13m 53s
Sample 2	4.00E10 (Ni^+)	2.15E15	0.217	3.26	15 h
Sample 2	1.80E11 (He^+)	1.5E14	0.017	0.004	13m 53s

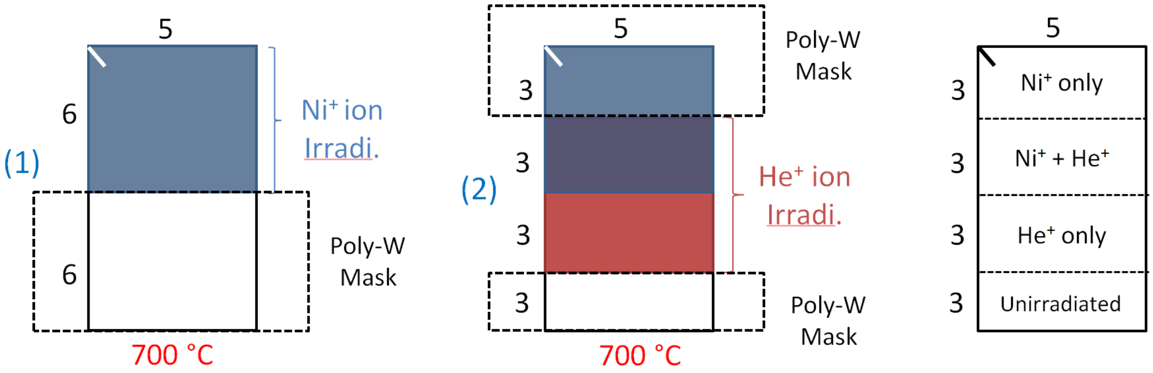

Figure 2. An illustration of two DPT W samples sequentially irradiated with Ni^+ and He^+ ions at different dose rates to produce three different irradiation regions with an additional unirradiated area. (1) 1.2 MeV Ni^+, normal, 2.15E16 Ni^+/cm^2, 700°C (Sample 1), 1.2 MeV Ni^+, normal, 2.15E15 Ni^+/cm^2, 700°C (Sample 2), and (2) 90 keV He^+, normal, 1.5E15 He^+/cm^2, 700°C (Sample 1), 90 keV He^+, normal, 1.5E14 He^+/cm^2, 700°C (Sample 2).

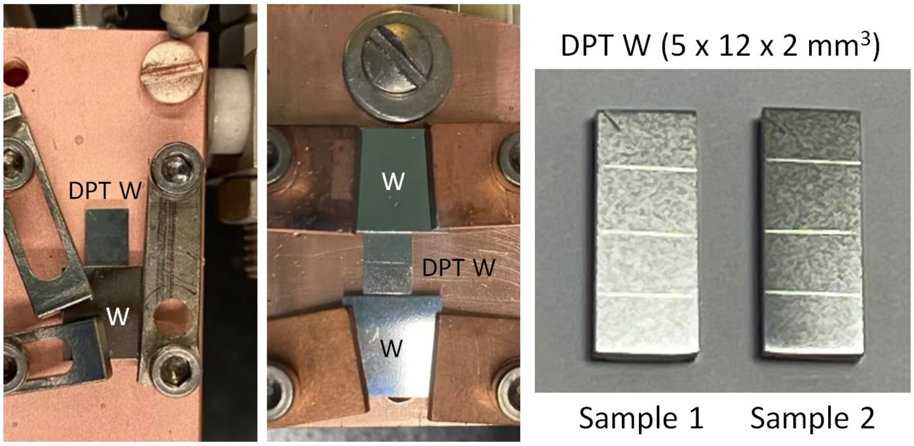

Ni^+ irradiation He^+ irradiation

Figure 3. Experimental setup for sequential Ni^+ and He^+ ion irradiations of a DPT W sample at 700°C. A picture of the two samples irradiated at different dose rates is also shown.

Figure 3 shows how the DPT W sample was mounted in the ion irradiation experiments. Polycrystalline W plates were used as masks that were clamped to hold the sample on a copper backing. A resistance heater was located behind the backing. The sample temperature of 700°C was monitored using a thermocouple on the copper backing to an accuracy of ±5°C or better. Figure 3 also shows the two actual samples after irradiation with engraved line markers to identify the four different regions. There is no visible coloring in the irradiated areas.

Results

The three irradiated regions and the unirradiated area on each of the DPT W samples will be used for microstructural examination to isolate different types of defects to study individual and combined irradiation effects, including (1) formation of dislocation loops from Ni^+ ion irradiation, (2) He cavity size and number density distributions in the absence of the pre-existing defects, and (3) those in the presence of defects. The microstructure in the damage band will be examined by TEM in NiFeW and along the NiFeW/W interphase boundaries. Depth profiles of the He cavities in NiFeW will be determined. The behavior of the He cavities along the interphase boundary will also be investigated. High-resolution TEM/STEM will be performed to image ion irradiation induced dislocation loops in NiFeW. To avoid focused ion beam (FIB) damage, TEM specimens will be prepared using dimple thinning and low-energy plasma polishing. The results from the two samples at dose rates of 2.17 and 0.217 dpa/h, along with our previous data at 21.7 dpa/h, will be compared and evaluated. Possible mechanisms of dose-rate effects on the loop characteristics and He behavior in NiFeW will be discussed.

Acknowledgements

This research was supported by the Office of Fusion Energy Sciences, U.S. Department of Energy and performed at Pacific Northwest National Laboratory under Contract DE-AC05-76RL01830. Ion irradiation experiments were performed at Texas A&M University.

References

[1] W. Jiang, D. Zhang , D. Li, J. Heo, Z. Wang, L.M. Zhang, N. Overman, T. Varga, Z. Hu, X. Wang, L. Shao, W. Setyawan, J. Nucl. Mater. 561 (2022) 153565.

[2] L.A. El-Guebaly, W. Setyawan, C.H. Henager Jr., R.J. Kurtz, G.R. Odette, Nucl. Mater. Energy 29 (2021) 101092.
[3] J.F. Ziegler, J.P. Biearsack, U. Littmark, *The stopping and Range of Ions in Solids* (Pergamon Press, New York, 1985); available at: http://www.SRIM.org/.
[4] ASTM, ASTM Standard E521-96 (2009), *Standard Practice for Neutron Radiation Damage Simulation by Charged-Particle Irradiation,* ASTM International, West Conshohocken, PA (2009).
[5] R.E. Stoller, M.B. Toloczko, G.S. Was, A.G. Certain, S. Dwaraknath, F.A. Garner, Nucl. Inst. Meth. Phys. Res. B. 310 (2013) 75.

4.5 TEMPERATURE EFFECTS ON HELIUM CAVITIES IN DUCTILE-PHASE-TOUGHENED TUNGSTEN

—W. Jiang, J. V. Haag IV, B. E. Matthews, W. Setyawan (Pacific Northwest National Laboratory), D. Chen (University of Houston)

OBJECTIVE

The aim of this work is to study the effects of irradiation temperature on the helium cavity size and number density in ductile-phase-toughened tungsten alloys.

SUMMARY

Ductile-phase-toughened tungsten (DPT W) alloys exhibit significantly higher fracture toughness as compared to pure tungsten (W). They have been investigated as candidate materials for application in the plasma-facing components (PFCs) of fusion reactors. The 87R DPT W in this study consists of W particles embedded in a ductile-phase NiFeW matrix. Our previous report described an ion irradiation experiment and presented some preliminary results for 87R DPT W irradiated at room temperature (RT) and 1000°C. As a continuation, we prepared new focused ion beam (FIB) samples. The TEM and EDS on the new samples have been examined. This report presents some of the new data for the He cavities and Ni-rich precipitates in 87R DPT W irradiated at RT and 1000°C.

PROGRESS AND STATUS

Introduction

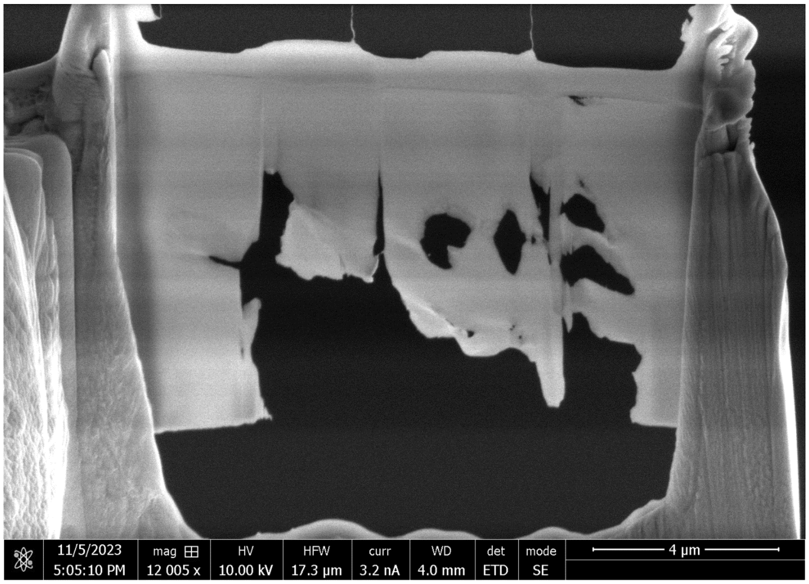

Figure 1. The FIB samples for 87R DPT W irradiated sequentially with Ni^{+} and He^{+} ions at 1000°C.

Sequential ion irradiation of 87R DPT W was performed at RT and 1000°C using 3.3 MeV Ni^{2+} at normal incidence to 3.0×10^{16} Ni^{2+}/cm^{2} and 750 keV He^{+} at 45° off the surface normal to 1.3×10^{16} He^{+}/cm^{2} [1]. The irradiation parameters were determined based on SRIM simulations. Large He cavities with a low number density was observed on the interphase boundary between W and NiFeW in the DPT W sample irradiated at 1000°C, but cavities in NiFeW phase did not appear [1]. The He cavities were also not visible in the W phase irradiated at 1000°C likely due to large foil thickness and FIB damage. For this reason, we prepared a new cross-sectional scanning transmission electron microscopy (STEM) specimen, as shown in Figure 1. The region of interest was capped in a Thermofisher G4 Hydra PFIB (plasma focused ion beam) dual-beam microscope with ~500 nm of e-beam W and 3 μm of W with a Xe ion beam. A lamella was then extracted and attached to a Cu grid using a standard lift-out procedure. Because Ga-FIBs have a more precise beam, lamella thinning was performed using a FEI Helios 600 Nanolab dual-beam FIB microscope. The lamella was thinned starting at a low tilt (±1.5° from 52°) with the Ga^+ ion beam at 30 kV. When the sample was roughly 200 nm thick, the sample was tilted to 54-55° (±2-3° from 52°), and the beam energy reduced to 5 kV for final thinning. At this step, W portions were targeted with a double pattern during milling to attempt to evenly thin because the sputtering rate of W is significantly smaller than that of NiFeW. When the lamella was electron transparent at an electron energy of 5 keV (lamella thickness<100 nm), the sample was tilted to 57° (±5° from 52°) and polished at 2kV. Fresnel defocusing technique was employed to observe cavities in the irradiated samples using a JEOL JEM-ARM 200CF aberration-corrected STEM operating at 200 kV.

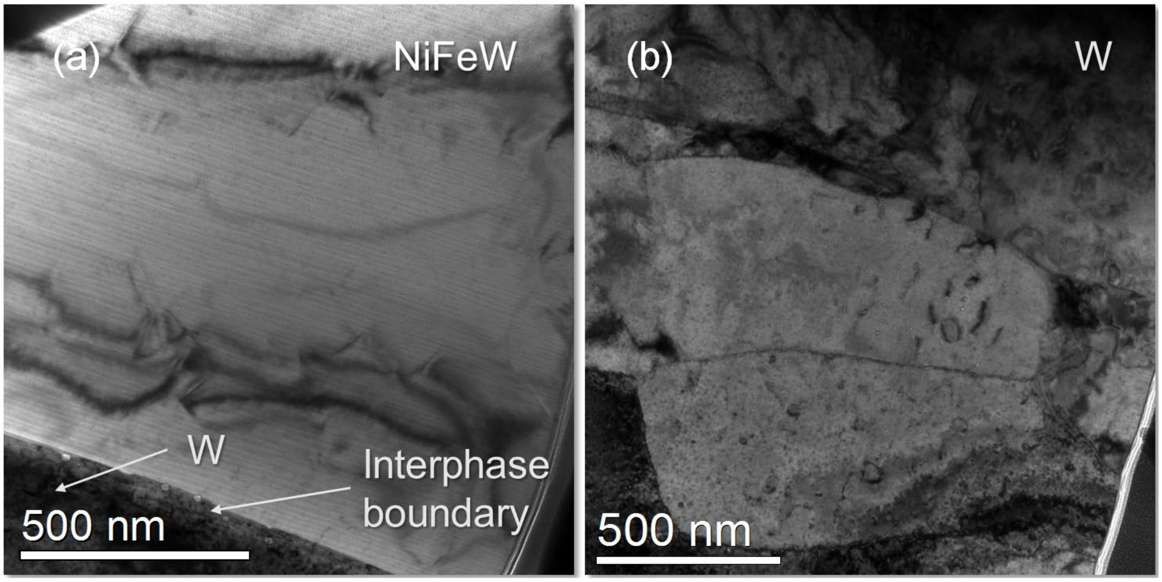

Figure 2. Under focused bright field TEM micrograph of 1000°C irradiated 87R DPT W in (a) NiFeW phase with an interphase boundary and (b) W phase.

Consistent with our previous observation [1], large cavities are observed at the interphase boundary, as shown in Figure 2(a). However, the NiFeW phase region presents no obvious cavities, which confirms our previous observation [1]. The result is in contrast to the data from 87R DPT W irradiated at 700°C (homologous temperature T_H = 0.56), where large cavities appeared in the NiFeW phase [2,3]. Vacancies and He atoms are expected to have a higher mobility at a higher temperature. It is possible that most vacancies produced during ion irradiation at 1000°C (T_H = 0.74) were annihilated with interstitials or diffused to the surface and disappeared. A large fraction of the implanted He atoms is also expected to be released during ion implantation at 1000°C. In contrast, although extremely small He cavities are observed in W phase region in the grain bulk under the same irradiation and implantation conditions, as shown in Figure 2(b). This behavior is similar to what has been observed in 700°C irradiated 87R DPT W [2,3].

It is also interesting to note precipitate formation within the bulk W, as shown in Figure 3(a). This precipitation occurs preferentially along dislocation lines. The EDS mapping indicates that these precipitates are Ni rich, with a length on the order of 10 nm. The precipitates are W depleted. The overall Fe counts are small and it is likely that the precipitates contain very little Fe, if any. The imaging area is around the peak maximum of the implanted Ni concentration at ~920 nm from the surface. Precipitation of the Ni-rich precipitates is likely a result of nucleation and growth processes, including Ni migration and trapping at the dislocation in W, followed by Ostwald ripening. Similar Ni-rich precipitates are also observed in a precipitated η-carbide phase [4] formed at the interphase boundary near the surface during ion irradiation at 1000°C, as shown in Figure 3(b). These Ni-rich precipitates are also W depleted, but could contain a small fraction of Fe, as the Fe map in Figure 3(b) suggests. The precipitates are randomly distributed, and no dislocation lines appear in the imaging area of the η-carbide precipitate phase.

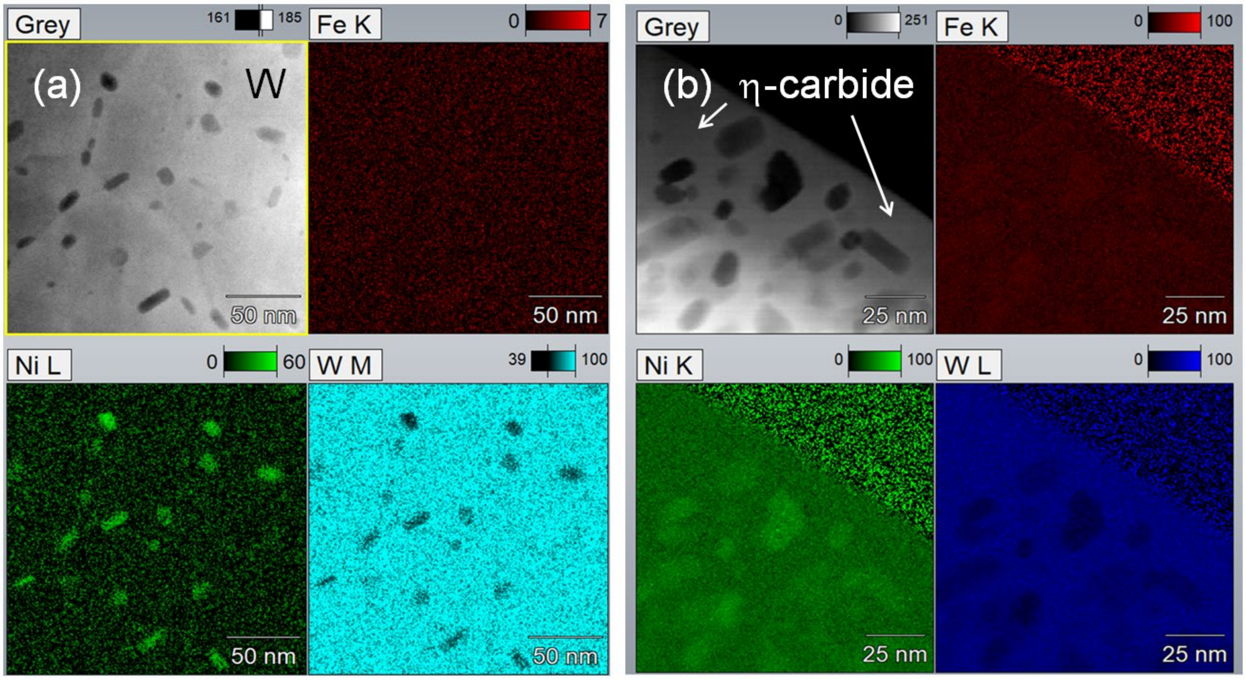

Figure 3. High magnification EDS mapping of Ni-rich precipitates in (a) the W phase and (b) precipitated η-carbide phase in 1000°C irradiated 87R DPT W.

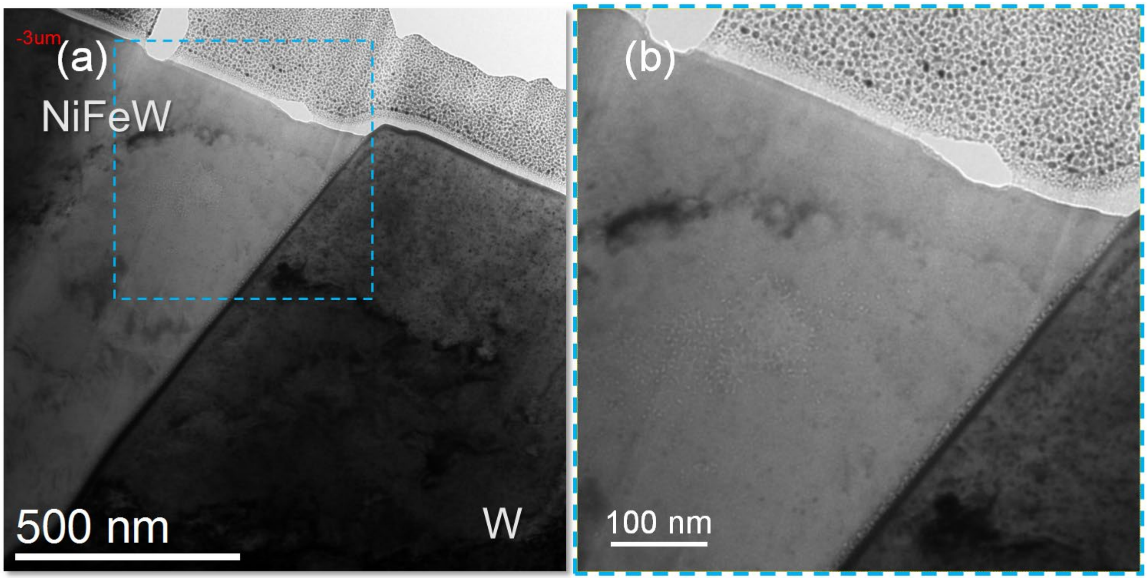

Figure 4. Under focused bright field TEM micrographs of RT irradiated with Ni$^+$ and He$^+$ ions 87R DPT W: (a) general view and (b) zoomed-in view.

It should be noted that in our previous report [1], we did not observe any cavities in RT irradiated 87R DPT W. One of the possible reasons was the large thickness of the TEM foil specimen. An additional specimen was prepared during this reporting period and TEM was repeated. The new data is shown in Figure 4. From the zoomed-in view of the surface area shown in Figure 4(b), the NiFeW phase region clearly exhibits small cavities in the grain bulk under the under-focus condition, but the W phase presents no discernable cavities. The interphase region presents a feature that appears to suggest there is an aggregation of He cavities along the boundary, but further examination at a high resolution is needed to confirm the feature. Vacancies are not expected to be mobile in either W or NiFeW at RT. Formation of small He cavities in NiFeW might be associated with beam heating during ion irradiation or FIB at nominally RT. Obviously, the small increase in the temperature is sufficient to activate or expedite He or possibly mono-vacancy migration in NiFeW during ion irradiation or FIB process, followed by nucleation and growth of He cavities. However, the same process does not occur in W. A higher temperature may be needed for the formation of He cavities in W.

Results

Data acquisition is nearly completed for 87R DPT W irradiated with Ni^{2+} and He^{+} ions at RT and 1000°C. In order of quantify the number density of the cavities, STEM-EELS will be applied to measure the local thickness of the TEM specimens where the cavities are distributed, followed by data analysis. Data comparison will be made at different irradiation temperatures, including those from 700°C irradiated 87R DPT W [2,3]. The temperature effects on the He cavity size and number density distributions will be assessed and possible mechanisms will be explored. Thermal annealing of the RT irradiated sample at 1000°C may be performed to study possible thermal precipitation of He cavities with the data to be compared to the those from 1000°C irradiated 87R DPT W. A manuscript will be prepared for publication of the complete results.

Acknowledgements

This research was supported by the Office of Fusion Energy Sciences, U.S. Department of Energy and performed at Pacific Northwest National Laboratory under Contract DE-AC05-76RL01830. An ion irradiation experiment was performed at the University of Houston.

References

[1] W. Jiang, J.V. Haag IV, W. Setyawan, D. Chen, Fusion Materials Semiannual Progress Report for Period Ending June 30, 2023, DOE/ER-0313/74, U.S. Department of Energy.
[2] W. Jiang, D. Zhang , D. Li, J. Heo, Z. Wang, L.M. Zhang, N. Overman, T. Varga, Z. Hu, X. Wang, L. Shao, W. Setyawan, J. Nucl. Mater. 561 (2022) 153565.
[3] W. Jiang, L. Kovarik, K. Kruska, Y. Fu, Z. Hu, L. Shao, W. Setyawan, Materialia 29 (2023) 101789.
[4] J.V. Haag IV, M.J. Olszta, D.J. Edwards, W. Jiang, W. Setyawan, “Characterization of boundary precipitation in a heavy ion irradiated tungsten heavy alloy under the simulated fusion environment”, Acta Materialia, 2024, in press; https://doi.org/10.1016/j.actamat.2023.119059.

4.6 HIGH-TEMPERATURE MECHANICAL TESTING OF W/NiFe DUCTILE-PHASE TOUGHENED W COMPOSITES

R. Prabhakaran, W. Setyawan (Pacific Northwest National Laboratory)

OBJECTIVE

The objective of this task is to investigate the high-temperature operating limit of W/NiFe ductile-phase (DPT) toughened W composites and to explore how hot-rolling may improve the high-temperature tensile and fracture toughness.

SUMMARY

This report summarizes the status of the elevated temperature mechanical test facility setup, annealing studies, and hot rolling operations to fabricate a new batch of DPT W-NiFe mechanical test specimens for obtaining room and elevated temperature mechanical properties.

PROGRESS AND STATUS

Introduction

Tungsten (W) is a promising candidate material for plasma-facing components (PFCs) due to its excellent high-temperature strength, low sputtering rate, good thermal conductivity, and high melting temperature. [1-2] However, the potential application of tungsten as a structural material in PFCs is limited due to its low ductility which will further degrade after irradiation. [3] Therefore, introducing a ductile phase (DP) to develop a tungsten composite could serve as an alternative route to overcome its limitations. The DPT process is a fracture toughness improvement concept that is being utilized to develop tungsten-based composites for fusion reactor divertor and plasma-facing materials. Liquid-phase sintered tungsten heavy metal alloys (WHAs), due to their balance of strength, ductility and toughness, are being considered to be a suitable alternative to monolithic polycrystalline W for fusion applications.

The low melting point of the alloying elements Fe and Ni being 1538°C and 1455°C, respectively, could restrict the operational space. However, to avoid recrystallisation of W and to preserve its original mechanical properties, the temperature should be kept anyway below 1300°C, which means that the improvement in ductility and toughness by using Fe and Ni remains expected, though to a lesser extent compared to room-temperature mechanical property improvement. [4] Determining the mechanical properties of DPT-W at elevated temperatures is indeed an important aim of this research.

As per the literature, the maximum service temperature for divertors is likely 1200-1300°C [4-6], and hence it is critical to obtain the elevated temperature mechanical properties of WHA. The issue of W fuzz has not been fully resolved and, if significant, it might lower the maximum temperature to about 700°C. [7-9] The melting temperature of the DP phase (near Ni:Fe weight ratio of 7:3) is ~1440°C.

Different thermomechanical plastic deformation processing routes, such as hot-rolling (HR), extrusion and swaging, can increase the strength of WHAs. [10-16] Researchers at Pacific Northwest National Laboratory (PNNL) have characterized the effects of the composite architecture on deep notch bend bar toughness for a 90 wt.% W–Fe–Ni WHA, hot rolled to different thickness reductions of 62, 74 and 87%. [17] As per our previous study, the deformed W and DP phases that form a ‘brick-and-mortar (BAM)’ like microstructure could improve strength by hot working, while enhancing the ductility and toughness, by creating a more distributed damage zone under deep notch bar loading. [17,18]

Researchers at PNNL have previously conducted tensile tests on as sintered 90W (purchased powders from MiTech; sintered at PNNL), 95W (two batches: MiTech and Plansee), 97W (two batches: MiTech and Plansee), and 90W-87R rolled materials (sintered at PNNL) using an Instron 5582 servo-mechanical test frame equipped with Epsilon ONE optical extensometer. [19,20] Recently, room temperature tensile testing was conducted using an Instron 8801 servo hydraulic test frame on as sintered 90W, 95W and 97W samples (MiTech), along with hot rolled 90W samples with various rolling reductions (57R, 78R and 86R), and the results can be found in our previous report. [21]

In the past, researchers have performed heat treatment on WHA to improve the mechanical properties, especially the ductility and fracture toughness. [22-24] Researchers at PNNL recently performed annealing studies on 90W-0R (MiTech) and 90W-86R (rolling performed at PNNL) at 1300°C for three different time periods (6, 12 and 24 hours) to evaluate its effect on the mechanical properties and microstructure, and the results could be found in our previous report. [25]

Currently, efforts are ongoing to understand the mechanical behavior of DPT W-NiFe alloys (as sintered and rolled samples) at elevated temperatures: 244°C ($0.3T_m$); 416°C ($0.4T_m$), 590°C ($0.5T_m$), 750°C ($0.6T_m$) and 933°C ($0.7T_m$), where T_m is the melting temperature of nickel (1723K; 1450°C). This report is focused in documenting the status of the elevated temperature mechanical test facility setup, hot rolling operations (90W) to fabricate a new batch of tensile and fracture toughness specimens to obtain elevated temperature mechanical properties, annealing studies (95W and 97W), and tensile testing at PNNL.

Experimental Procedure

Procurement of W–Fe–Ni alloys

Sintered 90, 95 and 97 weight % alloys were procured from MiTech to fabricate mechanical test samples for room and elevated temperature mechanical testing. Table 1 shows the lot information WHA alloys.

Table 1. Sintered W–Fe–Ni alloys procured from MiTech

Material	Vendor	Vendor Code	Lot Number	Lot Chemistry (wt.%)
90W	MiTech	HD 17D	36124	90.37 W; 6.82 Ni and 2.81 Fe
95W	MiTech	HD 18D	36843	95.11 W; 3.45 Ni and 1.44 Fe
97W	MiTech	HD 18.5	36910	97.08 W; 2.05 Ni and 0.87 Fe

Hot Rolling of 90 wt.% W–Fe–Ni WHA

During 2022, hot rolling was performed on the sintered 90 wt.% W–Fe–Ni alloy procured from MiTech (HD 17D; Lot # 36124). To perform hot rolling, the material (approximately 2” thick x 2” wide x 4” long) was sectioned into approximately 1” thick x 1” wide x 2.25” long pieces. The sample was preheated in a Lucifer model 7GT-M48 furnace (see Figure 1) at 1150°C for about 20 minutes. Hot rolling was performed at 1150°C by employing a Waterbury Farrell Two High/Four High 755 Rolling Mill (see Figure 1). Hot rolling was performed (10% reduction per pass; see Table 1) at 1150°C during the first two passes (from about 1.0” to 0.8”) and then it was performed at 900°C (from 0.80” to 0.14”). During the hot rolling process, the rolled material at various stages (interval:11-20R) was annealed at 1200°C for 3 hours with argon and hydrogen purges using a CM model 1516GSH2FL furnace (see Figure 2). All rolled plates were degassed to remove hydrogen using a Thermal Technologies/Brew furnace (model 121224MMS; see Figure 2) at 900°C for 60 minutes. Hot rolled samples with different thickness reductions (57R, 78R and 86R) were successfully fabricated and can be seen in Figure 3. Additional information about 2022 hot rolling operations can be found in the previous report. [21] Tensile test samples were obtained from these hot rolled plates and results can also be found in the previous report. [21]

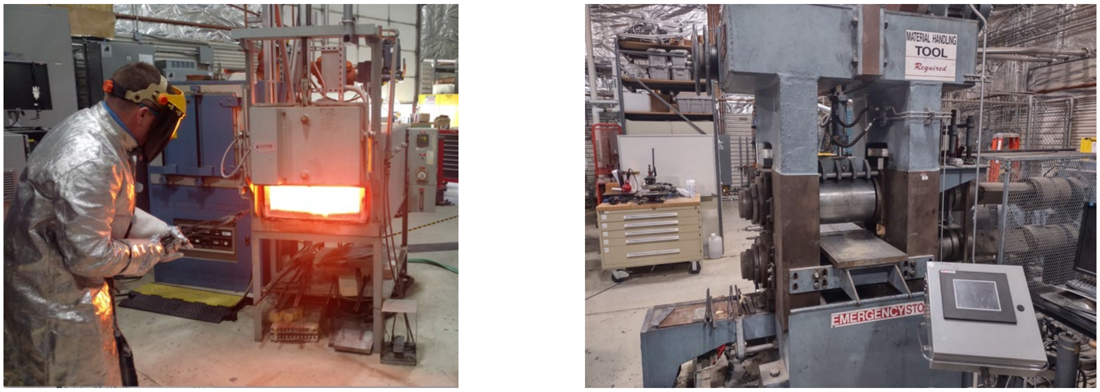

Figure 1. Preheating Lucifer Furnace and Waterbury Farrell Rolling Mill.

Figure 2. Left: CM Furnace utilized for 1200°C annealing during hot rolling process; Right: Thermal Technologies/Brew Furnace for degassing hydrogen.

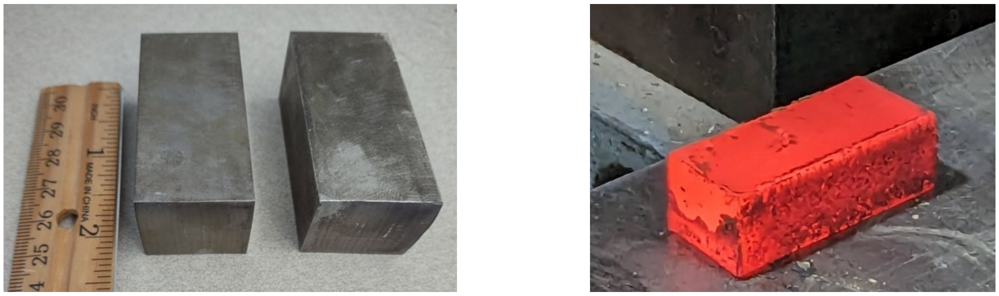

(a) Before hot rolling (1” thick x 1” wide x 2.25” long pieces) and during hot rolling

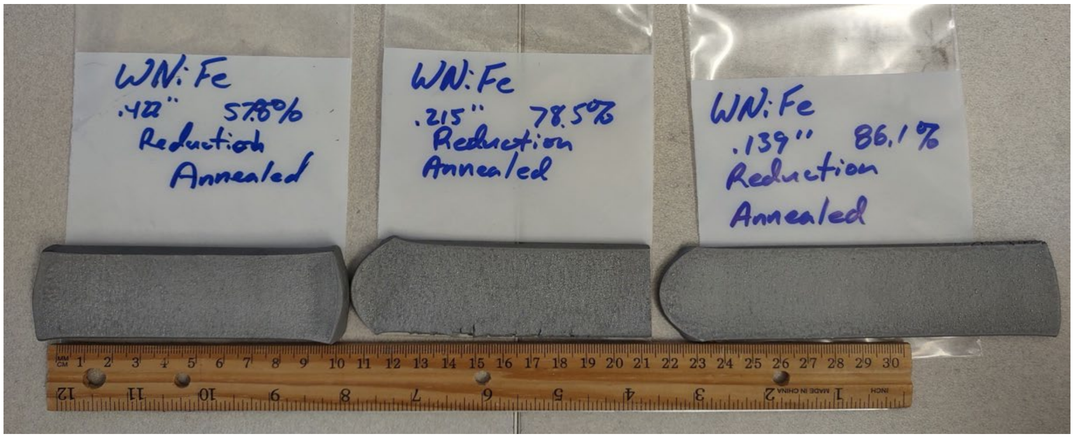

(b) After hot rolling and annealing

Figure 3. Hot rolled (thickness reductions: 57R, 78R and 86R) and annealed 90W–Fe–Ni plates/foils (Plate IDs: 2022/1-in/01A, B and C).

During 2023, hot rolling was performed on the sintered 90 wt.% W–Fe–Ni alloy procured from MiTech (HD 17D; Lot # 36124) to obtain hot rolled plates (see Table 1; 2023/1-in/01, 02 & 03) with two different thickness reductions: 66R (3:1 aspect ratio) and 83R (6:1 aspect ratio). Prior to hot rolling, the material (approximately 2” thick x 2” wide x 4” long) was sectioned into approximately 1” thick x 1” wide x 2” long pieces. Since the 2022 hot rolling study was successful on a one-inch-thick block, [21] similar rolling parameters (such as reduction per pass and rolling temperatures) were utilized (see Table 1) to prepare hot rolled samples (without any cracks) with different thickness reductions (66R and 86R; see Table 2 and 3), as shown in Figure 4. Annealing was performed periodically (interval: 14-23R) during hot rolling.

Table 1. Hot rolled 90W (MiTech Lot 36124) alloys at PNNL

Rolled Plate ID	Thickness Reduction (in)	Total Rolling Reduction (%)	Average Reduction per Pass (%)	Annealing Interval	Hot Rolling Temperatures and Notes
2022/1-in/01A	1.00 - 0.426	57	10	11-20R	1150°C (till 20R); 900°C
2022/1-in/01B	1.00 - 0.222	78	10		1150°C (till 20R); 900°C; noticed some edge cracking during 68R
2022/1-in/01C	1.00 - 0.139	86	10		1150°C (till 19R); 900°C
2023/1-in/01	1.060 - 0.355	66	10	14-23R	1150°C (till 19R); 900°C
2023/1-in/02	1.060 - 0.354	66	10		1150°C (till 19R); 900°C
2023/1-in/03	1.060 - 0.172	83	10		1150°C (till 19R); 900°C
2023/1-in/04	1.106 - 0.375	66	10 (till 17R) 20 (18-66R)	17-31R	1150°C
2023/1-in/05	1.106 - 0.191	83	10 (till 17R) 20 (18-83R)	17-31R	1150°C; leading edge began splitting longitudinally during 73R; trimmed split end off and continued further
2023/1-in/06	1.000 - 0.169	83	10	11-23R	1150°C
2023/1-in/07	1.000 - 0.169	83	10	11-23R	1150°C
2023/2-in/01	2.180 - 1.524	35	5 (till 12R) 10 (13-35R)	28R	1150°C (till 28R); 900°C; Material split horizontally during 6th pass (35R)
2023/2-in/02A	2.190 - 0.710	67	5 (till 60R) 10 (61-67R)	12-18R	1150°C; Noticed some edge cracking ~44R
2023/2-in/02B	2.190 - 0.358	83	5 (till 60R) 10 (61-83R)	12-18R	1150°C; Noticed some edge cracking ~44R
2023/2-in/03	2.160 - 0.361	83	5 (till 18R) 10 (19-33R) 20 (34R-83R)	15-39R	1150°C; Material split horizontally during 6th pass (33R); continued further
2023/2-in/04	2.160 - 0.035	34	5 (till 18R) 10 (19-33R)	18R	1150°C; Material split horizontally during 7th pass (after 33R);
2023/2-in/05	2.206 - 1.418	35	20	35R	1150°C; Material split horizontally on the leading-edge during 2nd pass (35R)
2023/2-in/07	2.170 - 1.397	35	20	15-20R	1150°C; Annealed after every pass; Material split alligator style during 3rd pass (35R)

Figure 4. Hot rolled plates obtained from sintered 90 wt.% W–Fe–Ni alloy (a) 66R thickness reduction (before final annealing): 2023/1-in/01 & 02 (b) 83R thickness reduction (before final annealing) (c) 83R thickness reduction (after final annealing): 2023/1-in/03.

Table 2. Hot rolling schedule of sintered 90 wt.% W–Fe–Ni alloy (2023/1-in/01) to prepare a plate with a 66R thickness reduction

Pass #	Thickness (Inches)		Buck (Inches)		Mill Set	Reduction %		Notes	Annealing interval
	Desired	Actual	Estimate	Actual	(inches)	Pass	Total		% Total Reduction
Start		1.060						1 piece, 1"x1"x 2" 8/15/2023	
1	0.954	0.956	0.020	0.022	0.934	9.81%	9.81%	1150C 20 min preheat	
2	0.859	0.859	0.020	0.020	0.839	10.15%	18.96%	1150C 20 min preheat	18.96%
Annealed 4 hours 1200C, Ar Purge then 100% H2					8/15/2023				
		0.851						Post anneal cold measurement	
3	0.764	0.765	0.020	0.021	0.744	10.11%	27.83%	900C 20 min preheat	
4	0.688	0.691	0.025	0.028	0.663	9.67%	34.81%	900C 12 min preheat	
5	0.621	0.615	0.030	0.024	0.591	11.00%	41.98%	900C 12 min preheat	23.02%
Annealed 4 hours 1200C, Ar Purge then 100% H2					8/22/2023				
		0.611						Post anneal cold measurement	
6	0.549	0.546	0.025	0.022	0.524	10.64%	48.49%	900C 20 min preheat	
7	0.491	0.491	0.025	0.025	0.466	10.07%	53.68%	900C 12 min preheat	
8	0.439	0.438	0.025	0.024	0.414	10.79%	58.68%	900C 12 min preheat	16.70%
Annealed 4 hours 1200C, Ar Purge then 100% H2					9/15/2023				
		0.432						Post anneal cold measurement	
9	0.389	0.383	0.025	0.019	0.364	11.34%	63.87%		
10	0.360	0.360	0.020	0.020	0.340	6.01%	66.04%		7.36%
Annealed 4 hours 1200C, Ar Purge then 100% H2					10/4/2023				
		0.355						Final dimension after annealing	
Average reduction per pass						9.96%	66.51%		

Table 3. Hot rolling schedule of sintered 90 wt.% W–Fe–Ni alloy (2023/1-in/03) to prepare a plate with an 83R thickness reduction

Pass #	Thickness (Inches)		Buck (Inches)		Mill Set	Reduction %		Notes	Annealing interval
	Desired	Actual	Estimate	Actual	(inches)	Pass	Total		% Total Reduction
Start		1.060						1 piece, 1"x1"x 2" 8/15/2023	
1	0.954	0.963	0.020	0.029	0.934	9.15%	9.15%	1150C 20 min preheat	
2	0.859	0.859	0.020	0.020	0.839	10.80%	18.96%	1150C 20 min preheat	18.96%
Annealed 4 hours 1200C, Ar Purge then 100% H2					8/15/2023				
		0.845						Post anneal cold measurement	
3	0.764	0.765	0.020	0.021	0.744	9.47%	27.83%	900C 20 min preheat	
4	0.688	0.691	0.025	0.028	0.663	9.67%	34.81%	900C 12 min preheat	
5	0.621	0.615	0.030	0.024	0.591	11.00%	41.98%	900C 12 min preheat	23.02%
Annealed 4 hours 1200C, Ar Purge then 100% H2					8/22/2023				
		0.611						Post anneal cold measurement	
6	0.549	0.546	0.025	0.022	0.524	10.64%	48.49%	900C 20 min preheat	
7	0.491	0.488	0.025	0.022	0.466	10.62%	53.96%	900C 12 min preheat	
8	0.439	0.437	0.025	0.023	0.414	10.45%	58.77%	900C 12 min preheat	16.79%
Annealed 4 hours 1200C, Ar Purge then 100% H2					9/15/2023				
		0.432						Post anneal cold measurement	
9	0.389	0.382	0.025	0.018	0.364	11.57%	63.96%	900C 15 min preheat	
10	0.344	0.346	0.020	0.022	0.324	9.42%	67.36%	900C 15 min preheat	
11	0.311	0.312	0.025	0.026	0.286	9.83%	70.57%	900C 10 min preheat	
12	0.281	0.280	0.025	0.024	0.256	10.26%	73.58%	900C 10 min preheat	14.81%
Annealed 4 hours 1200C, Ar Purge then 100% H2					10/4/2023				
		0.276						Post anneal cold measurement	
13	0.248	0.244	0.025	0.021	0.223	11.59%	76.98%		
14	0.219	0.212	0.025	0.017	0.195	13.11%	80.00%		
15	0.191	0.203	0.020	0.032	0.171	4.25%	80.85%		
16	0.182	0.175	0.025	0.018	0.157	13.79%	83.49%		9.91%
	.								
Annealed 4 hours 1200C in Ar Purge then 100% H2					10/11/2023				
		0.172							
Average reduction per pass						10.35%	83.77%	Final dimension after annealing	

During 2023, efforts were also made to perform hot rolling on sintered 90 wt.% W–Fe–Ni alloy procured from MiTech (HD 17D; Lot # 36124) with a larger starting thickness, to obtain a much thicker rolled plate (around 0.5 in thick) so that mechanical test samples can also be obtained in the thickness direction. Hence, the initial material (approximately 2” thick x 2” wide x 4” long) was sectioned into approximately two 2” thick x 2” wide x 2” long pieces. Sectioning was performed to obtain a material of a suitable mass that can be handled safely using tongs during hot rolling.

During the 2023 hot rolling study on a 2-inch cube (study 1; #2023/2-in/01), the block sample was preheated in a Lucifer model 7GT-M48 furnace (see Figure 1) at 1150°C for about 20 minutes. Hot rolling was performed at 1150°C employing a Waterbury Farrell Two High/Four High 755 Rolling Mill (see Figure 1) using a 5% reduction for the first three passes (2.18 to 1.90 inch) since the starting thickness was double (2” vs 1”) compared to 2022 rolling studies, and then switched to 10% reduction from the fourth pass (from 1.9 inch to 1.4 inch) as shown in Table 4. During the hot rolling process, the rolled material was annealed (purged with Argon for 70 minutes, followed by hydrogen purge and heating cycle; ramp up @5°C/min; dwell at 1200°C for 3 hours; ramp down via natural cooling @ 3-5°C/min; hydrogen purge continued until the furnace reached under 100°C while cooling down; followed by 70 minutes of Argon purge) using a CM model 1516GSH2FL furnace (see Figure 2) at various stages. During the sixth pass (when thickness was 1.5”), hot rolling was performed at 900°C and a 10% reduction was employed. The material got split horizontally during the sixth pass (35R), as shown in Figure 5. Lower hot rolling temperature (900°C vs. 1150°C), inappropriate reduction/pass and inadequate annealing interval could have played a role and additional rolling studies focused on parameters was required to obtain comprehensive information.

Table 4. Hot rolling schedule of sintered 90 wt.% W–Fe–Ni alloy (#2023/2-in/01); 5% reduction per pass until 12R and then 10% reduction per pass.

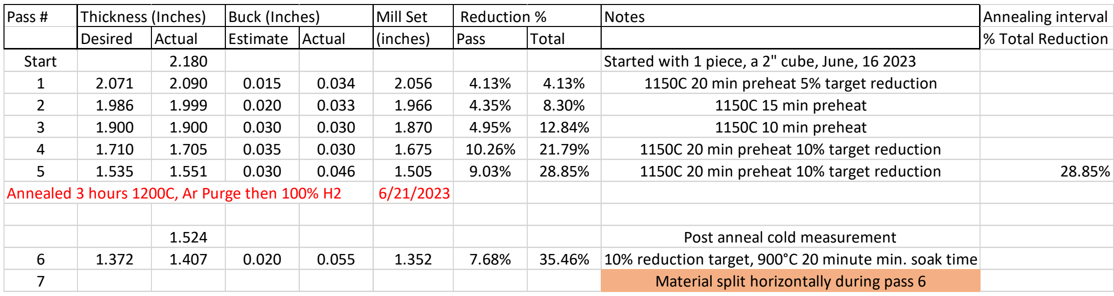

Pass #	Thickness (Inches)		Buck (Inches)		Mill Set	Reduction %		Notes	Annealing interval
	Desired	Actual	Estimate	Actual	(inches)	Pass	Total		% Total Reduction
Start		2.180						Started with 1 piece, a 2" cube, June, 16 2023	
1	2.071	2.090	0.015	0.034	2.056	4.13%	4.13%	1150C 20 min preheat 5% target reduction	
2	1.986	1.999	0.020	0.033	1.966	4.35%	8.30%	1150C 15 min preheat	
3	1.900	1.900	0.030	0.030	1.870	4.95%	12.84%	1150C 10 min preheat	
4	1.710	1.705	0.035	0.030	1.675	10.26%	21.79%	1150C 20 min preheat 10% target reduction	
5	1.535	1.551	0.030	0.046	1.505	9.03%	28.85%	1150C 20 min preheat 10% target reduction	28.85%
Annealed 3 hours 1200C, Ar Purge then 100% H2					6/21/2023				
		1.524						Post anneal cold measurement	
6	1.372	1.407	0.020	0.055	1.352	7.68%	35.46%	10% reduction target, 900°C 20 minute min. soak time	
7								Material split horizontally during pass 6	

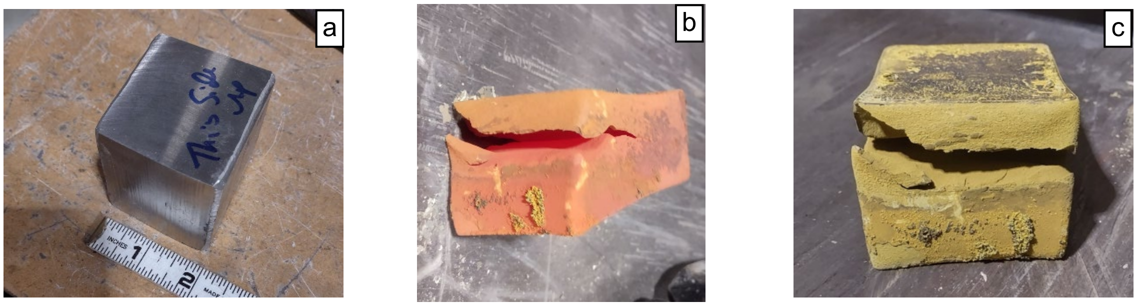

Figure 5. Hot rolled 90W–Fe–Ni (#2023/2-in/01); (a) before hot rolling; (b) sample got split horizontally during the 6th pass - before annealing (c) after annealing.

During Fall 2023, efforts were ongoing to move the rolling mill, furnaces, and other processing equipment to a different larger building and longer downtime (3-6 months) was expected to get these units back in service. Hence, we had a limited time during the second half of last year.

During the 2023 hot rolling study on a 2-inch cube (study 2; #2023/2-in/02), 1150°C was chosen as the hot rolling temperature for all the passes (unlike 2023 study #1). A 5% reduction per pass was not only employed for the initial stages (like study #1) since the starting thickness was larger (~2-inch vs. 1-inch), it was also continued for a much longer time, i.e., utilized for the first eighteen passes (from 2.2 inch to 0.87 inch; 60R; see Table 5) and then it was switched to 10% reduction per pass when there were indications (such as overhang/cracking) that suggested that reduction per pass was not being aggressive enough. The rolled plate showed some edge cracking when the total rolling reduction was ~44R. However, the rolled plate did not show any major cracking. This study showed that during future hot rolling, a 10% reduction per pass or a higher reduction could be employed at a much earlier stage (when the thickness is 1.00-1.50 inch). Figure 6 shows hot rolled and annealed 90W–Fe–Ni plate after 67R thickness reduction. The 67R plate was sectioned into two halves, and one-half was subjected to additional hot rolling (see Table 6) to get an 83R total reduction. Figure 6c shows a cross-sectional view of the rolled plate. Even though the outer surface appears rough and crusty, the bulk of the material inside (interior) looks good, as expected. Figure 7 shows hot rolled and annealed 90W–Fe–Ni plate after 83R thickness reduction.

Table 5. Hot rolling schedule of sintered 90 wt.% W–Fe–Ni alloy (#2023/2-in/02A); 1150°C and 5% reduction per pass until 60R and then 10% reduction) to prepare a plate with a 66R thickness reduction.

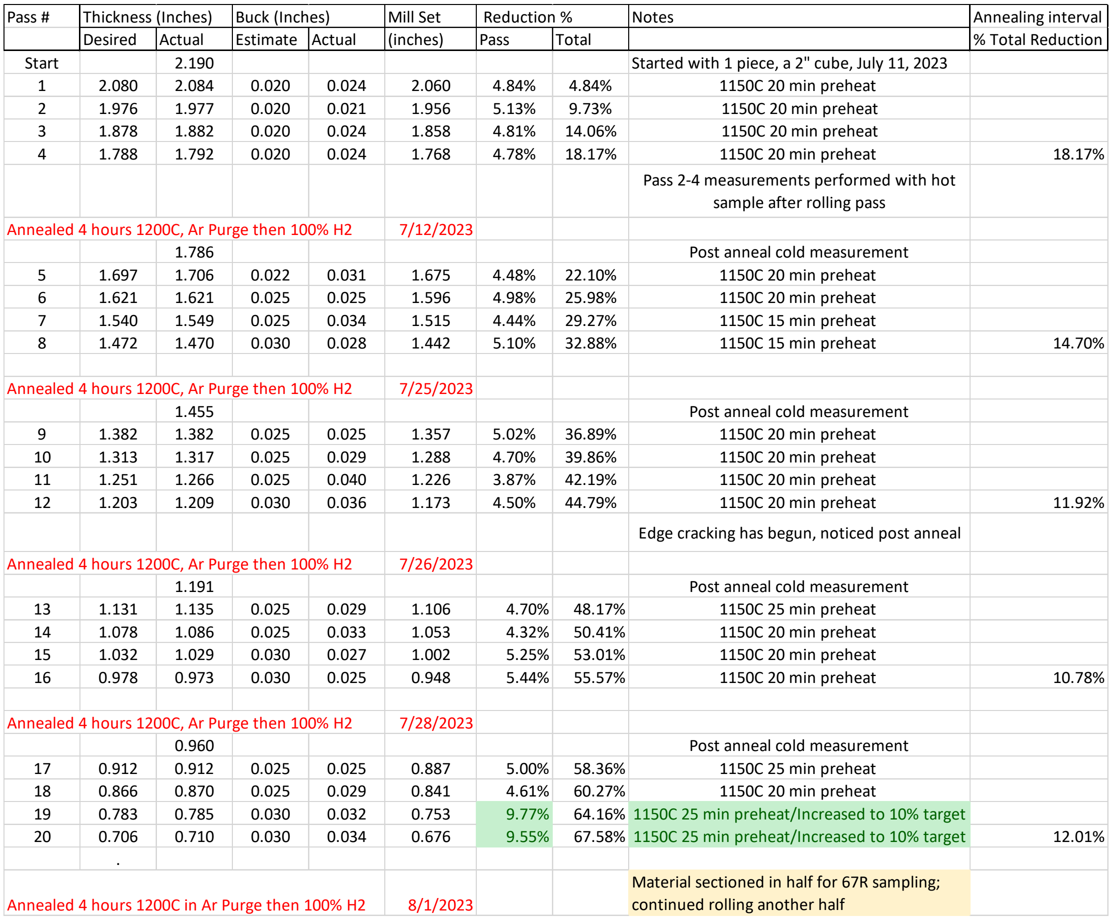

Pass #	Thickness (Inches)		Buck (Inches)		Mill Set	Reduction %		Notes	Annealing interval
	Desired	Actual	Estimate	Actual	(inches)	Pass	Total		% Total Reduction
Start		2.190						Started with 1 piece, a 2" cube, July 11, 2023	
1	2.080	2.084	0.020	0.024	2.060	4.84%	4.84%	1150C 20 min preheat	
2	1.976	1.977	0.020	0.021	1.956	5.13%	9.73%	1150C 20 min preheat	
3	1.878	1.882	0.020	0.024	1.858	4.81%	14.06%	1150C 20 min preheat	
4	1.788	1.792	0.020	0.024	1.768	4.78%	18.17%	1150C 20 min preheat	18.17%
								Pass 2-4 measurements performed with hot sample after rolling pass	
Annealed 4 hours 1200C, Ar Purge then 100% H2					7/12/2023				
		1.786						Post anneal cold measurement	
5	1.697	1.706	0.022	0.031	1.675	4.48%	22.10%	1150C 20 min preheat	
6	1.621	1.621	0.025	0.025	1.596	4.98%	25.98%	1150C 20 min preheat	
7	1.540	1.549	0.025	0.034	1.515	4.44%	29.27%	1150C 15 min preheat	
8	1.472	1.470	0.030	0.028	1.442	5.10%	32.88%	1150C 15 min preheat	14.70%
Annealed 4 hours 1200C, Ar Purge then 100% H2					7/25/2023				
		1.455						Post anneal cold measurement	
9	1.382	1.382	0.025	0.025	1.357	5.02%	36.89%	1150C 20 min preheat	
10	1.313	1.317	0.025	0.029	1.288	4.70%	39.86%	1150C 20 min preheat	
11	1.251	1.266	0.025	0.040	1.226	3.87%	42.19%	1150C 20 min preheat	
12	1.203	1.209	0.030	0.036	1.173	4.50%	44.79%	1150C 20 min preheat	11.92%
								Edge cracking has begun, noticed post anneal	
Annealed 4 hours 1200C, Ar Purge then 100% H2					7/26/2023				
		1.191						Post anneal cold measurement	
13	1.131	1.135	0.025	0.029	1.106	4.70%	48.17%	1150C 25 min preheat	
14	1.078	1.086	0.025	0.033	1.053	4.32%	50.41%	1150C 20 min preheat	
15	1.032	1.029	0.030	0.027	1.002	5.25%	53.01%	1150C 20 min preheat	
16	0.978	0.973	0.030	0.025	0.948	5.44%	55.57%	1150C 20 min preheat	10.78%
Annealed 4 hours 1200C, Ar Purge then 100% H2					7/28/2023				
		0.960						Post anneal cold measurement	
17	0.912	0.912	0.025	0.025	0.887	5.00%	58.36%	1150C 25 min preheat	
18	0.866	0.870	0.025	0.029	0.841	4.61%	60.27%	1150C 20 min preheat	
19	0.783	0.785	0.030	0.032	0.753	9.77%	64.16%	1150C 25 min preheat/Increased to 10% target	
20	0.706	0.710	0.030	0.034	0.676	9.55%	67.58%	1150C 25 min preheat/Increased to 10% target	12.01%
	.								
Annealed 4 hours 1200C in Ar Purge then 100% H2					8/1/2023			Material sectioned in half for 67R sampling; continued rolling another half	

a

b

c

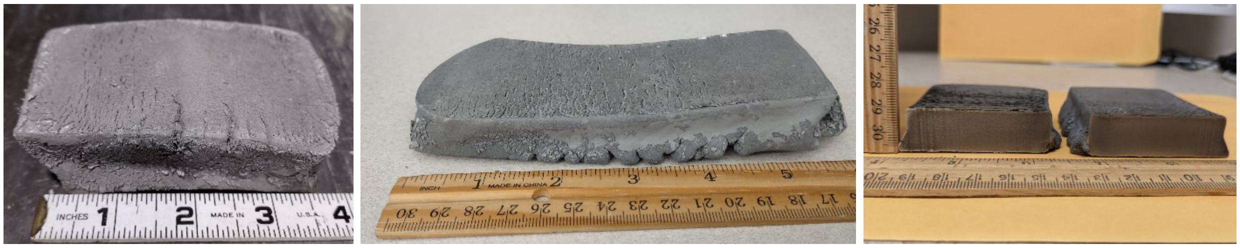

Figure 6. Hot rolled and annealed 90W–Fe–Ni plate (#2023/2-in/02A); (a) after 12th pass (44R); (b) after 20th pass (67R); (c) plate (67R) was sectioned in two pieces, one piece was rolled further, see Figure 7.

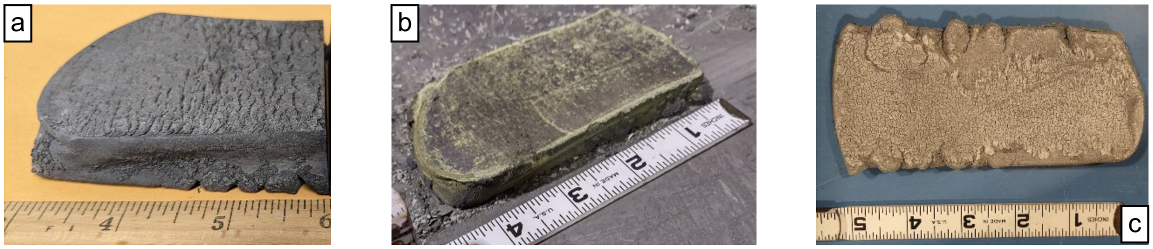

Figure 7. Hot rolled 90W–Fe–Ni plate (#2023/2-in/02B); (a) used one half of the 67R plate (see Figure 6c) for additional hot rolling; (b) after 24th pass (79R) before annealing; (c) after 26th pass (83R) after annealing.

Table 6. Hot rolling schedule of sintered 90 wt.% W–Fe–Ni alloy (#2023/2-in/02B): 1150°C and 5% reduction per pass until 60R and then 10% reduction to prepare a plate with an 83R thickness reduction.

Pass #	Thickness (Inches)		Buck (Inches)		Mill Set	Reduction %		Notes	Annealing interval
	Desired	Actual	Estimate	Actual	(inches)	Pass	Total		% Total Reduction
Start		2.190						Started with 1 piece, a 2" cube, July 11, 2023	
1	2.080	2.084	0.020	0.024	2.060	4.84%	4.84%	1150C 20 min preheat	
2	1.976	1.977	0.020	0.021	1.956	5.13%	9.73%	1150C 20 min preheat	
3	1.878	1.882	0.020	0.024	1.858	4.81%	14.06%	1150C 20 min preheat	
4	1.788	1.792	0.020	0.024	1.768	4.78%	18.17%	1150C 20 min preheat	18.17%
								Pass 2-4 measurements performed with hot sample after rolling pass	
Annealed 4 hours 1200C, Ar Purge then 100% H2					7/12/2023				
		1.786						Post anneal cold measurement	
5	1.697	1.706	0.022	0.031	1.675	4.48%	22.10%	1150C 20 min preheat	
6	1.621	1.621	0.025	0.025	1.596	4.98%	25.98%	1150C 20 min preheat	
7	1.540	1.549	0.025	0.034	1.515	4.44%	29.27%	1150C 15 min preheat	
8	1.472	1.470	0.030	0.028	1.442	5.10%	32.88%	1150C 15 min preheat	14.70%
Annealed 4 hours 1200C, Ar Purge then 100% H2					7/25/2023				
		1.455						Post anneal cold measurement	
9	1.382	1.382	0.025	0.025	1.357	5.02%	36.89%	1150C 20 min preheat	
10	1.313	1.317	0.025	0.029	1.288	4.70%	39.86%	1150C 20 min preheat	
11	1.251	1.266	0.025	0.040	1.226	3.87%	42.19%	1150C 20 min preheat	
12	1.203	1.209	0.030	0.036	1.173	4.50%	44.79%	1150C 20 min preheat	11.92%
								Edge cracking has begun, noticed post anneal	
Annealed 4 hours 1200C, Ar Purge then 100% H2					7/26/2023				
		1.191						Post anneal cold measurement	
13	1.131	1.135	0.025	0.029	1.106	4.70%	48.17%	1150C 25 min preheat	
14	1.078	1.086	0.025	0.033	1.053	4.32%	50.41%	1150C 20 min preheat	
15	1.032	1.029	0.030	0.027	1.002	5.25%	53.01%	1150C 20 min preheat	
16	0.978	0.973	0.030	0.025	0.948	5.44%	55.57%	1150C 20 min preheat	10.78%
Annealed 4 hours 1200C, Ar Purge then 100% H2					7/28/2023				
		0.960						Post anneal cold measurement	
17	0.912	0.912	0.025	0.025	0.887	5.00%	58.36%	1150C 25 min preheat	
18	0.866	0.870	0.025	0.029	0.841	4.61%	60.27%	1150C 20 min preheat	
19	0.783	0.785	0.030	0.032	0.753	9.77%	64.16%	1150C 25 min preheat/Increased to 10% target	
20	0.706	0.710	0.030	0.034	0.676	9.55%	67.58%	1150C 25 min preheat/Increased to 10% target	12.01%
Annealed 4 hours 1200C in Ar Purge then 100% H2					8/1/2023			Material sectioned in half for 67R sampling; continued rolling another half	
		0.700						Post anneal cold measurement	
21	0.630	0.629	0.030	0.029	0.600	10.14%	71.28%	1150C 20 min preheat	
22	0.566	0.560	0.030	0.024	0.536	10.97%	74.43%	1150C 10 min preheat	
23	0.504	0.506	0.030	0.032	0.474	9.64%	76.89%	1150C 10 min preheat	
24	0.455	0.452	0.030	0.027	0.425	10.67%	79.36%	1150C 10 min preheat	11.78%
Annealed 3 hours 1200C, Ar Purge then 100% H2					10/4/2023				
		0.445						Post anneal cold measurement	
25	0.400	0.394	0.030	0.024	0.370	11.46%	82.01%	1150C 20 min preheat	
26	0.372	0.368	0.030	0.021	0.347	6.60%	83.20%	1150C 10 min preheat	
Annealed 3 hours 1200C, Ar Purge then 100% H2					10/11/2023				
		0.358						Final dimension after annealing	
Average reduction per pass						6.34%	83.65%		

To prevent overhang/cracking during hot rolling, additional studies were conducted on 2” blocks. During the hot rolling (1150°C) study #3 and #4 (2023/2-in/03 and 04) involving two 2” cubes, a 5% reduction per pass was utilized during the initial phase only (until 18R). Table 7 shows the rolling schedule for block#3. The rolling schedule of block#4 looks similar until 33R; hence we did not include the table here. A 10% reduction per pass was utilized later. Both blocks underwent a total reduction until 27R without any issues. However, block#4 exhibited a horizontal split (Figure 8c) at 33R (sixth pass) and hence no additional rolling was performed on it. Block#3 did not exhibit any issue at 33R (Figure 9a); hence annealing was performed at this stage and hot rolling was continued but with a slightly aggressive reduction per pass (about 20%), and eventually obtained a hot rolled plate with an 83R total thickness reduction (see Figure 9b).

Table 7. Hot rolling schedule of sintered 90 wt.% W–Fe–Ni alloy (#2023/2-in/03): 1150°C; 5% reduction per pass until 18R; 10% reduction until 33R and then 20% to prepare a plate with an 83R thickness reduction.

Pass #	Thickness (Inches)		Buck (Inches)		Mill Set	Reduction %		Notes	Annealing interval
	Desired	Actual	Estimate	Actual	(inches)	Pass	Total		% Total Reduction
Start		2.160						Started with 1 piece, a 2" cube, 8/15/2023	
1	2.052	2.033	0.045	0.026	2.007	5.88%	5.88%	1150C 20 min preheat	
2	1.936	1.937	0.025	0.026	1.911	4.72%	10.32%	1150C 20 min preheat	
3	1.844	1.844	0.030	0.030	1.814	4.80%	14.63%	1150C 20 min preheat	
4	1.764	1.757	0.035	0.028	1.729	4.72%	18.66%	1150C 20 min preheat	18.66%
								Pass 2-4 measurements performed with hot sample after rolling pass	
Annealed 4 hours 1200C, Ar Purge then 100% H2					8/15/2023				
		1.740						Post anneal cold measurement	
5	1.566	1.564	0.035	0.033	1.531	10.11%	27.59%	1150C 20 min preheat	
6	1.408	1.432	0.035	0.060	1.372	8.44%	33.70%	1150C 20 min preheat	15.05%
								Block 4 split horizontally, decided to anneal this block (#3) at this time	
Annealed 4 hours 1200C, Ar Purge then 100% H2					8/22/2023				
		1.408						Post anneal cold measurement	
7	1.155	1.157	0.040	0.042	1.115	17.83%	46.44%	1150C 20 min preheat, reduction target increased to 18%	
8	0.926	0.921	0.045	0.040	0.881	20.40%	57.36%	1150C 15 min preheat, reduction target increased to 20%	
9	0.734	0.736	0.045	0.044	0.692	20.09%	65.93%	1150C 15 min preheat, splitting of block has begun	
10	0.589	0.579	0.050	0.040	0.539	21.33%	73.19%	1150C 15 min preheat	39.49%
Annealed 4 hours 1200C, Ar Purge then 100% H2					9/15/2023				
		0.574						Post anneal cold measurement	
11	0.459	0.459	0.033	0.033	0.426	20.03%	78.75%	1150C 20 min preheat	
12	0.367	0.366	0.030	0.029	0.337	20.26%	83.06%	1150C 10 min preheat	
	.								
Annealed 3 hours 1200C, Ar Purge then 100% H2					10/4/2023				
		0.361						Final dimension after annealing	
Average reduction per pass						13.22%	83.29%		

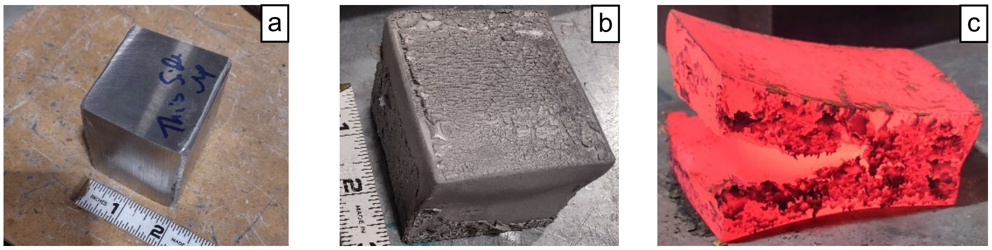

Figure 8. Hot rolled 90W–Fe–Ni (#2023/2-in/04); (a) starting block (b) after 4th pass (18R) before annealing (c) after 6th pass (33R) before annealing. Exhibited horizontal split. No additional rolling was performed.

a

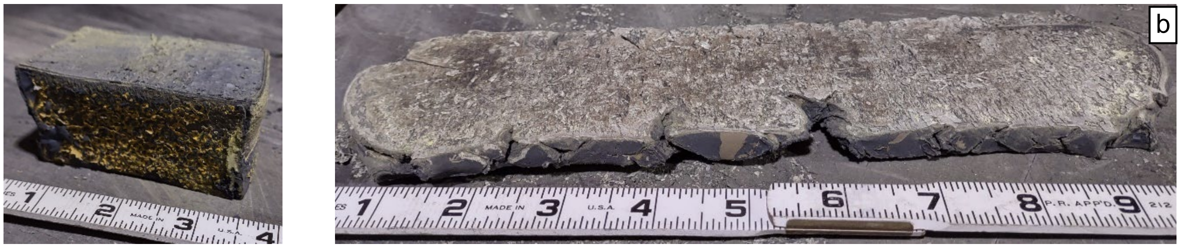

Figure 9. Hot rolled 90W–Fe–Ni plate (#2023/2-in/03); (a) after 4th pass (18R) before annealing; (b) after 12th pass (83R) after annealing.

Additional hot rolling studies were conducted on 2” cube blocks to study the effect of higher reduction per pass and reducing the interval between annealing. During the hot rolling (1150°C) study #5 and #7 (2023/2-in/05 and 07) involving two 2” cubes, a 20% reduction per pass was utilized (see Table 8 and 9). Block#5 exhibited a horizontal split (see Figure 9a) at 35R (second pass) and hence no additional rolling was performed on it. For block#7, even though the annealing interval was reduced, and annealing during hot rolling was performed every 15-20R, it still exhibited an alligator style split as shown in Figure 9b.

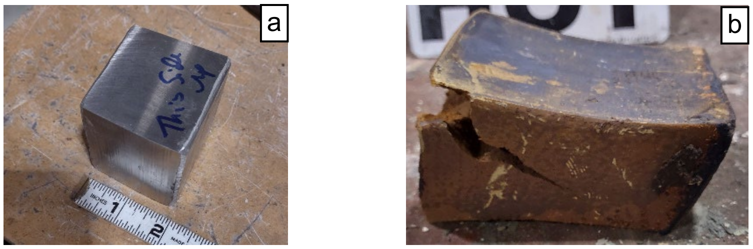

Figure 10. Hot rolled 90W–Fe–Ni (#2023/2-in/05); (a) starting block (b) after 2nd pass (35R).

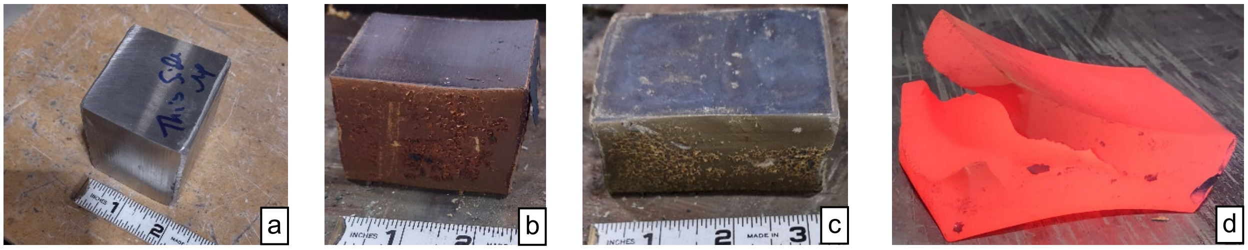

Figure 11. Hot rolled 90W–Fe–Ni (#2023/2-in/07) (a) before; (b) after 1st pass (19R) before annealing; (c) after 2nd pass (35R) before annealing; (d) after 3rd pass – alligator style split.

Table 8. Hot rolling schedule of sintered 90 wt.% W–Fe–Ni alloy (#2023/2-in/05); 1150°C and 20% reduction per pass.

Pass #	Thickness (Inches)		Buck (Inches)		Mill Set	Reduction %		Notes
	Desired	Actual	Estimate	Actual	(inches)	Pass	Total	
Start		2.206						
1	1.765	1.764	0.030	0.029	1.735	20.04%	20.04%	1150C 20 min preheat
2	1.412	1.418	0.030	0.036	1.382	19.61%	35.72%	1150C 20 min preheat
								Split horizontally on leading edge

Table 9. Hot rolling schedule of sintered 90 wt.% W–Fe–Ni alloy (#2023/2-in/06); 1150°C, 20% reduction per pass and annealing after every pass.

Pass #	Thickness (Inches)		Buck (Inches)		Mill Set	Reduction %		Notes	Annealing interval
	Desired	Actual	Estimate	Actual	(inches)	Pass	Total		% Total Reduction
Start		2.170							
1	1.736	1.738	0.030	0.032	1.706	19.91%	19.91%	1150C 25 min preheat	19.91%
Annealed 4 hours 1200C, Ar Purge then 100% H2					10/12/2023				
		1.731						Post anneal measurment	
2	1.385	1.397	0.030	0.042	1.355	19.30%	35.62%	1150C 25 min preheat	15.71%
Annealed 4 hours 1200C, Ar Purge then 100% H2					10/20/2023				
		1.389						Post anneal measurment	
3	1.111		0.030		1.081			1150C 25 min preheat	
Block split alligator style									

Table 10. Hot rolling schedule of sintered 90 wt.% W–Fe–Ni (#2023/1-in/06; 1150°C, 10% reduction per pass) to get a plate with an 83R total reduction.

Pass #	Thickness (Inches)		Buck (Inches)		Mill Set	Reduction %		Notes	Annealing interval
	Desired	Actual	Estimate	Actual	(inches)	Pass	Total		% Total Reduction
Start		1.000							
1	0.900	0.908	0.020	0.028	0.880	9.20%	9.20%	1150C 25 min preheat	
2	0.814	0.807	0.025	0.018	0.789	11.12%	19.30%	1150C 20 min preheat	19.30%
Annealed 4 hours 1200C, Ar Purge then 100% H2					10/16/2023				
		0.796						Post anneal cold measurement	
3	0.716	0.706	0.025	0.015	0.691	11.31%	29.40%	1150C 20 min preheat	
4	0.640	0.636	0.025	0.021	0.615	9.92%	36.40%	1150C 20 min preheat	
5	0.574	0.574	0.020	0.020	0.554	9.75%	42.60%	1150C 20 min preheat	23.30%
Annealed 4 hours 1200C, Ar Purge then 100% H2					10/20/2023				
		0.565						Post anneal cold measurement	
6	0.515	0.510	0.020	0.015	0.495	9.73%	49.00%	1150C 20 min preheat	
7	0.457	0.458	0.020	0.019	0.439	10.20%	54.20%	1150C 10 min preheat	
8	0.412	0.410	0.020	0.018	0.392	10.48%	59.00%	1150C 10 min preheat	16.40%
Annealed 4 hours 1200C, Ar Purge then 100% H2					10/23/2023				
		0.403						Post anneal cold measurement	
9	0.362	0.375	0.020	0.013	0.362	6.95%	62.50%	The mill errantly set at the desired value, didn't include the buck. 1150C 20min	
10	0.338	0.335	0.020	0.027	0.308	10.67%	66.50%	1150C 10 min preheat	
11	0.301	0.298	0.020	0.017	0.281	11.04%	70.20%	1150C 10 min preheat	11.20%
Annealed 4 hours 1200C, Ar Purge then 100% H2					10/25/2023				
		0.293						Post anneal cold measurement	
12	0.264	0.258	0.020	0.014	0.244	11.95%	74.20%	1150C 20 min preheat	
13	0.217	0.223	0.015	0.021	0.202	13.57%	77.70%	1150C 10 min preheat	
14	0.201	0.199	0.020	0.018	0.181	10.76%	80.10%	1150C 10 min preheat	
15	0.179	0.183	0.020	0.014	0.169	8.04%	81.70%	1150C 10 min preheat	
16	0.170	0.178	0.000	0.009	0.169	2.73%	82.20%	Zero "spring pass" made 1150C 10min	12.00%
Annealed 4 hours 1200C, Ar Purge then 100% H2					10/27/2023				
		0.169							
Average reduction per pass						9.84%	83.10%	Final dimension after annealing	

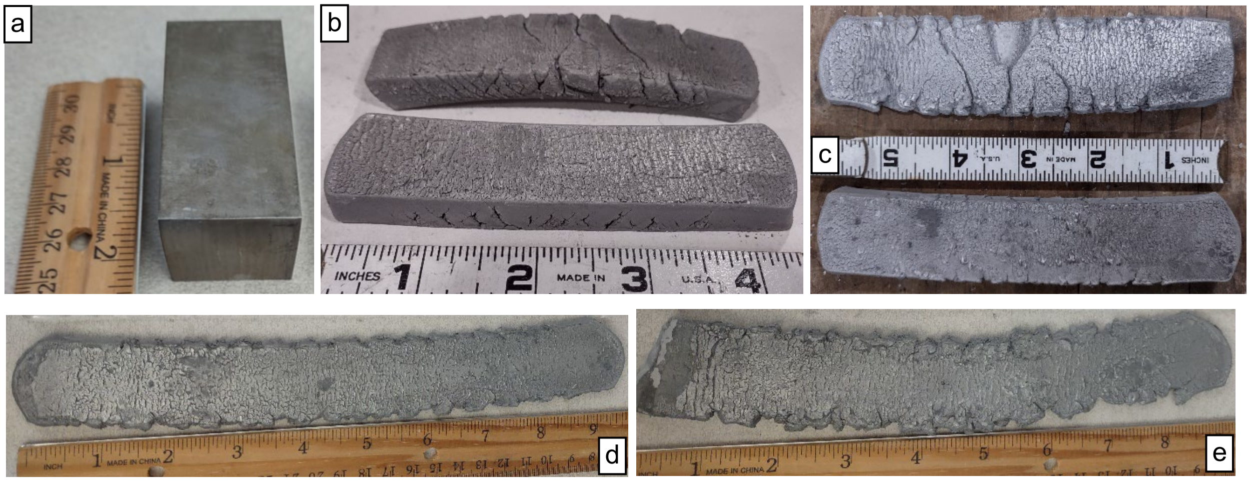

Figure 12. Hot rolled 90W–Fe–Ni rolled and annealed plate (#2023/1-in/06 and 07); (a) before; (b) after 8th pass (59R); (c) after 11th pass (70R); (d) after 16th pass (83R); plate#6; (e) after 16th pass (83R); plate#7.

Since most hot rolling studies on 2” cube blocks were conducted at 1150°C (all stages of reduction, i.e., all passes), efforts were made to utilize a similar rolling temperature for 1” blocks. During the hot rolling (1150°C) study #6 and #7 (2023/1-in/06 and 07) involving two 1” blocks, a similar 10% reduction per pass (2023 study; see Table 3) was utilized and the only difference was the rolling temperature (1150°C during all stages vs. 1150°C until ~19R and then 900°C). Table 10 shows the rolling schedule for block#6 to obtain a plate with an 83R total reduction. The rolling schedule of block#7 looks similar; hence we did not include the table here. Block#7 exhibited some transverse split at 36R, and it continued further at 59R and 70R (see Figure 12b and c). Block#6 exhibited minor edge cracking only during these stages. Even though, an 83R total reduction was successfully obtained from blocks #6 and #7, its appearance along with cracking (Figure 12 d and e) is significantly different (inferior) from 1” blocks hot rolled at 1150/900°C combination (see Figure 3 and 4).

Table 11. Hot rolling schedule of sintered 90 wt.% W–Fe–Ni (#2023/1-in/04; 1150°C, 10% reduction per pass until 17R and 20% later) to get a plate with a 66R total reduction.

Pass #	Thickness (Inches)		Buck (Inches)		Mill Set	Reduction %		Notes	Annealing interval
	Desired	Actual	Estimate	Actual	(inches)	Pass	Total		% Total Reduction
Start		1.106						1 piece, 1"x1"x 2" 8/22/2023	
1	0.995	0.996	0.020	0.021	0.975	9.95%	9.95%	1150C 20 min preheat	
2	0.896	0.915	0.020	0.039	0.876	8.13%	17.27%	1150C 20 min preheat	17.27%
Annealed 4 hours 1200C, Ar Purge then 100% H2					8/22/2023				
		0.905						Post anneal cold measurement	
3	0.724	0.718	0.032	0.026	0.692	20.66%	35.08%	1150C 20 min preheat Reduction target now 20%	
4	0.574	0.564	0.035	0.025	0.539	21.45%	49.01%	1150C 20 min preheat	31.74%
Annealed 4 hours 1200C, Ar Purge then 100% H2					9/15/2023				
		0.564						Post anneal cold measurement	
5	0.451	0.448	0.025	0.022	0.426	20.57%	59.49%	1150C 20 min preheat	
6	0.376	0.378	0.020	0.022	0.356	15.63%	65.82%	1150C 10 min preheat	16.82%
Annealed 4 hours 1200C in Ar Purge then 100% H2					10/4/2023				
		0.375						Final dimension after annealing	
Average reduction per pass						16.06%	66.09%		

a

b

Figure 13. Hot rolled 90W–Fe–Ni (#2023/1-in/04); (a) before; (b) after 6th pass (66R) before annealing.

Table 12. Hot rolling schedule of sintered 90 wt.% W–Fe–Ni (#2023/1-in/05; 1150°C, 10% reduction per pass until 17R and 20% later) to get a plate with an 83R total reduction.

Pass #	Thickness (Inches)		Buck (Inches)		Mill Set	Reduction %		Notes	Annealing interval
	Desired	Actual	Estimate	Actual	(inches)	Pass	Total		% Total Reduction
Start		1.106						1 piece, 1"x1"x 2" 8/22/2023	
1	0.995	0.996	0.020	0.021	0.975	9.95%	9.95%	1150C 20 min preheat	
2	0.896	0.914	0.020	0.038	0.876	8.23%	17.36%	1150C 20 min preheat	17.36%
Annealed 4 hours 1200C, Ar Purge then 100% H2					8/15/2023				
		0.903						Post anneal cold measurement	
3	0.724	0.716	0.032	0.024	0.692	20.71%	35.26%	1150C 20 min preheat Reduction target now 20%	
4	0.574	0.564	0.035	0.025	0.539	21.23%	49.01%	1150C 20 min preheat	31.65%
Annealed 4 hours 1200C, Ar Purge then 100% H2					9/18/2023				
		0.564						Post anneal cold measurement	
5	0.451	0.454	0.025	0.028	0.426	19.50%	58.95%	1150C 20 min preheat	
6	0.363	0.361	0.025	0.023	0.338	20.48%	67.36%	1150C 10 min preheat	18.35%
7	0.289	0.288	0.025	0.024	0.264	20.22%	73.96%	1150C 10 min preheat, leading edge began splitting longitudinally	
Annealed 4 hours 1200C, Ar Purge then 100% H2					10/4/2023				
		0.285						Post anneal cold measurement	
8	0.228	0.225	0.025	0.022	0.203	21.05%	79.66%	1150C 15 min preheat - split end trimmed off before rolling	
9	0.188	0.193	0.020	0.025	0.168	14.22%	82.55%	1150C 10 min preheat	8.59%
Annealed 4 hours 1200C, Ar Purge then 100% H2					10/11/2023				
		0.191						Final dimension after annealing	
Average reduction per pass						17.29%	82.73%		

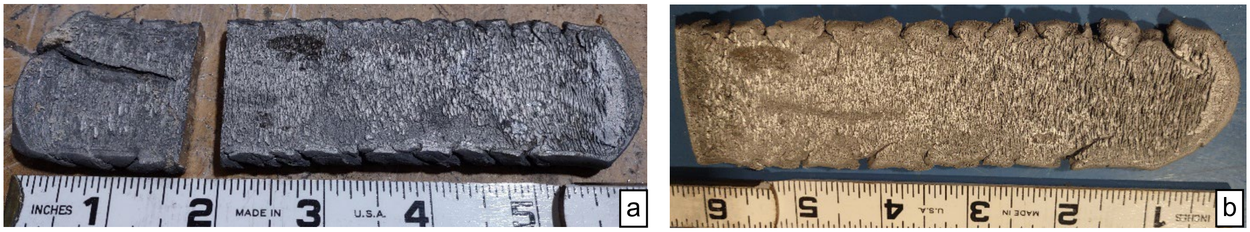

Figure 14. Hot rolled and annealed 90W–Fe–Ni plate (#2023/1-in/05); (a) after 7th pass (73R) – noticed a longitudinal split; sectioned it off and continued rolling; (b) after 9th pass (83R).

Two 1” blocks were also utilized to study the effect of higher rolling temperature (1150°C; all stages) and higher reduction per pass (after the initial phase). During this hot rolling study #4 and #5 (2023/1-in/04 and 05), a 10% reduction per pass was utilized during the initial phase only (until 17R). An aggressive 20% reduction per pass was utilized later. Table 11 shows the rolling schedule for block#4. Figure 13 shows the hot rolled plate with a 66R total reduction after six passes. Table 12 shows the rolling schedule for block#5. The hot rolled plate (from block#5) with a 73R total reduction (Figure 14a) exhibited a large longitudinal split. Hence, a small portion was sectioned off and additional rolling was performed to get to plate with an 83R total reduction in thickness (Figure 14b). Even though, both 66R and 83R total reductions were successfully obtained from blocks #4 and #5, respectively, its appearance along with cracking (Figure 13 and 14) is significantly different (inferior) from 1-in blocks hot rolled at 1150/900°C combination (see Figure 3 and 4) at a 10% reduction per pass.

Based on current studies, it appears that hot rolling at 1150/900°C combination at a 10% reduction per pass (to get plates with 66R and 83R total reductions) seems optimal for a 1” starting thickness. However, the thickness of hot rolled plates with total reductions of 66R (3:1 aspect ratio) and 83R (6:1 aspect ratio) obtained from 1” blocks are about 0.35” and 0.17”, and these are inadequate to prepare mechanical test specimens on the thickness side.

The thickness of hot rolled plates with total reductions of 66R (3:1 aspect ratio) and 83R (6:1 aspect ratio) obtained from 2” blocks are about 0.71” and 0.36”, and these are adequate to prepare mechanical test specimens on the thickness side. Even though, hot rolled plates with 66R and 83R total reductions with various combinations of rolling parameters were successfully obtained from 2” blocks, its appearance along with cracking is significantly different (inferior) from 1” blocks hot rolled at 1150/900°C combination with a 10% reduction per pass (see Figure 3 and 4). Additional hot rolling studies were not performed during Fall 2023 due to equipment move to a different building. It would take about 3-6 months to resume the hot rolling task.

Currently, efforts are ongoing to prepare tensile and metallographic/SEM specimens using a wire EDM. During Spring 2024, SEM, EBSD and tensile testing would be performed to evaluate the hot rolled 66R and 83R specimens (obtained from both 1” and 2” blocks, as the starting material). Based upon these results, additional studies to determine optimum hot rolling parameters for 2” blocks may be performed during late Spring-early Summer 2024.

Tensile Specimen Fabrication

Sub-size tensile specimens, as shown in Figure 15, were machined (single orientation) using an EDM (electrical discharge machining) from as sintered 90W, 95W and 97W samples. Tensile specimens (multiple orientations, as shown in Figure 15) are being fabricated from hot rolled (66R and 83R) plates obtained from the 2023 hot rolling study (from both 1” and 2” blocks as the starting material).

Tensile specimens are being fabricated to perform testing at room and elevated temperatures (244°C, 416°C, 590°C, 750°C and 933°C, based on 0.3-0.7T_m, where T_m is the melting temperature of nickel in Kelvin). The nominal gage width, gage thickness and reduced length of a sub-size tensile specimen are 1.684 mm, 0.762 mm, and 5.029 mm, respectively. The total length and shoulder width of the sub-size tensile specimen are 16.104 mm and 4.013 mm, respectively.

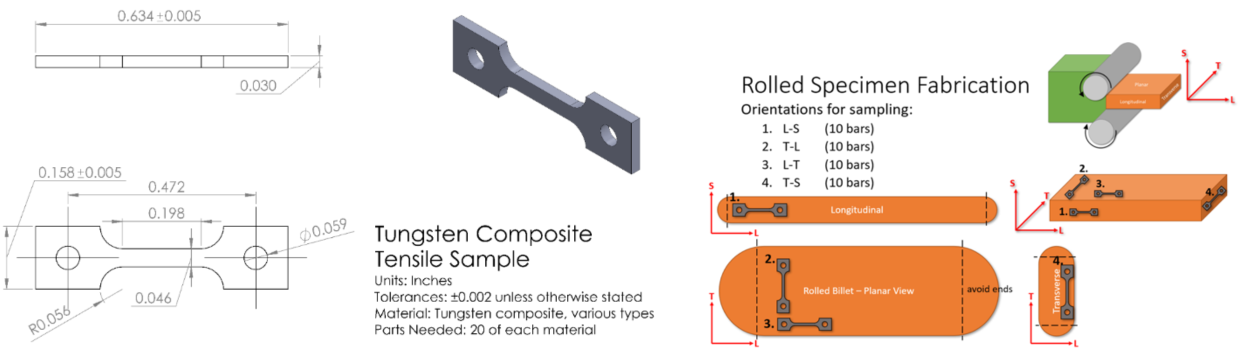

Figure 15. Left: Subsize tensile specimen design; Right: Specimen orientations for rolled specimens.

Annealing studies (1300°C) on DPT W-NiFe alloys

The Materials Research Furnaces, Inc (MRF) furnace was utilized for performing elevated temperature annealing studies on DPT W-NiFe (as-sintered 90W-0R and hot rolled 90W-86R) tensile samples at 1300°C (under 5-10 milliTorr vacuum) for three different annealing times (6 hours; 12 hours; 24 hours). The hot rolled (86R) samples from the 2022 rolling study was utilized for the annealing study, along with as-sintered tensile samples. The melting temperatures of W, Ni and Fe are 3422°C, 1455°C and 1535°C, respectively and it is essential to consider the vapor pressure chart for various metals. During the first-half of 2023, elevated temperature (1300°C) annealing studies on 90W-0R and 90W-86R for different durations were performed on tensile samples. All sides (top and bottom wide faces; gage section thickness direction also) of the tensile samples that were utilized for the 1300°C annealing study were polished to at least 1-micron condition. ASTM Standard E8/E8M was utilized for performing tensile testing and data analysis, [26] and the tensile, SEM and EBSD results can be obtained from the previous report. [25]

As mentioned in the previous report, [25] 1300°C annealing studies on 90W-0R samples showed that the 0.2% offset YS (yield strength) values were similar for samples annealed for 6 and 12 hours but it increased by about 11% when the duration was 24 hours. The UTS (ultimate tensile strength) values increased slightly for all durations, and it was the highest (11% increase) for the 24-hour condition. Annealing increased both uniform elongation (UE) and total elongation (TE) irrespective of the duration. The 1300°C annealing for 12 hours resulted in the highest UE (118% increase) and TE (197% increase) values when compared to un-annealed samples. It is necessary to test additional specimens annealed for 6 hours, since two tested specimens showed a slightly larger scatter in UE and TE values when compared to other durations. The 1300°C/24-hour annealed samples showed a slightly larger scatter in YS and UTS values. The 1300°C/12-hour annealed samples showed the least scatter for all tensile properties. Based upon the available information, it appears that annealing at 1300°C for 12 hours is optimal for as sintered 90W-7Ni-3Fe samples. Annealing could help to homogenize the microstructure and heal processing damage, which is also an issue for the toughness properties of material in the as sintered condition. [23,27]

As mentioned in the previous report, [25] the 1300°C annealing performed on 90W-86R samples reduced the 0.2% offset YS and UTS irrespective of the durations and the lowest YS (19% decrease) and UTS (9% decrease) was observed for 12-hours. Annealing increased the uniform elongation (UE) irrespective of the durations and the highest UE (27% increase) was observed for 6-hours. Annealing reduced the TE slightly (5% decrease) for 24-hour duration, however, the TE increased as the annealing duration was reduced, and the 6-hour duration resulted in the highest TE (39% increase). It is necessary to test additional specimens for 12 hours since specimen availability was an issue at that time. In general, annealed samples did not exhibit much scatter in the YS, UTS, UE and TE values (except the 24-hour duration that showed some scatter in TE values). Based upon the available information, it appears that annealing at 1300°C for 6 hours is optimal for hot rolled (86R) 90W-7Ni-3Fe samples.

Our previous work showed that is necessary to perform additional annealing studies and then perform tensile testing of 90W-0R (6 hours) and 90W-86R (12 hours) to get better statistics and to determine the optimum annealing time.[25] During 2022, polishing (to at least 1200 grit condition) was only performed on the top and bottom wide faces (not on the thickness direction) of the tensile specimens obtained from as-sintered (90W, 95W, 97W) and hot-rolled (2022 batch of 86R, 78R and 57R) materials to remove minor cracks and local residual stresses due to EDM. Tensile test results and analysis of these samples can be found in the previous report. [21] During 2023, a study was performed using as sintered 90W-0R samples to determine if it is necessary to polish the tensile specimen's thickness sides also besides polishing the two flat sides. As mentioned in our previous report, the results showed that it is not necessary to polish the thickness sides (which is more labor intensive and prone to error due to hand polishing). [25]

Table 13. Status of 1300°C (5-10 milliTorr vacuum) annealing studies on sintered and hot rolled WHA

Material	1300°C annealing				Tensile flat sides polished	Tensile thickness sides polished	Tensile testing
	0 h	6 h	12 h	24 h			
90-0R	✓	-	-	-	✓	-	✓
95-0R	✓	-	-	-	✓	-	✓
97-0R	✓	-	-	-	✓	-	✓
90-0R	-	✓	✓	✓	✓	✓	✓
90-86R (from 1-in block)	-	✓	✓	✓	✓	✓	✓
90-0R	-	x	✓	✓	✓	-	x
90W-66R (from 1-in block)	-	x	x	-	x	-	x
90W-66R (from 2-in block)	-	x	x	-	x	-	x
90W-83R (from 1-in block)	-	x	x	-	x	-	x
90W-83R (from 2-in block)	-	x	x	-	x	-	x

NOTE: Symbols: ✓ denotes performed; - denotes not required; x denotes to be performed

Figure 16. Tensile samples annealed at 1300°C for 24 hours using the MRF furnace.

Currently, efforts are ongoing to perform 1300°C annealing on the recently hot rolled 66R and 83R samples (obtained from both 1" and 2" blocks), as shown in Table 13. Alumina crucibles are being utilized for the annealing study. The alumina crucibles were positioned in such a way that it is at the center of the heat zone, as shown in Figure 16. Tensile specimens from each condition were placed inside alumina crucibles. Once the samples were placed inside, the furnace door was closed, and the roughing pump was turned on until the vacuum levels reached 5-10 milliTorr. The temperature of the MRF furnace was gradually increased at a ramp rate of 3-5°C/min until it reached 1300°C. The samples were then annealed for a particular annealing time and then the furnace hot zone was shut down so that the samples can cool down via natural cooling. The furnace does not have any other cooling system. The vacuum level was maintained until the samples reached the ambient temperature. Figure 16 shows the typical condition of the tensile samples after 1300°C annealing.

Elevated Temperature Mechanical Test Facility Setup

Instron 8801 servo hydraulic mechanical test system

Instron 8801 is a servo hydraulic fatigue testing system that could be employed to perform static and dynamic mechanical tests at ambient and elevated temperatures. Additional information on this test frame can be found in the previous report. [28]

Elevated temperature tensile test fixture

Currently, efforts are ongoing to understand the mechanical behavior of DPT W-NiFe alloys (as sintered and rolled samples) at elevated temperatures: 244°C (0.3T_m); 416°C (0.4T_m), 590°C (0.5T_m), 750°C (0.6T_m) and 933°C (0.7T_m), where T_m is the melting temperature of nickel (1723K; 1450°C). The MRF furnace has a usable work zone of 3.5" dia. x 4.0" high. It has water-cooled pull rods (17-4 PH stainless steel) on either side of the furnace, and a tensile fixture that can withstand elevated temperatures without any water cooling is required. Based upon material availability, machinability, cost, and mechanical properties at elevated temperatures, TZM was chosen as the fixture material. TZM an acronym for the molybdenum alloy 'titanium-zirconium-molybdenum', is a molybdenum alloy containing 0.5% titanium, 0.08% zirconium, 0.02% carbon and the balance molybdenum. The TZM material was procured, and the tensile fixture fabrication was performed at PNNL. Additional information about the TZM fixture (see Figure 17) can be seen in the previous report. [29]

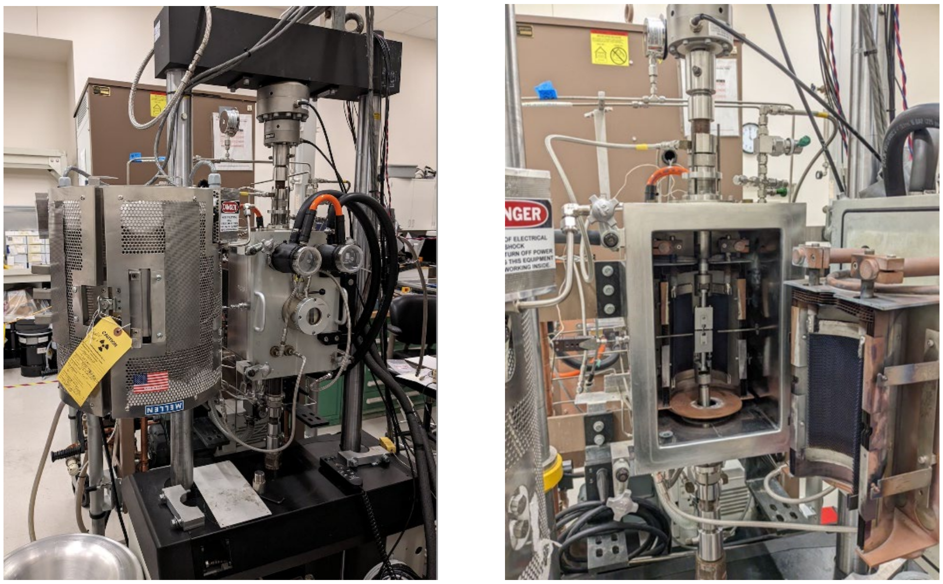

Figure 17. The MRF furnace (1600°C) along with Instron 8801 mechanical test frame and tensile test fixture.

MRF model M-4x6-M-1600-V&G furnace

The PNNL has an MRF Model M-4x6-M-1600-V&G front-loading furnace with a usable work zone of 3.5" diameter x 4.0" high, and a maximum operating temperature of 1600°C. The hot zone is a 180° split design with tungsten mesh heating elements for operation in vacuum (50-100 milliTorr) and inert gas (Ar, N_2 or Ar/O_2 gas mixture). Additional information about this furnace can be found in previous reports. [28,29] Figure 17 shows the photo of the MRF furnace along with the Instron 8801 mechanical test frame and tensile test fixture. Annealing studies on DPT W-NiFe (as-sintered and rolled) at 1300°C (under 10-15 milliTorr vacuum) are being performed using this furnace (see section D).

<u>Elevated temperature tensile testing</u>

A trial tensile testing using a 95W-0R tensile specimen was recently performed at 750°C under Argon atmosphere. An Instron 8801 servo-hydraulic mechanical testing system was utilized for conducting tensile testing in the displacement control mode. The specimen gage width and thickness were measured using calipers prior to tensile testing. The displacement rate during tensile testing was constant at a crosshead speed of 0.06 mm/min (1 micron/s), which can be converted to an estimated strain rate of 1.99E-4/s for specimens with a 5.029 mm reduced length. Subsize tensile specimens were shoulder loaded instead of pin loaded to avoid tear out at the pin hole and warping of the pins. The ASTM Standard E8/E8M was utilized for performing tensile testing and data analysis. [26]

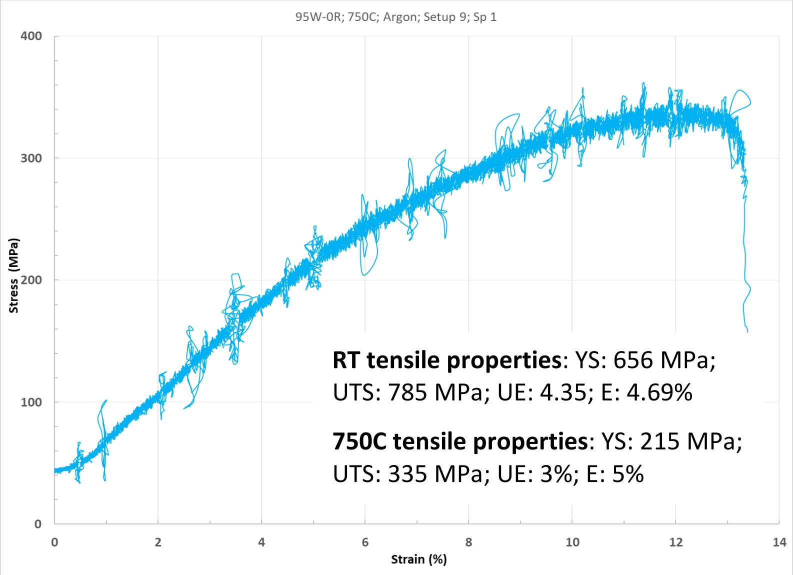

Figure 18. Engineering stress strain curve of 95W-0R at 750°C (under argon purge) trial testing.

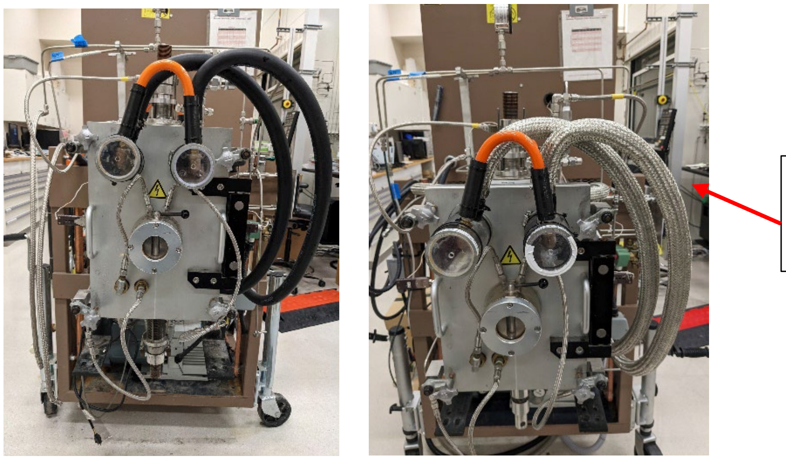

Shielding wrapped around the high current low voltage power cables to reduce noise in the tensile data.

Figure 19. Electromagnetic interference shielding wrapped around the power cable to reduce noise in the tensile data.

Load, displacement, and time were recorded during tensile testing. The displacement was measured from the crosshead movement. The load data was obtained from the load cell. Engineering stress-strain curve was generated by using load-displacement data recorded during testing along with initial specimen gage width, thickness, and reduced length. This curve was used to determine 0.2% offset yield strength (YS), UTS, UE, and TE.

During the trial tensile testing of 95W-0R at 750°C under argon atmosphere, periodic noise was observed in the load-displacement curve (see Figure 18). Earlier, trial testing was performed at room temperature (without turning on the furnace) by placing the tensile fixture inside the MRF furnace under argon atmosphere, and this noise was not seen. These trial tests under argon atmosphere at both room temperature and 750°C showed that the noise is present only when the furnace is running. The MRF furnace vendor confirmed our finding and mentioned that it is due to the high current (1000s of A) and low voltage (below 10 V) can result in electromagnetic interference and it can affect sensitive equipment like an Instron load cell present near the power cable. They suggested to wrap the power cables using an electromagnetic interference shielding, and Figure 19 shows the setup after adding this shielding. Efforts are ongoing to perform additional trial tests at elevated temperature and confirm the absence of noise in the tensile data while the furnace is on.

Results

The following activities are being planned to be performed:

- Perform additional 1300°C annealing and room temperature tensile testing of 90W-0R, and the newly hot-rolled 90W-66R and 90W-83R to get better statistics and determine the final optimum annealing time.
- Fabricate mechanical test (tensile and fracture toughness) and microcopy (SEM, EBSD) sample from recently rolled materials (90W-66R and 90W-83R) and as sintered 90W, 95W and 97W.
- Perform elevated temperature tensile testing of annealed (as sintered and hot rolled) samples: 244°C (0.3T_m); 416°C (0.4T_m), 590°C (0.5T_m), 750°C (0.6T_m) and 933°C (0.7T_m), where T_m is the melting temperature of nickel (1723K; 1450°C).
- Perform room and elevated temperature fracture toughness testing of annealed (as sintered and hot rolled) samples.

Acknowledgments

The authors would like to acknowledge the support of Mark Rhodes for performing hot rolling of 90W WHA samples and coordinating the annealing and degassing operations. This research was supported by the U.S. Department of Energy, Office of Science, Office of Fusion Energy Sciences, through Contract No. AT2030110-13784 and was performed at the PNNL, which is operated by Battelle for the U.S. Department of Energy under Contract No. DE-AC05-76RL0-1830.

References

[1.] S. Wurster, et al., *Recent progress in R&D on tungsten alloys for divertor structural and plasma facing materials.* Journal of Nuclear Materials, 442 (2013) S181.

[2.] D. Stork, et al., *Developing structural, high-heat flux and plasma facing materials for a near-term DEMO fusion power plant: the EU assessment.* Journal of Nuclear Materials, 455 (2014) 277.

[3.] A. Hasegawa, et al., *Neutron irradiation effects on the microstructural development of tungsten and tungsten alloys.* Journal of Nuclear Materials, 471 (2016) 175.

[4.] R. Neu, et al., *Investigations on tungsten heavy alloys for use as plasma facing material,* Fusion Eng. Des. 124 (2017) 450.

[5.] R. Neu, et al., *Results on the use of tungsten heavy alloys in the divertor of ASDEX Upgrade*, J. Nucl. Mater. 511 (2018) 567.

[6.] M. Alam, et al., *The effect of hot rolling on the strength and fracture toughness of 90W-7Ni3Fe tungsten heavy metal alloys*, Materials Science & Engineering A 824 (2021) 141738.

[7.] G.M. Wright, et al., *Comparison of tungsten nano-tendrils grown in Alcator C-Mod and linear plasma devices*, J. Nucl. Mater. 438 (2013) S84.

[8.] D. Dasgupta, et al., *Prediction of temperature range for the onset of fuzz formation in helium-plasma-implanted tungsten*, Surf. Sci. 698 (2020) 121614.

[9.] Q. Yang, et al., *Nanostructured fuzz growth on tungsten under low-energy and high-flux He irradiation*, Sci. Rep. 5 (2015) 1.

[10.] X. Gong, et al., *Effect of tungsten content on microstructure and quasi-static tensile fracture characteristics of rapidly hot extruded W-Ni-Fe alloys*, Int. J. Refract. Metals Hard Mater. 30 (2012) 71.

[11.] X. Gong, et al., *Microstructure and highly enhanced mechanical properties of fine-grained tungsten heavy alloy after one-pass rapid hot extrusion,* Mater. Sci. Eng. 528 (2011) 3646.

[12.] Z.S. Levin, K. Ted Hartwig, *Hardness and microstructure of tungsten heavy alloy subjected to severe plastic deformation and post-processing heat treatment*, Mater. Sci. Eng. 635 (2015) 94.

[13.] Y. Yang, et al., *Microstructure and mechanical properties of a hothydrostatically extruded 93W-4.9Ni-2.1Fe alloy*, Mater. Sci. Eng. 435 (2006) 620.

[14.] Y. Yu, H. Hu, et al., *Microstructure evolution and recrystallization after annealing of tungsten heavy alloy subjected to severe plastic deformation*, J. Alloys Compd. 685 (2016) 971.

[15.] Y. Yu, et al., *Effect of heat treatment on microstructure and mechanical properties of hot-hydrostatically extruded 93W-4.9Ni-2.1Fe alloy*, J. Alloys Compd. 622 (2015) 880.

[16.] Z.H. Zhang, et al., *Deformation characteristics of the 93W-4.9Ni-2.1Fe tungsten heavy alloy deformed by hydrostatic extrusion*, Mater. Sci. Eng. 435 (2006) 632.

[17.] C. Henager Jr., et al., *Ductile-phase toughened tungsten for plasma-facing materials in fusion reactors*, Int. J. Powder Metall. 53 (2017) 53.

[18.] B.N. Nguyen, et al., *Tailoring ductile-phase toughened tungsten hierarchical microstructures for plasma-facing materials*, J. Nucl. Mater. 540 (2020) 152382.

[19.] J. Wang, et al., *Tensile testing and microstructural characterization of ductile phase toughened W-NiFe alloys*, in Fusion materials Semiannual Progress Report for the Period Ending June 30, 2020.

[20.] J. Wang, et al., *Microstructural characterization and mechanical testing of ductile-phase toughened tungsten*, in Fusion materials Semiannual Progress Report for the Period Ending December 31, 2019.

[21.] R. Prabhakaran, et al., S*tatus of the elevated temperature mechanical test faciity, hot rolling and tensile testing at PNNL*, PNNL-SA-181771, Vol 73, Chapter 4, in Fusion Materials Semiannual Progress Report for Period Ending December 31, 2022, DOE/ER-0313/73, U.S. Department of Energy, 2023.

[22.] R.M. German, L.L. Bourguignon, Powder Met. Def. Technol., 6 (1984), 117.

[23.] M. Li, et al., *Impact of heat treatment on tensile properties of 97W-2Ni-1Fe heavy alloy*, Journal of Nuclear Materials 512 (2018) 1.

[24.] M.E. Alam, G.R. Odette, *Improving the fracture toughness and ductility of liquid-phase sintered WNiFe tungsten heavy alloys by high-temperature annealing*. Materials 16 (2023) 916.

[25.] R. Prabhakaran, et al., *High temperature mechanical testing of W/NiFe ductile-phase toughened W composites*, PNNL-SA-188793, Vol 74, Chapter 4, in Fusion Materials Semiannual Progress Report for Period Ending June 30, 2022, DOE/ER-0313/74, U.S. Department of Energy, 2023.

[26.] ASTM E8/E8M-21, Standard Test Methods for Tension Testing of Metallic Materials, ASTM International, West Conshohocken, PA, 2021.

[27.] M.E. Alam, G.R. Odette, *On the influence of specimen size and geometry on the fracture toughness of tungsten heavy metal alloys*. J. Nucl. Mater. 571 (2022) 154025.

[28.] R. Prabhakaran, et al., *Status of the elevated temperature mechanical test facility setup at PNNL*, PNNL-SA-170069, In Fusion Materials Semiannual Progress Report for period ending December 31, 2021, DOE/ER-0313/71, US Department of Energy, 2022.

[29.] R. Prabhakaran, et al., “*Status of the elevated temperature mechanical test facility setup at PNNL*”, PNNL-SA-176100, In Fusion Materials Semiannual Progress Report for Period Ending June 30, 2022, DOE/ER-0313/72, U.S. Department of Energy, 2022.

4.7 BORON DOPED TUNGSTEN FOR FUSION PFCS—X.-Y. Yu, T. Graening, G. Parker, Y. Katoh (Oak Ridge National Laboratory)

OBJECTIVE

The objective of this project is to determine: 1) if boron is added into the tungsten plates via the usual route of powder metallurgy and hot rolling and 2) if boron is incorporated at the desired quantity.

SUMMARY

The ALMT prepared boron (B) doped tungsten (W) plates were characterized using microscale spectroscopy and microscopy including depth profiling of time-of-flight secondary ion mass spectrometry (ToF-SIMS) and inductively coupled plasma mass spectrometry (ICP-MS) analysis. Boron was detected at the surface of the doped W plates using SIMS and verified using ICP-MS. Raman and scanning electron microscopy (SEM) results were reported previously [1]. The relative abundance of *m/z*$^+$ 10.9837 B$^+$ was determined using SIMS depth profiling and high mass resolution mass spectral analysis. Comparisons between the 0.1 at.% B and 0.01 at.% B plates showed a reasonable 10:1 difference in the *m/z*$^+$ 10.9837 B$^+$ peak. However, only the surfaces of the rolled plates have B, and their abundances decreased sharply into the bulk of the metal plate. Our findings indicate that the manufacturing process needs revisions and optimization.

PROGRESS AND STATUS

Doping a small amount of B can reduce recrystallization of W effectively [2, 3]. B-doping ductilizes W and is beneficial for additive manufacturing (AM) of W, by reducing the embrittling behavior at grain boundaries [4]. For that reason, B-doping can potentially offer benefits to a plasma facing component (PFC) performance. Therefore, understanding basic properties of B-doped W is useful for developing materials for fusion applications. The ALMT prepared two B-doped W plates via powder metallurgy and hot rolling, which nominally have 0.1 at.% B and 0.01 at.% B, respectively. A W plate without B doping was also provided as the reference material.

Pieces from all three rolled plates were sectioned and the top surface of the rolled plates was polished to a 0.5 μm finish and approximately 1.2 cm (L) by 1 cm (W) in dimension, followed by a chemical polishing step. These pieces were used for ToF-SIMS depth profiling and Raman mapping. Residues of the metal pieces were used for chemical analysis using ICP-MS. More than 20 measurements in high- and low-resolution mode have been performed on boron-doped materials have been performed to verify the depth distributions of boron using ICP-MS.

The ToF-SIMS spectral and depth profiling were performed using an IONTOF V instrument (IONTOF GmbH, Münster, Germany). Surface mapping of unirradiated manufactured tungsten plates was acquired in the static mode. A 30 keV Bi$_3$P$^+$P was used as the analysis beam, and data was collected in both negative and positive ion modes. The mass spectrometer mode was used to acquire spectra with high mass resolution for 400 scans rastering over an area of 500 μm × 500 μm. All SIMS mass spectra were mass calibrated using C$^+$, CHRR$_2$RP$^+$P, Al$^+$, and ^{41}K$^+$P for the positive ions. During dynamic depth profiling, 2 keV cesium (CsP$^+$P) beam was used as the sputter beam and the 30 keV BiP333$_3$$^+$P beam was used as the analysis beam. The Cs$^+$ beam rastered over a 500 μm × 500 μm surface for sputtering and Bi$_3$P$^+$P rastered over 150 μm × 150 μm area for analysis for 450 scan. The AFM measurements of the crater were 2 μm in depth. Depth profiles were acquired using the non-interlaced mode to reduce the charging effect in addition to applying the electron flood gun. The raster size of mass spectra, depth profiles, and images was set at 128 × 128 pixels.

Experimental Procedure

ToF-SIMS Depth Profiling

In SIMS depth profiling, it is possible to use a Cs^+ beam to detect MCs^+ or MCs_2^+ cluster ions, where M is the element of interest and MCs^+ and MCs_2^+ are ions of M combined with one or two Cs atoms.[6] The advantages of following MCs^+ and MCs_2^+ ions during SIMS analysis are the reduction of the matrix effect and the ability to detect element unambiguously using either the MCs^+ or MCs_2^+ for elements that are more electronegative (e.g., H, C, N, O). Figure 1 depicts the depth profiling results of 0.1 at% B tungsten plate in the positive mode. Similarly, Figure 2 depicts the depth profiling results of 0.01 at% B tungsten plate in the positive mode.

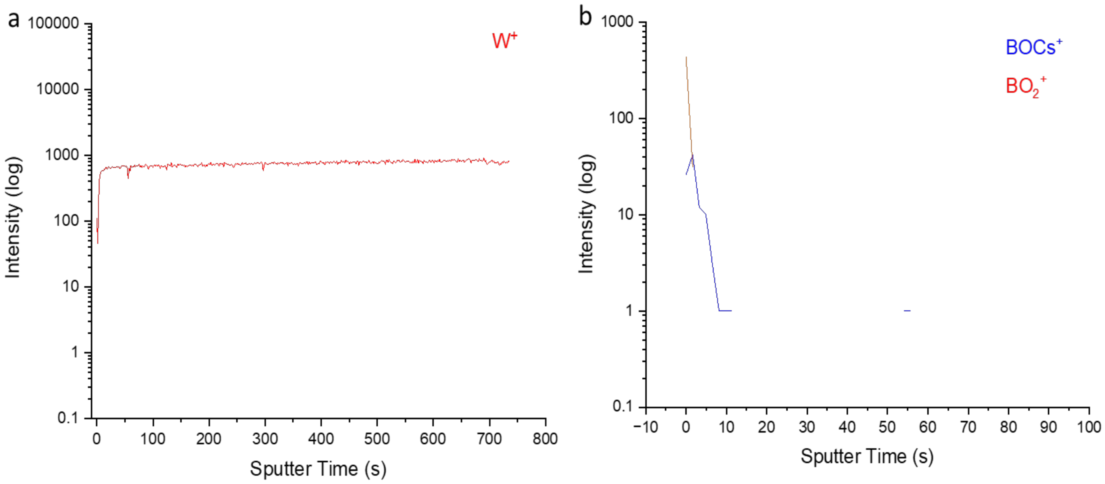

Figure 1. The ToF-SIMS depth profiling of the 0.1 at% B tungsten plate: (a) W^+ and (b) $BOCs^+$ and BO^+ results.

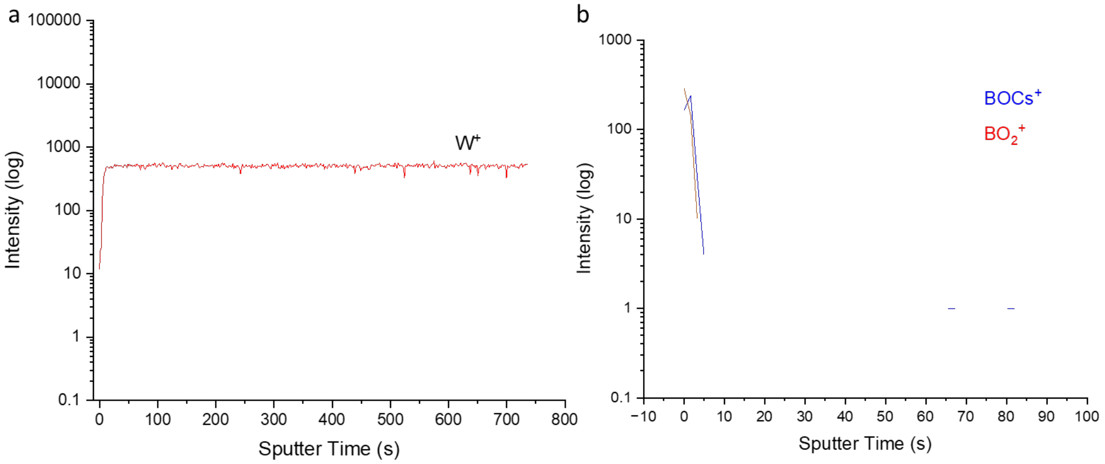

Figure 2. The ToF-SIMS depth profiling of the 0.01 at% B tungsten plate: (a) W^+ and (b) $BOCs^+$ and BO^+ results.

Since the amount of B in the surface is close to SIMS static detection limit, we use other peaks indicative of B in the depth profiling plots, such as m/z^+ 159.92 $BOCs^+$ and m/z^+ 38.01 BO_2^+. The B^+ peak itself is low and close to the static SIMS detection limit, therefore, it is better to use MCs^+ or oxides of boron to indicate boron distributions. Taking the m/z^+ 10.98 B^+ from the 0.1 at.% B plate and 0.01 at.% B plate, respectively, and dividing the averaged relative peak areas of three replicates, the ratio of the 0.1 at.% B to 0.01 at.% B is arrived at 9.30 ± 1.04 with error propagation. Therefore, the surface abundance of B is close to the designed 10 times difference between the two plates.

The depth profiling results indicate that the boron only stays at the surface. Also, boron does not dissolve into the bulk of the tungsten after the top few nanometers. In contrast, the abundance of W, namely m/z^+ 183.96 W^+ remained constant during depth profiling, suggesting uniform distribution of tungsten throughout the top two micrometers. The 800 s sputtering time corresponds to 2 μm crater depth. The peaks, such as m/z^+ 159.92 $BOCs^+$ and m/z^+ 38.01 BO_2^+, which are related to boron, reduced sharply in the depth profiles (Figures 1 and 2). This observation indicates that only about 5 nm of the surface the polished metal coupon has boron diffused into the structure. Even considering that approximately 1 mm of the original plate materials may be taken off during sample preparation, the total boron incorporated into the tungsten plate is still in the top micrometer of the material. Our SIMS findings suggest that the manufacturing process needs optimization. Similarly, we use WCs^+ and WCs_2^+ to show the depth profiling of W, as these peaks do not have saturation issues and they should reflect the abundance of W of the specimens of interest as expected.

ICP-MS Finding

Best results have been achieved in low resolution modes, which provided the highest sensitivity (W signal intensity ~1×10^{13} cps or 1×10^{7} cps/ppm on W), due to the ion beams practically reaching the detectors without physical restriction by focusing slits.

The boron sensitivity is higher than 2×10^{6} cps / ppm and the background signal is about 300 cps. That shows that easily parts per billion levels can be measured on all isotopes not having isobaric interferences overlapping with the analyte signal. The overlapping interference signal on the ^{10}B isotope is from $^{40}Ar^{4+}$. Unfortunately, this interference does not allow evaluation of the $^{10}B/^{11}B$ ratios accurately in these modes. However, even in the low-resolution mode, we can estimate that boron isotopes are very close to their natural abundances in both boron-doped samples and their mass fractions are in the range of 0.03 ppm and not 0.01 wt%. The ICP-MS results indicate that the Boron in the plates is close to the analytical detection limit. Also, the boron distributions in the two plates are not distinguishable using this bulk analysis approach.

Combining results from ToF-SIMS and ICP-MS infers that the presence of boron is limited to the surface of the polished W plate. The relative abundance ratio of boron of the 0.1 at.% B plate to that of 0.01 at.% B on the plate surface is approximately 10 as desired. However, boron is not fully incorporated into the material structure.

Results

The SIMS and ICP-MS results will be combined with SEM and Raman with a focus on the determination of the B distribution and quantification in a manuscript. To assure quantification of boron, an ion irradiated sample may also be prepared and used in the SIMS depth profile analysis. This result can be used as a reference to calibrate the AM prepared tungsten plates with different amounts of B more accurately. Future research will focus on post-irradiation examination of the B doped tungsten coupons after they are deployed in a neutron irradiation campaign.

References

[1] X.-Y. Yu, T. Graening, G. Yang, and Y. Katoh, “Boron-Doped Tungsten for Fusion PFCS”, U.S. DOE Office of Fusion Energy Science, Fusion Materials, Semiannual Progress Report, DOE/ER-0313/74 (2023).

[2] C. Fan, X. Hu, Recovery and recrystallization of warm-rolled tungsten during helium thermal desorption spectroscopy annealing, Journal of Nuclear Materials 569 (2022) 153914.

[3] A. Hasegawa, T. Miyazawa, D. Itou, T. Hattori, K. Yohida, S. Nogami, Helium effects on recovery and recrystallization of powder metallurgically processed tungsten, Physica Scripta 2020(T171) (2020) 014016.

[4] Y. Liu, X. Liu, C. Lai, J. Ma, X. Meng, L. Zhang, G. Xu, Y. Lu, H. Li, J. Wang, S. Chen, Boriding of tungsten by the powder-pack process: Phase formation, growth kinetics and enhanced neutron shielding, International Journal of Refractory Metals and Hard Materials 110 (2023) 106049.

[5] D. Marseilhan, J.P. Barnes, F. Fillot, J.M. Hartman, P. Holliger, Quantification of SiGe layer composition using MCs^+ and MCs_2^+ secondary ions in ToF-SIMS and magnetic SIMS, Applied Surface Science 255 (2008) 1412.

[6] P. Holliger, F. Laugier, J.C. Dupuy, SIMS depth profiling of ultrashallow P, Ge, and As implants in Si using MCs_2^+ ions, Surface and Interface Analysis 34 (2002) 472.

4.8 MICROSTRUCTURAL EVOLUTION IN HOT-ROLLED AND HIGH-TEMPERATURE ANNEALED 90W-7Ni3Fe TUNGSTEN HEAVY ALLOY

—M.E. Alam, G. R. Odette (University of California Santa Barbara), J.V. Haag IV, C.H. Henager Jr., W. Setyawan (Pacific Northwest National Laboratory)

OBJECTIVE

The objective of this study is to understand the effect of hot-rolling and high-temperature annealing on the microstructure of rolled 90W-7Ni3Fe tungsten heavy alloys for the nuclear fusion reactor application.

SUMMARY

The mechanical properties of the as-sintered (AS) and hot-rolled (HR) to 62, 74 and 87% thickness reduction (R) of a 90W-7Ni3Fe tungsten heavy alloy (WHA) have been reported previously. The 87R plate was given a processing heat treatment at 1400°C/3h (87RHT), while the others were not. The AS/87RTH WHA shows a very stable crack with a maximum load fracture toughness, $K_{Jm} \approx 107 \pm 12$ MPa√m, while the 62R/74R fractured elastically and unstably at $K_{Im} \approx 35 \pm 2$ MPa√m at room temperature (RT) test. The hardness and tensile stress of these WHAs show opposite trends to the toughness and tensile ductility due to the development of hardened subgrain structure in W-particles. A 1300°C/24h annealing in vacuum has been performed to soften the HR WHAs, resulting in much higher toughness for all, averaging ≈ 125 ± 12 MPa√m. Scanning electron microscopy and electron backscatter diffraction showed that annealing recovers the hardening microstructures in the 62R and 74R WHA. The lower strength promotes crack tip microcracking shielding, which increases the fracture toughness.

PROGRESS AND STATUS

Introduction

Considering their favorable attributes, including satisfactory lower temperature tensile strength, ductility, fracture toughness, manufacturability, and cost-effectiveness, the WNiFe WHAs are emerging as a highly viable substitute for the brittle and low-toughness monolithic tungsten (W) for the plasma-facing components like first-wall and divertors in nuclear fusion environment [1–7]. Application-specific properties can be achieved by manipulating the microstructure via severe-plastic deformation like warm or hot-rolling, extrusion [8,9]. In a previous publication [10], the effects of HR and processing heat-treatment (HT) on the liquid phase sintered (LPS) 90W7Ni3Fe (90W, wt.%) WHA plates on key mechanical properties were characterized. Hot rolling reduction from AS and an 87% thickness, followed by a final processing HT at 1400 °C/3 h (87RHT), resulted in much higher fracture toughness than found in the corresponding plates at 62% (62R) and 74% (74R) reductions, which did not undergo a final processing HT. The large reduction in toughness was attributed to the higher strength of the plates, absent annealing. In this new study, we have identified the microstructural basis with refined scanning electron microscopy (SEM) and electron back-scattered diffraction (EBSD) for the property changes, and to characterize the related effects of a final 1300°C/24 h anneal of the four previously HR conditions. Additional annealing resulted in similar properties, with improved toughness, in all four conditions, consistent with the observed recovery of the strengthening microstructures.

Experimental Procedure

Commercially available 90W7Ni3Fe (wt.%) WHA was obtained from Mi-Tech Metals, Indianapolis, IN, as an LPS plate, which we refer to the AS 90W WHA. Another set of plates were also obtained from the same vendor in a green compact form, was first sintered at 1200°C in hydrogen (H_2), degassed at 1000°C in vacuum, followed by LPS at 1500°C in H_2, and again degassed in vacuum at 1000°C. These plates were sequentially HR at Pacific Northwest National Laboratory (PNNL), initially at 1150°C with two reduction passes of 5% followed by 15% to 32% reductions at 900°C, with intermediate 1400°C/3h anneals down to final thickness reductions of 62%, 74%, and 87% [3,10]. The 87% condition was further HT at 1400°C for 3h in 50Ar: 50H_2 (87RHT), while the 62% and 74% conditions were not HT (62R and 74R). Details of the processing history can be found in Table 1 and shematially presented in Figure 1. Note, the final rolling temperature (900°C) is hot-rolling for the DP constituents, with a W-Ni-Fe ternary eutectic temperature of ≈ 1465°C [11,12]. However, this is barely a warm-rolling temperature for W with melting temperature, T_m ≈ 3420°C [13–15]. However, for simplicity, we have adopted the term ‘hot-rolling’ to describe the bi-phasic WHA composite rolling process, as is commonly done by other researchers in [8,9,16]. Again, since the effect of annealing is the major focus of the new study reported here, all the AS and HR WHAs were vacuum ($3x\ 10^{-8}$ torr) annealed at 1300°C for 24h, with heating and cooling rates of 5°C/min. Unless otherwise noted, here ‘annealing’ refers to this 1300°C/24h annealed condition.

Table 1. The Hot-rolling history of a 90W WHA plate

Pass #	Thickness (inches)		Buck (inches)		Mill Set	Reduction %		Notes:
	Desired	Actual	Estimate	Actual	(inches)	Pass	Total	
0		**1.05**						
1	0.998	0.995	0.025	0.022	0.973	5		T=1150C 15 min preheat
2	0.995	0.946	0.022	0.02	0.923	5	**10**	T=1150C 6 min preheat
		0.933		Anneal 3 hours at 1400C in 50:50 H2/Ar on 6-5-14				
3	0.793	0.792	0.036	0.037	0.757	15		T=900C; 15 min preaheat
4	0.673	0.68	0.037	0.044	0.636	14		T=900C; 4 min preheat
5	0.578	0.58	0.044	0.046	0.534	15	**46**	T=900C; 4 min preheat
Edge cracking		0.578		Anneal 3 hours at 1400C in 50:50 H2/Ar (Met # 14-02-1)				
6	0.376	0.394	0.044	0.062	0.332	32	**62**	T=900C; 15 min. (**SPLIT**)
Split from edge		0.395		Anneal 3 hours at 1400C in 50:50 H2/Ar (Met # 14-02-2)				
7	0.269	0.276	0.06	0.067	0.209	30	**74**	T=900C; 4 min preheat
Edges casued sample to crack upon rolling.				Anneal 3 hours at 1400C in 50:50 H2/Ar (Met # 14-02-3)				
8	0.188	0.176	0.068	0.056	0.12	32		T=900C; 4 min preheat
9	0.12	**0.125**	0.056	0.06	0.064	32	**87**	T=900C; 4 min preheat(SPLIT)

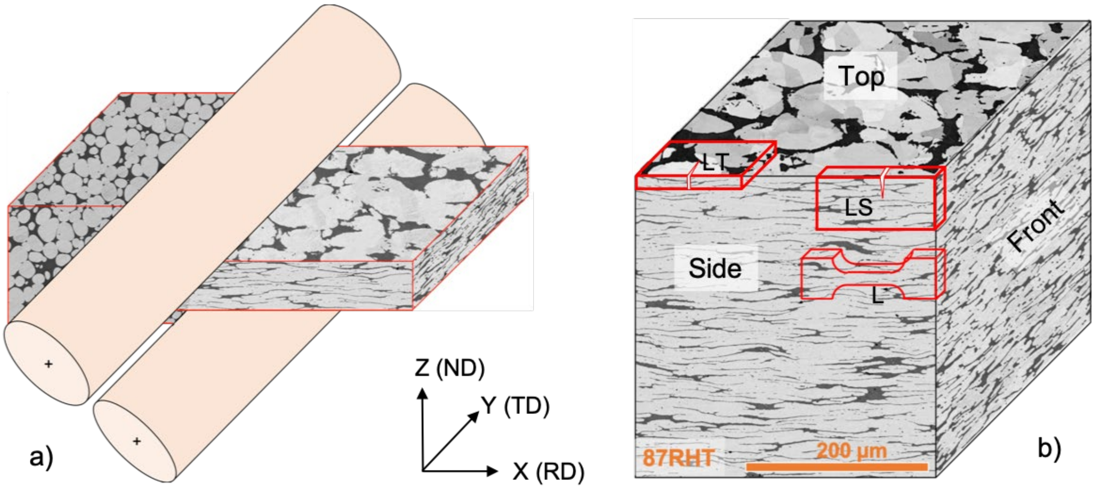

Figure 1. a) The 3D schematic illustration of the rolling process; and, b) a 3D representation of the hot-rolled 87RHT WHA microstructure. The three-point bend (3PB) bar LT, LS, and tensile in L orientations and definitions of various plane views are also shown.

The microstructures probed in this study include: a) the morphology of AS to 87RHT W powders in various states of HR deformation, which are referred to as particles in the WHA composite; b) the effect of HR deformation on the corresponding DP morphology; and, c) microstructural hardening features that develop in the W-particles and DP, such as twins, dislocations, grains, and grain boundary substructures.

Microstructural characterization involved pre- and post-deformation optical microscopy, SEM, energy dispersive x-ray spectroscopy (EDS), and EBSD on the various HR and annealed WHA conditions. The EBSD analyses were conducted using a JEOL 7600 SEM equipped with an Oxford Symmetry detector and operated at 20 kV. Low voltage and current (5 kV, 0.80 nA) SEM was used to characterize the W-particles, grains, and subgrains, as well as the DP area percent. Higher voltage and current (15 kV, 1.6 nA) were used to observe pre-and post-test specimen side and fracture surfaces. The SEM-EDS was used to measure the compositions of the W and DP.

Mechanical testing details were reported in [10] thus are only briefly summarized here. A LECO M-400A semi-automated hardness tester was used to measure Vickers microhardness (HV) at a 500 g_f load with 10-second dwell time [10,17]. A minimum of 10 indentations were made on top, side, front faces of polished bend bars (see Figure 1), both before and after the final anneal. At least three uniaxial tensile tests were carried out using sub-sized coupon dogbone specimens in the L orientation (see Figure 1b), with nominal gage section length/width/thickness dimensions of 5.0/1.0/0.7 mm. The tests were at a strain rate of 10^{-3}/s on an MTS 810 servo-hydraulic universal load frame, following the general ASTM E8M-15a Standard [18]. Fracture toughness tests were carried out on fatigue pre-cracked, single-edge notch bend (SENB) bar specimens with nominal dimensions of 25.4/4.0/1.75 mm, at a cross-head speed of 0.04 mm/min, generally following the ASTM E1921-20 Standard [19] to calculate both elastic (here, $K_{Ic} = K_{Im}$) and elastic-plastic (K_{Jm}) fracture toughness at the point of maximum load (P_m) in the load-displacement (P-d) curve.

Results

Mechanical Properties

The HV results are summarized in Table 2 and plotted in Figure 2a. In summary, the HV initially increases by ≈ 26% between the AS (≈ 321 kg_f/mm^2) and 62R/74R (≈ 405 kg_f/mm^2) conditions, then decreases at 87RHT to a value (333 ± 3 kg_f/mm^2) that is almost the same as for the AS WHA. No significant HV variation is observed in the various plate locations. Figure 2a and Table 2 show that annealing at 1300°C/24h softens all the plate locations to ≈ 346 ± 6 kg_f/mm^2 for the 62Ra/74Ra, which are also similar to the 87RHTa at 346 ± 6 kg_f/mm^2 and are ≈ 8% higher than the AS (321 ± 9 kg_f/mm^2) or ASa (319 ± 8 kg_f/mm^2).

Table 2. The RT Vickers microhardness (HV) for all the WHA conditions

Rolling and annealing conditions	HV on top, kg_f/mm^2	HV on front, kg_f/mm^2	HV on side, kg_f/mm^2	Average HV kg_f/mm^2
AS	321 ± 9			321 ± 9
ASa	319 ± 8			319 ± 8
62R	411 ± 15	397 ± 10	395 ± 9	401 ± 9
62Ra	339 ± 7	349 ± 13	350 ± 10	346 ± 6
74R	407 ± 10	419 ± 9	400 ± 14	409 ± 10
74Ra	339 ± 14	349 ± 13	351 ± 9	346 ± 6
87RHT	331 ± 9	336 ± 8	332 ± 7	333 ± 3
87RHTa	337 ± 12	352 ± 12	350 ± 11	346 ± 8

The RT tensile test data are shown in Figures 2b-d and summarized in Table 3. The 0.2% offset yield (σ_y) and ultimate (σ_u) stress trends are similar to those for HV. As expected, the uniform (ε_u) and total (ε_t) elongation vary inversely with strength. Annealing reduces the 62R and 74R σ_y and σ_u ≈ 15 to 24%. However, the ASa and 87RHTa WHA soften by only ≈ 5%. Note, the σ_y for 74Ra is ≈ 18% and 25% higher than the AS and ASa conditions (Table 3). The annealing 62R and 74R WHA doubles the ε_t from ≈ 7% to 15%, while the ASa and 87HTa ε_t is unaffected. However, compared to the AS WHA, the ε_t is lower in all the annealed HR conditions (Table 3 and Figure 2d).

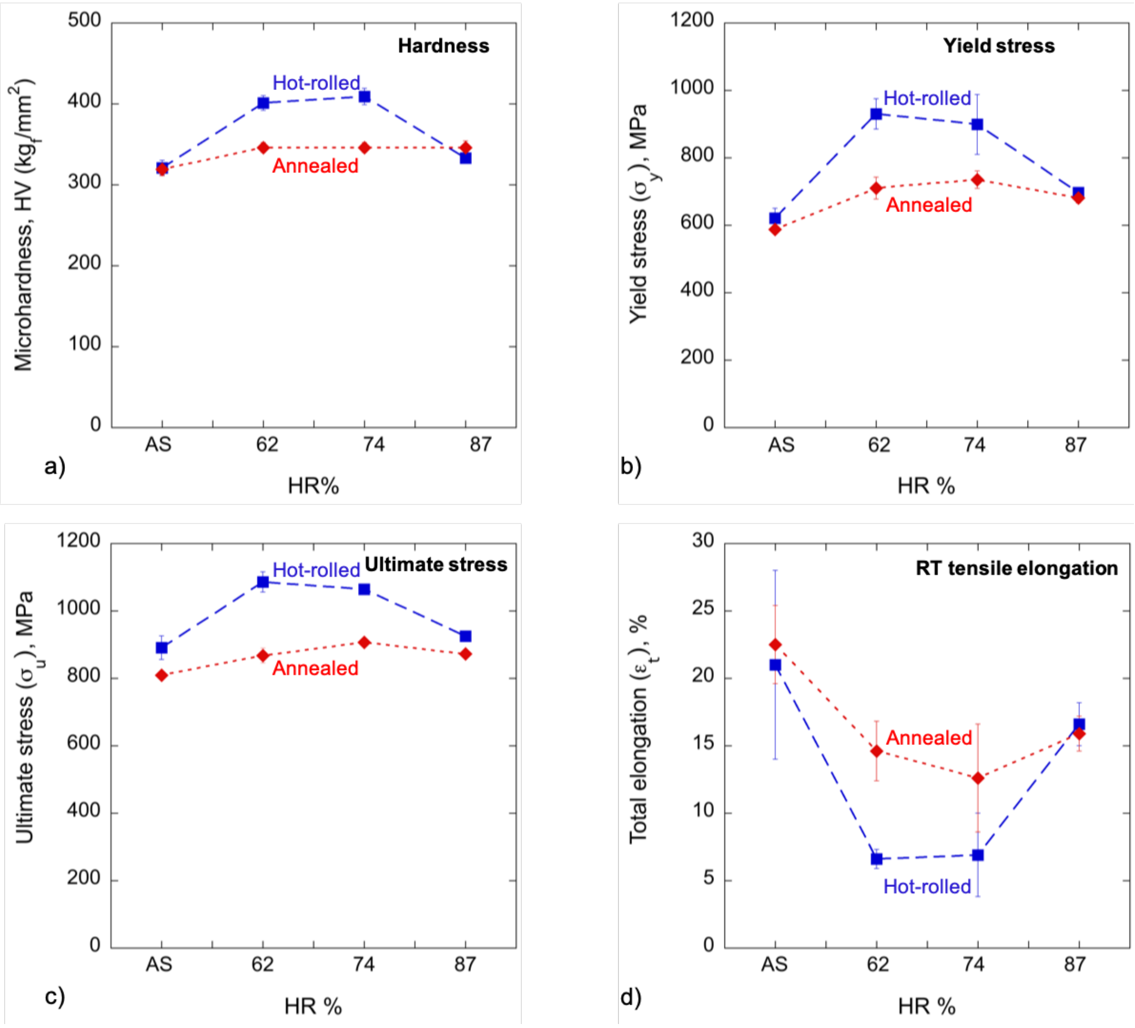

Figure 2. a) RT Vicker's microhardness (HV) for all plate views; b) RT 0.2% yield stress (σ_y); c) RT ultimate tensile stress (σ_u); and d) total elongations (ε_t) for all of the WHA conditions.

Normalized SENB fracture test load-displacement (P_n-d) curves are shown in Figure 3a-c. The maximum load elastic (K_{Im}) and elastic-plastic toughness (K_{Jm}) results are summarized in Table 4, and the K_{Jm} are plotted in Figure 3d. The load (P) is normalized to account for differences in the crack length (depth), as $P_n = 0.25P/(1-a/W)^2$ [6]. The AS and 87RHT tests show extensive crack blunting and stable crack growth, with a maximum load fracture toughness, K_{Jm} ≈ 97 ± 18 MPa√m for the AS condition, and 116 ± 20 MPa√m for the 87RHT WHA (Table 4 and Figure 3a, c) [6,10]. In contrast, the 62R/74R conditions experienced elastic, unstable crack propagation, with a much lower elastic fracture toughness of K_{Im} ≈ 35 ± 2 MPa√m (Table 4 and Figure 3b). Note, even these low K_{Ic} values are still ≈ 3 to 9 times higher than the typical fracture toughness of monolithic tungsten (K_{Ic} ≈ 8 ± 4 MPa√m) [10,20].

Table 3. The RT tensile properties of the HR [10] and annealed WHAs

Rolling and annealing conditions	σ_y, MPa	σ_u, MPa	ε_u, %	ε_t, %
AS	621 ± 29	891 ± 35	18 ± 4	21 ± 7
ASa	588 ± 12	809 ± 11	17.3 ± 1.0	22.5 ± 2.9
62R	930 ± 45	1086 ± 30	6.2 ± 0.7	6.6 ± 0.7
62Ra	710 ± 32	868 ± 22	11.7 ± 1.0	14.6 ± 2.2
74R	899 ± 89	1064 ± 8	6.6 ± 2.8	6.9 ± 3.1
74Ra	735 ± 26	907 ± 12	10.1 ± 1.7	12.6 ± 4.0
87RHT	697 ± 8	925 ± 6	12.3 ± 0.9	16.6 ± 1.6
87RHTa	681 ± 15	872 ± 12	12.8 ± 1.8	15.9 ± 1.3

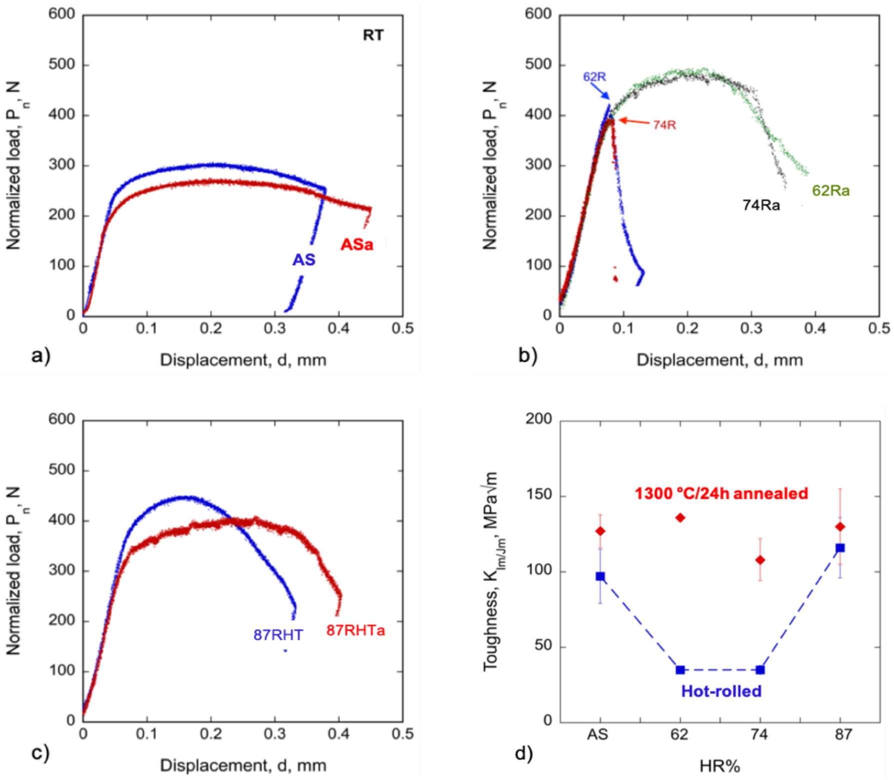

Figure 3. Representative RT normalized load-displacement (P_n -d) curves for: a) AS; b) 62R and 74R; and c) 87RHT; and d) their corresponding average K_{Jm} or K_{Im} before and after annealing.

Representative P_n-d stable crack curves for the HR and annealed 62Ra and 74Ra tests are shown in Figure 3b. The annealed condition tests were unloaded at a post-maximum loads (P_m) of ≈ 0.6-0.8P_m (Figures 3a-c). The K_{Jm} increased to a similar value in all the annealed WHA, averaging ≈ 125 ± 12 MPa√m (Figure 3d). The largest increase to ≈ 122 ± 20 MPa√m was in the 62Ra/74Ra WHA, from their HR condition value of K_{Im} ≈ 35 ± 2 MPa√m. Annealing has little effect on elastic K_{Im} (Table 4).

Table 4. The RT maximum load K_{Im} and K_{Jm} fracture toughness for all of the WHA conditions

Specimen orientation	Rolling and annealing conditions	K_{Im}, MPa√m	K_{Jm}, MPa√m	Fracture mode
LS/LT	AS	36 ± 4	97 ± 18*	Stable
	ASa	37 ± 0	127 ± 11	Stable
LS	62R	35 ± 2	35 ± 2*	Unstable
	62Ra	41 ± 2	136 ± 1	Stable
LS	74R	35 ± 3	35 ± 3*	Unstable
	74Ra	39 ± 3	108 ± 14	Stable
LS	87RHT	39 ± 2	116 ± 20*	Stable
	87RHTa	41 ± 0	130 ± 25	Stable

The RT microhardness and tensile stresses (both σ_y and σ_u) exhibit significantly higher values for the HR 62R and 74R compared to both the AS and HR 87RHT WHA. Conversely, fracture toughness and tensile elongation follow opposite trends. The 1300°C/24h annealing process results in minimal variations in mechanical properties (HV, σ_y, σ_u, ε_t, and K_{Jm}) across all four plate conditions. It is expected that the lower strength of annealed WHA leads to higher ductility and fracture toughness, as shown in Tables 2-4.

Microstructure

It is important to understand the microstructural basis for the strength-toughness variations for the HR conditions, as well as the reason why all of these properties are approximately independent of the HR thickness reduction after final 1300°C/24h annealing. Therefore, refined SEM and in-depth EBSD analysis were conducted in this study on all eight plate conditions. The SEM is primarily utilized to assess the morphology of W-particles, grains, and subgrain structures. On the other hand, EBSD is employed to examine aspects such as W-particles low angle grain boundary, DP grain and twin boundary, phase morphology, as well as kernel average misorientation (KAM).

SEM analysis

The EDS element maps and peak scans in both the HR and annealed conditions, confirm that, as expected, the bcc W-particles are ≈ 100% pure W, while the fcc DP contains ≈ 50Ni, 30W, and 20Fe (wt. %) [10]. Three-dimensional (3D) SEM micrographs of the polished and etched plates at various HR reductions have been reported in [10]. Although the morphology remains unaltered, it's worth noting that the statistics related to AS and HR W-particles have been obtained through a recent analysis conducted with optimized SEM settings. In summary, AS WHA contains roughly spherical pure W particles, with an average diameter of ≈ 17 ± 7 μm, surrounded by an interconnected honeycomb web of the NiWFe DP, (see Figures 1a, 4a, and Reference [10]). Larger thickness reductions lead to increasingly deformed and anisotropically oriented W-particles, still largely surrounded by the deformed DP (see Figures 4b-d and 3D views in Figures 1d-f in Reference [10]), consistent with similar studies [9,21,22]. The average W-particle deformations along rolling (X), transverse (Y), and thickness (Z) directions are respectively: ≈ 39/27/9 μm at 62R; 62/29/7 μm at 74R; and 82/30/6 μm at 87RHT, as shown in Table 5 and Figures 1 and 4. In the 87RHT condition, the W-particles (the bricks) are deformed into highly irregular, crenulated, wavy, and partly interconnected blades, separated by thin NiWFe DP layers (the mortar). Starting at 74R, and increasing significantly at 87RHT, HR also entraps some DP into the highly deformed W particles as shown in Figures 4f and 2g in Reference [10]. In 87RHT, the W particle aspect ratio (PAR) increases from 1.2 at AS to ≈ 3 in the plate face (X-Y) and ≈ 14 in the plate side (X-Z) view.

Newly acquired, backscattered electron (BSE) SEM images in Figure 4 reveal channeling contrast, indicative of grain structures in the W-particles (Figures 4b-d). The W-grains are defined as any featureless area inside the W-particle with a dimension larger than 5 μm, see Figure 5b. The average W grain size is 17 ± 7 μm, 14 ± 6 μm, and 16 ± 7 μm in the AS, 62R, and 74R conditions, respectively, but coarsens to 21 ± 10 μm at 87RHT, likely due to the final 1400°C/3h processing heat treatment (see Table 5 for top-view (X-Y) plane). The average X/Y W-grain aspect ratio (GAR) increases from 1.2 for the AS to ≈ 2.0 in the HR WHAs (Table 5). Figures 4b and c also show that the 62R/74R contain W-subgrain structures, defined as features in the W-particles smaller than 5μm. These, and corresponding higher magnification SEM images shown in Figures 5b and c, suggest that the subgrains are larger in the 74R compared to the 62R condition.

The formation of similar sub-grain structures in the W-particles was also observed in other cold/warm/hot-rolled/extruded 90W to 95W-NiFe WHAs [8,9,16,21–23]. For example, a transmission electron microscopy (TEM) study by Levin et al. [21] reported ≈ 270-470 nm of W subgrains in the 300°C cold-worked 90W-8Ni-2Fe WHA, while Yang et al. [9,16] found cellular sub-structures with lengths of about 500-600 nm and widths of 200-300 nm in a 1200°C hot-hydrostatically extruded (with 75% area reduction) 93W-4.9Ni-2.1Fe WHA.

It is important to point out that the final HR temperature in this study of 900°C (see Table 1) is barely a warm deformation temperature for W [14,15]. At 900°C, this is far lower than the recovery-recrystallization temperature of pure W of ≈ 1300°C to 1800°C [16,24]. Warm-rolling deformation increases the dislocation density, and initially long and straight screw dislocations tangle, eventually forming forest substructures and low-angle boundaries [9,23]. In contrast, W-particles in the 87RHT condition contain only coarser grains (>5 μm), and no subgrains are observed, due to the 1400°C/3h final processing HT, which leads to recovery-recrystallization [8,15]. Subgrain structures are not observed in the AS condition (Figures 4a and 5a).

Table 5 also summarizes the effects of 1300°C/24h anneal (indicated by ‘a’) on the W-particle morphology, in the AS and HR WHA. As shown in Figures 4a, d, e, h, and 5a, d, e, h, the 1300°C/24h anneal has little or no effect on the AS and 87RHT conditions. This is understandable since the AS condition was not deformed, and since 87RHT was already heat treated at 1400°C for 3h. In contrast, WHA particles and grains undergo significant coarsening after annealing in the 62R/74R WHA. W-particle coarsening is largest in the 62R (39/27/9 μm vs. 51/31/10 μm, Figures 4b, f). This phenomenon is attributed to the diffusion of W atoms from smaller to larger W-particles. Coarsening is enhanced by steep concentration gradients between small particles, especially those with small radius tips, adjacent to the larger particles, especially those with flatter facets. The W-grains in 62R/74R also coarsen after annealing, with average sizes increasing from 14 ± 6 μm to 20 ± 10 μm for 62R and from 16 ± 7 μm to 22 ± 10 μm for 74R (Table 5, and Figure 4). No W-subgrain structures are observed after annealing in the 62Ra/74Ra WHAs. Similar observations are reported in [9,15,21,25]. In summary, the most significant finding from the SEM characterization is that the observation of W-subgrain structures in 62R/74R (Figures 4b, c and 5b, c), which are almost entirely recovered after the 1300°C/24h anneal (Figures 4f,g and 5f,g).

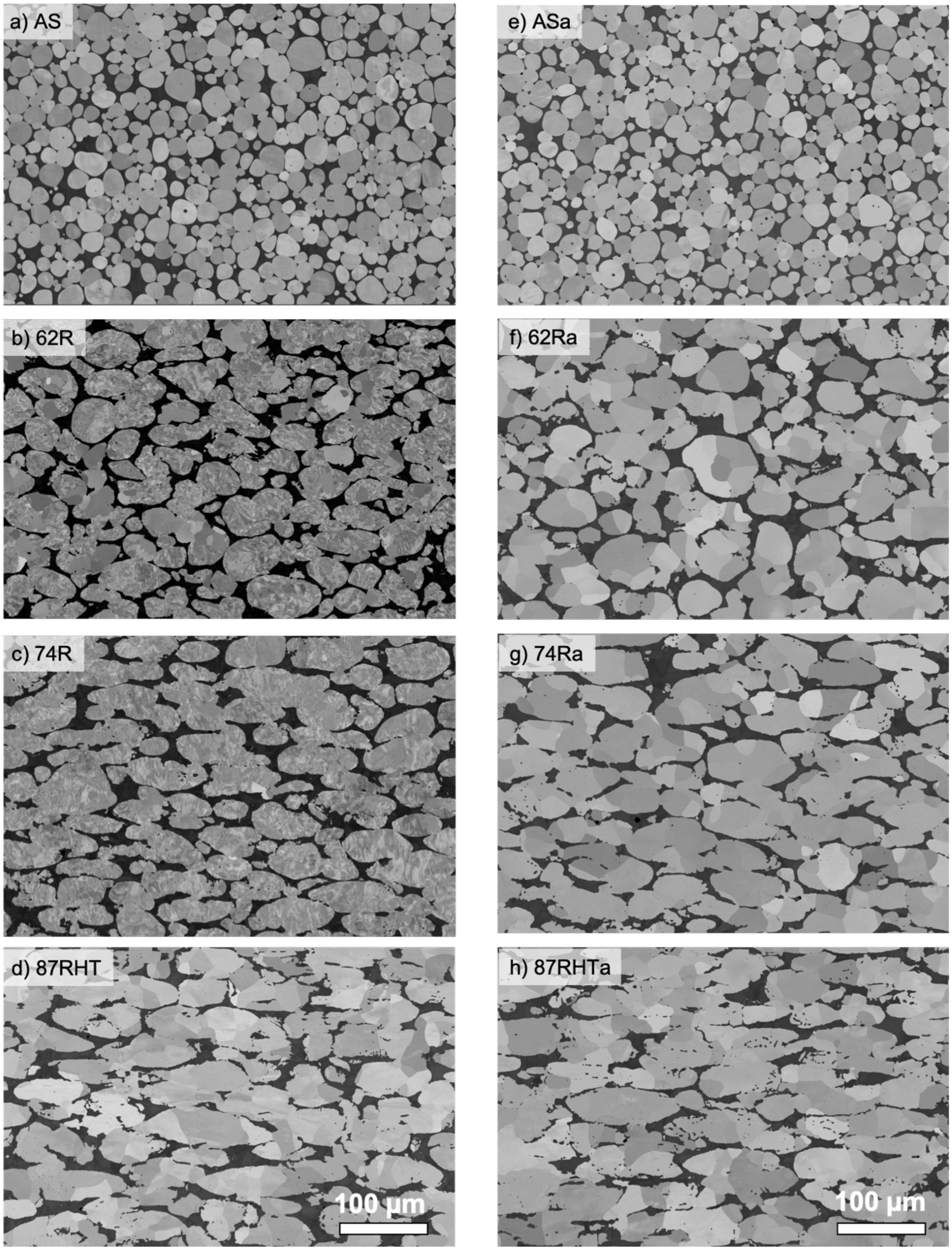

Figure 4. Top (X-Y) plate view SEM micrographs of the (a-d) HR and (e-h) annealed AS, 62R, 74R, and 87RHT WHA, respectively. The scale bar is 100 µm in all cases

Table 5. Tungsten particles, and grain morphology and DP area fraction (%) for all of the WHA conditions

Rolling and annealing conditions	W-particles			W-grains				DP (%)
	Length (X), (µm)	Width (Y), (µm)	Thickness (Z), µm	Length (X), (µm)	Width (Y), (µm)	Average, µm	GAR	
AS	16.5 ± 6.7			18.0 ± 7.2	15.1 ± 6.5	16.5 ± 6.7	1.2 ± 0.3	16.7 ± 3.6
ASa	17.0 ± 6.8			18.8 ± 7.3	15.3 ± 6.5	17.0 ± 6.8	1.3 ± 0.3	18.6 ± 0.8
62R	31 ± 19	27 ± 9	9 ± 3	17.4 ± 7.5	10.0 ± 4.9	14 ± 6	1.9 ± 0.7	17.8 ± 1.1
62Ra	51 ± 23	31 ± 8	10 ± 3	25.7 ± 12.6	14.7 ± 7.9	20 ± 10	1.9 ± 0.7	21.6 ± 0.3
74R	62 ± 23	29 ± 10	7 ± 2	19.5 ± 7.9	11.7 ± 5.3	16 ± 7	1.8 ± 0.5	19.9 ± 1.1
74Ra	68 ± 18	30 ± 9	8 ± 2	28.3 ± 12.9	16.2 ± 7.8	22 ± 10	1.9 ± 0.8	19.5 ± 0.7
87RHT	82 ± 28	30 ± 10	6 ± 2	28.0 ± 14.6	14.3 ± 7.4	21 ± 10	2.1 ± 0.7	21.1 ± 1.3
87RHTa	84 ± 31	31 ± 7	6 ± 2	29.2 ± 13.4	16.1 ± 6.6	23 ± 9	1.9 ± 0.7	18.9 ± 1.0

DP = ductile phase; GAR = grain aspect ratio; AS= as-sintered; ASa = AS that annealed at 1300°C/24h.

The basic structure of the DP does not change after annealing (see Table 5 and Figure 4 for the top-view scan). In the AS condition, grains are not visible in the DP, or are very large (>100 µm) and statistically are too few in number to consider. In contrast, refined DP grains are observed in all the HR, as well as in the HR and annealed WHAs. The grains are smaller in 62R (≈ 3.3 µm)/74R (3.7 µm), and slightly coarser in 87RHT (≈ 4.3 µm). The DP grains are similar (≈ 4.6 µm) before and after annealing in all the HR WHAs. The DP annealing twins are observed in all the HR WHAs and increase with increasing rolling reductions and after annealing. Further details of the DP grain morphology and twinning are discussed in the EBSD analysis part.

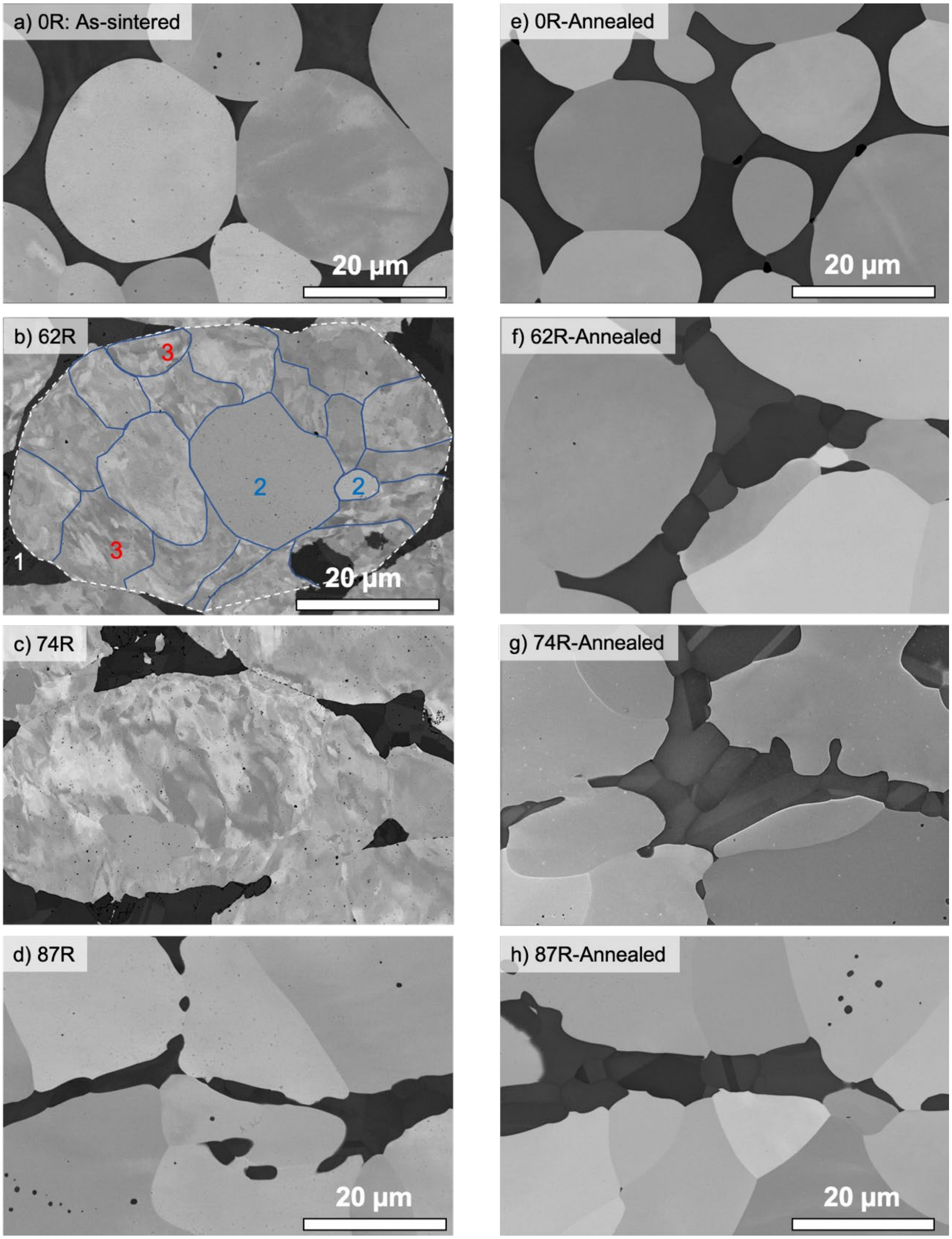

Figure 5. Higher magnification SEM micrographs of the (a-d) hot-rolled, and (e-h) annealed 0R, 62R, 74R, and 87R WHA, respectively. Figure b defines the W-particles (1: the white and larger broken boundary), grains (2: featureless area at the solid and blue boundaries), and subgrains (3: smaller features inside the solid-blue boundaries). Note, only the top-view images are shown here. The scale bar is 20 μm for all cases.

EBSD analysis

The EBSD was used to characterize all of the eight WHA conditions to gain further understanding on the microstructural and mechanical property changes. Figure 6 shows the inverse pole figure (IPF) maps for the HR WHA in the left column (Figure 6a-d) before, and after annealing in the right column (Figures 6e-h). Figure 7 shows an enhanced view of the DP. The DP in the HR condition does not show a mottled intragranular contrast, as is observed in the W particles. All the IPF maps shown in Figures 6 and 7 are the Y component of the side view scan (X-Z plane) in Figure 1. This corresponds to indexing the maps in the Normal Direction (ND) for all rolled plates. All components (IPF X, Y, and Z) for each scan are shown in Figure 8. The focus here is on grain and twin boundaries, phase morphologies, and kernel average misorientation (KAM) distributions. Texture development is not considered.

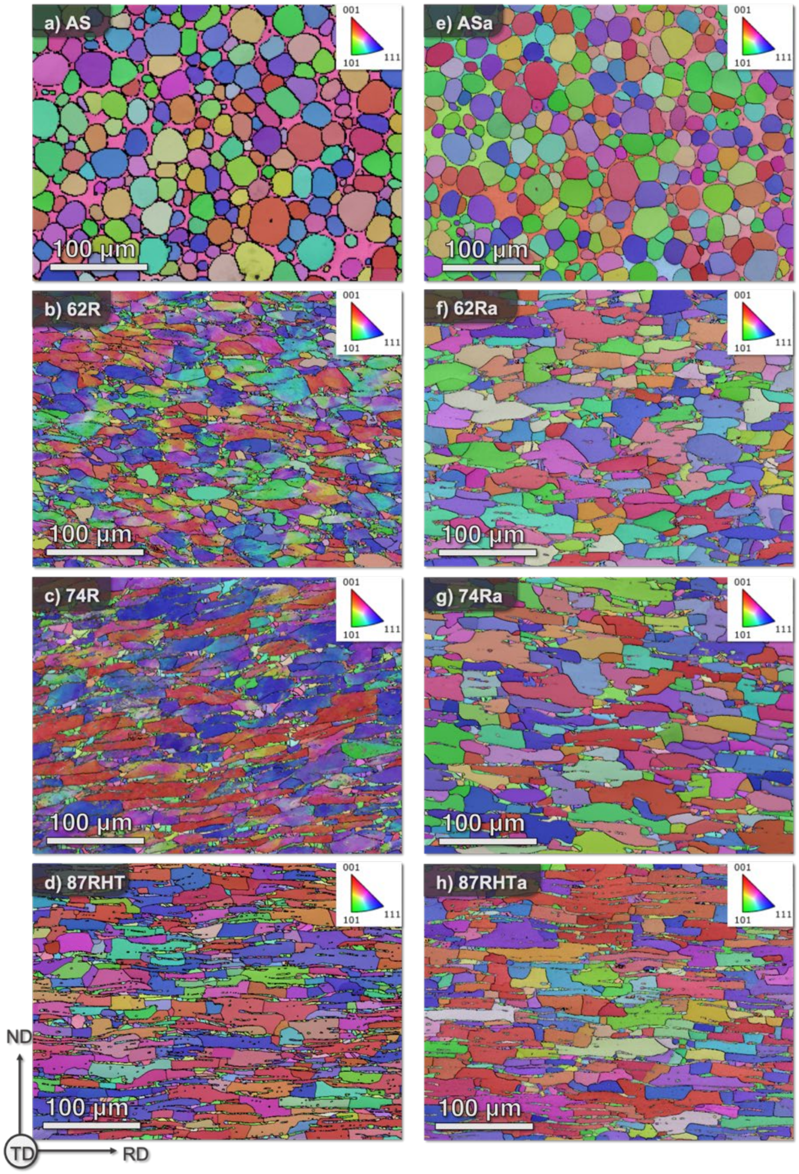

Figure 6. The EBSD IPF maps of the grain structure in the AS and HR conditions before (a-d) and after (e-h) annealing. The IPF Y index IPF maps are in the ND for the HR plates.

A 10° cut-off misorientation angle was used to identify the W and DP grain boundaries. The EBSD IPF maps in Figure 6 for the HR WHA show that the initially roughly spheroidal AS W-particles are increasingly deformed into pancake shapes, with increasing length and width and decreasing thickness (Figure 4 and Table 5). The EBSD images in Figure 7 show that the AS W-particles are surrounded by a nearly continuous boundary-free DP before (Figure 7a) and after (Figure 7e) annealing. The side-view scan shows HR divides the DP grains into rectangular shapes, mainly by inducing twin formation, as shown in Figures 7b, c, d. For 62R and 74R, the major (M) and minor (m) axes are 4.6/2.1 µm and 4.9/2.5 µm, respectively, shown in Table 6. As in the W-grains, the DP regions divided by twins are also larger in the 87RHT condition at 6.7/1.9 µm in the side-view (Figure 7d, and Table 6). Note, the grain aspect ratio also increases with increasing HR, mainly due to the reduction of thickness of DP. The 1300°C/24h anneal increases the average twinned region size of 62R and 74R to dimensions close to 87RHT and 87RHTa, with an average dimension of 6.8/2.4 µm (Table 6). Thus, a larger Hall-Petch contribution likely contributes to the higher strength in the 62R and 74R conditions.

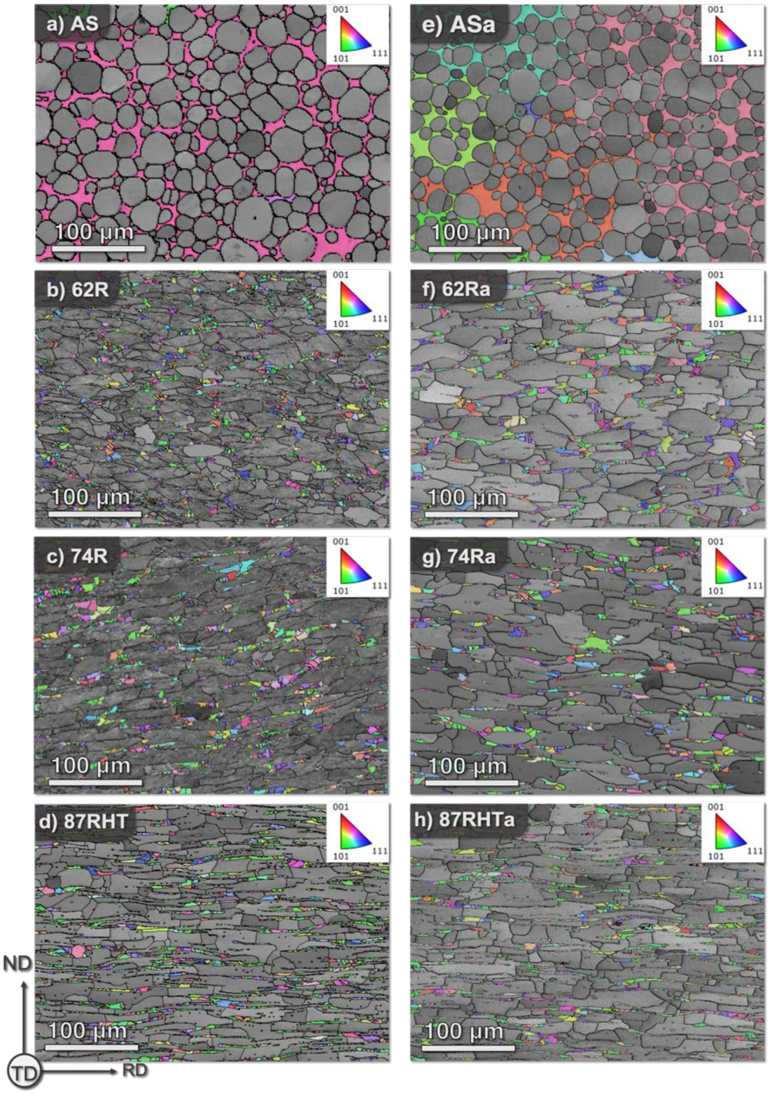

Figure 7. The IPF maps of the isolated DP grain structure, highlighting the grain refinement in the AS and HR conditions both before (a-d) and after (e-h) annealing. The Y-indexed IPF is in the ND orientation for the HR plates.

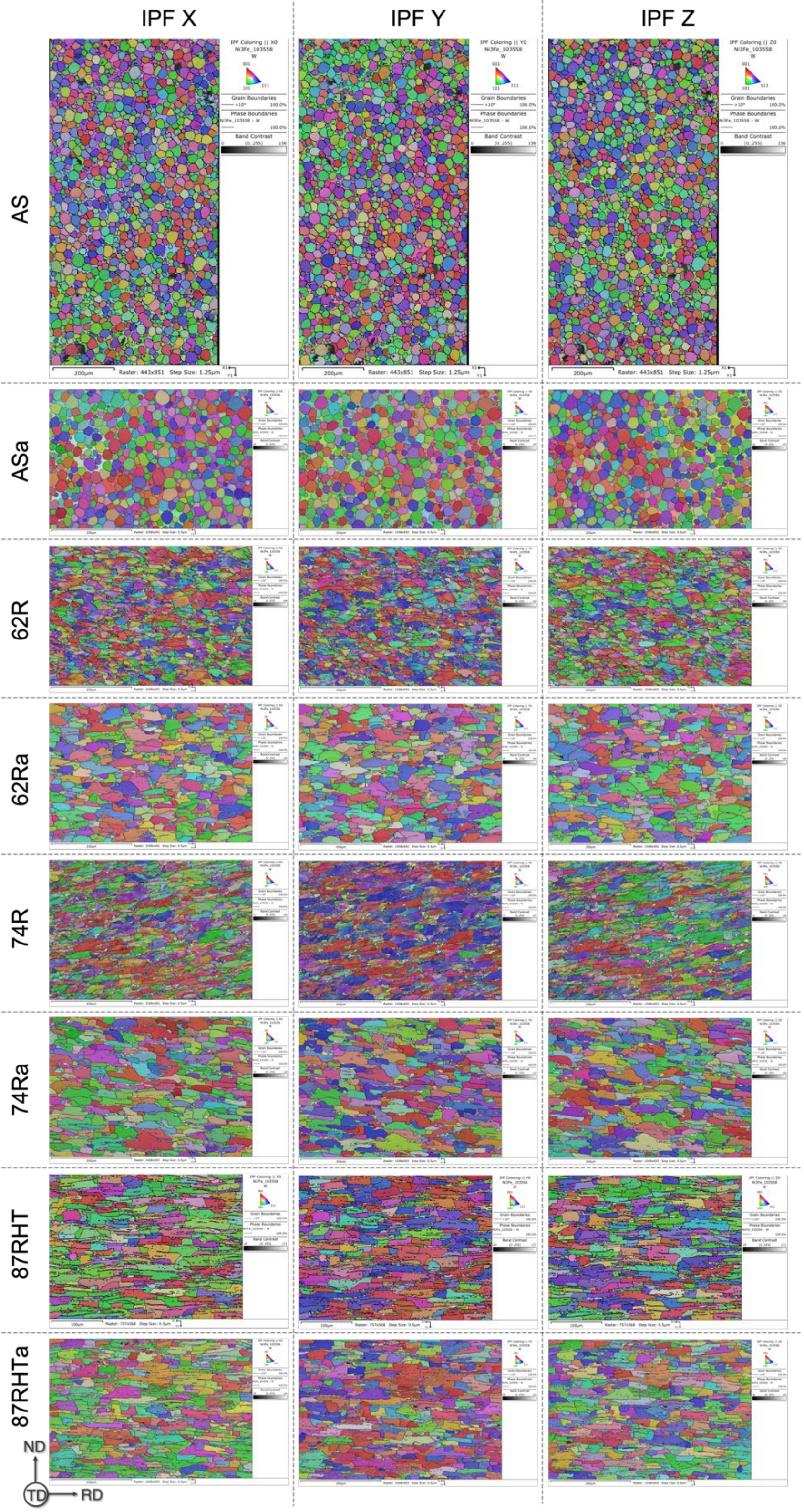

Figure 8. The EBSD IPF maps of the grain structure in the as-sintered and hot-rolled samples.

Table 6. Ductile phase grain morphology for all of the WHA conditions for side-surface (X-Z) view

Annealing Condition	Major, M, μm	Minor, m, μm	Average size = (M+m)/2, μm	GAR= M/m
62R	4.6 ± 2.1	2.1 ± 0.9	3.3 ± 1.3	2.5 ± 1.2
62Ra	6.6 ± 3.5	2.7 ± 1.2	4.6 ± 2.2	2.6 ± 1.2
74R	4.9 ± 2.3	2.5 ± 1.1	3.7 ± 1.5	2.2 ± 0.9
74Ra	6.7 ± 3.6	2.3 ± 1.2	4.5 ± 2.1	3.2 ± 1.7
87RHT	6.7 ± 4.2	1.9 ± 1.1	4.3± 2.4	3.8 ± 2.4
87RHTa	7.2 ± 3.9	2.1 ± 1.1	4.7 ± 2.2	3.9 ± 2.2

As seen in Figures 7 and 9, Σ3 annealing twins are the dominant DP boundary in the HR and annealed conditions. Higher magnification images of the twins in 87RHT are shown in Figure 9. The DP Σ3 grain boundary fractions, which are summarized in Table 7, are defined as the combined length of Σ3 boundaries, divided by the total boundary length. The twinning fraction increases with HR and all cases are greater than 60%. Note, nickel-based alloys are well known to develop Σ3 annealing twin boundaries after deformation [26–28]. Annealing increases the DP twinning (Table 7, Figure 7). Since they are not removed by annealing, it is not surprising that twinning increases significantly between the 62R/74R and 87RHT conditions.

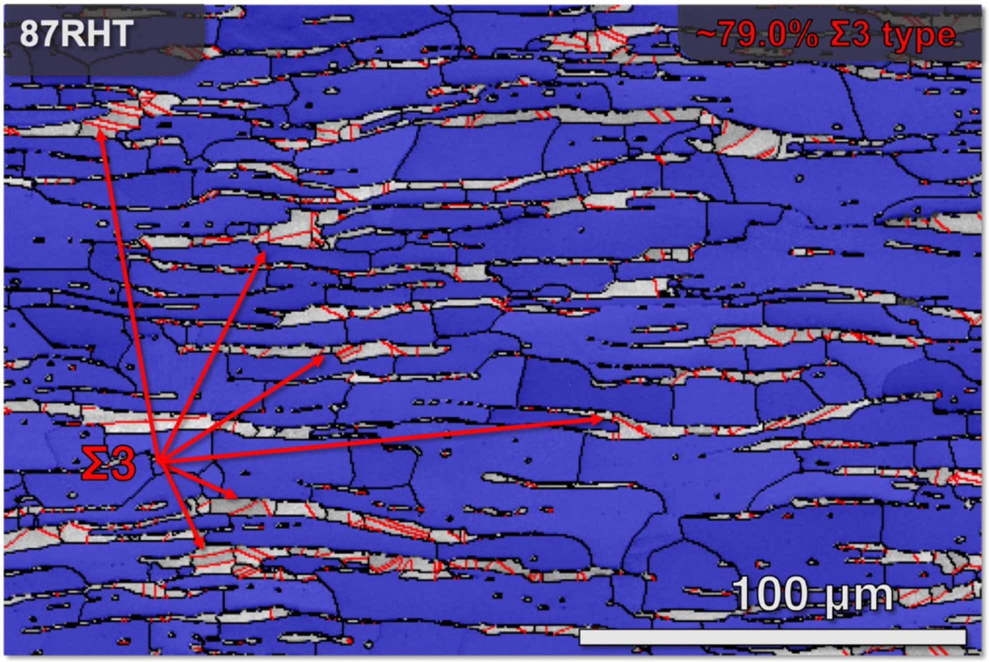

Figure 9. The EBSD micrograph of the 87RHT condition highlighting (in red) all Σ3-type twin boundaries in the DP (in grey). In this case, approximately 80% of the DP grain boundaries are Σ3. The W-particles are shown in blue.

Table 7. The fraction (%) of DP Σ3 grain boundaries for all of the WHA conditions

Rolling reduction (%)	HR (%)	AN (%)
AS	-	-
62R	62.1	87.5
74R	71.6	76.4
87RHT	79.0	92.0

As shown in Figure 10, the grain boundary misorientation distributions in the W-particles are similar for the AS and 87RHT conditions but differ in 62R and 74R WHA. The distributions, common to AS and 87RHT, and all the annealed conditions, increase between ≈ 0° and 45°, then decrease close to 0% fraction at angles greater than ≈ 60°. This is referred to as a Mackenzian, hyper-spherical harmonic expansion distribution [29]. In contrast, 62R and 74R exhibit a high frequency of low-angle grain boundaries (LAGB, <10°). The LAGBs impede dislocation glide, leading to an increase in strength. However, the grain boundary misorientation distributions in the DP are nearly identical (not shown here) in all the truly HR and annealed conditions.

The KAM maps measure the average misorientations of each point in a crystal with respect to its neighbors, reflecting the presence of geometrically necessary dislocations (GND) and residual stresses [30–33]. The KAM maps for the WHA conditions are shown in Figure 11. As expected, the KAM intensity profile for the AS WHA lies near 0°, indicating low residual stresses and GND densities (Figure 11a). In contrast, 62R and 74R W-particles, in Figures 11b-c, show a high density of low-angle (< 5°) misorientations, which were notably absent in the 87RHT and all of the 1300°C annealed (Figures 11d-h) conditions. These KAM maps are consistent with the misorientation angle distributions in Figure 10, and support the conclusion that the recovery occurs in all the HR and annealed conditions, consistent with the results reported in [14,25].

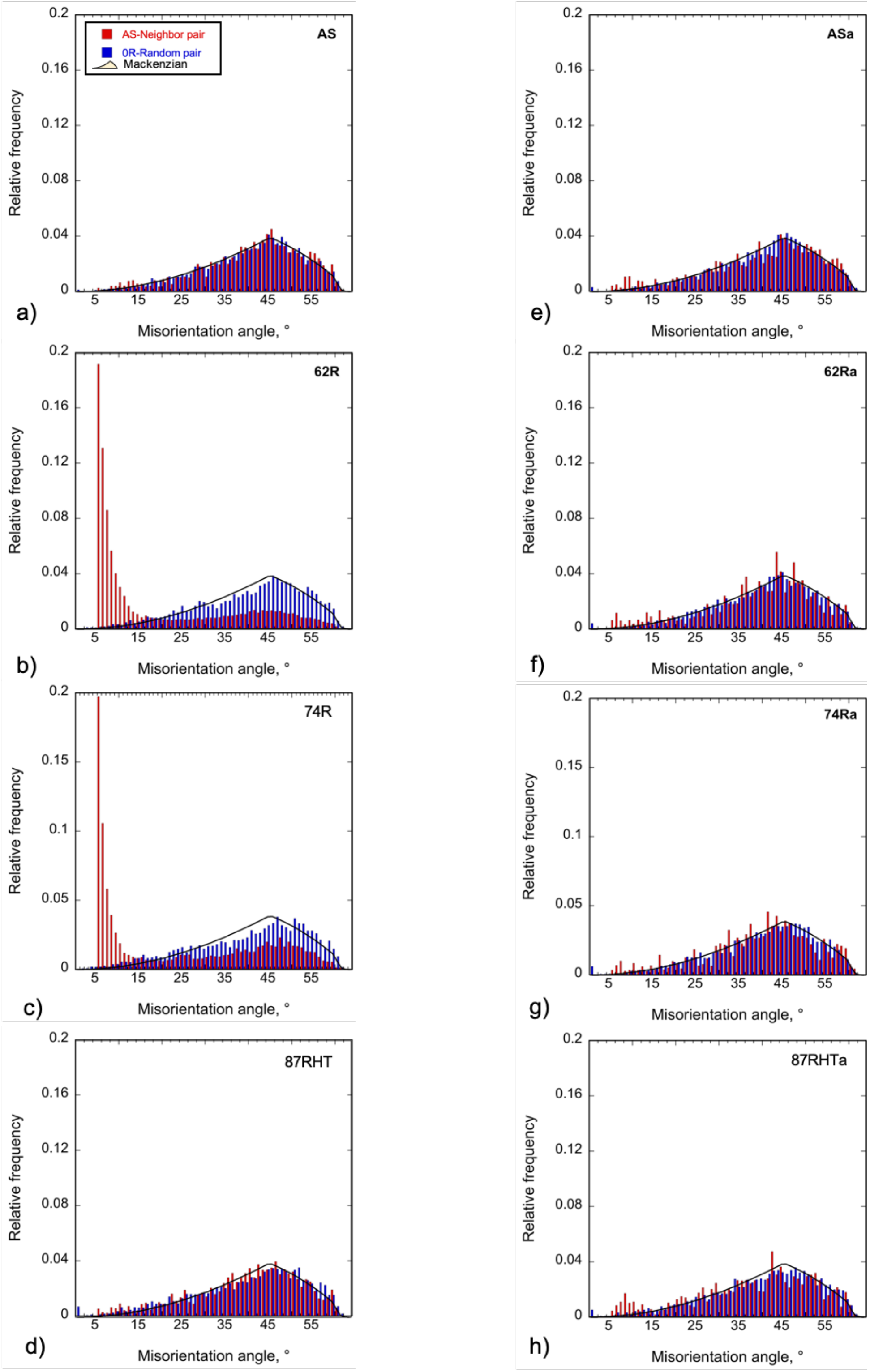

Figure 10. Misorientation angle distributions in the W-phase for AS and HR W-particles before (a-d) and after (e-h) annealing. Here, the scan is normal to the plate side.

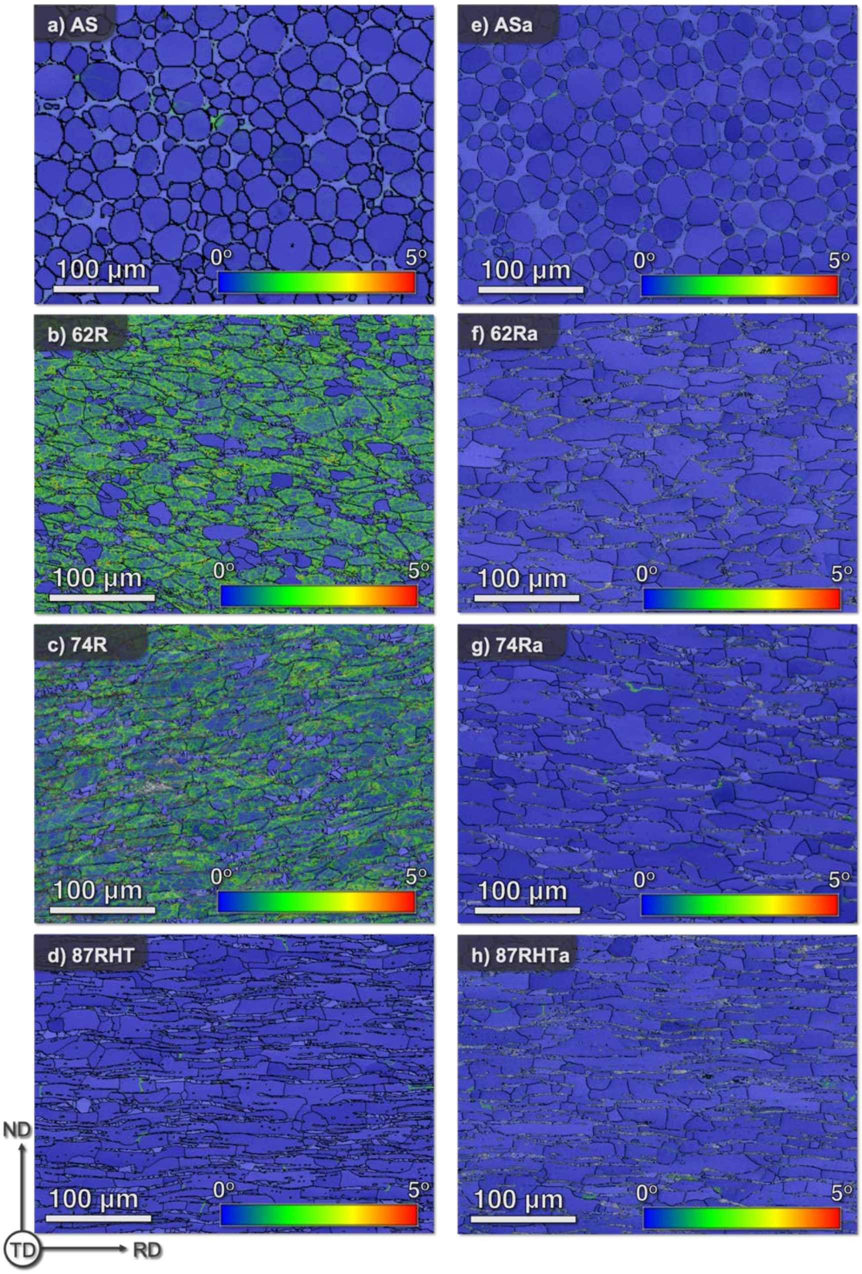

Figure 11. Kernel average misorientation maps for the AS and HR conditions before (a-d) and after (e-h) annealing. The color bar indexes the intragranular misorientation in degrees.

In summary, EBSD was utilized to qualitatively explore the relation between microstructure and mechanical properties in the various WHA conditions. The 62R and 74R conditions were found to have a high degree of misorientation, high density of LAGB in W domains. These observations are consistent with the SEM analysis and responsible for the higher strength in 62R and 74R compared to the AS and 87RHT WHAs.

Future Work

Table 8 attempts to summarize the large number of observations reported here to establish the processing-microstructure-property relations for all the conditions in this study. Annealing improves the LS orientation fracture toughness of all four WHA HR conditions, especially for the 62R/74R WHA, leading to a similar average K_{Jm} ≈ 125 ± 12 MPa√m. The improved WHA fracture toughness (and tensile ductility) after annealing is associated with reduced strength. The reduced strength in the initially stronger and more brittle 62R and 74R HR conditions is, in turn, due to the recovery of high GND densities and subgrain structures, as well as coarsening of internal W-particle grain sizes, DP grain sizes, and possibly lower residual stresses.

Table 8. The summary of processing-microstructure-property relationship for all the WHA conditions

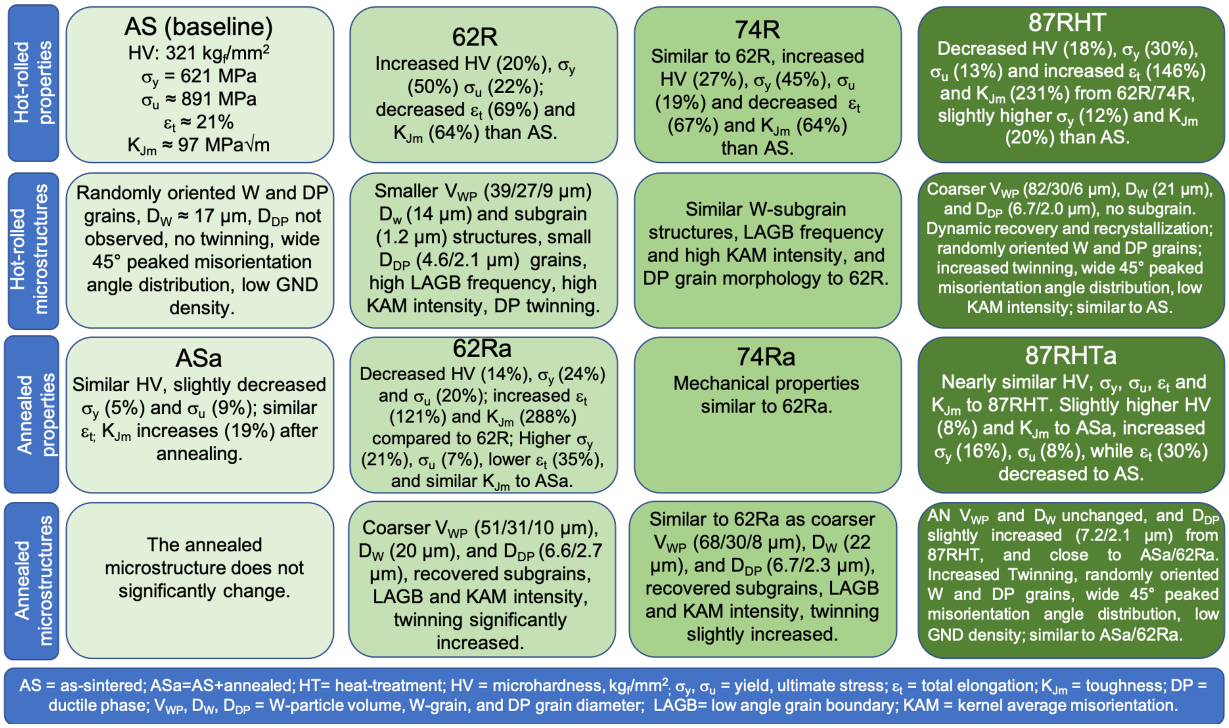

Hot-rolled properties	AS (baseline) HV: 321 kg_f/mm^2 σ_y = 621 MPa σ_u ≈ 891 MPa ε_t ≈ 21% K_{Jm} ≈ 97 MPa√m	62R Increased HV (20%), σ_y (50%) σ_u (22%); decreased ε_t (69%) and K_{Jm} (64%) than AS.	74R Similar to 62R, increased HV (27%), σ_y (45%), σ_u (19%) and decreased ε_t (67%) and K_{Jm} (64%) than AS.	87RHT Decreased HV (18%), σ_y (30%), σ_u (13%) and increased ε_t (146%) and K_{Jm} (231%) from 62R/74R, slightly higher σ_y (12%) and K_{Jm} (20%) than AS.
Hot-rolled microstructures	Randomly oriented W and DP grains, D_W ≈ 17 μm, D_{DP} not observed, no twinning, wide 45° peaked misorientation angle distribution, low GND density.	Smaller V_{WP} (39/27/9 μm) D_w (14 μm) and subgrain (1.2 μm) structures, small D_{DP} (4.6/2.1 μm) grains, high LAGB frequency, high KAM intensity, DP twinning.	Similar W-subgrain structures, LAGB frequency and high KAM intensity, and DP grain morphology to 62R.	Coarser V_{WP} (82/30/6 μm), D_W (21 μm), and D_{DP} (6.7/2.0 μm), no subgrain. Dynamic recovery and recrystallization; randomly oriented W and DP grains; increased twinning, wide 45° peaked misorientation angle distribution, low KAM intensity; similar to AS.
Annealed properties	ASa Similar HV, slightly decreased σ_y (5%) and σ_u (9%); similar ε_t; K_{Jm} increases (19%) after annealing.	62Ra Decreased HV (14%), σ_y (24%) and σ_u (20%); increased ε_t (121%) and K_{Jm} (288%) compared to 62R; Higher σ_y (21%), σ_u (7%), lower ε_t (35%), and similar K_{Jm} to ASa.	74Ra Mechanical properties similar to 62Ra.	87RHTa Nearly similar HV, σ_y, σ_u, ε_t and K_{Jm} to 87RHT. Slightly higher HV (8%) and K_{Jm} to ASa, increased σ_y (16%), σ_u (8%), while ε_t (30%) decreased to AS.
Annealed microstructures	The annealed microstructure does not significantly change.	Coarser V_{WP} (51/31/10 μm), D_W (20 μm), and D_{DP} (6.6/2.7 μm), recovered subgrains, LAGB and KAM intensity, twinning significantly increased.	Similar to 62Ra as coarser V_{WP} (68/30/8 μm), D_W (22 μm), and D_{DP} (6.7/2.3 μm), recovered subgrains, LAGB and KAM intensity, twinning slightly increased.	AN V_{WP} and D_W unchanged, and D_{DP} slightly increased (7.2/2.1 μm) from 87RHT, and close to ASa/62Ra. Increased Twinning, randomly oriented W and DP grains, wide 45° peaked misorientation angle distribution, low GND density; similar to ASa/62Ra.

AS = as-sintered; ASa=AS+annealed; HT= heat-treatment; HV = microhardness, kg_f/mm^2; σ_y, σ_u = yield, ultimate stress; ε_t = total elongation; K_{Jm} = toughness; DP = ductile phase; V_{WP}, D_W, D_{DP} = W-particle volume, W-grain, and DP grain diameter; LAGB= low angle grain boundary; KAM = kernel average misorientation.

The results reported here further demonstrate that high WHA toughness requires the formation of a large population of widely distributed arrested and blunted crack tip plastic zone microcracks. Microcrack shielding reduces both the elastic modulus and stress concentrations, in the crack tip region [34]. Further, DP plastic deformation at arrested W-particle cleavage microcracks, dissipates additional energy, increasing the critical J-integral for initiation of crack growth. These contributions lead to K_{Jm} values of about 100 MPa√m, or more. Microcracking also leads to stable crack growth and strong resistance curve behavior [6]. In the absence of extensive microcracking, WHA experiences elastic fracture at much lower K_{Im} = 35 ± 2 MPa√m. However, even absent extensive microcracking, crack tip plasticity still increases WHA toughness relative to monolithic W.

Thus, a key question is what controls microcracking. Clearly, it is related to the strength of the composite and the composite constituents. That is, there is a classical tradeoff between higher strength and lower toughness. This is shown in Fig. 12 where all of the HR and annealed $K_{J/Im}$ are plotted against the corresponding WHA flow stress (σ_{fl}), taken as $\sigma_{fl} = (\sigma_y + \sigma_u)/2$. The $K_{J/Im}$ systematically decreases with σ_{fl} at a rate of 0.45 MPa√m/MPa. While the micromechanics is undoubtedly complex, qualitatively higher strength enables planar macrocracks and microcracks to link before more widely distributed plastic zone microcracking occurs.

Notably, the AS WHA $K_{J/Im}$ also decreases with σ_{fl} at an approximately similar rate, however, there are only two paired data points in this case. The addition of AS and annealed (unrolled) 92.5W and 95W WHA to the AS 90W follows a similar trend [35]. The extrapolated HR K_{Jm} are about 45 MPa√m higher than the AS WHA, which may reflect a modest benefit of the HR composite brick-and-mortar type architecture in the LS orientation. Figure 12 also shows the effect of increasing σ_{fl}, on the AS 90W WHA $K_{J/Im}$, associated with tests at lower temperatures [6]. However, in this case, $K_{J/Im}$ decreases with σ_{fl} at a lower rate of ~ 0.11 MPa√m/MPa. This difference may be due to damage and residual stresses introduced by HR.

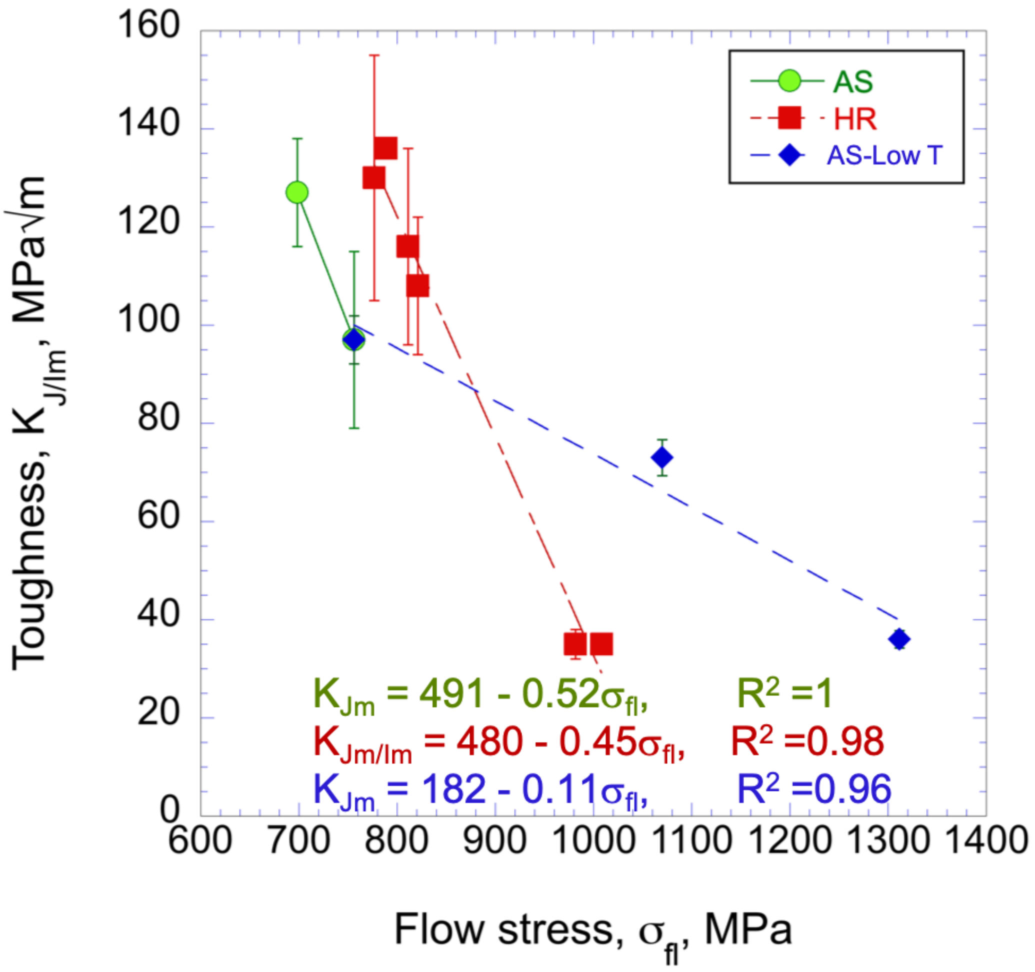

Figure 12. Flow stress versus the LS RT fracture toughness for the various WHA conditions. The green circles are for the AS condition, while the red squares are for the various HR conditions. The blue diamonds are for AS condition tests at and below RT.

The results in Figure 12 should be viewed as qualitative trends. However, even the qualitative insights obtained from this study will be useful in informing detailed micromechanical modeling of deformation and fracture of WHA. They also offer a partial framework for designing improved WHA. For example, the results presented here suggest that DP alloys that have lower yield stresses accompanied by high strain hardening rates, as is the case for the NiWFe DP used in this case [36,37], would contribute to higher toughness, without greatly compromising strength. However, detailed finite element (or even crystal plasticity) micromechanical deformation and fracture models are urgently needed, not only for better performance predictions but also to reduce the amount of experimental data required to develop and apply WHA for challenging fusion applications.

Acknowledgments

We acknowledge the support provided by the U.S. Department of Energy (DOE) through the Office of Fusion Energy Sciences under contract to UCSB DOE-Fusion (DE-FG02-94ER54275) and PNNL (DE-AC05-76RL0-1830, AT2030110-13784). The U.S. National Science Foundation supported the California Nanoscience Institute (CNSI) and provided the microscopic facilities critical for the success of this research.

References

[1] P. Norajitra, R. Giniyatulin, W. Krauss, V. Kuznetsov, I. Mazul, I. Ovchinnikov, J. Reiser, M. Rieth, V. Widak, Current status of He-cooled divertor development for DEMO, Fusion Eng. Des. 84 (2009) 1429–1433.

[2] E. Gaganidze, A. Chauhan, H.C. Schneider, D. Terentyev, G. Borghmans, J. Aktaa, Fracture-mechanical properties of neutron irradiated ITER specification tungsten, J. Nucl. Mater. 547 (2021) 152761.

[3] C. Henager Jr, W. Setyawan, T. Roosendaal, N. Overman, B. Borlaug, E. Stevens, K. Wagner, R. Kurtz, G.R. Odette, B. Nguyen, K. Cunningham, Ductile-phase toughened tungsten for plasma-facing materials in fusion reactors, Int. J. Powder Metall. 53 (2017) 53–69.

[4] J. Reiser, J. Hoffmann, U. Jäntsch, M. Klimenkov, S. Bonk, C. Bonnekoh, M. Rieth, A. Hoffmann, T. Mrotzek, Ductilisation of tungsten (W): On the shift of the brittle-to-ductile transition (BDT) to lower temperatures through cold rolling, Int. J. Refract. Met. Hard Mater. 54 (2016) 351–369.

[5] B. Gludovatz, S. Wurster, A. Hoffmann, R. Pippan, Fracture toughness of polycrystalline tungsten alloys, Int. J. Refract. Met. Hard Mater. 28 (2010) 674–678.

[6] M.E. Alam, G.R. Odette, On the remarkable fracture toughness of 90 to 97W-NiFe alloys revealing powerful new ductile phase toughening mechanisms, Acta Mater. 186 (2020) 324–340.

[7] M.E. Alam, G.R. Odette, On the Influence of Specimen Size and Geometry on the Fracture Toughness of Tungsten Heavy Metal Alloys, J. Nucl. Mater. 571 (2022) 154025.

[8] X. Gong, J.L. Fan, F. Ding, M. Song, B.Y. Huang, Effect of tungsten content on microstructure and quasi-static tensile fracture characteristics of rapidly hot-extruded W-Ni-Fe alloys, Int. J. Refract. Met. Hard Mater. 30 (2012) 71–77.

[9] Y. Yu, H. Hu, W. Zhang, X. Xu, Microstructure evolution and recrystallization after annealing of tungsten heavy alloy subjected to severe plastic deformation, J. Alloys Compd. 685 (2016) 971–977.

[10] M.E. Alam, J. Wang, C.H. Henager, W. Setyawan, G.R. Odette, The effect of hot rolling on the strength and fracture toughness of 90W–7Ni3Fe tungsten heavy metal alloys, Mater. Sci. Eng. A. 824 (2021) 141738.

[11] R. Bollina, R.M. German, Heating rate effects on microstructural properties of liquid phase sintered tungsten heavy alloys, Int. J. Refract. Met. Hard Mater. 22 (2004) 117–127.

[12] A. Pathak, A. Panchal, T.K. Nandy, A.K. Singh, Ternary W-Ni-Fe tungsten heavy alloys: A first principles and experimental investigations, Int. J. Refract. Met. Hard Mater. 75 (2018) 43–49.

[13] J.R. Davis, Properties and Selection: Nonferrous Alloys and Special-Purpose Materials, 10th ed., Vol 2. ASM Handbook, ASM, Metal Park, Ohio, 1993.

[14] Y. Li, Z. Du, J. Fan, Y. Lv, Y. Lv, L. Ye, P. Li, Microstructure and texture evolution in warm-rolled fine-grained tungsten, Int. J. Refract. Met. Hard Mater. 101 (2021) 105690.

[15] A. Alfonso, D. Juul Jensen, G.N. Luo, W. Pantleon, Thermal stability of a highly-deformed warm-rolled tungsten plate in the temperature range 1100-1250 °C, Fusion Eng. Des. 98–99 (2015) 1924–1928.

[16] Y. Yang, H. Lianxi, W. Erde, Microstructure and mechanical properties of a hot-hydrostatically extruded 93W-4.9Ni-2.1Fe alloy, Mater. Sci. Eng. A. 435–436 (2006) 620–624.

[17] M.E. Alam, G.R. Odette, The comparative strength and fracture toughness properties of commercial 95W-3.5Ni1.5Fe and 95W-3.5Ni1.5Cu tungsten heavy alloys, Nucl. Mater. Energy. 36 (2023) 101467.

[18] ASTM E8M-15a, ASTM E8/E8M - 15a: Standard test methods for tension testing of metallic materials, in: Annu. B. ASTM Stand., ASTM International, 100 Barr Harbor Drive, PO Box C700, West Conshohocken, PA 19428-2959, United States, 2015.

[19] ASTM E1921-20, Standard Test Method for Determination of Reference Temperature , To , for Ferritic Steels in the Transition Range, in: Annu. B. ASTM Stand., ASTM International, 100 Barr Harbor Drive, PO Box C700, West Conshohocken, PA 19428-2959, United States, 2020: pp. 1–25.

[20] G.R. Odette, E. Stergar, D. Gragg, K. Fields, J. Heathcote, C.H. Henager, R. J. Kurt, W-Alloy and Composite Fracture test Method Development and Initial Exploration of Ductile Phase Toughening, Usion React. Mater. Progr. Semiannu. Prog. Rep. DOE0313/52 (2012) 89–102.

[21] Z.S. Levin, K. Ted Hartwig, Hardness and microstructure of tungsten heavy alloy subjected to severe plastic deformation and post-processing heat treatment, Mater. Sci. Eng. A. 635 (2015) 94–101.

[22] Z.H. Zhang, F.C. Wang, S.K. Li, L. Wang, Deformation characteristics of the 93W-4.9Ni-2.1Fe tungsten heavy alloy deformed by hydrostatic extrusion, Mater. Sci. Eng. A. 435–436 (2006) 632–637.

[23] Z. Zhaohui, W. Fuchi, Research on the deformation strengthening mechanism of a tungsten heavy alloy by hydrostatic extrusion, Int. J. Refract. Met. Hard Mater. 19 (2001) 177–182.

[24] B.C. Allen, D.J. Maykuth, R.I. Jaffee, The recrystallization and ductile-brittle transition behaviour of tungsten-effect of impurities on polycrystals prepared from single crystals, J. Inst. Met. 90 (1961) 120–128.

[25] K. Tsuchida, T. Miyazawa, A. Hasegawa, S. Nogami, M. Fukuda, Recrystallization behavior of hot-rolled pure tungsten and its alloy plates during high-temperature annealing, Nucl. Mater. Energy. 15 (2018) 158–163.

[26] J. V. Haag IV, D.J. Edwards, C.H. Henager, W. Setyawan, J. Wang, M. Murayama, Characterization of Ductile Phase Toughening Mechanisms in a Hot-Rolled Tungsten Heavy Alloy, Acta Mater. 204 (2020) 116523.

[27] S. Xia, B.X. Zhou, W.J. Chen, W.G. Wang, Effects of strain and annealing processes on the distribution of Σ3 boundaries in a Ni-based superalloy, Scr. Mater. 54 (2006) 2019–2022.

[28] Y. Yu, W. Zhang, E. Wang, Effect of heat treatment on microstructure and mechanical properties of hot-hydrostatically extruded 93W-4.9Ni-2.1Fe alloy, J. Alloys Compd. 622 (2015) 880–884.

[29] J.K. Mason, C.A. Schuh, The generalized Mackenzie distribution: Disorientation angle distributions for arbitrary textures, Acta Mater. 57 (2009) 4186–4197.

[30] G. Sanchez Chavez, S. Farid Estefen, T. Gurova, A. Leontiev, L. Silva Gomes, S. Bottega Peripolli, Redistribution of grain boundary misorientation and residual stresses of thermomechanically simulated welding in an intercritically reheated coarse grained heat affected zone, Metals (Basel). 11 (2021).

[31] A. Deal, I. Spinelli, A. Chuang, Y. Gao, T. Broderick, Measuring residual stress in Ti-6Al-4V with HR-EBSD, using reference patterns from annealed material, Mater. Charact. 175 (2021) 1–23.

[32] Y. Zhang, T. Yu, R. Xu, J. Thorborg, W. Liu, J. Tischler, A. Godfrey, D. Juul Jensen, Local residual stresses and microstructure within recrystallizing grains in iron, Mater. Charact. 191 (2022) 112113.

[33] C. Moussa, M. Bernacki, R. Besnard, N. Bozzolo, About quantitative EBSD analysis of deformation and recovery substructures in pure Tantalum, IOP Conf. Ser. Mater. Sci. Eng. 89 (2015).

[34] J.W. Hutchinson, Crack Tip Shielding by Micro-Cracking in Brittle Solids, Acta Metall. 35 (1986) 1605–1619.
[35] M.E. Alam, G.R. Odette, Improving the Fracture Toughness and Ductility of Liquid Phase Sintered WNiFe Tungsten Heavy Alloys by High-Temperature Annealing, Materials (Basel). 16 (2023) 916.
[36] K.E. Knipling, G. Zeman, J.S. Marte, S.M. Kelly, S.L. Kampe, Effect of dissolved tungsten on the deformation of 70Ni-30Fe alloys, Metall. Mater. Trans. A Phys. Metall. Mater. Sci. 35 A (2004) 2821–2828.
[37] A.S. Rao, P. Manda, M.K. Mohan, T.K. Nandy, A.K. Singh, Microstructure, Texture, and Mechanical Behavior of As-cast Ni-Fe-W Matrix Alloy, Metall. Mater. Trans. A Phys. Metall. Mater. Sci. 49 (2018) 1140–1151.

Note: A modified version of this report has been recently published in Materials Science of Engineering A journal.

1. M.E. Alam, J.V. Haag IV, W. Setyawan, C.H. Henager Jr, G. R. Odette, “On the effect on high-temperature annealing on the microstructure and mechanical properties of a hot-rolled 90W7Ni3Fe tungsten heavy alloy”, Materials Science and Engineering A xxx (2024) 146200.

4.9 DETERMINATION OF TRANSMUTATION ISOTOPIC PRODUCTS FROM IRRADIATED TUNGSTEN—X.-Y. Yu, W. Zhong, L. Howard, Y. Katoh (Oak Ridge National Laboratory)

OBJECTIVE

The objective of this project is to determine the post-neutron irradiation transmutation products of tungsten (W) using high resolution time-of-flight secondary ion mass spectrometry (ToF-SIMS). The primary goal is to demonstrate that ToF-SIMS can offer sufficient mass resolution to resolve isotopic products of W resulting from neutron irradiation.

SUMMARY

We performed detailed ToF-SIMS spectral analysis of reference tungsten alloys containing rhenium (Re) and osmium (Os) to establish the baseline spectra of unirradiated alloy mass spectra and obtain characteristic mass to charge ratios (*m/z*). Such information is useful to assist peak identification and potentially used as quantification references to provide insights into transmutation pathways of irradiated tungsten alloys.

PROGRESS AND STATUS

Three alloys of different compositions, $W_3Re_{0.7}Os$, $W_5Re_{0.3}Os$, and $W_{10}Re_{0.5}Os$, were studied using ToF-SIMS. A ToF-SIMS V spectrometer (IONTOF GmbH, Münster, Germany) was used to analyze the irradiated tungsten samples. The SIMS analysis was performed using a 30 keV pulsed bismuth (Bi_3^+) primary beam ion under high vacuum of 4.8×10^{-8} mbar during measurements. The Bi_3^+ primary ion beam scanned over a 150 × 150 μm^2 area with a resolution of 256 by 256 pixels. The spectrum was acquired for 10 scans. The primary ion doses in all measurements were lower than the static limit, and the damage artifacts resulting from the Bi_3^+ primary ion beam was negligible. The mass resolutions of the detected peaks in the SIMS spectrum are in the range of 8000 to 11,000, varying from sample to sample depending on the sample roughness. Mass spectra were calibrated using CH^+, CH_2^+, Si^+, W^+, and Bi^+ in the positive ion mode using the SurfaceLab software version 7.0.

Figure 1 depicts the ToF-SIMS spectral plot of the unirradiated tungsten alloy, $W_3Re_{0.7}Os$, in the m/z^- range of 220 – 490 in the negative ion mode. In the negative ion mode, oxide peaks are more evident. Characteristic peaks include but not limited to m/z^- 231.93 $^{184}WO_3^-$, m/z^- 234.94 ReO_3^-, and m/z^- 239.94 OsO_3^-. Clustering is common in the spectra, additional peaks were observed in higher masses, such as m/z^- 447.87 $W_2O_5^-$, m/z^- 266.94 ReO_5^-, and m/z^- 479.88 $W_2O_7^-$. The preliminary SIMS analysis illustrates that the surface oxidation of W, Re, and Os and corresponding peaks with reasonable mass resolution.

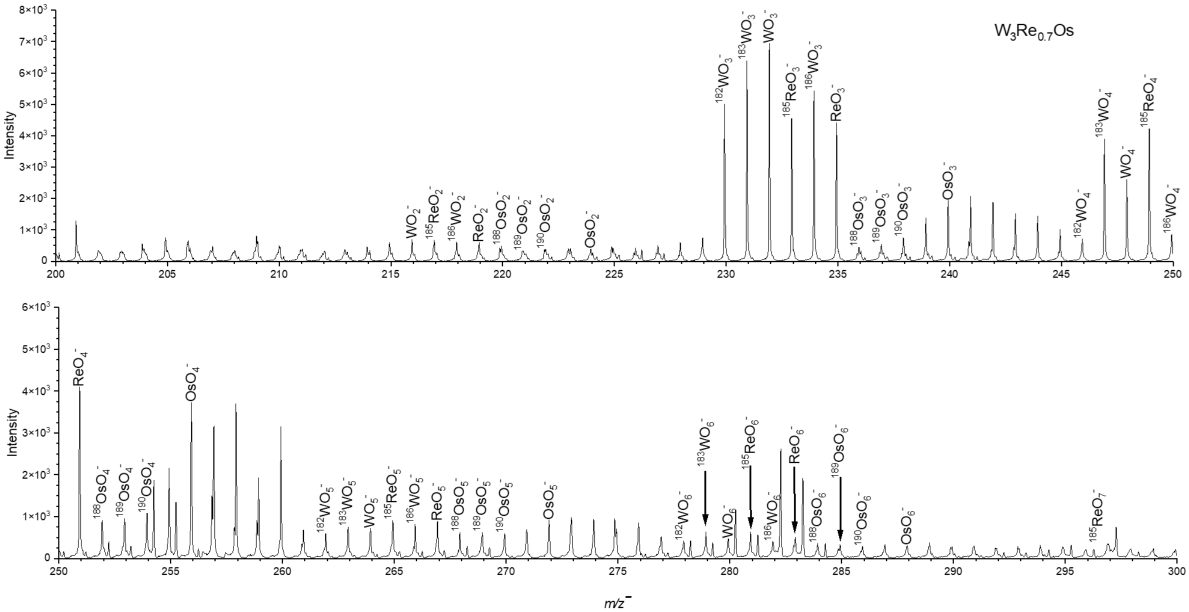

Figure 1. The ToF-SIMS spectral comparison of the tungsten alloy $W_3Re_{0.7}Os$ in the m/z^- range of 220 – 490 in the negative ion mode.

Comparisons of the alloy spectra show some similarities of peaks and fragmentation patterns. Additional analysis and peak identification are ongoing. The SIMS spectral results will be included in a paper reporting SIMS spectral characteristic peaks and peak identification.

Results

A manuscript outlining the current study on neutron-irradiated tungsten samples [1] is currently underway and is nearing submission to a peer-reviewed journal. Future research will continue SIMS spectral analysis of reference alloys and single crystal tungsten specimens. This effort is intended to demonstrate SIMS's capabilities in revealing transmutation products and establish the technical foundation of product identification and quantification to further the understanding of neutron displacement damage on mechanical property changes and improve our insights of transmutation on tungsten materials.

References

[1] X.-Y. Yu, Y.-R. Lin, L. Howard, and Y. Katoh, "Determination of Transmutation Isotopic Products from Irradiated Tungsten", U.S. DOE Office of Fusion Energy Science, Fusion Materials, Semiannual Progress Report, DOE/ER-0313/74 (2023)

5. HYDROGEN AND HELIUM EFFECTS

5.1 HYDROGEN ISOTOPE IMPLANTATION AND RETENTION IN POLYCRYSTAL TUNGSTEN—W. Zhong (Oak Ridge National Laboratory)

OBJECTIVE

The objective of this work is to characterize the hydrogen retention and desorption behaviors in polycrystal tungsten. Low energy deuterium was implanted on tungsten at room temperature followed by thermal desorption spectroscopy to examine the deuterium retention and desorption from the implantation.

SUMMARY

A 10 keV deuterium D_2^+ (5keV/ D) was implanted on polycrystal tungsten with the flux of ~6 × 10^{16} D/m^2/s under vacuum on the order of 10^{-7} Torr at room temperature. Three different D fluences were implanted, and thermal desorption spectroscopy experiments were performed to 900°C immediately after the implantation. Deuterium desorption peaks were observed at ~100˚C, and they did not change significantly as a function of fluences. The deuterium desorption spectroscopy results did not change significantly after the fluence of 2.16 × 10^{20} D/m^2, which indicated that this fluence is close to D_2 saturation in W from the implantation at room temperature.

PROGRESS AND STATUS

10keV D_2^+ (5keV/ D) was implanted on a polycrystal tungsten with a flux of ~6 × 10^{16} D/m^2/s. The SRIM was used to calculate the deuterium distribution and damage from implantation per D fluence of 1 × 10^{19} D/m^2. The displacement energy for W was 90eV for calculation. Figure 1 shows the peak of deuterium concentration is at ~30nm with the deuterium content of 2260 atomic parts per million (appm). Small damage is also expected from the D implantation, with its peak at ~15nm.

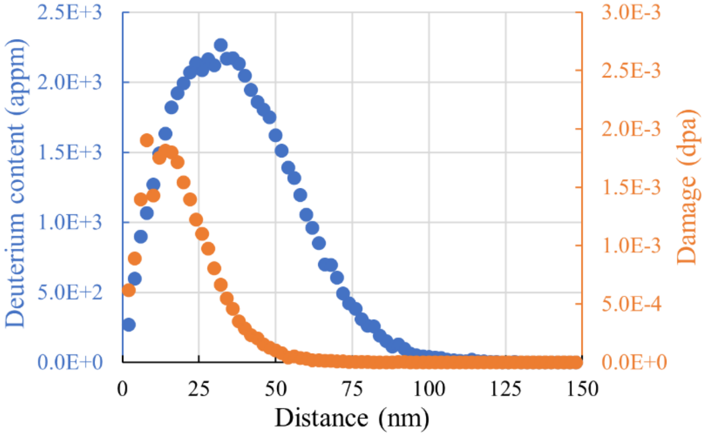

Figure 1. The SRIM calculation on deuterium depth profile and damage dose with the fluence of 1 × 10^{19} D/m^2 using K-P quick calculation.

Electron backscatter diffraction (EBSD) was used to characterize the grain structure of tungsten. Figure 2a shows the inverse pole figure of tungsten that was used in this work. The sample exhibits larger grains with [001] and [101] direction normal to the sample surface. Smaller island grains are also observed inside the large grains, and they mostly have the [111] direction normal to the surface.

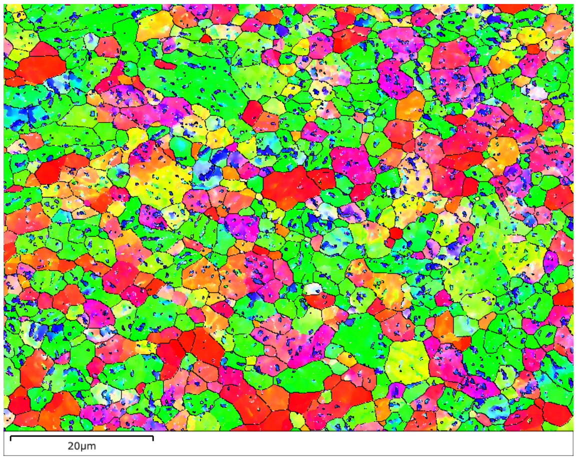

Figure 2. Grain structure of tungsten for deuterium implantation and desorption experiment.

Thermal desorption spectroscopy (TDS) experiment was performed within 1 hour after the deuterium implantation. The D-implanted sample was inserted into a quart tube with a K-type thermal couple in proximity to the sample. The quartz tube was pumped to the pressure on the order of 1 × 10^{-8} Torr at room temperature before starting the heating. The TDS was performed at a ramping rate of 0.5˚C/s to the maximum temperature of 900˚C. Deuterium signal was measured by quadruple mass spectrometer Pfeiffer PrismaPlus QME-220 and it was calibrated using the deuterium standard leak with D_2 constant leak rate of 1.04 × 10^{-12} mol/s from Vacuum Technology Inc. Figure 3 shows the desorbed D_2 flux as a function of temperature for D-implanted tungsten. Three implantations with different deuterium fluences were performed, i.e. 7.2 × 10^{19}, 2.16 × 10^{20} and 6.48 × 10^{20} D/m^2. After deuterium implantation, a desorption peak at ~100˚C is observed, and the peak temperature does not change significantly with fluence. In addition, the D_2 retention does not change significantly after 2.16 × 10^{20} D/m^2, which indicates that this fluence is close to D_2 saturation in W from the room temperature implantation.

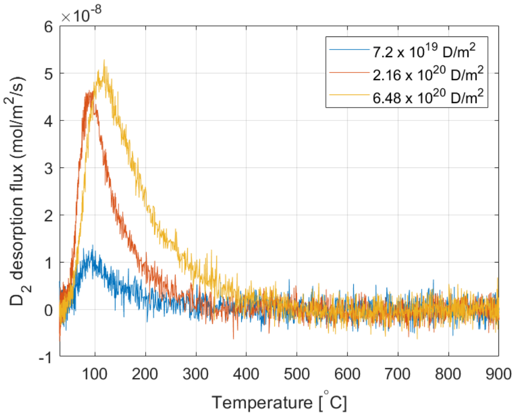

Figure 3. The D_2 desorption flux as a function of temperature after D_2 implantation at room temperature.

Results

Deuterium implantation and retention experiment will be performed on irradiated W to understand the irradiation effect on deuterium retention.

6. FUSION CORROSION AND COMPATIBILITY SCIENCE

6.1 COMPATIBILITY BETWEEN SiC AND PRE-OXIDIZED AND ALUMINIZED F82H IN FLOWING PbLi AT 550°-650°C

—M. Romedenne, C. De Lamater-Brotherton, B. A. Pint (Oak Ridge National Laboratory), Y. Zhang (Tennessee Technological University)

OBJECTIVE

This task is investigating the possibility of increasing the Pb-Li temperature in the dual coolant lead-lithium (DCLL) blanket concept in order to improve the overall system efficiency. Prior work investigated monometallic thermal convection loops (TCLs) with commercial FeCrAlMo alloy APMT. The current experiments have progressed to evaluating dissimilar materials effects in flowing Pb-Li between more fusion relevant materials, monolithic SiC and aluminized alloy F82H (Fe-8Cr-2W), to establish a maximum operating temperature for operation in flowing eutectic Pb-Li.

SUMMARY

Flowing testing at 600°-700°C showed significant interaction between chemical vapor deposition (CVD) SiC and FeCrAl so subsequent experiments reduced the temperature to 550°-650°C and included aluminized and pre-oxidized F82H specimens in APMT tubing. The first 1,000 h TCL experiment found a limited reaction with SiC particularly in the cold leg including the formation of Fe- and Cr-rich carbides and silicides. In an effort to study the reaction kinetics, an identical TCL experiment was conducted for 2,000 h and completed in September 2023. However, the initial results from this TCL showed less reaction among the specimens, which is a good indication for this technology. Characterization of specimens exposed for 2,000 h in flowing Pb-Li is presented.

PROGRESS AND STATUS

Introduction

The DCLL blanket concept (with eutectic Pb-16 at.% Li and He coolants) has been a leading U.S. design for a DEMO/FPP-type fusion reactor [1]. Typically, reduced activation ferritic martensitic (RAFM) steel is envisioned as a structural material. However, PbLi compatibility will then limit the DCLL to ~475°C metal temperature because Fe and Cr readily dissolve in PbLi above 500°C and RAFM Eurofer 97 plugged a PbLi loop at 550°C [2,3]. Following 10 years of static PbLi testing [4-6], a series of four monometallic APMT TCLs were operated with increasing peak temperatures from 550° to 700°C [7-9] to study the compatibility of APMT with and without pre-oxidation at 1000°C to form α-Al_2O_3 in flowing PbLi where changes in solubility with temperature can drive mass transfer [2,10]. The next TCL (#5) included CVD SiC and oxide dispersion strengthened (ODS) FeCrAl [11] specimens with APMT tubing and discovered a remarkable dissimilar materials reaction with large FeCrAl mass losses and carbides and silicides forming on the SiC specimens [12]. Figure 1 shows dissolution rates in these recent TCL experiments compared to literature values [2,13]. Linear dissolution is assumed, particularly for the Oak Ridge National Laboratory (ORNL) TCL experiments which were all performed for 1000 h. A 6th TCL reduced the peak temperature to 650°C because the most severe dissolution was observed above 675°C. In addition, the ODS FeCrAl specimens were replaced with pack aluminized F82H RAFM steel. Because the most severed dissolution was observed on bare specimens, all of the metal specimens were pre-oxidized. By reducing the TCL temperature, the dissimilar material reaction was significantly reduced with only small mass gains for the CVD SiC specimens [14]. The goal of the 7th TCL experiment was to repeat this experiment for 2,000 h to better understand the kinetics of the dissolution reaction.

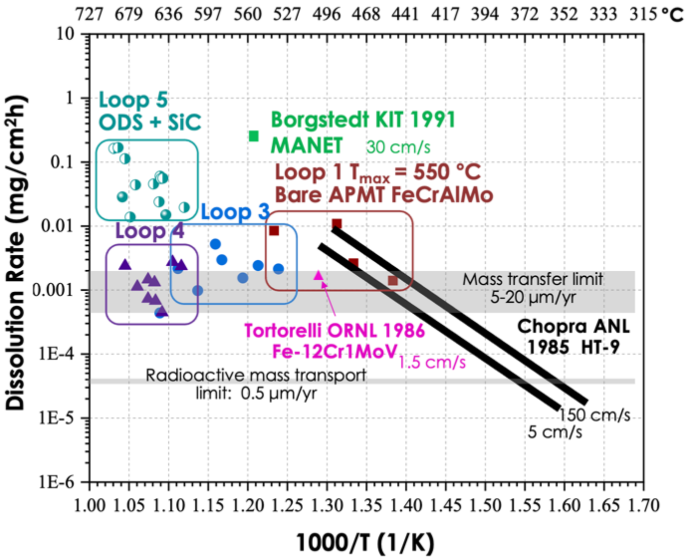

Figure 1. Literature Pb-Li dissolution rates compared to recent ORNL TCL results assuming all rates are linear after 1,000 h, adapted from [14].

Experimental Procedure

The details of the TCL (~1 m tall and 0.5 m wide) and its operation have been previously described [7-9,12,14,15]. The TCL APMT tubing was pre-oxidized for 8 h at 1050°C in air. The hot and cold leg specimens were coupons (25 x 18.5 x 1 mm^3) of CVD SiC (12) and aluminized F82H (10) and F82H SS-3 type tensile (25 x 4 x 0.9 mm) specimens. Four APMT coupons were included for comparison to prior experiments and pre-oxidized for 2 h at 1000°C in air. All 24 of the aluminized F82H specimens were pre-oxidized for 2 h at 800°C in air. The 20 specimens in each chain were connected with APMT wire. More details about the specimens and the coating process were presented previously [14,15]. Rectangular coupons of unalloyed tungsten were attached at the bottom of each specimen chain to act as a "sinker" to keep the relatively low-density specimen chains from floating in the PbLi. The temperature gradient in the TCL was ~115°C from 535-650°C and the velocity was measured [7] as 0.9 cm/s. After operation, the entire loop was filled with a cleaning solution (1:1:1 mixture of ethanol, hydrogen peroxide, and acetic acid) and later specimens were cleaned individually with the same solution. Specimens were weighed before and after exposure using a Mettler Toledo model XP205 balance with an accuracy of ±0.04 mg. The post-exposure specimens have been characterized using scanning electron microscopy (SEM) (ZEISS model Gemini 460) along with energy dispersive spectroscopy (EDS) and X-ray diffraction (XRD) using a Malvern PANalytical X'Pert PRO diffractometer with Cu Kα radiation in the Bragg-Bentano geometry.

Results

The specimen mass change of all the specimens is shown in Figure 2a and compared to the prior 1,000 h TCL experiment. The mass change is plotted as a function of the estimated specimen temperature, which was slightly different between the two experiments. The figure is intended to show that the mass changes were small with most specimens experiencing a slight mass gain. Generally, more mass gain was observed for the F82H specimens after 2,000 h compared to 1,000 h. Figure 2b includes only the CVD SiC specimens in both experiments to emphasize that the set of specimens exposed for 1,000 h exhibited mass gains (open symbols) except for one specimen while the second set of specimens exposed for 2,000 h showed less mass change. Because the CVD SiC is somewhat brittle, the mass loss for several specimens was attributed to chipping during handling.

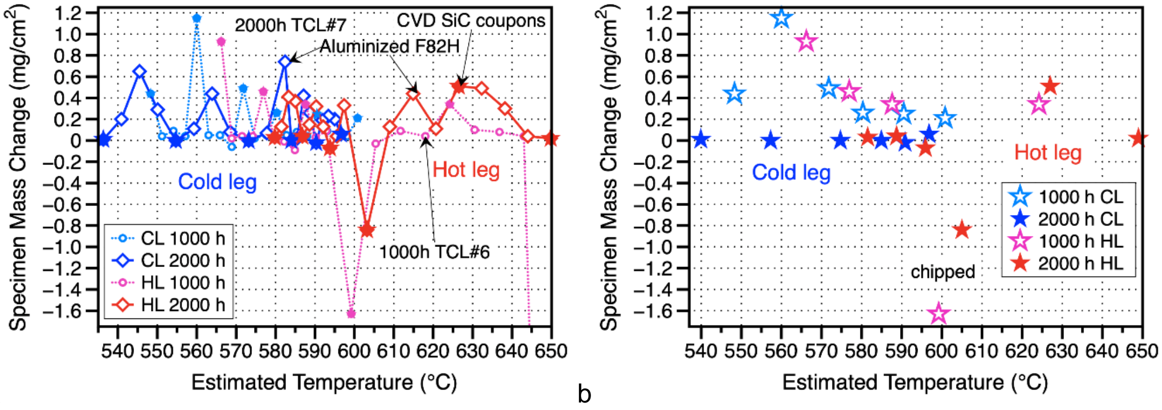

Figure 2. Specimen mass changes plotted versus the estimated exposure temperature in flowing PbLi after 2,000 h (TCL #7) and 1,000 h (TCL #6) (a) all of the specimens and (b) the CVD SiC specimens.

All of the CVD SiC specimens were sectioned to examine the surface. For example, Figure 3 shows some indication of Cr and Fe deposits on the surface of the specimen exposed in the hot leg at 603°C. This is the chipped specimen in Figure 2b with a mass loss of -0.84 mg/cm^2. The SiC specimen exposed at 627°C in the hot leg with a mass gain of 0.51 mg/cm^2 was the only specimen to show Fe_3Si and $MoSi_2$ XRD peaks, Figure 4. For the pre-oxidized specimens, most showed α-$LiAlO_2$ peaks, which is consistent with the predicted [16,17] and observed [18] transformation of alumina to $LiAlO_2$ in PbLi. An example for the F82H coupon exposed at 644°C (mass gain 0.04 mg/cm^2) is shown in Figure 5.

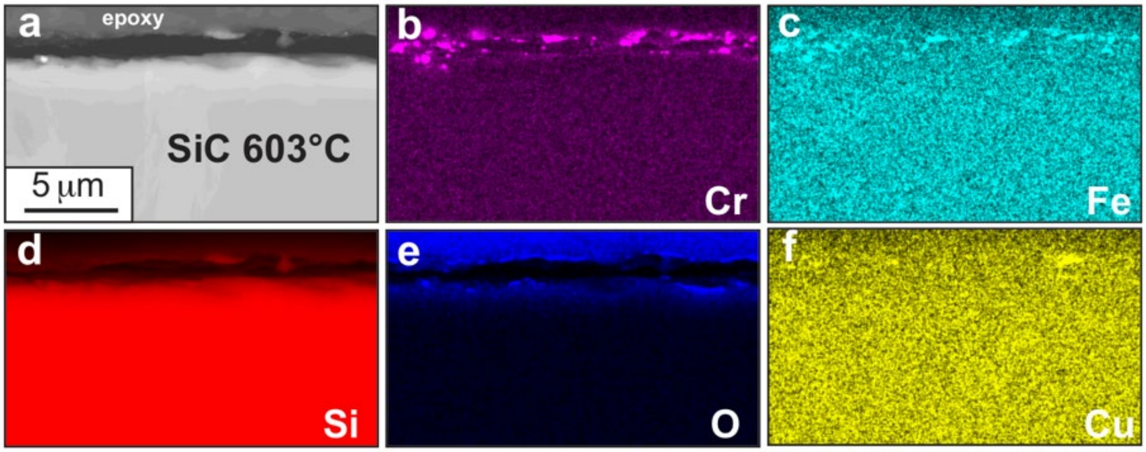

Figure 3. (a) SEM secondary electron image of SiC specimen exposed for 2,000 h in flowing PbLi at and (b-d) associated EDS maps of the same region, 650°C HL.

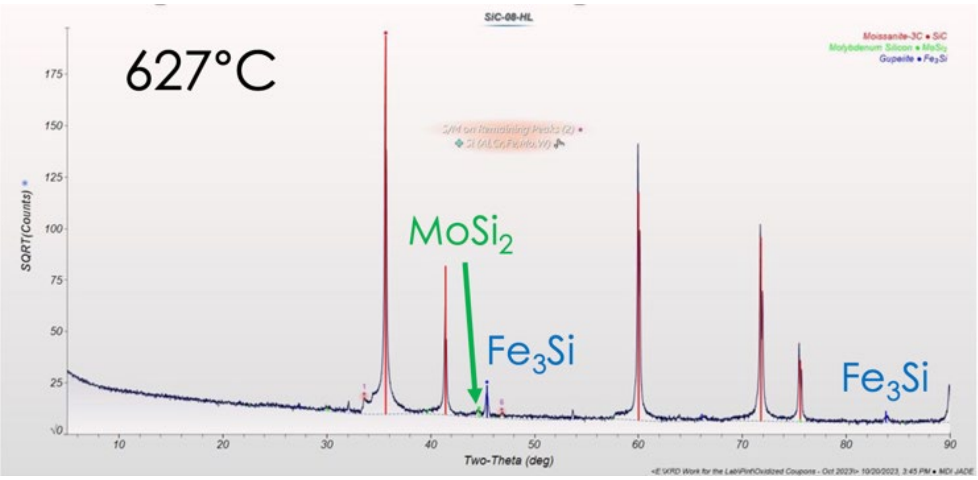

Figure 4. The XRD spectra of the CVD SiC specimen exposed for 2,000 h in flowing PbLi at 627°C.

<u>Future work</u>

The characterization of the remaining specimens will be completed for a forthcoming publication. Rather than continue additional testing. The next focus will be on replacing APMT tubing with aluminized steel tubing including T92 as a surrogate for RAFM steel and 316H as a non-magnetic alternative for a future forced convection loop to test compatibility in the presence of a magnetic field.

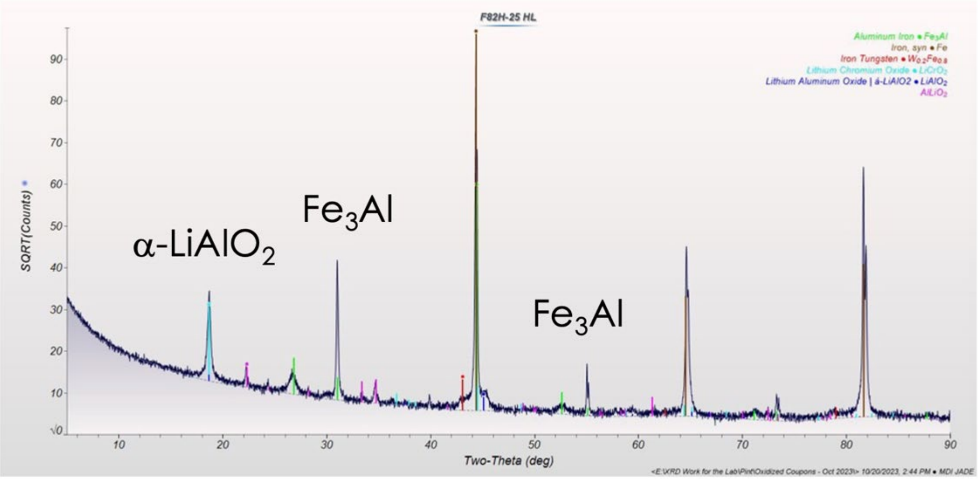

Figure 5. The XRD spectra of the aluminized F82H coupon exposed for 2,000 h in flowing PbLi at 644°C.

References

[1] M. Abdou, et al., Fusion Sci. Technol. 47 (2005) 475.
[2] O. K. Chopra, et al., Fusion Technol. 8 (1985) 1956.
[3] J. Konys, et al., J. Nucl. Mater. 386-88 (2009) 678.
[4] B. A. Pint J. L. Moser and P. F. Tortorelli, Fusion Eng. Design 81 (2006) 901.
[5] B. A. Pint, S. Dryepondt, K. A. Unocic and D. T. Hoelzer, JOM 66 (2014) 2458.
[6] K. A. Unocic, D. T. Hoelzer and B. A. Pint, Mater. High Temp. 32 (2015) 123.
[7] S. J. Pawel and K. A. Unocic, J. Nucl. Mater. 492 (2017) 41.
[8] J. Jun, et al., J. Nucl. Mater. 528 (2020) 151847.
[9] B. A. Pint, et al., Fusion Sci. Technol. 77 (2021) 761.
[10] J. H. DeVan, J. Nucl. Mater., 85-86 (1979) 249.
[11] S. Dryepondt, et al., J. Nucl. Mater. 501 (2018) 59.
[12] B. A. Pint, J. Jun and M. Romedenne, Fusion Eng. Design 166 (2021) 112389.
[13] H. U. Borgstedt and H. D. Rohrig, J. Nucl. Mater. 179 (1991) 596.
[14] M. Romedenne, Y. Zhang, Y.-F. Su, B. A. Pint, J. Nucl. Mater. 581 (2023) 154465.
[15] M. Romedenne, C. De Lamater-Brotherton, B. A. Pint, Y. Zhang, DOE/ER-0313/74 (2023) 131.
[16] P. Hubberstey, T. Sample and A. Terlain, Fusion Technol., 28 (1995) 1194.
[17] P. Hubberstey, J. Nucl. Mater. 247 (1997) 208.
[18] B. A. Pint and K. L. More, J. Nucl. Mater. 376 (2008) 108.

6.2 EVALUATION OF SiC COMPATIBILITY WITH 2LiF-BeF$_2$ MOLTEN SALT BY CALCULATED THERMODYNAMICS

—B. Lamm, T. Koyanagi (Oak Ridge National Laboratory)

OBJECTIVE

The compatibility of SiC with molten salts is of fundamental importance for the use of SiC in molten salt breeder blankets. The SiC and 2LiF-BeF$_2$ molten salt (FLiBe) are considered here, based on calculated thermodynamic equilibrium, to identify potential corrosion byproducts.

SUMMARY

The use of SiC as a structural material in molten salt liquid breeder blanket designs requires an evaluation of the compatibility of SiC with molten salts, including 2LiF-BeF$_2$ (FLiBe). Calculations of the thermodynamic equilibrium between SiC+FLiBe, SiC+FLiBe+H_2O, and SiC+FLiBe+H_2O+Metal (Metal = Fe, Ni) were analyzed to determine the likely extent of corrosion, the corrosion products formed, and examine potential corrosion pathways in a breeder blanket using SiC and FLiBe.

PROGRESS AND STATUS

Experimental Procedure

SiC+FliBe and SiC+FliBe+H_2O

Initial calculations for the combination SiC + FLiBe were made from 1:1 to 1:10 SiC/FliBe (mole ratio). No reaction was observed, suggesting that SiC is stable in the presence of perfectly pure FLiBe. However, as with other molten chloride and fluoride salts, FLiBe is hygroscopic and can retain water even after intensive drying procedures.[1] Based on hot extraction of oxygen from FLiBe used at Oak Ridge National Laboratory (ORNL), up to 300 wppm of water is present in dry FLiBe,[2] which corresponds to 0.0018 mol H_2O per mole of FLiBe. Based on this, calculations for the system SiC + FLiBe + H_2O were made for 1:1:0.0018-0.018 SiC:FLiBe:H_2O, results shown in Figure 1. The addition of water results in the formation of additional liquid, solid, and gas species.

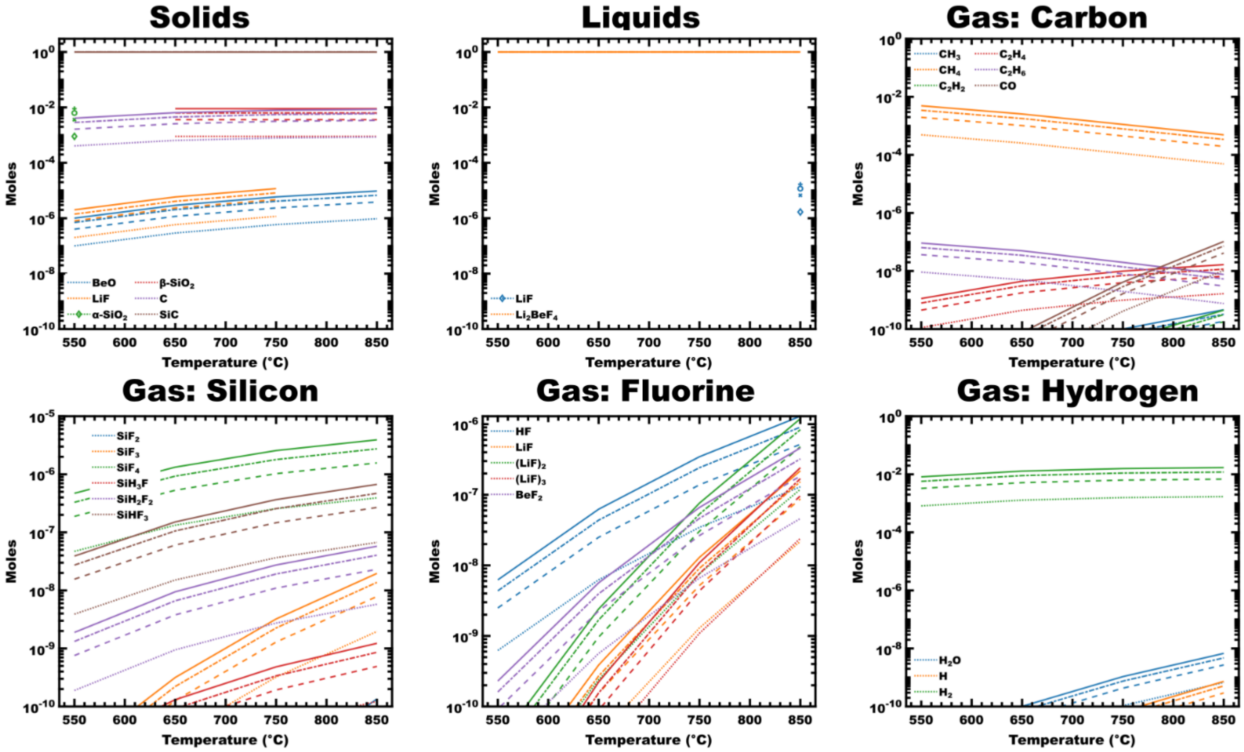

Figure 1. Equilibrium species present based on the initial conditions of 1 SiC | 1 (2LiF-BeF$_2$) | "a" H_2O, molar amounts, where amounts of a = 0.0018, 0.0072, 0.0126, and 0.018 correspond respectively to dotted lines, dash lines, dot-dash lines, and solid lines.

The most significant new solids formed (~1:1000 concentration *vs.* SiC) are carbon and SiO_2. In operation, these materials can be expected to form near the SiC/FLiBe interface. Carbonaceous pitting has been observed on the surface of monolithic high-purity SiC following exposure to FLiBe.[2] Other species formed are less than 10^{-4} mol, and include BeO and LiF.

The only new liquid formed is LiF, and only at 850°C. As the melting point of LiF is 848°C, this is not considered to be of significant concern during the normal operation of FLiBe-containing circulators in operation.

In the pure SiC/FLiBe mixtures, no gases are expected to be present as a result of reaction. The introduction of water to this mixture, however, results in the formation of 20 significant gas species (where significant was arbitrarily selected as $>10^{-10}$ mol at equilibrium). Of the carbon-containing gases, the most significant species is methane (CH_4), which forms at $>10^{-4}$ mol at all temperatures for nearly all amounts of water present initially. The remaining species formed at $<10^{-6}$ mol, and include CH_3, C_2H_2, C_2H_4, C_2H_6, and CO.

Apart from CO, all of these species are flammable. The system considered C_xH_y species up to x = 10, so no heavier hydrocarbons are expected at equilibrium in significant amounts. As temperature increases, the most stable hydrocarbons (CH_4 and C_2H_6) decompose into less stable species, as is expected based on previous kinetics investigations of hydrocarbon chemistry.[3] Silicon-containing species include silicon fluorides and hydrofluorides, all at $<10^{-5}$ mol. These gases are regarded as corrosive and flammable. It is worth mentioning here that previous research has indicated the formation of Si-F ionic species (e.g. SiF_6^{2-}) as products of SiC-FLiBe reaction;[4] however, liquid ionic species were not included in these calculations due to software limitations. Next, other fluoride gases, including HF, LiF and LiF oligomers, and BeF_2 are expected to form at <10^{-6} mol. Concentrations of these gases increase sharply with temperature. Finally, the remaining gases are H_2O, H_2, and H. Initial amounts of water were on the order of 10^{-3}-10^{-2} mol, but at equilibrium are <10^{-8} mol for all temperatures and initial concentrations. The most significant species in this subset is H_2, which is >10^{-3} mol at all temperatures for nearly all initial amounts of water.

Metal contaminants

Exposures of monolithic high-purity SiC to FLiBe resulted in the formation of carbon-rich pits with metal inclusions (e.g. Fe and Ni).[2] More generally, corrosion in molten salt is known to be sensitive to transition metal impurities.[1] The effect of iron and nickel impurities in the molten salt were modeled by including 0-0.5 mol of Fe or Ni to 1 SiC | 5 FLiBe | 0.09 H_2O mixtures, shown in Figure 2.

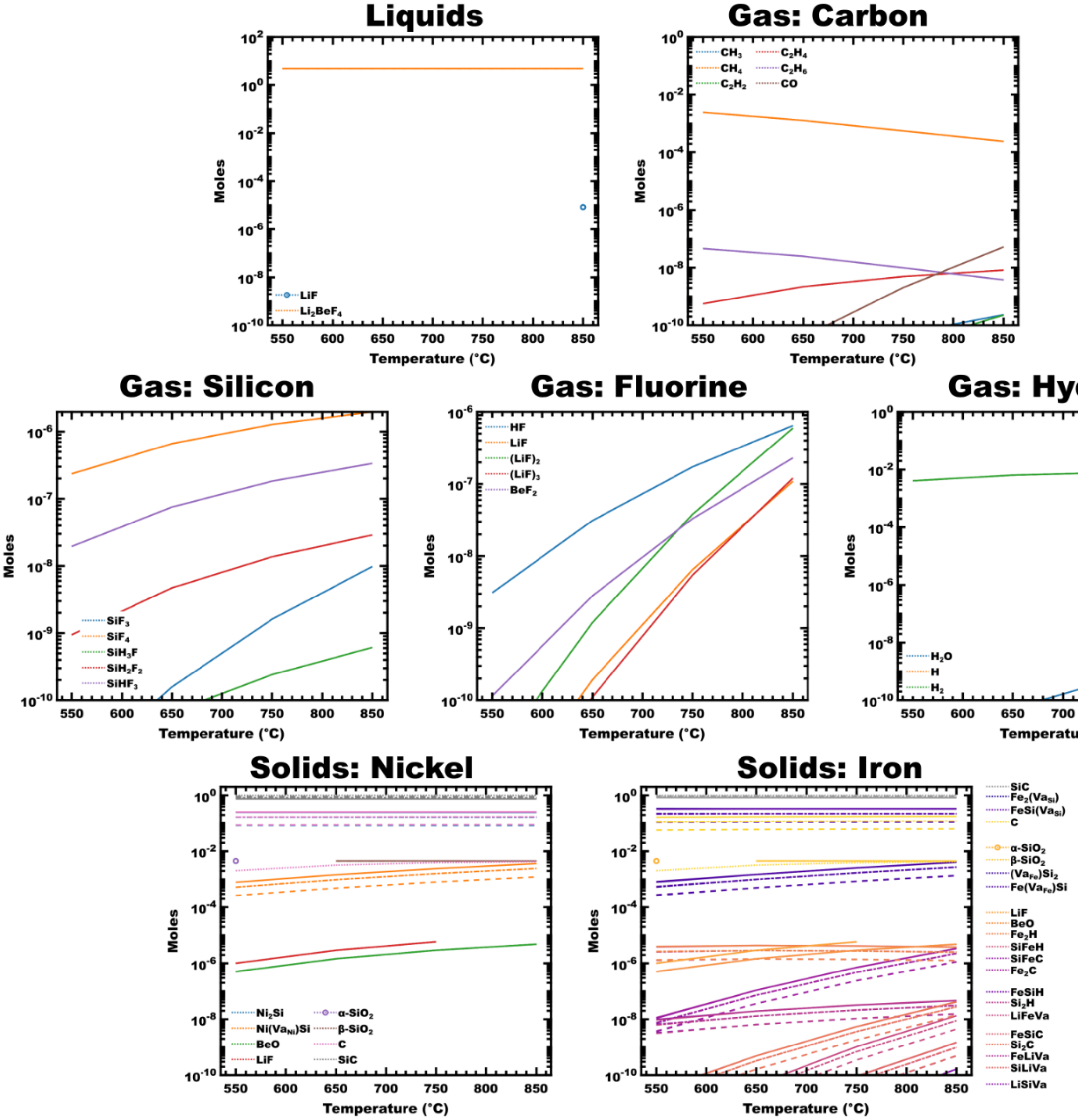

Figure 2. Equilibrium species present based on the initial conditions of 1 SiC | 5 (2LiF-BeF_2) | 0.09 H_2O | "a" mol M (M = Fe or Ni), molar amounts, where amounts of a = 0, 0.166, 0.333, and 0.5 correspond respectively to dotted lines, dash lines, dot-dash lines, and solid lines.

The addition of iron or nickel to the mixture does not affect the gas or liquid species present or their respective concentrations. However, new solid species are present with the addition of either transition metal.

In the case of nickel, a larger decrease in the amount of SiC present can be observed, compared to the metal-free case. This corresponds to the formation of 1:1 Ni_2Si/NiSi (overlapping in blue and orange, Figure 2 "Solids: Nickel"), as well as a sharp increase in the amount of free carbon formed.

There is a more complex mixture of products formed upon the addition of iron. As with nickel, iron decreases the amount of SiC present compared to the metal free case. This is primarily due again to the increased formation of free carbon, as well as the formation of several Fe-Si species with variable occupancy and substitutions. For example, both Fe_2Si and $FeSi_2$ crystalline species are expected to form, but vacancies in either the Fe or Si sites are expected. Substitutions with H, Li, or C can also occur, forming, for example, $C_{Fe}Si_2$ in the place of $FeSi_2$. The exact implications of these species is the subject of further study, however the overall result is that Fe- or Ni-containing solids are expected to form on the surface of SiC in combination with increased formation of carbon pits as observed in monolithic high-purity SiC.[2]

Results

Continuing efforts include the molten salt exposure of SiC/SiC composites to evaluate the differences in corrosion between types of SiC fiber, and in comparison, to monolithic high-purity SiC. Thermodynamic calculations are also underway to include the different impurities present in selected types of SiC fiber.

References

[1] K. Sridharan, T.R. Allen, Corrosion in Molten Salts, in: F. Lantelme, H. Groult (Eds.), Molten Salts Chemistry, Elsevier, Boston, MA, USA, 2013, pp. 241-267.
[2] T. Koyanagi, J.J. Lee, J.R. Keiser, H. Gietl, Y. Katoh, Corrosion characteristics of monolithic SiC materials in beryllium-bearing molten fluoride salt, Corrosion Science 220 (2023) 111301.
[3] W. Benzinger, K.J. Hüttinger, Chemical vapor infiltration of pyrocarbon —II. The influence of increasing methane partial pressure at constant total pressure on infiltration rate and degree of pore filling, Carbon 36(7-8) (1998) 1033-1042.
[4] J. Xi, H. Jiang, C. Liu, D. Morgan, I. Szlufarska, Corrosion of Si, C, and SiC in molten salt, Corrosion Science 146 (2019) 1-9.

7. ADVANCED MANUFACTURING

No contributions this reporting period.

8. MECHANISMS AND ANALYSIS

8.1 APPLICATION OF WEAK-BEAM DARK-FIELD STEM FOR DISLOCATION LOOP ANALYSIS—Y. Lin, S. J. Zinkle, J. D. Arregui-Mena (Oak Ridge National Laboratory), M. G. Burke (Idaho National Laboratory)

Extended Abstract: Full manuscript submitted to Microscopy and Microanalysis

OBJECTIVE

Explore the application of weak-beam dark-field (WBDF) - scanning transmission electron microscopy (STEM) methods for irradiation-induced defect analysis in crystalline materials, with a specific focus on dislocation loop imaging and analysis.

SUMMARY

Nanoscale dislocation loops formed by irradiation can significantly contribute to both irradiation hardening and embrittlement of materials when subjected to extreme nuclear reactor environments. This study explores the application of STEM-WBDF methods for quantitative irradiation-induced defect analysis in crystalline materials, with a specific focus on dislocation loop imaging and analysis. A high-purity Fe-5 wt. % Cr model alloy was irradiated with 8 MeV Fe^{2+} ions at 450°C to a fluence of 8.8×10^{19} m^{-2}, inducing dislocation loops for analysis. While transmission electron microscopy (TEM) has traditionally been the primary tool for dislocation imaging, recent advancements in STEM technology have reignited interest in using STEM for defect imaging. This study introduces and compares three STEM-WBDF methods, demonstrating their effectiveness in suppressing background contrasts, isolating defect information for dislocation loop type classification, providing finer dislocation line images for small loop analysis, and presenting inside-outside contrast for identifying loop nature. Experimental findings indicate that STEM-WBDF methods surpass traditional TEM approaches, yielding clearer and more detailed images of dislocation loops. The study concludes by discussing the potential applications of STEM-WBDF techniques in defect analysis, emphasizing their adaptability across various material systems beyond nuclear materials.

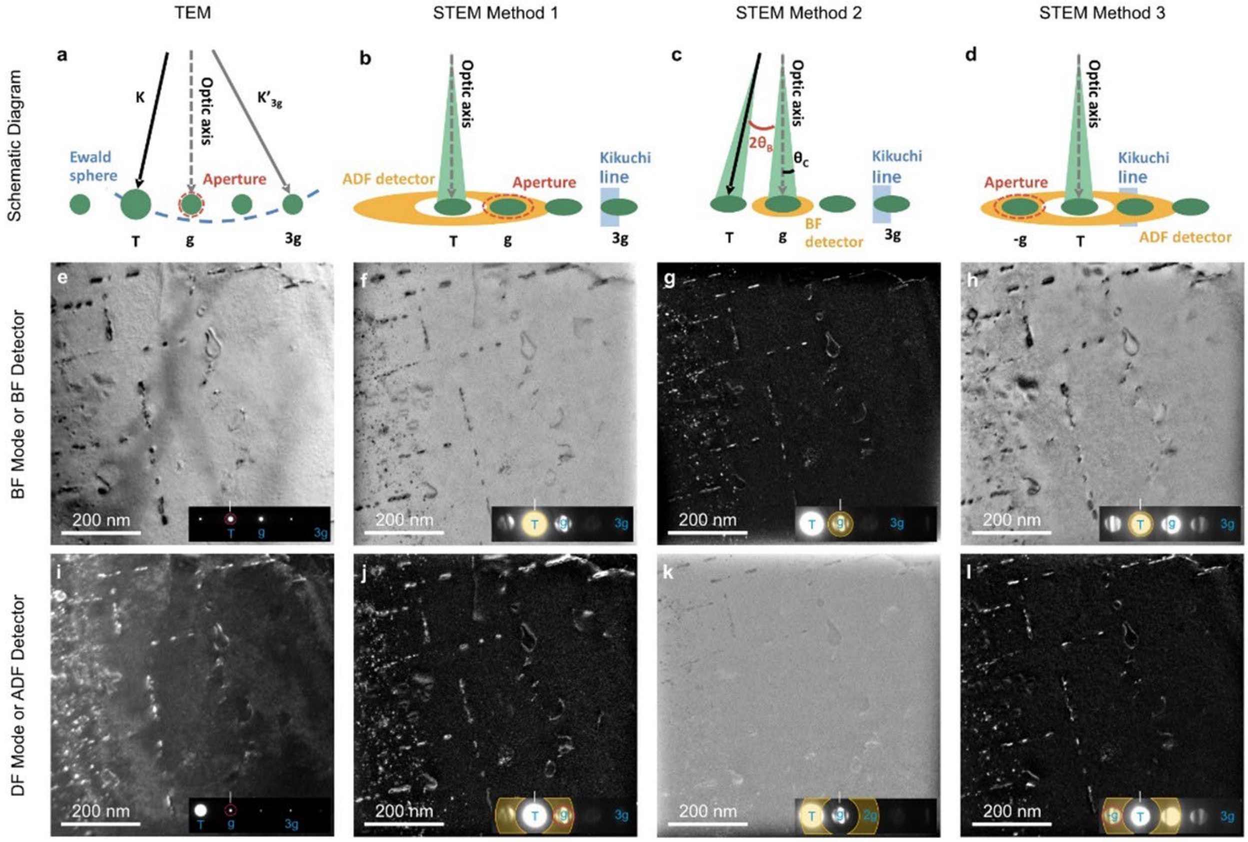

Figure 1. Collection of Bright-Field (BF) and WBDF micrographs of dislocation loops in irradiated Fe-5Cr, captured through various TEM and STEM techniques: (a-d) schematic diagram illustrating the imaging conditions; (e) TEM-BF and (i) TEM-WBDF micrographs (column 1); (f) STEM-BF and (j) STEM-WBDF micrographs using STEM Method 1 (column 2); (g) STEM-BF and (k) STEM-WBDF micrographs using STEM Method 2 (column 3); (h) STEM-BF and (l) STEM-WBDF micrographs using STEM Method 3 (column 4). The T is the direct beam and g is the diffraction beam with g=011.

Results

Future work will focus on integrating STEM-WBDF methods with 4D-STEM strain mapping and electron tomography techniques.

9. MODELING AND COMPUTATIONAL STUDIES

9.1 PREDICTIVE MODELING OF HE BUBBLE ACCUMULATION IN NANOSTRUCTURED FERRITIC ALLOYS—K. Pitike, W. Setyawan (Pacific Northwest National Laboratory)

SUMMARY

The overall objective of this work is to develop a predictive model of helium bubble accumulation and distribution in irradiated nanostructured ferritic alloys under relevant fusion environments. As a first step, we have developed an accurate Fe-He machine learning potential (version MLP1) based of deep neural network that is intended to study defect binding in He clusters and small He_nV bubbles in pure BCC-Fe. This work was recently published in *J. Nucl. Mater*. [1]. In this reporting period, we employ MLP1 to calculate the activation energies of trap-mutation (TM), a process in which an over-pressurized He cluster/bubble releases the pressure by creating one or more vacancies in He_nV bubbles and He_n clusters. These activation energies are intended to be used in kinetic Monte Carlo or rate theory simulations to study the growth of He bubbles. We are actively writing a manuscript on the kinetics of TM, expected to be submitted in the next quarter. In addition, we are extending MLP1 to describe larger bubbles, by training MLP2 on configurations with bubbles containing 1-9 vacancies and He gas interacting with various BCC-Fe surface terminations.

PROGRESS AND STATUS

Introduction

Developing Fe-He machine learning potential to describe thermodynamics of He_n clusters and all He_nV_m bubbles

Here we report our work on extending the Fe-He MLP1 to not only describe the thermodynamics of He_n clusters and small He_nV bubbles but also for large He_nV_m bubbles, that may contain more than one vacancy. In our previous reports, we have presented the binding energies of He with He_nV_2 and He_nV_3 bubbles. In this report, we present our methodology to train Fe-He MLP2, which can predict the binding energies of He_nV_m bubbles up to m=9. The training data for Fe-He MLP2, encompass configurations from ab initio molecular dynamics (AIMD), He_nV_m bubbles, for m=1 to 3, several surface terminations of BCC-Fe, and He-gas interacting with surfaces.

Accurate estimation of the binding energies of He or vacancy (V) with He_n cluster or He_nV_m bubble is crucial to advance the fundamental understanding of radiation damage in nano structured ferritic alloys. First-principles based density functional theory (DFT) is typically used to calculate the accurate binding energies. However, calculating the accurate binding energies for large He_nV_m bubbles is prohibitively expensive due to the computational cost of large supercells. Hence, a machine learning potential – trained on DFT data, obtained from relevant configurations – could be used to calculate accurate binding energies at a much smaller cost. In our previous work [1] we have developed a first Fe-He MLP1 to accurately describe the binding energies of He with He_n clusters and small He_nV bubbles with only one vacancy. Extending the MLP's ability for accurate estimation of binding energies for large He_nV_m bubbles can be achieved by further training the MLP with atomic configurations that represent larger He bubbles. So far, we have sampled atomic configurations of He_nV_m bubbles (m=1 to 9) using DFT. We have used m=1 to 3 bubbles for the training and reserved m=4 to 9 for testing. For bubbles containing more than 1 vacancy, we have used a 5x5x5 supercell. We have also sampled slab configurations in which the vacuum is filled with varying concentration of He gas. The varying concentration of He gas in the surface-gas configurations will effectively represent the He gas pressure in the He_nV_m gas bubbles. The slab configurations are intended to mimic He-matrix interaction in large bubbles.

Step 1: Testing MLP2

The MLP2 was trained with surface-gas configurations, He$_nV$, He$_nV_2$ and He$_nV_3$ bubbles. As mentioned above, the bubbles or vacancy clusters with more than 3 vacancies were not included in the training data. Here we present the MLP2's capability to (1) predict the correct ground state of V_m clusters and (2) total energies and forces of He$_nV_m$ bubbles that were not included in the training set.

Figure 1 presents the comparison of (a) energies and (b) forces predicted by MLP plotted against DFT data for V$_m$ clusters and He$_nV_m$ bubbles with m>4. Here we find that the mean absolute errors (MAE) for energies and forces are 0.7 meV/atom and 0.04 eV/Å, respectively. Even though these configurations were not included in the training data, the MAE values for energies and forces are comparable to that of configurations included in the training data. Furthermore, we evaluate the MLP2' ability to predict the correct ground state for V_m clusters. Figure 2(a) compares the MLP vs DFT formation energies for several configurations of V_m clusters up to m=9. MLP calculations were done using a 12x12x12 supercell, whereas DFT validation was done using a 5x5x5 supercell. We find that the MLP predicts the correct ground state configuration in each case from m=4 to 9. The ground state configuration is verified by running DFT calculations for the low energy configurations predicted by MLP. We find that the thermodynamic stability order of the configurations agrees between MLP and DFT. Furthermore, the mean absolute error for the formation energies of V_m clusters is 175 meV. Figure 2(b) shows the ground state structures of V_m clusters. For m=2, the second vacancy is thermodynamically stable at second nearest neighbor (2NN). For m=3, the third vacancy takes the intermediate position between the two vacancies such that the first two vacancies are in its first nearest neighbor (1NN) position. For m=4, the additional vacancy is added to form two 2NN bonds with the first two vacancies and 1NN bond with the third vacancy, forming a tetrahedral structure. From m=5 to 9, each successive vacancy is added to the previous vacancy cluster to form additional face sharing tetrahedron with the previous cluster.

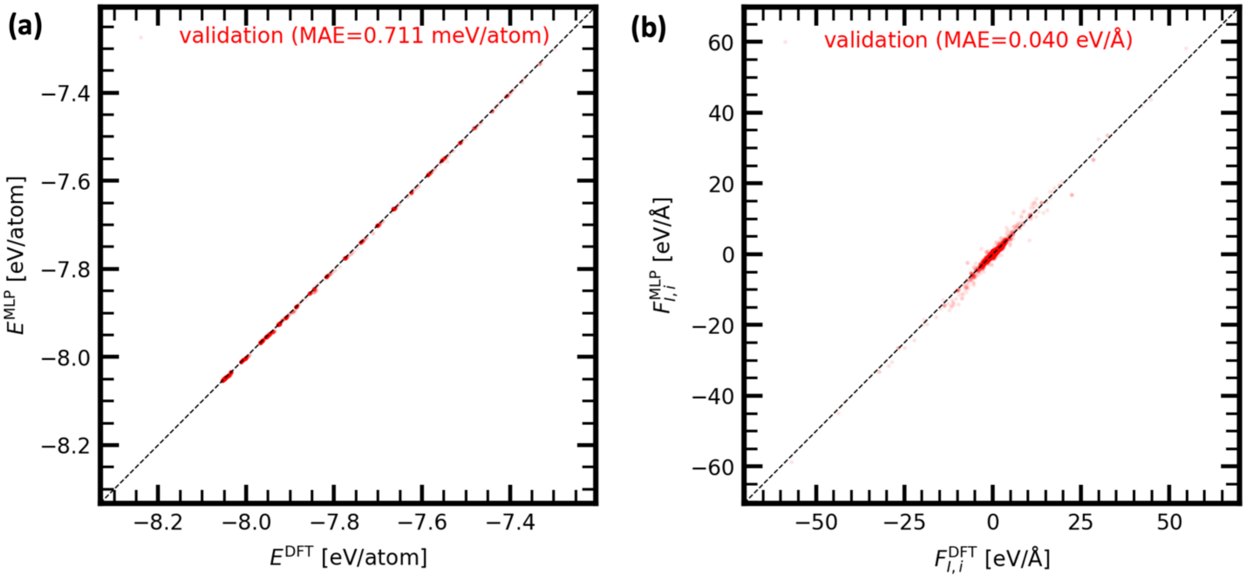

Figure 1. Comparison of MLP and DFT (a) energies (b) forces for V_m clusters and He$_nV_m$ bubbles with m>3. Note that even though, none of these configurations were included in the training data, the mean absolute error for both energies (MAE=0.7 eV/atom) and forces (MAE=0.04 eV/Å) are small.

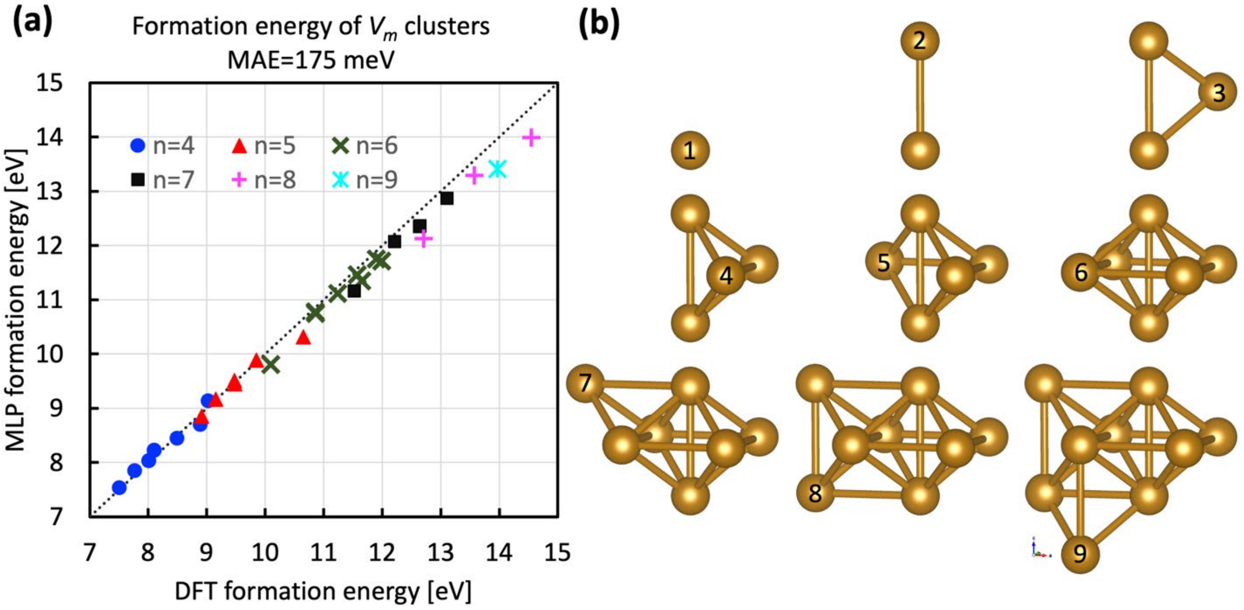

Figure 2. (a) DFT vs MLP formation energies of various configurations of V_m vacancy clusters. (b) The ground state configuration of each V_m cluster up to m=9. The succussive additional vacancy for each cluster is marked by the value of m.

Step 2: Predicting binding energies of He and V with He_nV_m bubbles.

It is well known that an interstitial He or a vacancy binds strongly with a He_nV_m bubble. However, the availability of these binding energies was limited to n<20 and m<4 due to prohibitive computational cost of DFT and limited accuracy of empirical potentials. However, with the development of Fe-He MLP2 along with demonstrated computational accuracy, we can calculate these binding energies with near-DFT accuracy and small computational cost. We calculate the binding energies of He with He_nV_m bubble until the bubble trap mutates. We have considered bubbles up to m=9. The defect reactions and the equations to calculate binding energies are given in the following.

Defect reactions:

$$\mathrm{He} + \mathrm{He}_{n-1}V_m \rightarrow \mathrm{He}_nV_m$$
$$V + \mathrm{He}_nV_{m-1} \rightarrow \mathrm{He}_nV_m$$

Binding energy equations:

$$E_b[\mathrm{He} + \mathrm{He}_{n-1}V_m] = E_{\mathrm{MLP}}[\mathrm{He}_{\mathrm{tet}}] + E_{\mathrm{MLP}}[\mathrm{He}_{n-1}V_m] - E_{\mathrm{MLP}}[\mathrm{He}_nV_m] - E_{\mathrm{MLP}}[\mathrm{Fe}_{\mathrm{pristine}}]$$
$$E_b[V + \mathrm{He}_nV_{m-1}] = E_{\mathrm{MLP}}[V] + E_{\mathrm{MLP}}[\mathrm{He}_nV_{m-1}] - E_{\mathrm{MLP}}[\mathrm{He}_nV_m] - E_{\mathrm{MLP}}[\mathrm{Fe}_{\mathrm{pristine}}]$$

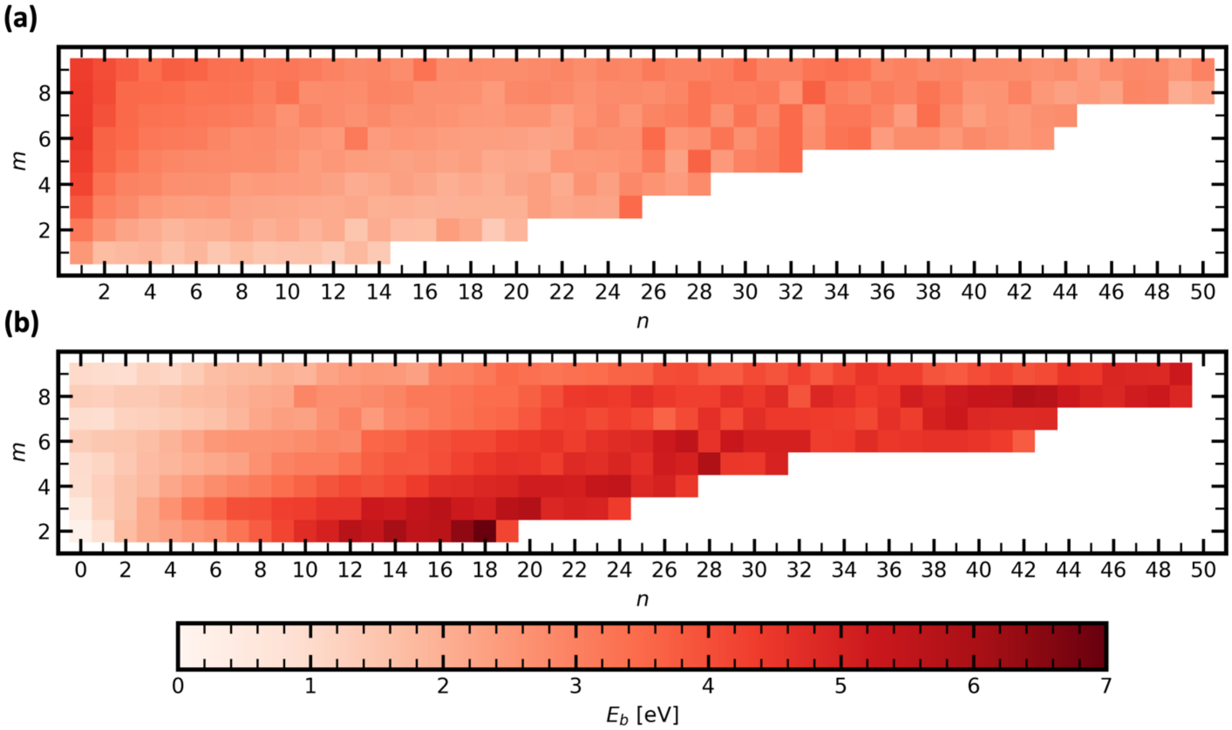

Figure 3. (a) 2D heat maps for binding energy of He atom with $He_{n-1}V_m$ bubble, $E_b[He + He_{n-1}V_m]$. (b) 2D heat maps for binding energy of vacancy with He_nV_{m-1} bubble, $E_b[V + He_nV_{m-1}]$.

Figure 3 presents the 2D heat maps for binding energy of (a) He with $\mathrm{He}_{n-1}V_m$, $E_b[\mathrm{He} + \mathrm{He}_{n-1}V_m]$, and (b) *V* with He_nV_{m-1}, $E_b[V + \mathrm{He}_{n-1}V_m]$, leading to formation of a bigger He_nV_m bubble. Note that the binding energy values are calculated until the bubble trap mutates. We find the MLP2 estimates that the trap mutation of a He_nV bubble occurs at *n*=15, differing from the DFT and MLP1 prediction of *n*=17. We are actively working to train a new potential to resolve this problem. The binding energies were calculated by employing a 12x12x12 supercell, containing 3456-*m* Fe atoms and *n* He atoms. In the case of each bubble, 10 configurations generated from NVT molecular dynamics were optimized to find the minimum energy configuration. From Figure 3 we can infer the following:

1) For small values of *n* (*n*<7), the binding energy of a He atom with $\mathrm{He}_{n-1}V_m$ bubble increases with *m*. Which means that, a He absorbed by a bubble with a greater number of vacancies is thermodynamically stable than a smaller bubble.
2) At constant *m*, i.e., for bubbles with same number of vacancies, the binding energy of He with a $\mathrm{He}_{n-1}V_m$ bubble changes non-monotonically with *n*. However, the decrease in binding energies with n is not significant. This observation differs from the binding energies calculated in previous works using empirical potentials [2-4] and DFT [5]. For example, for the He binding energies compiled from literature in Figure 4(a) of Ref [1], the slope of binding energies range between -0.052 eV/He to -0.07 eV/He. However, the slope of binding energies calculated using MLP1 and MLP2 is approximately -0.018 eV/He. Hence, the rate of decrease in the binding energies of He with He_nV bubble is smaller than previous studies. This may be due to fact that DFT studies using small supercells do not account for the periodic boundary effects and the classical empirical potentials are chemically inaccurate than MLP.
3) At constant *m*, the vacancy binding energy increases with *n*. This result can also be explained as: since the pressure increases with number of He atoms, the pressure inside the bubble is alleviated by adding a vacancy to bubble thereby decreasing the pressure.

Figure 4 presents the binding energy data from Figure 3, plotted against He/*V* ratio. The He and V binding energies are plotted as blue shade circles and brown shade triangles, respectively. In this representation, we can infer that the vacancy binding energies increase with He/V ratio. Furthermore, the He binding energies tend to decrease with He/V ratio. However, in the case of bubbles with *m*>6, the binding energies saturate between ~3.5 to ~2.5 eV. In the case of bubbles with *m*≤6, the binding energies decreases further to saturate at ~2 eV.

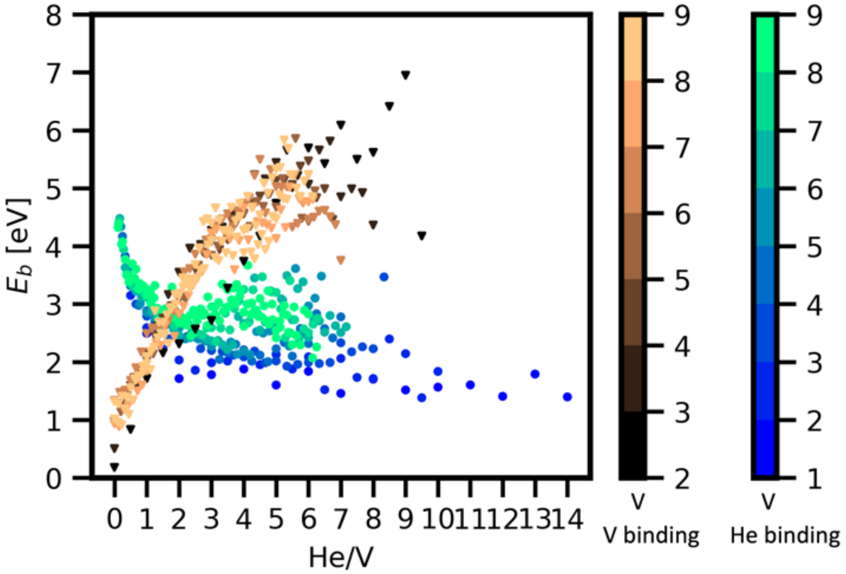

Figure 4. Binding energies of He (blue shades) and V (brown shades) plotted against He/V ratio of bubble calculated with MLP2.

We plan to further utilize MLP1 and MLP2 to estimate the He equation of state in BCC-Fe and temperature dependence of He and *V* binding energies with the He_nV_m bubble. We also plan to expand the Fe-He MLP2 to include interactions with H. This will be achieved by training the MLP with several configurations including: H interactions with BCC-Fe bulk, point defects and surfaces.

Acknowledgments

This research was supported by the U.S. Department of Energy, Office of Science, Office of Fusion Energy Sciences, through Contract No. AT2030110-13784 and was performed at the Pacific Northwest National Laboratory (PNNL), which is operated by Battelle for the U.S. Department of Energy under Contract No. DE-AC05-76RL0-1830. The research was performed using resources available through Research Computing at PNNL.

References

[1] K. C. Pitike, W. Setyawan, "Accurate Fe–He machine learning potential for studying He effects in BCC-Fe" J. Nucl. Mater. 574 (2023) 154183.
[2] F. Gao, H. Deng, H. Heinisch, R. Kurtz, “A new Fe–He interatomic potential based on ab initio calculations in α-Fe”, J. Nucl. Mater. 418 (2011) 115.
[3] T. Seletskaia, Y. Osetskiy, R. Stoller, G. Stocks, “Development of a Fe–He interatomic potential based on electronic structure calculations”, J. Nucl. Mater. 355 (2007) 367370.
[4] P.H. Chen, X.C. Lai, K.Z. Liu, X.L. Wang, B. Bai, B.Y. Ao, Y. Long, “Development of a pair potential for Fe–He by lattice inversion”, J. Nucl. Mater. 405 (2010) 156.
[5] P. Zhang, C. Zhang, R. Li, J. Zhao, “He-induced vacancy formation in bcc Fe solid from first-principles simulation”, J. Nucl. Mater. 444 (2014) 147.

9.2 MECHANICAL PROPERTIES AND RADIATION EFFECTS IN FUSION MATERIALS—Y. Osetskiy, G. Samolyuk (Oak Ridge National Laboratory)

OBJECTIVE

The objective of this task is to obtain a better understanding of the atomic-scale mechanisms operating in fusion materials. Two main groups of effects are under consideration: mechanisms of radiation damage and properties of irradiated materials. The main materials studied are ferritic and tungsten-based alloys. Main techniques applied are density functional theory (DFT), classical and DFT molecular dynamics (MD), and elasticity theory.

SUMMARY

An extensive atomic-scale study was carried out to investigate the detailed mechanisms of dislocation dynamics in the environment of radiation-induced obstacles in ferritic alloys and tungsten. Interactions between a moving ½<111>{110} edge dislocation and spherical obstacles in the size range 1 to 9 nm diameter were modeled by molecular dynamics. At this stage, we investigated processes at 300 K in Fe and 600 K in W, which are the same homologous temperatures $T_H \approx 0.16T_M$ for these materials (T_M is the corresponding melting temperature). Physical parameters of the computational model such as dislocation length and density, strain rate, and their effects on the accuracy and uncertainty of simulation results were investigated. The main aim was to obtain and compare obstacle strength parameters for different obstacles for application within the dispersed barrier hardening (DBH) model.

PROGRESS AND STATUS

Introduction

In the first stage, we obtained and compared parameters for voids, He-filled bubbles, Cu-precipitates and rigid obstacles in Fe, and voids and Re-precipitates in W. At the current stage we considered geometrical features of dislocation obstacle interactions. So far, in estimating mechanical properties change, i.e. flow stress in DBH model, due to certain obstacles, their averaged characteristics such as mean size, *D*, and number density, *N* , used as parameters together with the obstacle strength parameter, α :

$$CRSS = M\alpha\mu b\sqrt{ND}, \qquad (1)$$

where *M* is the Taylor factor that we omit here, and $1/\sqrt{ND}$ is an estimation of the mean distance between obstacles. All obstacles are assumed the same with the same parameter α. Previous studies [1] allowed us to estimate the α value treating the atomistic modeling results within the Bacon-Kocks-Scattergood (BKS) continuum modeling [2,3]. However, all these approaches considered that the moving dislocation intersects obstacle exactly at its equator [4, 5].

In the current research we investigated the geometry effects in dislocation-obstacle interactions in bcc Fe-matrix by modeling different obstacle position relatively to the dislocation slip plane. We used classical molecular dynamics modeling systems uf of up to 10^7 mobile atoms depending on the obstacle size. All models were made at 300 K ambient temperatures, at strain rate $5x10^5$ s^{-1} which is equivalent to the steady state dislocation velocity ~14 m/s. We consider here geometry when the extra-half plane, forming an edge dislocation, is above the dislocation slip plane. These effects are not considered in any modern approach. The obvious assumption is that the obstacle strength is defined by the size, i.e. diameter, of the of the obstacle by the dislocation slip plane. However, we demonstrate that these effects are more complicated and depend on the obstacle type. In general, the effect is asymmetric due to asymmetry of the stress distribution around an edge dislocation. For example, there is a negative pressure region below the dislocation slip plane and the positive pressure region above it. This affect interaction with obstacles that have either negative or positive volume dilatation. Also, earlier observed dislocation induced phase transformation in coherent Cu-precipitates [6] show quite strong asymmetry when the Cu-precipitate equator is below or above the slip plane. The critical resolved shear stress (CRSS) is higher when slip plane is below the equator and a higher level of phase transformation occurs under influence of the dislocation positive pressure.

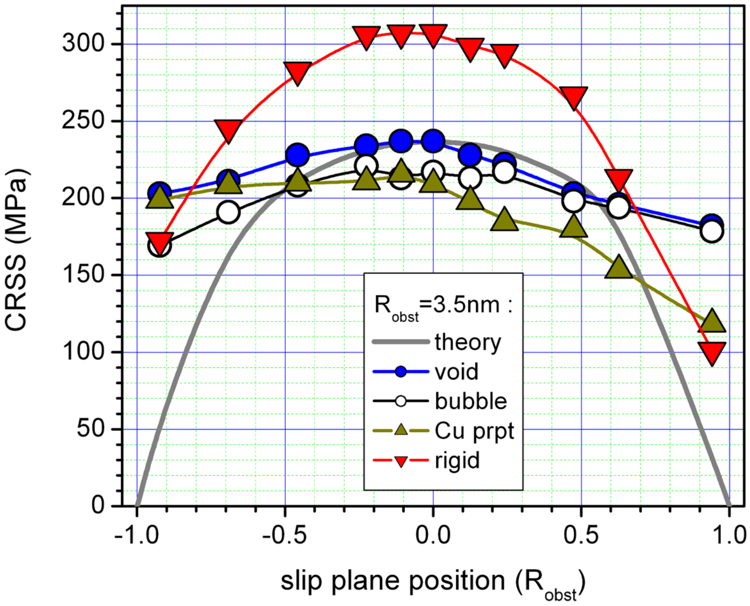

Figure 1. Critical resolved shear stress for different spherical obstacles of radius *R* = 3.5 nm as function of the ½<111>[110] edge dislocation slip plane relatively to the equator. Gray line presents theoretical estimation normalized per the current CRSS for the void.

An example of CRSS dependence versus the position of the dislocation slip plane – negative position means the slip plane is below the obstacle equator, is presented in Figure 1. Critical resolved shear stress for different spherical obstacles of radius *R* = 3.5 nm as function of the ½<111>[110] edge dislocation slip plane relatively to the equator. Gray line presents theoretical estimation normalized per the current CRSS for the void. for different obstacles of radius R = 3.5nm. The thick grey line indicates dependence estimated from the diameter of intersected obstacle segment.

Several effects can be observed, the most visible are:

1. An asymmetry of CRSS versus the position of slip plane: CRSS is higher when slip plane is below the equator.
2. The effect is different for different obstacles. For example, voids and bubble CRSS is weakly dependent on the slip plane position, whereas it is much more sensible in the case of the rigid obstacle.
3. All obstacles still have quite significant CRSS values when the dislocation does not intersect it physically.

An important observation is that all obstacles generate nonzero CRSS even when dislocation does not intersect obstacle physically and dislocation interacts with the obstacle only via their strain/stress fields. This, together with a generally weaker dependence of the CRSS versus the slip plane distance leads to the conclusion that all obstacles are effectively stronger than just geometrical objects of a certain size and shape.

Results

More obstacle sizes and ambient temperatures will be considered to investigate the corresponding effects. The theoretical model to consider these effects will be developed.

References

[1] Fusion Materials Research at Oak Ridge National Laboratory in Fiscal Year 2022, ORNL/SPR-2023/2953 (draft).
[2] D. J. Bacon, U. F. Kocks and R. O. Scattergood, The effect of dislocation self-interaction on the Orowan stress, Philos. Mag., 28 (1973) 1241.
[3] R.O. Scattergood and D.J. Bacon, The strengthening effect of voids, Acta. Metall., 30 (1982) 1665.
[4] Y. Osetsky, Atomic scale mechanisms of void strengthening in tungsten, Tungsten, 3 (2021) 65.
[5] Y. Osetsky, Strengthening of tungsten by coherent rhenium precipitates formed during low fluence irradiation, , Tungsten, 4 (2022) 20.
[6] D.J.Bacon and Y.N.Osetsky, Mechanisms of hardening due to copper-precipitates in α-Iron, Philos. Mag., 89 (2009) 3333.

9.3 FIRST PRINCIPLES STUDY OF BULK AND RADIATION INDUCED DEFECTS PROPERTIES OF TiB_2

—Y. Osetskiy, G. Samolyuk (Oak Ridge National Laboratory)

OBJECTIVE

The objective of this task is to obtain an understanding of the bulk and radiation induced defect properties of TiB_2 and atomic-scale mechanisms operating in TiB_2 under neutron irradiation. Two main groups of effects are under consideration: a) properties of point defects, their interactions and mobility, and b) microstructure evolution mechanisms under irradiation and its effect to the material mechanical and physical properties. Main techniques applied are density functional theory (DFT), classical and DFT molecular dynamics (MD), elasticity theory, and kinetic Monte Carlo modeling.

SUMMARY

Ultra-high temperature ceramics (UHTC), and particularly TiB_2, are considered very promising materials for plasma-facing components. Having exceptional high temperature properties, these materials, however, are not thoroughly tested for specific plasma facing phenomena and the mechanisms of radiation effects in them are mostly unknown. A new research line within the Oak Ridge National Laboratory (ORNL) Fusion Materials program was initiated with the main aim of understanding mechanisms of radiation damage phenomena in TiB_2 and developing predictive modeling capabilities.

PROGRESS AND STATUS

Introduction

In the first stage, we utilize a first principle-based approach to study basic properties of TiB_2, including bulk physical properties, radiation induced defects, and their interactions. Electronic structures and energies have been calculated within the density-functional theory [1] using the generalized gradient approximation (GGA) and the Perdew-Burke-Ernzerhof (PBE) [2] parametrization of the electronic exchange-correlation functional. Total energies and electronic structure were calculated using the plane-wave basis projector augmented-wave approach [3] as implemented in the Vienna Ab-initio Simulation Package (VASP) [4]. The high accuracy of modeling results was provided by the high inner energy cut-off, 520 eV, and low ionic energy convergency criterion, 10^{-6} eV. Supercells of different sizes, up to ~700 atoms, were used to investigate cell size effects on defects' energy and structure. First calculations have confirmed that basic properties of point defects, vacancy, and interstitial atoms in both sublattices, are well converged in supercell with less than ~400 atoms. This can be seen in Figure 1, where size dependences of vacancy formation energy in Ti and Be sublattices are presented.

Several positions of deuterium (D) atom in the TiB_2 bulk where tested. The absolute value to D-interstitial is not important for D implanted to the TiB_2 bulk due to plasma irradiation. However, the relative energy provides information on the most probable position in the bulk. The most stable configuration is presented in Figure 2. Note the asymmetric position of the D atom out of the hexagonal plane.

Results

For predicting H (D) retention and desorption needs, we plan to develop a kinetic Monte Carlo model; a set of parameters describing H clustering and mobility will be necessary. We therefore plan to model vacancy-H clatters, their behavior at different temperatures, and mobility parameters for H in the TiB_2 bulk, i.e. migration mechanisms and transition state energies. The model developed will be able to calculate H desorption kinetics and will be verified with experimental observations.

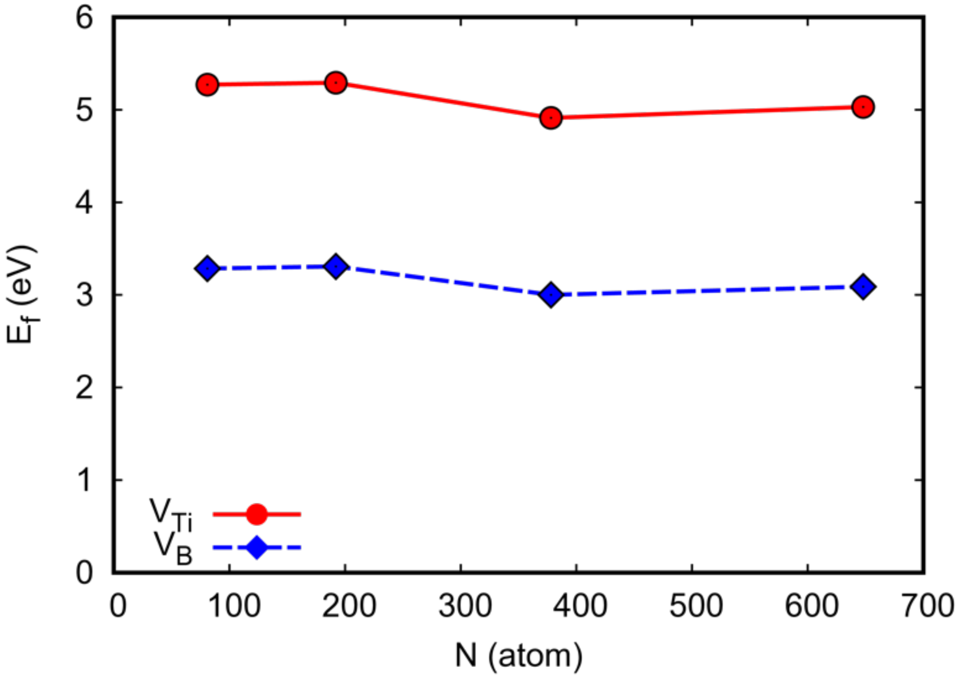

Figure 1. Convergence of vacancy formation energy in Ti and B sublattices vs the modelled supercell size.

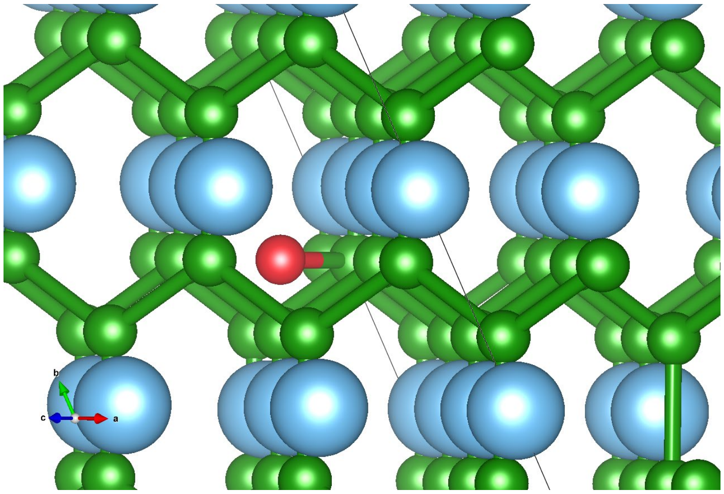

Figure 2. Atomic structure of TiB_2 and a stable position of H interstitial atom. Large blue speres are titanium atoms, small green spheres are boron atoms, red sphere is a hydrogen atom. A cross-platform program, VESTA, has been used to visualize the structure [5].

Another direction of modeling activity is understanding mechanisms and parameters for predicting dislocation loops nucleation and growth. We will model single interstitials and their clusters for estimating the structure of the most probable dislocation loops.

References

[1] W. Kohn and L. J. Sham, Self-Consistent Equations Including Exchange and Correlation Effects, Phys. Rev. 140, 1133 (1965).

[2] J.P. Perdew, K. Burke, and M. Ernzerhof, Generalized Gradient Approximation Made Simple, Phys. Rev. Lett. 77, 3865 (1996).

[3] P. E. Blöchl, Projector augmented-wave method, Phys. Rev. B 50, 17953 (1994).

[4] Vienna Ab initio Simulation Package, http://cms.mpi.univie.ac.at/vasp/.

[5] K. Momma and F. Izumi, "VESTA 3 for three-dimensional visualization of crystal, volumetric and morphology data," J. Appl. Crystallogr., 44, 1272-1276 (2011).

9.4 PREDICTING DISPLACEMENT DAMAGE FOR ION IRRADIATION: ORIGIN OF THE OVERESTIMATION OF VACANCY PRODUCTION IN SRIM FULL-CASCADE CALCULATIONS

—Y Lin, R. Stoller (Oak Ridge National Laboratory), S. Zinkle (University of Tennessee)

Extended Abstract: Full manuscript published in Current Opinion in Solid State and Materials Science 27-6 (2023) 101120 (https://doi.org/10.1016/j.cossms.2023.101120)

OBJECTIVE

The aim of this research is to investigate and comprehend the significant discrepancies observed in vacancy estimations between the full-cascade (F-C) and quick calculation (Q-C) options within the widely used computer code SRIM.

SUMMARY

Ion irradiation and implantation have wide applications that demand accurate determination of displacement damage profile and distribution of implanted ion concentration. The prediction of vacancies is especially important to determine displacements per atom (dpa), the standard parameter of primary radiation damage in materials. However, significant discrepancies exist in estimations of vacancies between full-cascade (F-C) and quick calculation (Q-C) options in the popular computer code SRIM. This study inspected the SRIM code, and a relatively new code called Iradina, which uses a similar methodology, to develop an understanding of the origin of vacancy overestimation in the F-C options for SRIM and Iradina. We found that the default values of thresholds (namely final energy in SRIM and replacement energy in Iradina) in displacement production calculations results in excessively large number of calculated vacancies and very few replacements. After conducting multiple calculations using SRIM, Iradina, and MARLOWE (all based on the binary collision approximation), a comparison of the results indicates that there is a shortcoming in the SRIM and Iradina F-C methodology for treating near-threshold collisions. This issue is responsible for the deficiency of replacements and excess of calculated vacancies in the SRIM and Iradina F-C results. Drawing on the principles of collision physics, we propose recommendations for modifying the source codes to address these issues.

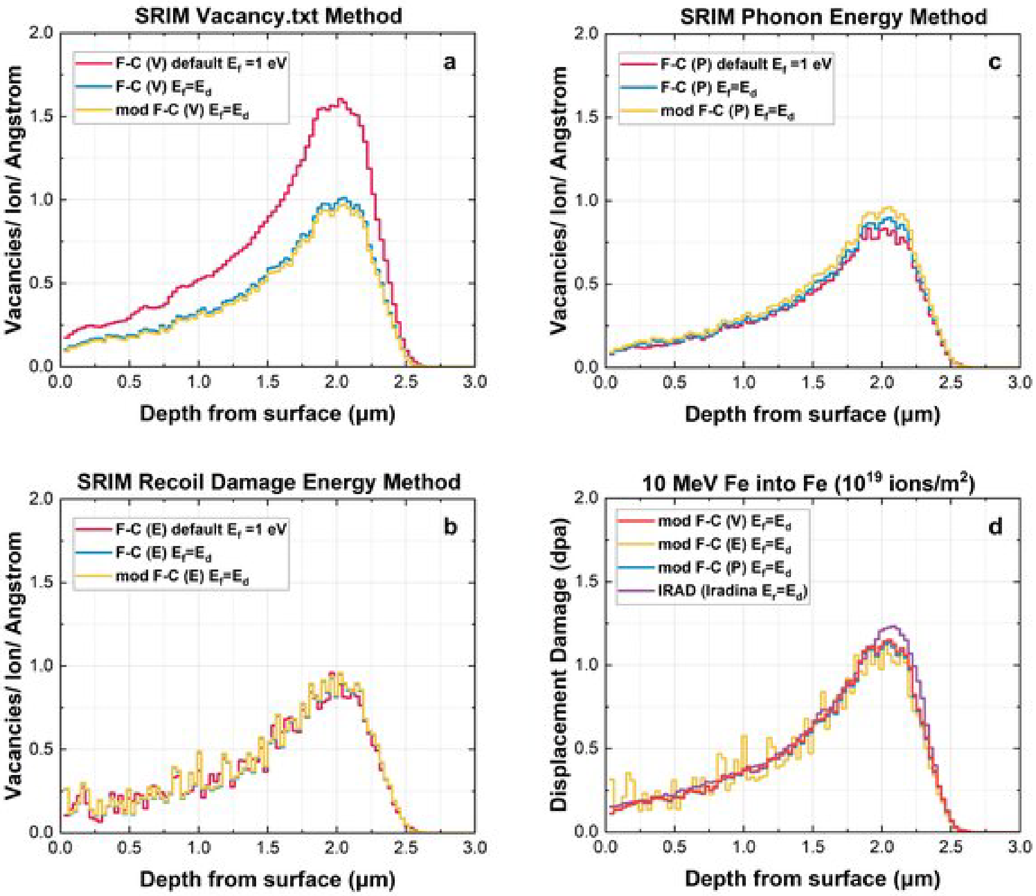

Figure 1. Comparison of various SRIM vacancy calculation methods for 10 MeV Fe ions in a Fe target: (a) Vacancy.txt methods, (b) Recoil damage energy methods, (c) Phonon energy methods, and (d) dpa depth profiles. (F-C: full cascade option, Q-C: quick calculation option, “(V)”: vacancy.txt method, “(E)”: recoil damage energy method, “(P)”: phonon energy method, mod: modified).

Results

Future work will focus on improving the IRAD software.

10. FUSION SYSTEM DESIGN

No contributions this reporting period.

11. IRRADIATION & TESTING METHODS, EXPERIMENTS AND SCHEDULES

11.1 UKAEA COLLABORATION PROJECT—T.S Byun, J.W. Geringer, Y. Lin, Y. Katoh (Oak Ridge National Laboratory), A. Gandy (United Kingdom Atomic Energy Authority)

OBJECTIVE

The United Kingdom Atomic Energy Authority (UKAEA) is engaged in exploring critical challenges related to the realization of fusion energy, including fundamental research on structural materials that can survive the harsh environments envisaged inside a future fusion reactor. The required research needs to use irradiation and post-irradiation testing and evaluation capabilities at UKAEA and Oak Ridge National Laboratory (ORNL). The ORNL is under contract to perform preparation, neutron irradiation, and post-irradiation examination/evaluation (PIE) of the select materials to determine their suitability for use in fusion energy systems. This requires the use of unique ORNL facilities including the High Flux Isotope Reactor (HFIR), Irradiated Materials Examination and Testing (IMET) hot cell facility, and Low Activation Materials and Development Analysis (LAMDA) laboratory. This collaboration also includes shipping of irradiated materials and performing PIE at UKAEA.

The objective of this collaboration program is to perform systematic studies on the irradiation-induced changes in the structural materials envisaged for fusion reactor applications. The main outcomes of the research include comprehensive understanding of the irradiation-induced phenomena including materials degradation mechanisms and informative feedback to the fusion materials development and characterization activities, including the steels development works at UKAEA and ORNL.

SUMMARY

This collaborative research focuses to investigate the behavior of fusion structural materials under irradiation. The materials of interest, in order of priority, include the Fe-Cr binary alloys, high-Cr ODS alloys, CNA alloys, FM steel welds, austenitic stainless steels, Cu alloys and SiC/SiC composites. The two thrusts of the program are: (i) a PIE campaign on existing HFIR irradiated materials at ORNL and (ii) a new HFIR irradiation/PIE campaign for a select set of materials. The PIE activities include mechanical testing, physical property measurement, and microscopy at IMET and LAMDA facilities, which also include micromechanical testing and microscopy on irradiated materials at UKAEA. In addition to the funding for the PIE and irradiation activities at ORNL, UKAEA will dispatch assignees for PIE tasks.

PROGRESS AND STATUS

- The program is in various PIE campaign stages of previously irradiated materials. Current focus on JP-30/31 and FMP capsules. Hardness testing was completed for the specimens from JP capsules and some FMP rabbits. Mechanical testing to follow on the specimens of JP-30/31 capsules.
- Respective ODS and binary alloys samples were transferred to LAMDA to start with microscopy.
- HFIR irradiation for the three capsules achieved 2 dpa and will be continued for 3 more cycles.

Results

- Testing and evaluation for irradiated and non-irradiated materials will be continued.
- Sample shipments (BOR-60 irradiated steels and samples after FIB) to UKAEA are prepared and expected to be completed during 2024.
- The first group of UKAEA visitors is expected to visit ORNL for Jan 29 thru Feb 16, 2024. Two visitors will be staying for two and three weeks respectively. The first assignment is mainly focused on steel evaluations. The second assignment for 1 visitor will follow the first, for which work will focus on testing of ceramic (SiC) samples.

11.2 EUROFUSION COLLABORATION PROJECT—T.S Byun, J.W. Geringer, T. Graening, Y. Katoh (Oak Ridge National Laboratory), M. Reith (Karlsruhe Institute of Technology)

OBJECTIVE

The Karlsruhe Institute of Technology (KIT), as a EUROfusion project, seeks to produce blanket, baseline, design-relevant materials properties data for EUROFER material variants. Oak Ridge National Laboratory (ORNL) is under contract to assist the neutron irradiation and materials testing and evaluation tasks by preparation, irradiation, and post-irradiation examination/evaluation (PIE) of the steels to determine their suitability for use in fusion energy systems. This requires the use of several unique ORNL facilities including the High Flux Isotope Reactor (HFIR), Irradiated Materials Examination and Testing (IMET) hot cell facility, and Low Activation Materials Development and Analysis (LAMDA) laboratory.

SUMMARY

The Phase I contract ended in 2019 after completing Phase 1a project. Later, both KIT and ORNL intended to continue the collaboration project in the field of neutron irradiation and PIE for qualification of EUROfusion materials in simulated fusion reactor environments. The current KIT-ORNL collaboration program has two subprojects: One (Phase 1b) project is to perform the PIE of specimens that are still irradiated within the Phase 1a (EUROfusion LOT-I campaign) KIT-ORNL contract. This Phase 1b project (LOT-I PIE) can be started as soon as HFIR irradiation is completed. The second project targets at the investigation of neutron irradiation damage by gas transmutation in 9%Cr steels based on isotopic tailoring. The KIT-ORNL application (Phase 2) includes various elements: (1) Extending an already running irradiation of EUROFER-54Fe to 25 dpa, (2) 54Fe and 58/60 Ni isotope procurement, fabrication of isotopic tailored EUROFER-type materials, and machining samples, (3) design and fabrication of irradiation capsules, (4) neutron irradiation to approximate target levels of 12-15, and >50 dpa, (5) PIE of EUROFER-54Fe from point (1), and (6) PIE of isotopic tailored materials from point (2) after 12-15 dpa.

PROGRESS AND STATUS

- The Phase-1b capsules were disassembled in 2023 and PIE activities have been continued: microhardness, temperature monitor and electrical resistivity measurements were performed for the specimens from Phase 1b (Target 25+ dpa @ ~200 – 400 ºC, SS-J3 & M4CCVN) rabbits (14 in total).
- Production of Ni-58 isotope doped RAFM alloys with high helium generation rate in HFIR irradiation is underway. The HFIR irradiation for these materials will begin in the FY.

Results

- The PIE activities for the Phase-1b specimens including mechanical testing will be continued during 2024.
- Next rabbit shipment (FMP-rabbits 30-35 dpa) after cycle 408 (~July 2024) is expected.
- We expect to finish the design and assembly of 12 new rabbits and start irradiation during before summer 2024. Material production of target alloys (Ni-58 added Fe-9Cr/Eurpfer-97 steels) is ready and six alloy variations will be included in the new rabbit irradiation campaign.
- The first dataset of post-irradiation examination (PIE, phase 1) to be reported by March 2024.

11.3 HFIR IRRADIATION EXPERIMENTS—C. On (Oak Ridge National Laboratory)

OBJECTIVE

The goal of this report is to describe the progress of the neutron irradiation experiments that were performed in the High Flux Isotope Reactor (HFIR) and the operating status of HFIR.

SUMMARY

During the six-month period starting from July 1st to December 31, 2023, a total of thirty-four rabbit capsules continued their irradiation. Two rabbits have completed the scheduled irradiation.

PROGRESS AND STATUS

Neutron irradiation experiments were performed in support of the research and development of fusion reactor materials using various materials irradiation facilities in the High Flux Isotope Reactor. The reactor operating history for the period from July 1– December 31, 2023, is detailed in Table 1.

Table 1. HFIR operating record for the semi-annual FY2023

Cycle Number	Cycle Start Date	Cycle End Date	Power (MWD)
502	July 18	August 12	2138.24
503	August 29	September 24	2177.95

All the fusion materials program irradiation experiments performed during this period (FY2023) used the nominally two-inch rabbit capsules, with no full-length target rod nor instrumented reflector position capsules within that period. Thirty-four target zone rabbit capsules remain in the reactor to complete the scheduled irradiations. These capsules are listed in Table 2 along with condensed information on the material, specimen type, temperature, fluence, and period of irradiation. Two rabbits have completed the scheduled irradiation as shown in in Table 3.

Table 2. The rabbit capsules to continue irradiation in HFIR

Experiment Designation	Primary Materials	Specimen Types	Irradiation Temperature (°C)	Max Exposure (dpa)	Number of Reactor Cycles	HFIR Cycles Start–End
FH11	F82H-IEA / F82H-mod3	Tensile	300	80	46	496 – 541
FH12	F82H-IEA / F82H-mod3	Tensile	400	80	46	496 – 541
FH13	F82H-IEA / F82H-mod3	Tensile	500	80	46	496 – 541
FH21	F82H-IEA / F82H-mod3	Bend Bar	300	80	55	496 – 550

FH22	F82H-IEA / F82H-mod3	Bend Bar	300	80	55	496 – 550
FH23	F82H-IEA / F82H-mod3	Bend Bar	400	80	55	496 – 550
FH24	F82H-IEA / F82H-mod3	Bend Bar	400	80	55	496 – 550
FH25	F82H-IEA / F82H-mod3	Bend Bar	500	80	48	496 – 543
FH26	F82H-IEA / F82H-mod3	Bend Bar	500	80	48	496 – 543
FH31	F82H-IEA / F82H-mod3	Tensile	300	50	29	500 – 528
FH32	F82H-IEA / F82H-mod3	Tensile	400	50	29	500 – 528
FH33	F82H-IEA / F82H-mod3	Tensile	500	50	29	500 – 528
FH41	F82H-IEA / F82H-mod3	Bend Bar	300	50	35	500 – 534
FH42	F82H-IEA / F82H-mod3	Bend Bar	300	50	35	500 – 534
FH43	F82H-IEA / F82H-mod3	Bend Bar	400	50	29	500 – 528
FH44	F82H-IEA / F82H-mod3	Bend Bar	400	50	29	500 – 528
FH45	F82H-IEA / F82H-mod3	Bend Bar	500	50	29	500 – 528
FH46	F82H-IEA / F82H-mod3	Bend Bar	500	50	29	500 – 528
FMP07	F82H	Tensile	300	20	21	487 – 507
FMP08	F82H	Tensile	300	80	45	487 – 531

FMP11	F82H	Tensile	385	20	21	488 – 508
FMP12	F82H	Tensile	385	80	45	488– 532
FMP14	F82H	Tensile	525	20	21	484 – 504
FMP17	F82H	Tensile/MPC*	650	80	45	484 – 528
FMP22	F82H	Bend Bar	300	20	21	488 – 508
FMP23	F82H	Bend Bars	300	80	45	488 – 532
JCR11-03	SiC/SiC	Mini Bend Bar	950	200	100	487 – 586
JCR11-05	SiC/SiC	Mini Bend Bar	950	200	115	444 – 568
JCR11-08	SiC/SiC	Mini Bend Bar	950	200	115	444 – 560
JCR11-11	SiC/SiC	Mini Bend Bar	950	100	55	448 – 524
SCF4	SiC/SiC	Mini Flexure Bar	250	100	90	457 – 547
SCF5	SiC/SiC	Mini Flexure Bar	250	200	45	457 – 511
SCF9	SiC/SiC	Mini Flexure Bar	600	200	90	457 – 548
SCF11	SiC/SiC	Mini Flexure Bar	950	100	57	458 – 517

*MPC: Multi-Purpose Coupon

Table 3. The rabbit capsules that completed irradiation in cycle 502

Experiment Designation	Primary Materials	Specimen Types	Irradiation Temperature (°C)	Max Exposure (dpa)	Number of Reactor Cycles	HFIR Cycles Start–End
FR12	Joint W Alloy	Disc (D6)	300	1.2	6	497 – 502
SCF8	SiC/SiC	Mini Flexure Bar	600	100	45	457 – 502